Università degli Studi di Trieste

XXXIV ciclo del dottorato di ricerca in

Fisica

Toward a joint analysis of the galaxy power spectrum and bispectrum in redshift space

Settore scientifico-disciplinare: Astronomia e Astrofisica

Dottorando:

Federico Rizzo

Coordinatore:

Prof. Francesco Longo

Supervisore di tesi:

Prof. Emiliano Sefusatti

Anno accademico 2020-2021

Declaration

I hereby declare that this thesis is my original work and it has been written by me in its entirety. I have duly acknowledged all the sources of information which have been used in the thesis.

This thesis has also not been submitted for any degree in any university previously.

Federico Rizzo
Trieste, June 2022

Abstract

Future spectroscopic galaxy redshift surveys will observe the Large-Scale Structure (LSS) of the Universe over large volumes with the goal of testing the Standard Cosmological Model with high accuracy. This will be achieved thanks to the developments of LSS studies directed towards the optimisation of the extraction of cosmological information from correlation functions of the observed galaxy distribution. These efforts focused on the progressive refinement of the theoretical Perturbation Theory modelling, and on the optimisation of the estimators that provide measurements, reaching an agreement for current N-body simulations of the order of sub-percent level between the two. This work aims to build the tools required for the joint analysis of the redshift-space power spectrum and bispectrum, fully exploiting the content of their anisotropic signal, and to characterize the parameter constraints that can be expected from such analysis.

In a first stage, together with my collaborators, I investigate the benefit of a power spectrum and bispectrum joint analysis in real space in terms of the improvement, with respect to a power spectrum-only study, of parameter posteriors extracted from a likelihood analysis. In doing so, we take advantage of a set of 300 N-body simulations and an even larger set of mock catalogs. In this work I also explore different options to define the range the validity of the real-space bispectrum model with respect to those usually found in the literature, and assess the advantages resulting from the adoption of these definitions in terms of constraints on bias parameters.

Afterwards, I focus on extending my results to Fourier space, discussing the main goal of my Ph.D. project, i.e. the estimate and analysis of the galaxy bispectrum multipoles. For this project we adopt the same simulations used for the power spectrum and bispectrum joint analysis in real space. We fit measurements of the bispectrum $\ell = 0, 2, 4$ multipoles with a tree-level model in perturbation theory that depends on linear and nonlinear bias parameters as well as on the growth rate of density fluctuations. We find that the range of validity of the tree-level model, for the total volume of the N-body simulations, of about 1000 $\mathrm{Gpc}^3\,h^{-3}$, reaches a maximum wavenumber of $0.08\,\mathrm{Mpc}\,h^{-1}$ for the monopole, while it is limited to 0.06 and $0.045\,\mathrm{Mpc}\,h^{-1}$ respectively for quadrupole and hexadecapole. We confirm results of previous forecast studies saying that the addition of the quadrupole to the analysis allows for significant improvements, specially on f

constraints. Finally, we compare our numerical estimate for the covariance with its theoretical prediction in the Gaussian approximation and find the latter to work remarkably well.

Eventually I discuss two projects to which I have provided a minor contribution, one dealing with the derivation of an expression to compute the the convolution of bispectrum predictions with the survey window, and the other studying the additional constraining power provided by the redshift-space bispectrum multipoles to the power spectrum ones.

Contents

Chapter 1

Introduction

Studies about the nature of the Universe and the fundamental interactions that govern its physical evolution focus today on testing the Standard Cosmological Model against several probes, with the Cosmic Microwave Background, gravitational waves, and standard candles being some notable examples. In addition, the large-scale distribution of matter and galaxies revealed in weak lensing and galaxy surveys has been playing an increasingly large role in the last years.

Spectroscopic galaxy surveys, in particular, provide a three-dimensional picture of the Large-Scale Structure. The correlation function of the galaxy distribution, or its Fourier Transform, the power spectrum, are in this case the main observables. This represents the probability of finding two galaxy at a given spatial separation and constitutes the main characterisation of the galaxy field statistical properties.

An important feature imprinted on the galaxy 2-point correlation function is the peak due to baryonic acoustic oscillations in the early Universe. Given the well-understood underlying physics, this has been recognised as a cosmological standard ruler, allowing to constrain the late-time accelerated expansion of the Universe. Another important aspect of the 2-point correlation function is the anisotropy induced by Redshift Space Distortions (RSD) [94]. This effect is linked to the intrinsic nature of distance measurements along the line of sight in spectroscopic surveys based on the redshift determination and Hubble's law. The peculiar velocity of the galaxy, however, adds to the Hubble expansion and alter the measured distance and thus the final spectra. This anisotropy, controlled at large scales by the matter velocity, can be use to constrain the growth rate of structures.

The study of these features of the galaxy 2-point function or power spectrum do not fully exploit their information content. The most recent analyses of the BOSS galaxy survey aim at the so-called "Full Shape" analysis of the power spectrum [90, 39, 95, 152], mostly thanks to the refinement of theoretical models in the last decade.

If the galaxy distribution was a Gaussian random field, its statistical properties would be completely encoded in its 2-point function. While the Planck experiment showed that the Gaussian picture is a very good description of the density perturbations during early stages of the Universe, non-Gaussianity is induced by gravitational instability, non-linear galaxy

bias and RSD, and spreads the information content from the 2-point to over higher-order correlation functions. Moreover, despite current bounds from the CMB, a certain level of non-Gaussianity could still be detected in the initial conditions, providing important information of the model of inflation describing the very early Universe [37]. It is therefore imperative for the upcoming surveys to go beyond the analysis of two-point statistics in order to extend and strength the results from the standard analysis of the two-point correlation function and power spectrum.

The lowest order statistics to quantify non-Gaussianity is the 3-point correlation function or, in Fourier-space, the bispectrum. This represents the excess probability, with respect to an uncorrelated, Poisson distribution to find a triplet of glaaxies forming a triangle of a given size and shape. The first bispectrum measurements provided a first test of early models of gravitational instability on large-scales [18], nonlinear bias [59, 105] and local non-Gaussian Initial Conditions [93, 145]. Besides, bispectrum measurements provide additional, "perpendicular" information in the full-shape analysis, lifting degeneracies between model parameters present in the case of the single power spectrum. Several recent works focus on the derivation of model parameter constraints from the joint analysis of 2 and 3-point statistics [64, 67, 68, 121, 39, 127] showing that the addition of this observable helps improve these constraints by a significant level.

A proper analysis pipeline for the bispectrum, however, is still being defined. For instance, while the power spectrum analysis takes routinely full advantage of the anisotropy induced by RSD in terms of a multipole expansion (see e.g. [4, 139]), past bispectrum analyses have always been limited to the monopole, with the notable but very recent exception of [38]. Nonetheless, as in the power spectrum case, the anisotropic signal carries additional information and a complete analysis should take advantage of this contribution. A few of forecast works considered the relevance of the full anisotropic bispectrum [158, 61, 170, 77, 28] remarking that we can expect additional information in the higher-order multipoles of the bispectrum, although the exact extent of improvement on parameters constraints depend on several assumptions on the parameters considered, the covariance model, and survey features.

My Ph.D. work addresses the analysis of the redshift-space bispectrum in terms of its multipoles, monopole, quadrupole and hexadecapole providing a rigorous and extensive comparison of measurements in numerical simulations to the tree-level predictions in perturbation theory, adopting the definition of [147]. We perform a likelihood analysis sharing the same methodology of references [119] and [118]. In particular, our work constitutes the natural continuation the study started with these papers exploring in details the challenges of a joint analysis of the galaxy power spectrum and bispectrum, there limited to real-space. Our aim, for the future, will be to give a full redshift-space analysis of power spectrum and bispectrum, using an extended multipoles decomposition for both the observables.

Each of these works focus on a single extension to our pipeline, and meticulously investigates several methodological choices. The first work of this series [119], presented a full likelihood analysis of the bispectrum monopole in real space. This opening paper also presents extensively the tools adopted for this works, namely: our likelihood code to perform Monte Carlo Markov Chains (MCMC) for the evaluation of posterior distributions, the reference set of 300 N-body simulations of Dark Matter halos used as data vector, and the set of 10,000 mocks generated by the approximate Pinocchio code used to compute the covariance matrix. A second paper [118], to which I directly contributed, considers the joint likelihood posteriors of power spectrum and bispectrum in real space. This will be described in Chapter 4. The main work of this thesis, described in chapter 5, extends the analysis to bispectrum multipoles in redshift space. We describe the cosmological inference results for the bispectrum multipoles alone in order to provide tools to interpret future work, already in preparation, that will combine power spectrum and bispectrum multipoles together. This will be mentioned in the last chapter along with extensions to the analysis pipeline that will eventually enable the analysis on actual data from a survey with non-trivial geometry.

The whole work is of particular relevance for the upcoming Euclid spectroscopic galaxy survey which is expected to be launched in 2024 and that will provide observations over a large fraction of the sky, $15000\,\mathrm{deg}^2$, in a redshift range $0.2 \leq z \leq 1.8$, still unobserved by present-day LSS missions. Part of my Ph.D was carried out as a member of the Euclid Collaboration where I worked in the Level 3 Galaxy Clustering Organisation Unit, the team responsible for the development of scientific data analysis software that will provide official measurements of the correlation functions of the galaxy distribution. In this work, Chapter3 is dedicated to the description of the power spectrum and bispectrum estimator codes that I developed, that will eventually contribute to the official Euclid data analysis Pipeline and that I used as well for almost all measurements mentioned in this thesis.

Chapter 2

The Large Scale Structure of the Universe

2.1 Introduction on Cosmology

2.1.1 Einstein Field Equations

From its very first stages [52], the attempts to provide a mathematical description of the Universe structure, as a whole, had deep roots in the Theory of General Relativity (GR). At present, the validity of such description holds up even to observations of extreme events in the cosmos [1]. According to this interpretation (and differential geometry), the Einstein tensor governs the local curvature of a differentiable mainfold on which a symmetric, smooth and non-degenerate metric $g_{\mu\nu}$ is defined. Such object is given by

$$G_{\mu\nu} = R_{\mu\nu} - \frac{1}{2} g_{\mu\nu} R \,, \tag{2.1}$$

where $R_{\mu\nu}$, the Ricci tensor, and R, the Ricci scalar, depend solely on the metric. This object is symmetric and is only subject to variations in the second-order partial derivatives of the metric tensor and on the square first order ones.

In GR, the Einstein tensor is directly related to the stress-energy tensor

$$T_{\mu\nu} = (\rho + p) u_\mu u_\nu - p g_{\mu\nu} \tag{2.2}$$

describing the matter-energy distribution in terms of the density ρ, velocity u_α and pressure p of a fluid that permeates and flows in space, through the Einstein Field Equations (EFE)

$$G_{\mu\nu} - \Lambda g_{\mu\nu} = \frac{8\pi G}{c^4} T_{\mu\nu} \,, \tag{2.3}$$

where the Λ-term corresponds to a constant contribution to the overall curvature that can be absorbed by $T_{\mu\nu}$. This equation describes how the curvature is sourced by the matter-energy distribution through the stress-energy tensor which acts on the metric through its second derivatives.

2.1.2 Friedmann Equations

Along with GR, the modern description of the Universe is built upon the assumption that matter is distributed homogeneously and isotropically on large scales. This hypothesis, which goes with the name of Cosmological Principle (CP), allows to define a reference frame where matter can be considered (at first order) at rest and where cosmic distances and time intervals are described by the metric

$$ds^2 = g_{\mu\nu}dx^\mu dx^\nu = c^2dt^2 - a^2(t)\left[\frac{dr^2}{1-\mathcal{K}r^2} + r^2d\theta^2 + r^2\sin^2\theta d\varphi^2\right]. \tag{2.4}$$

This is the Friedmann-Lemaitre Robertson Walker (FLRW) metric [137] [167] which describes the behavior of space-time differentials in a homogeneous and isotropic universe free to expand or contract. This behavior is described through scale factor $a(t)$. The spatial coordinates in equation (2.4) are called comoving coordinates[1] and t is the cosmic time, the temporal coordinate measured by comoving observers at each point (r, θ, φ).

We can then insert the FLRW metric in the EFE to obtain differential equations for the scale factor, the Friedmann equations. The only non-vanishing Ricci tensor components are

$$R_{00} = -3\frac{\ddot{a}}{a} \tag{2.5}$$

$$R_{ii} = \left[\frac{\ddot{a}}{a} + 2\left(\frac{\dot{a}}{a}\right)^2 + \frac{2\mathcal{K}}{a^2}\right]g_{ii} \tag{2.6}$$

and the Ricci scalar is

$$R = -6\left[\frac{\ddot{a}}{a} + \left(\frac{\dot{a}}{a}\right)^2 + \frac{\mathcal{K}}{a^2}\right]. \tag{2.7}$$

Writing the time and spatial component separately, the Einstein tensor becomes

$$G_{00} = 3\left(\frac{\dot{a}}{a}\right)^2 + \frac{3\mathcal{K}}{a^2} \tag{2.8}$$

$$G_{ii} = -\left[2\frac{\ddot{a}}{a} + \left(\frac{\dot{a}}{a}\right)^2 + \frac{\mathcal{K}}{a^2}\right]g_{ii}\,. \tag{2.9}$$

Under CP, the existence of a frame under which matter can be considered at rest at first order allows to write the stress-energy tensor of equation (2.2) for a perfect fluid as a

[1] In Cosmology, two types of coordinates are ususally used: proper and comoving. The first ones are defined in a static system of reference so that space elements enlarge as the Universe expands. In the second case, the metric follows the expansion of the universe, so that volume elements remain constant. The two are related through the scale factor by $dx = dl/a$.

diagonal with

$$T_{00} = \rho g_{00} \tag{2.10}$$

$$T_{ii} = -\, p g_{ii}\,. \tag{2.11}$$

Friedmann equations result from replacing the Einstein tensor for the FLRW metric (2.8) and the expression for the stress-energy tensor under the perfect-fluid approximation (2.10) in the EFE (2.3), giving

$$\left(\frac{\dot{a}}{a}\right)^2 = \frac{8\pi G}{3}\rho + \frac{\Lambda}{3} - \frac{\mathcal{K}}{a^2} \qquad \text{Friedmann I} \tag{2.12}$$

$$\frac{\ddot{a}}{a} = -\,\frac{4\pi G}{3}\Big(\rho + 3p\Big) + \frac{\Lambda}{3} \qquad \text{Friedmann II} \tag{2.13}$$

where, from now on, we adopt the usual notation $c = 1$, and the second equation is gathered by subtracting from it (2.12), to remove the $(\dot{a}/a)$ dependence present in the original form. These equations govern the evolution of the scale factor $a(t)$ in an isotropic and homogeneous universe filled by a perfect fluid of density ρ and pressure p.

2.1.3 Energy content of the Universe

An additional step can be taken by considering an equation of state for the perfect fluid

$$p = w\rho\,, \tag{2.14}$$

where w contains information on the fluid properties. Assuming the shear components to be negligible in the early Universe, the condition of momentum conservation $\nabla_\mu T_{\mu,\nu} = 0$ can be solved under the perfect-fluid approximation, giving

$$\rho \sim a^{-3(1+w)}\,. \tag{2.15}$$

For ordinary, non-relativistic matter, $w = 0$ and $\rho_m \sim a^{-3}$; for radiation, $w = 1/3$ and $\rho_r \sim a^{-4}$; for a constant energy density, $\rho_\Lambda \sim a^0$ so that $w = -1$. The contribution of the different species to the stress-energy tensor is traditionally formulated in terms of the density parameters, defined with respect to the value of the total matter-energy density which would correspond to a flat geometry $\mathcal{K} = 0$, $\rho_{\rm crit}$:

$$\Omega_j(t) = \frac{\rho_j(t)}{\rho_{\rm crit}(t)}\,, \tag{2.16}$$

where

$$\rho_{\rm crit} = \frac{3H^2(t)}{8\pi G} \simeq 1.87847 \cdot 10^{-29} (h^2\,{\rm g\,cm^{-3}}) \tag{2.17}$$

and $h = H_0/100$ is just a convenient way of writing the Hubble parameter, i.e. the value of the present-day Hubble parameter in units of $100\,{\rm km\,s^{-1}\,Mpc^{-1}}$. The current estimates of

the density parameters refer to the data collected by the Planck mission and are reported in Table 2.1.

At present day the dominant energy source is Dark Energy (DE), responsible for the late-time accelerated expansion. The true origin of this component is still object of great debate in the scientific community and much of the current observational efforts are directed towards uncovering its nature. The expansion of the Universe was first observed by Hubble [87]. This discovery forced Einstein to reject his choice of introducing an additional parameter Λ in the EFE during his attempts to extrapolate the local metric of the Universe outside of the domain of cosmological observations. At that time, Λ emerged from the desire to obtain a static solution to a homogeneous universe which turend out to be inconsistent with the first observation of cosmic expansion. Ironically, this quantity was reconsidered after the discovery of the expansion acceleration, confirmed nowadays by observations of the Cosmic Microwave Background (CMB) [129], of Type-Ia Supernovae [133, 134] and Baryonic Acoustic Oscillations (BAO) [4]. In Friedmann equations (2.12) and (2.13), it is described by the Λ parameter, the cosmological constant, and can be absorbed in the stress-energy tensor as a component providing a constant energy budget which sources the accelerated expansion at late times. A possible physical interpretation of this term is *vacuum energy*. However, problems arise when one tries to relate such form of energy to the respective Quantum Mechanical definition of vacuum-state energy fluctuations. In particular, the value of the energy density calculated assuming this Quantum Mechanics origin clashes with the one resulting from cosmological observations by nearly 60 orders of magnitude. Another issue with the cosmological constant model is the *coincidence problem*, the fact that the Ω_Λ being very close to present mass density of the Universe could be more than a fortuitous event.

Over the years, other models have been proposed to give an alternative explanation for the accelerated expansion. Among these, time-evolving DE models like *Quintessence* [173] and Modified Gravity (MG) models [92], postulating deviations of from standard GR equations on cosmological scales, have been explored. Although these theories are able to solve the coincidence problem (Quintessence) or both (MG), many models of the second class have been recently ruled out [104] since the observation of the black hole-black hole merger event of [1]. This represents the first detection of gravitational waves, confirming Einstein prediction of 1916 and providing tests of gravity in the strong-field regime. Relating the mass and spin of the final object to the same quantities of original mergers, and testing the phase of the gravitational waveform no evidence for disagreement with GR has been observed. Next-generation galaxy redshift surveys envision to provide accurate tomographic measurements on the equation of state parameter describing DE at multiple redshifts, and therefore will possibly be able to rule out Quintessence or models for which w deviates significantly from -1.

Matter represents almost 30% of the total density but only 4% is ascribable to baryons. The main contribution is supplied by an unknown form of matter, which is expected have

a low interacting cross-section with ordinary matter and light. Evidence for its existence dates back to 1933, when Zwicky observed that the gravitational virial mass derived from the dynamics of the Coma cluster, was much higher than that estimated from the luminous content through a well-known empirical relation translating brightness to mass. Today, hints to the existence of this elusive component have grown over the years, the rotation curves of spiral galaxies [138], studies on intra-cluster motions [174], gravitational lensing measurements, and CMB experiments [85], [129] being only few of them. The nature of this component is still debated and many particle candidates have been proposed. Cold Dark Matter (CDM) is a particular model of Dark Matter (DM) defined in such a way that it is non-relativistic when it decouples from radiation and was introduced by Peebles [123] to predict temperature fluctuations compatible with CMB limits, and since then it has been overly refined [159] [10].

Finally, relativistic species include radiation and relativistic neutrinos and account for only 0.001% of the total energy density at present time.

Substituting the expressions for (2.16) in the Friedmann equations (2.12) and (2.13), governing the evolution of the scale factor in terms of the energy content of the universe, gives

$$H^2(t) = H_0^2[\Omega_{r,0}a^{-4}(t) + \Omega_{m,0}a^{-3}(t) + \Omega_{\Lambda,0} + (1-\Omega_0)a^{-2}]\,, \tag{2.18}$$

where the null indices indicate that the density parameters are evaluate at present time. After inserting the current values of these parameters, measured by observations, this equation can be solved returning the time-evolution of $H(t)$. Consequently, it is possible to identify the phases in which a particular component has dominated the energy content of the Universe. In first approximation, looking at the dependence of the different terms in the equation above on the scale factor, one can predict three main stages. At early times, we expect an era during which the dynamics is dominated by relativistic species (*Radiation Dominated* era). Then, after the equivalence of matter and radiation contribution $\Omega_{r,0}(1+z_{\rm eq}) = \Omega_{m,0}$, non relativistic matter is expected to dominate the energy budget (*Matter Dominated* era). These relative contributions decrease in time and eventually the cosmological constant becomes the main energy component (*DE Dominated* era).

2.1.4 Initial Conditions

Before ending this section, we want to clarify the scenario which seeded the particular conditions we observe in the Universe today. A well known concept is that taking $t \to 0$, leads to a singularity problem where the overall temperature and other physical quantities diverge to ∞. This situation corresponds to a time when Quantum Mechanics effects dominate. As a result of the continuous expansion, the Universe cooled and the physics became governed by the laws we have outlined in this section. The picture arising from this description, known as Standard Model of Cosmology, however, is not free of problems. Let

us consider the most relevant.

The picture arising from observations of the CMB yields a Universe homogeneous and isotropic on large scales, yet made by a several number of disconnected regions which have never been in causal contact. Therefore, it is difficult to explain why all these regions show the same temperature values. This goes with the name of *horizon problem*. In addition, the present-day density of the Universe is very close to critical density $\Omega_{\rm tot} \sim 1$ (*flatness problem*), which is difficult to explain, for if an initial curvature would had been present $\Omega_{\rm tot} \neq 1$ in the primordial Universe, this could only increase in time. The present observations of a vanishing curvature thus, require that the primordial one would had been even smaller in magnitude, resulting in a fine-tuning problem.

These problems are solved by the inflationary paradigm [78]. The exponential expansion characterising the inflationary paradigm would boost the comoving radius of the horizon reachable by photons, providing a way to solve the horizon problem. As a matter of fact, according to the inflationary model of [78], two sky patches that appear disconnected on the CMB plane, were actually part of the same connected region before the inflationary expansion. Moreover, this hypothesis would also solve the flatness problem since, as a result of the expansion, the curvature radius would exponentially increase, leading $\Omega_{\rm tot}$ to 1. Several models have been proposed over the years as possible implementation of the mechanism, and today inflation is still a hot topic in Cosmology [20, 9, 48, 79]. For the sake of this work, it is worth to mention that apart from the solutions to the problems above that motivated its introduction, inflation provides an explanation to the origin of matter perturbations that seed the formation of late-times collapsed structures.

To summarize, the equations we have discussed in this section describe a Universe that obeys GR and where the fabric of space-time is described in terms of space-time elements that obey to the FLRW metric, under the assumption of homogeneity and isotropy. This space, filled with a matter-energy distribution that is described in terms of a perfect fluid, expands with an accelerated rate. The expansion is described in terms of a scale factor that obeys Friedmann equations and which undergoes three different evolutionary states according to the epoch we consider it (which, in turn, depends on the specific component that dominates the total energy budget). According to present-day observations, we have $\Omega_\Lambda \simeq 0.7$, $\Omega_m \simeq 0.3$, $\Omega_r \simeq 10^{-4}$, $\Omega_c \simeq 0.25$. This description, coupled with the most appreciated models for DE and DM, the cosmological constant Λ and CDM, make up the ΛCDM Standard Model of Cosmology, usually combined with the inflationary paradigm. This model proved successful in describing many observational evidences such as the early Universe, the accelerated expansion at late-times, and the distribution of matter on large scales, which preserves imprints of processes that shaped its history, and represents the most established explanation for most present day observations.

However, this is not the end of the story as questions related to the true nature of cosmic

Table 2.1: Present-day density parameters from Planck analysis [129], $\Omega_{m,0}$ and $\Omega_{\Lambda,0}$ estimated from temperature power spectra (TT), polarisation spectra (EE), cross spectra (TE), and Low-ℓ HFI EE polarisation (LowE), or estimated from its results, $\Omega_{r,0}$ and $\Omega_{c,0}$.

Density source	Relative abundance
$\Omega_{m,0}$	0.3166 ± 0.0084
$\Omega_{\Lambda,0}$	0.6834 ± 0.0084
$\Omega_{r,0}$	$\sim 9.23640 \cdot 10^{-5}$
$\Omega_{c,0}$	0.2649 ± 0.0026

accelerated expansion, DM, and Inflationary models, remain that are still unanswered at the moment. Future observations aim at refine current constraints on the cosmological model parameters and probe epochs that remain mostly uncovered. Some of these missions will couple an exceptional redshift depth with an incredible angular aperture, observing the Universe over large sky areas and will take measurements of remarkable accuracy which will allow to study LSS with unprecedented subtlety.

2.2 Statistics of classical random fields

The easiest and most general description to study the matter density perturbations is in terms of classical random fields, variables that assume a stochastic value in each point of space. Statistical properties of matter perturbations can then be computed from moments of these objects[2]. Given a random field $\psi(\mathbf{x})$ with Probability Distribution Function (PDF) $\mathcal{P}(\psi)$, its n-order moment is given by

$$\langle \psi^n \rangle = \int \mathrm{d}\psi \, \psi^n \mathcal{P}(\psi) \,, \tag{2.19}$$

while its multi-point moments, expressing the degree of correlation of the random field at different positions, are

$$\langle \psi(\mathbf{x}_1) \dots \psi(\mathbf{x}_n) \rangle = \int \mathrm{d}\psi_1 \dots \mathrm{d}\psi_n \, [\psi_1 \dots \psi_n] \, \mathcal{P}\big(\psi_1, \dots, \psi_n\big) \,, \tag{2.20}$$

and are often called n-point correlation functions.

In LSS studies theoretical predictions are defined in terms of ensemble averages. However, when comparing to observations we are limited by having at our disposal a single Universe.

[2]Meaning that knowing all the moments of a random field is potentially equivalent to having its PDF.

We must assume therefore that ensamble averages are equivalent to volume integrals, so that

$$\int \mathrm{d}\psi\, \psi \mathcal{P}(\psi) = \lim_{V\to\infty} \frac{1}{V} \int_V \mathrm{d}^3\mathbf{x}\, \psi(\mathbf{x})\,. \tag{2.21}$$

This is the hergodic hypothesis. We should also assume, of course, that the observed volume represents a "fair sample" of the Universe.

In Cosmology we usually focus on two types of random fields: the matter density contrast δ and the density contrast of a distribution of objects that trace the matter field, as galaxies δ_g, or DM halos δ_h. These quantities represent at each point the local variation in the matter density $\rho(\mathbf{x})$ or galaxy/halo number count $n_{g/h}(\mathbf{x})$ with respect to its mean value, computed over a large volume. In order to avoid duplication, in the following description we will only discuss equations regarding one of the random fields, the matter density contrast, as equations for δ_h and δ_g are equivalent to the ones we will derive for δ. Neglecting for the moment the time component, and writing the equations for ρ, we have

$$\rho(\mathbf{x}) = \bar{\rho}\,[1 + \delta(\mathbf{x})]\,, \tag{2.22}$$

where $\bar{\rho} = \langle\rho(\mathbf{x})\rangle$, with $\langle\rangle$ representing the ensemble average operator.

Before proceeding, we want to point-out that in general one can distinguish between a connected and an unconnected contribution to a correlation function. For the two-point correlation of (2.22), we have

$$\langle\rho(\mathbf{x}_1)\rho(\mathbf{x}_2)\rangle = \langle\rho(\mathbf{x}_1)\rangle\langle\rho(\mathbf{x}_2)\rangle + \langle\rho(\mathbf{x}_1)\rho(\mathbf{x}_2)\rangle_c\,, \tag{2.23}$$

where the second term corresponds to the connected contribution to the two-point correlation function of the matter density field ξ. Taking the ensemble average of ρ, it is straightforward that $\langle\rho(\mathbf{x})\rangle = \bar{\rho}$ returns $\langle\delta(\mathbf{x})\rangle = 0$, so that

$$\begin{aligned}\langle\rho(\mathbf{x}_1)\rho(\mathbf{x}_2)\rangle &= \bar{\rho}^2\langle[1+\delta(\mathbf{x}_1)][1+\delta(\mathbf{x}_2)]\rangle \\ &= \bar{\rho}^2[1 + \langle\delta(\mathbf{x}_1)\rangle + \langle\delta(\mathbf{x}_2)\rangle + \langle\delta(\mathbf{x}_1)\delta(\mathbf{x}_2)\rangle] \\ &= \bar{\rho}^2[1 + \xi(\mathbf{x}_1 - \mathbf{x}_2)]\end{aligned} \tag{2.24}$$

where, under the assumption of CP, ξ only depends on the modulus $|\mathbf{x}_1 - \mathbf{x}_2|$. The function ξ is the connected term of two-point correlation function of the matter density contrast δ, and corresponds to the connected term of the two-point correlation function of the matter density distribution ρ, measuring the excess probability to find two particular values of the density contrast, $\delta(\mathbf{x}_1)$ and $\delta(\mathbf{x}_2)$, at a given distance $|\mathbf{x}_1 - \mathbf{x}_2|$,

$$\xi(|\mathbf{x}_1 - \mathbf{x}_2|) = \langle\delta(\mathbf{x}_1)\delta(\mathbf{x}_2)\rangle_c\,. \tag{2.25}$$

Higher order correlations can be written in terms of a connected term plus products of lower order connected correlation functions,

$$\begin{aligned}\langle\psi(\mathbf{x}_1)\dots\psi(\mathbf{x}_n)\rangle = &\langle\psi(\mathbf{x}_1)\dots\psi(\mathbf{x}_n)\rangle_c \\ &+ \langle\psi_1\rangle_c\langle\psi_2\dots\psi_n\rangle_c + \text{cyc.} \\ &+ \langle\psi_1\psi_2\rangle_c\langle\psi_3\dots\psi_n\rangle_c + \text{cyc.} \\ &+ \dots \\ &+ \langle\psi_1\rangle_c\langle\psi_2\rangle_c\dots\langle\psi_n\rangle_c\,.\end{aligned} \tag{2.26}$$

As a result, all the information about a given random field, encoded in its Probability Distribution Function (PDF), can be investigated by studying the connected part of its correlation functions.

For a Gaussian random field, the PDF for a single point is

$$\mathcal{P}[\psi] = \frac{1}{\sqrt{2\pi}\sigma}\exp\left(-\frac{1}{2}\frac{\psi^2}{\sigma^2}\right), \tag{2.27}$$

while for n points we have

$$\mathcal{P}[\psi(\mathbf{x}_1),\dots,\psi(\mathbf{x}_n)] = \frac{1}{\sqrt{(2\pi)^n \det\mathbb{C}}}\exp\left(-\frac{1}{2}\psi_i\mathbb{C}_{ij}\psi_j\right), \tag{2.28}$$

where all the statistical properties are encoded in the two-point correlation function, $\mathbb{C}_{ij} = \langle\psi(\mathbf{x}_i)\psi(\mathbf{x}_j)\rangle$, and all other higher-order correlation functions being equally zero.

COBE mission, by observing the CMB proved that the temperature fluctuations arising from the last-scattering surface are indeed Gaussian [56]. These temperature fluctuations relate to energy density perturbations of the primordial Universe so that we can treat them as initial conditions of our description which, therefore, can be very well described by 2PCF alone.

After recombination, during Matter Dominated era, perturbations in the matter density grow under the effect of gravity in a non-linear way, developing a characteristic non-Gaussian signature that can be probed by higer-order correlation functions. As non-Gaussianity in the matter distribution grows due to gravitational instability, the information content originally present in the two-point correlation function will be transferred to higher order correlation functions, such as three-point:

$$\zeta = \langle\delta(\mathbf{x}_1)\,\delta(\mathbf{x}_2)\,\delta(\mathbf{x}_3)\rangle_c\,. \tag{2.29}$$

This is the reason behind high order correlation functions being extremely sensitive to gravitational collapse models and a possible, small non-Gaussian component in the initial conditions. However, as we will see, other non-linear effects exist who can source a non-

vanishing contribution to high order correlation functions in the galaxy distribution: galaxy bias and redshift space distortion being the main responsibles.

2.3 Fourier Space

A useful way to study the evolution of cosmological perturbations is working in Fourier space. Fourier Transforms (FT) allow to decompose a signal in its spatial frequencies and therefore study how fluctuations behave on different scales. We assume the following convention for the FT of a field $\phi(\mathbf{x})$ and its inverse transformation:

$$\mathrm{FT}[\phi(\mathbf{x})] \equiv \phi(\mathbf{k}) \equiv \int \frac{\mathrm{d}^3x}{(2\pi)^3}\, e^{-i\mathbf{k}\cdot\mathbf{x}}\, \phi(\mathbf{x})\,, \tag{2.30}$$

$$\mathrm{iFT}[\phi(\mathbf{k})] \equiv \phi(\mathbf{x}) \equiv \int \mathrm{d}^3k\, e^{i\mathbf{k}\cdot\mathbf{x}}\, \phi(\mathbf{k})\,. \tag{2.31}$$

In general, the Fourier transform of a random field is a complex-valued random field. If the original, configuration-space field is such that $\phi(\mathbf{x}) \in R$, then its Fourier transform is equal to its complex conjugate under $\mathbf{k} \to -\mathbf{k}$, $\phi(\mathbf{k}) = \phi^*(-\mathbf{k})$.

Taking the two-point correlation function of the FT of the density contrast $\delta(\mathbf{k})$, gives

$$\langle \delta(\mathbf{k}_1)\delta(\mathbf{k}_2)\rangle = \int \frac{\mathrm{d}^3x_1}{(2\pi)^3}\, e^{-i\mathbf{k}_1\cdot\mathbf{x}_1} \int \frac{\mathrm{d}^3x_2}{(2\pi)^3}\, e^{-i\mathbf{k}_2\cdot\mathbf{x}_2}\, \langle \delta(\mathbf{x}_1)\delta(\mathbf{x}_2)\rangle\,. \tag{2.32}$$

Under the assumption of homogeneity and isotropy, $\langle \delta(\mathbf{x}_1)\delta(\mathbf{x}_2)\rangle = \xi(|\mathbf{x}_1 - \mathbf{x}_2|)$ therefore, for $\mathbf{y} = \mathbf{x}_1 - \mathbf{x}_2$, we can rewrite

$$\begin{aligned} \langle \delta(\mathbf{k}_1)\delta(\mathbf{k}_2)\rangle &= \int \frac{\mathrm{d}^3x_1}{(2\pi)^3}\, e^{-i(\mathbf{k}_1+\mathbf{k}_2)\cdot\mathbf{x}_1} \int \frac{\mathrm{d}^3y}{(2\pi)^3}\, e^{-i\mathbf{k}_2\cdot\mathbf{y}}\, \xi(y) \\ &= \delta_D(\mathbf{k}_1 + \mathbf{k}_2) P(k_2)\,, \end{aligned} \tag{2.33}$$

where $P(k)$ is the power spectrum that, as consequence of CP assumptions, depends only on the modulus of $k \equiv |\mathbf{k}| = |\mathbf{k}_1| = |\mathbf{k}_2|$. Moreover, this equation shows that the two-point correlation function and the power spectrum are the FT of one another

$$\mathrm{FT}[\xi(x)] = P(k)\,, \tag{2.34}$$

$$\mathrm{iFT}[P(k)] = \xi(x)\,. \tag{2.35}$$

Similarly, starting from the three-point correlation function of equation (2.29), we can compute the Fourier-space three-point counterpart of $\delta(\mathbf{k})$ as

$$\langle \delta(\mathbf{k}_1)\delta(\mathbf{k}_2)\delta(\mathbf{k}_3)\rangle = \delta_{\mathrm{D}}(\mathbf{k}_1 + \mathbf{k}_2 + \mathbf{k}_3) B(\mathbf{k}_1, \mathbf{k}_2)\,. \tag{2.36}$$

$B(\mathbf{k}_1, \mathbf{k}_2)$ is the bispectrum of the matter density contrast. Under the usual assumptions

of homogeneity and isotropy, it depends only on wavenumber triplets that form a closed triangle of sides k_1, k_2, k_3. Just as the power spectrum is the FT of the two-point correlation function, the bispectrum can be obtained as the FT of the three-point correlation function, and encodes the same properties of being sensitive to gravitational instability, non-Gaussian initial conditions, bias, Redshift Space Distortions, and broadly speaking to all those effects that introduce some non-linearity in the density contrast distribution that eventually contributes to the non-Gaussianity of the fields.

2.4 Matter evolution

2.4.1 Eulerian Dynamics

In order to extract cosmological information out of observations, it is crucial to develop a theoretical description that allows us to make predictions for the observed quantities.

In the standard cosmological model, the formation of cosmic structures is described by the evolution of a uniform and isotropic matter distribution in an expanding universe, under the effect of gravity. Homogeneity and isotropy, however, hold only in a statistical sense, and small perturbations δ in the matter distribution grow due to gravitational instability into collapsed objects that eventually merge into larger structures such as galaxy clusters.

On large scales, an analytical description of this phenomenon is possible as long as δ remains small. In this case, the adoption of the fluid approximation is perfectly reasonable due to the collisionless nature of CDM, as long as the velocity dispersion of DM particles is negligible. Moreover, considering scales much larger than the Hubble horizon H and velocities $u \ll c$ makes the Newtonian approximation a fair simplification.

On smaller scales this description ceases to be valid as perturbations approach $\delta \sim 1$, yet we will show that it is still possible to look for a perturbative solution using as perturbed field the density contrast.

We choose to write the following equations in terms of the conformal time τ, related to the cosmic time by $dt = a(\tau)d\tau$, and of the comoving coordinates $\mathbf{x}$, related to the physical ones by $\mathbf{r} = a(\tau)\mathbf{x}$. The evolution of the matter density perturbations $\delta(\mathbf{x}, \tau)$ in its most general form, i.e. without any approximation, is determined by the continuity equation ([19])

$$\frac{\partial \delta(\mathbf{x}, \tau)}{\partial \tau} + \nabla \cdot \{[1 + \delta(\mathbf{x}, \tau)]\, \mathbf{u}(\mathbf{x}, \tau)\} = 0\,, \tag{2.37}$$

and the Euler equation

$$\frac{\partial \mathbf{u}(\mathbf{x}, \tau)}{\partial \tau} + \mathcal{H}(\tau)\mathbf{u}(\mathbf{x}, \tau) + \big[\mathbf{u}(\mathbf{x}, \tau) \cdot \nabla\big]\mathbf{u}(\mathbf{x}, \tau) = -\nabla\Phi(\mathbf{x}, \tau) - \frac{1}{\rho}\nabla_j(\rho\sigma_{ij})\,, \tag{2.38}$$

describing respectively the conservation of matter and energy momentum. $\mathbf{u}(\mathbf{x}, \tau)$ is the

peculiar velocity field, σ_{ij} is the anisotropic stress tensor, and $\mathcal{H} = Ha$.

In the single-stream approximation, expected to be valid at large-scales, σ_{ij} is neglected. So an additional equation is needed in order to find a solution for two remaining unknowns δ and $\mathbf{u}$. This is the Poisson equation, relating perturbations in the matter distribution to the gravitational field Φ

$$\nabla^2\Phi = 4\pi G\bar{\rho}(\tau)\delta(\mathbf{x},\tau) = \frac{3}{2}\Omega_m(\tau)\mathcal{H}^2(\tau)\delta(\mathbf{x},\tau)\,. \tag{2.39}$$

This is the set-up for the so-called Standard Perturbation Theory.

Linear Perturbation Theory

Neglecting second-order contributions in the perturbed fields, δ and the velocity divergence $\theta \equiv \nabla\cdot\mathbf{u}$, the set of equations (2.37) and (2.38) can be linearised, to give:

$$\frac{\partial\delta(\mathbf{x},\tau)}{\partial\tau} + \theta(\mathbf{x},\tau) = 0 \tag{2.40}$$

$$\frac{\partial\mathbf{u}(\mathbf{x},\tau)}{\partial\tau} + \mathcal{H}(\tau)\mathbf{u}(\mathbf{x},\tau) = -\nabla\Phi(\mathbf{x},\tau)\,. \tag{2.41}$$

The linear Euler equation (2.41) describing the evolution of the velocity field can be decomposed in two parts, one addressing the velocity divergence θ and the other the vorticity $\mathbf{w}$,

$$\frac{\partial\theta(\mathbf{x},\tau)}{\partial\tau} + \mathcal{H}(\tau)\theta(\mathbf{x},\tau) + \frac{3}{2}\mathcal{H}^2(\tau)\Omega_m(\tau)\delta(\mathbf{x},\tau) = 0\,, \tag{2.42}$$

$$\frac{\partial\mathbf{w}(\mathbf{x},\tau)}{\partial\tau} + \mathcal{H}(\tau)\mathbf{w}(\mathbf{x},\tau) = 0\,. \tag{2.43}$$

We can neglect the vorticity since, for a perfect fluid, $\sigma_{ij} = 0$, and equation (2.43) implies that any initial contribution to vorticity decays with the Hubble expansion as $\mathbf{w} \propto a^{-1}$. Then, substituting equation (2.40) in equation (2.42), gives

$$\frac{\partial^2\delta(\mathbf{x},\tau)}{\partial\tau^2} + \mathcal{H}(\tau)\frac{\partial\delta(\mathbf{x},\tau)}{\partial\tau} - \frac{3}{2}\mathcal{H}^2(\tau)\Omega_m(\tau)\delta(\mathbf{x},\tau) = 0\,. \tag{2.44}$$

Assuming $\delta(\mathbf{x},\tau)$ to be separable in its time and space part, $\delta(\mathbf{x},\tau) = D(\tau)\,\delta_{\rm I}(\mathbf{x})$, equation (2.44) becomes a second order differential equation for D, which gives two independent solutions, D_+ and D_-, so that the general solution is

$$\delta(\mathbf{x},\tau) = D_+(\tau)\,\delta_+(\mathbf{x}) + D_-(\tau)\,\delta_-(\mathbf{x}) \tag{2.45}$$

with $\delta_{+/-}$ describing the initial distribution $\delta_{\rm I}$. In a matter dominated, Einstein de-Sitter Universe, $D_+ \propto a$ and $D_- \propto a^{-3/2}$. Neglecting the decaying mode,

$$\begin{aligned}\langle\delta(\mathbf{k}_1,\tau)\delta(\mathbf{k}_2,\tau)\rangle &= \int\frac{\mathrm{d}^3x_1}{(2\pi)^3}\int\frac{\mathrm{d}^3x_2}{(2\pi)^3}\,e^{-i\mathbf{x}_1\cdot k_1}e^{-i\mathbf{x}_2\cdot\mathbf{k}_2}\,\langle\delta(\mathbf{x}_1,\tau)\delta(\mathbf{x}_2,\tau)\rangle \\ &= D_+^2(\tau)\int\frac{\mathrm{d}^3x_1}{(2\pi)^3}\int\frac{\mathrm{d}^3x_2}{(2\pi)^3}\,e^{-i\mathbf{x}_1\cdot\mathbf{k}_1}e^{-i\mathbf{x}_2\cdot\mathbf{k}_2}\,\langle\delta_{\rm I}(\mathbf{x}_1)\delta_{\rm I}(\mathbf{x}_2)\rangle \\ &= \delta_{\rm D}(\mathbf{k}_1+\mathbf{k}_2)D_+^2(\tau)P_I(k_2)\end{aligned} \tag{2.46}$$

so that, given eq. (2.32), in the linear regime the power spectrum at time τ can be computed by rescaling the initial-time linear power spectrum P_I by the linear growth factor D_+,

$$P_L(k,\tau) = D_+^2(\tau)P_I(k)\,. \tag{2.47}$$

This implies that, in the linear regime, the shape of the power spectrum is preserved in time, therefore each Fourier mode k evolves independently. Moreover, if the initial distribution $\delta_+(\mathbf{x})$ is Gaussian, this property is preserved as long as the evolution is linear.

$P_I(k)$ is directly related to the power-law power spectrum of curvature perturbations originated during inflation, $P_I \sim k^{n_s}$. Such power law is then altered during the subsequent evolution during radiation and matter domination leading to a suppression on the small scales which entered the horizon before matter-radiation equality. The linear power spectrum accounts for these effects through the Transfer Function $T(k)$, so that its scale-dependence is given by

$$P_L(k) \sim\ k^{n_s}\,T(k)\,. \tag{2.48}$$

Although the spectral index of an exactly scale-invariant power spectrum, predicted by the fine-tuning of the flatness in the scalar field potential, should be $n_s = 1$, in many, standard inflationary models a small tilt due to the slow-rolling inflaton potential is expected. Remarkably, measurements of the CMB power spectrum from Planck constrain n_s to 0.9652 ± 0.0042 showing that while close to one, a small deviation is in fact observed.

Non-linear Perturbation Theory

In the large-scale limit, where the perturbed fields are small, Linear PT is able to provide a good description of the growth of density fluctuations as measured, for instance, in numerical simulations. This agreement stops when non-linear effects become important, at much smaller scales, around $\sim 0.1\,h\,\mathrm{Mpc}^{-1}$. Nevertheless, relying on PT, it is possible to extend theoretical predictions beyond the linear regime.

PT assumes that it is possible expand the general fields around their linear solution as

$$\begin{aligned}\delta(\mathbf{x},\tau) &= \sum_n \delta^{(n)}(\mathbf{x},\tau) \\ \theta(\mathbf{x},\tau) &= \sum_n \theta^{(n)}(\mathbf{x},\tau)\,,\end{aligned} \tag{2.49}$$

where, $\delta^{(1)} \sim \delta_L$, $\delta^{(2)} \sim \delta_L^2$, and so on. Stopping the series at second-order, the evolution of the perturbed fields is derived by solving the fully non-linear equation (2.38). In Fourier space, dropping for semplicity the explicit time-dependence,

$$\begin{aligned}\frac{\partial\delta(\mathbf{k})}{\partial\tau} + \theta(\mathbf{k}) &= -\int \mathrm{d}^3k_1\mathrm{d}^3k_2\,\delta_\mathrm{D}(\mathbf{k}-\mathbf{k}_{12})\,\alpha(\mathbf{k}_1,\mathbf{k}_2)\,\theta(\mathbf{k}_1)\,\delta(\mathbf{k}_2) \\ \frac{\partial\theta(\mathbf{k})}{\partial\tau} + \mathcal{H}\theta + \frac{3}{2}\Omega_m\mathcal{H}^2\delta(\mathbf{k}) &= -\int \mathrm{d}^3k_1\mathrm{d}^3k_2\,\delta_\mathrm{D}(\mathbf{k}-\mathbf{k}_{12})\,\beta(\mathbf{k}_1,\mathbf{k}_2)\theta(\mathbf{k}_1)\,\theta(\mathbf{k}_2)\end{aligned} \tag{2.50}$$

where the functions

$$\alpha(\mathbf{k}_1,\mathbf{k}_2) = \frac{(\mathbf{k}_1+\mathbf{k}_2)\cdot\mathbf{k}_1}{k_1^2} \quad , \quad \beta(\mathbf{k}_1,\mathbf{k}_2) = \frac{k_{12}^2\cdot(\mathbf{k}_1\cdot\mathbf{k}_2)}{2k_1^2k_2^2}\,, \tag{2.51}$$

are responsible of the mode-couplings between perturbations of different scale $\mathbf{k}_1$ and $\mathbf{k}_2$. As a consequence, the evolution of a given mode $\mathbf{k}$ ceases to be independent from other scales when progressing from large to small scales, where the linear approximation fails. Moreover, in such a regime, all the modes for which $\mathbf{k}_1+\mathbf{k}_2=\mathbf{k}$ holds, will contribute to the second-order non-linear dynamics.

Working in the limit for an Einstein de Sitter Universe, with $\Omega_m = 1$ and $\Omega_\Lambda = 0$, equations (2.50) become homogeneous in the time component and can be separated in their time and space parts. As a result, each term in the expansion (2.49) can be written as the product of a time-dependent coefficient and a spatial-dependent term

$$\delta(\mathbf{k},\tau) = \sum_n D_+^n(\tau)\delta^{(n)}(\mathbf{k})\,. \tag{2.52}$$

The evolution of the density and velocity divergence fields is then obtained by multiplying the time-independent solution, specified in terms of the initial, linear solution δ_I for the corresponding growth factor,

$$\delta^{(n)}(\mathbf{k}) = \int \mathrm{d}^3q_1 \ldots \int \mathrm{d}^3q_n\,\delta_\mathrm{D}(\mathbf{k}-\mathbf{q}_{1\ldots n})\,F_n(\mathbf{q}_1,\ldots,\mathbf{q}_n)\,\delta_I(\mathbf{q}_1)\ldots\delta_I(\mathbf{q}_n)\,, \tag{2.53}$$

$$\theta^{(n)}(\mathbf{k}) = \int \mathrm{d}^3q_1 \ldots \int \mathrm{d}^3q_n\,\delta_\mathrm{D}(\mathbf{k}-\mathbf{q}_{1\ldots n})\,G_n(\mathbf{q}_1,\ldots,\mathbf{q}_n)\,\delta_I(\mathbf{q}_1)\ldots\delta_I(\mathbf{q}_n)\,. \tag{2.54}$$

$F^{(n)}$ and $G^{(n)}$ are symmetrized kernels that couple the $\mathbf{q}_1,\ldots,\mathbf{q}_n$ scales, such that $\mathbf{q}_1 + \ldots + \mathbf{q}_n = \mathbf{k}$ holds, contributing to the evolution of the mode $\mathbf{k}$. The second-order kernels

$F_2(\mathbf{k}_1, \mathbf{k}_2)$ and $G_2(\mathbf{k}_1, \mathbf{k}_2)$ are

$$F_2(\mathbf{k}_1, \mathbf{k}_2) = \frac{5}{7} + \frac{1}{2}(\hat{k}_1 \cdot \hat{k}_2)\left(\frac{k_1}{k_2} + \frac{k_2}{k_1}\right) + \frac{2}{7}(\hat{k}_1 \cdot \hat{k}_2)^2 \,, \tag{2.55}$$

$$G_2(\mathbf{k}_1, \mathbf{k}_2) = \frac{3}{7} + \frac{1}{2}(\hat{k}_1 \cdot \hat{k}_2)\left(\frac{k_1}{k_2} + \frac{k_2}{k_1}\right) + \frac{4}{7}(\hat{k}_1 \cdot \hat{k}_2)^2 \,. \tag{2.56}$$

For a more general cosmology with $\Omega_m \neq 1$, $\delta^{(n)}(\mathbf{x}, \tau)$ is not be separable, however it turns out that the same kernels provide a very good approximation to the nonlinear solution, provided that the growth factor D is the correct one.

Correlation functions

We now turn to the predictions for the Fourier-space observables, specifically the power spectrum and the bispectrum. In what is about to come and throughout this work, we will sometimes adopt the following notation to shorten equations and simplify their interpretation: $\delta(\mathbf{k}, \tau) = \delta_{\mathbf{k}}(\tau)$ - often omitting the time component, $\delta_{\mathbf{k}}$.

Starting from the definition (2.32) and replacing the expansion (2.52), gives

$$\begin{aligned}
\langle \delta_{\mathbf{k}_1}\, \delta_{\mathbf{k}_2} \rangle &= \langle (\delta^{(1)}_{\mathbf{k}_1} + \delta^{(2)}_{\mathbf{k}_1} + \delta^{(3)}_{\mathbf{k}_1} + ...)(\delta^{(1)}_{\mathbf{k}_2} + \delta^{(2)}_{\mathbf{k}_2} + \delta^{(3)}_{\mathbf{k}_2} + ...) \rangle \\
&= \langle \delta^{(1)}_{\mathbf{k}_1}\, \delta^{(1)}_{\mathbf{k}_2} \rangle + \langle \delta^{(2)}_{\mathbf{k}_1}\, \delta^{(2)}_{\mathbf{k}_2} \rangle + \Big(\langle \delta^{(1)}_{\mathbf{k}_1}\, \delta^{(3)}_{\mathbf{k}_2} \rangle + \langle \delta^{(3)}_{\mathbf{k}_1}\, \delta^{(1)}_{\mathbf{k}_2} \rangle \Big) + \mathcal{O}[\delta_L^6] \\
&= \delta(\mathbf{k}_1 + \mathbf{k}_2) \big[P_L(k_2) + P_{1-\text{loop}}(k_2) + \mathcal{O}[\delta_L^6] \big] \,,
\end{aligned} \tag{2.57}$$

where

$$\langle \delta^{(2)}_{\mathbf{k}_1} \delta^{(2)}_{\mathbf{k}_2} \rangle = 2 \int \mathrm{d}^3 q \, F_2^2(\mathbf{k} - \mathbf{q}, \mathbf{q}) P_L(|\mathbf{k} - \mathbf{q}|) P_L(q) \,, \tag{2.58}$$

$$\langle \delta^{(1)}_{\mathbf{k}_1} \delta^{(3)}_{\mathbf{k}_2} \rangle = 6 P_L(k) \int \mathrm{d}^3 q \, F_3(\mathbf{k}, \mathbf{q}, \mathbf{k} - \mathbf{q}) P_L(q) \,. \tag{2.59}$$

The first-order contribution corresponds to the linear solution, and higher-order terms in the linear density field are expected to give a subdominant contribution to the total power spectrum, with odd powers vanishing for Gaussian initial conditions. The 1-loop power spectrum is the next contribution after the linear one and is expected to become relevant at mildly non-linear scales, where the linear solution ceases to give an accurate description of the evolution of perturbations.

An analogous treatment for the three-point statistics of the density field in Fourier space gives

$$\begin{aligned}
\langle \delta_{\mathbf{k}_1}\, \delta_{\mathbf{k}_2}\, \delta_{\mathbf{k}_3} \rangle &= \langle (\delta^{(1)}_{\mathbf{k}_1} + \delta^{(2)}_{\mathbf{k}_1} + \delta^{(3)}_{\mathbf{k}_1} + ...)(\delta^{(1)}_{\mathbf{k}_2} + \delta^{(2)}_{\mathbf{k}_2} + \delta^{(3)}_{\mathbf{k}_2} + ...)(\delta^{(1)}_{\mathbf{k}_3} + \delta^{(2)}_{\mathbf{k}_3} + \delta^{(3)}_{\mathbf{k}_3} + ...) \rangle \\
&= \langle \delta^{(2)}_{\mathbf{k}_1}\, \delta^{(1)}_{\mathbf{k}_2}\, \delta^{(1)}_{\mathbf{k}_3} \rangle + \langle \delta^{(1)}_{\mathbf{k}_1}\, \delta^{(2)}_{\mathbf{k}_2}\, \delta^{(1)}_{\mathbf{k}_3} \rangle + \langle \delta^{(1)}_{\mathbf{k}_1}\, \delta^{(1)}_{\mathbf{k}_2}\, \delta^{(2)}_{\mathbf{k}_3} \rangle + \mathcal{O}[\delta_L^{(6)}] \,.
\end{aligned} \tag{2.60}$$

The first-order contribution to the bispectrum (*tree-level*), induced by gravitational instability, corresponds to

$$B_{\rm tree}(k_1, k_2, k_3) = 2F_2(k_1, k_2)P_L(k_1)P_L(k_2) + \text{cyc.} \tag{2.61}$$

Higher-order contributions can be computed, with the lowest, the 1-loop term, accounting for contributions at sixth order in the linear density field.

2.4.2 Lagrangian Dynamics

An alternative description of the evolution of density perturbations was first provided by Zel'dovich [171]. While the perturbation and velocity fields are the main unknowns in the Eulerian picture, in the Lagrangian description displacement fields are the relevant degree of freedom. In particular, the displacement field ψ follows shifts of fluid elements from their original positions $\mathbf{q}$ such that the final position at time t is

$$\mathbf{x}(\mathbf{q}, t) = \mathbf{q} + \psi(\mathbf{q}, t)\,, \tag{2.62}$$

with $\psi(\mathbf{q}, t = 0) = 0$. The equation of motion for the position $\mathbf{x}$ of the volume-element is

$$\frac{\partial^2 \mathbf{x}}{\partial t^2} + 2\mathcal{H}\frac{\partial \mathbf{x}}{\partial t} = -\frac{1}{a^2}\nabla_{\mathbf{x}}\Phi \tag{2.63}$$

where Φ is the gravitational potential. We can take the gradient of this equation so that the resulting $\nabla^2\Phi$ on the r.h.s. can be replaced by the matter perturbations δ via Poisson equation, so that

$$\frac{\partial^2}{\partial t^2}(\nabla_{\mathbf{x}}\mathbf{x}) + 2\mathcal{H}\frac{\partial}{\partial t}(\nabla_{\mathbf{x}}\mathbf{x}) = -4\pi G\bar{\rho}\,\delta(\mathbf{x})\,. \tag{2.64}$$

Finally, from matter conservation is possible to relate the Eulerian matter density $\delta(\mathbf{x})$ to the Jacobian $J(\mathbf{q})$ of the coordinate transformation between initial and final coordinates $\mathbf{q}$ and $\mathbf{x}$ as

$$1 + \delta(\mathbf{x}) = \frac{1}{J(\mathbf{q})}\,, \tag{2.65}$$

and therefore to the displacement field $\Psi(\mathbf{q})$.

The solution is then obtained by expanding perturbatively the displacement field,

$$\psi(\mathbf{q}, t) = \sum_n \psi^{(n)}(\mathbf{q}, t)\,. \tag{2.66}$$

In the linear approximation we have

$$\nabla_{\mathbf{x}} \cdot \psi \simeq \nabla_{\mathbf{q}}\psi^{(1)}\,, \tag{2.67}$$

$$J(\mathbf{q}) \simeq 1 + \nabla_{\mathbf{q}}\psi^{(1)}\,, \tag{2.68}$$

and equation (2.63) becomes

$$\frac{\partial^2}{\partial t^2}(\nabla_{\mathbf{q}}\psi^{(1)}) + 2\frac{\partial}{\partial t}(\nabla_{\mathbf{q}}\psi^{(1)}) = 4\pi G\bar{\rho}\,\nabla_{\mathbf{q}}\psi^{(1)}\,. \tag{2.69}$$

Noting the analogy with (2.44), we have

$$\nabla_{\mathbf{q}}\psi^{(1)} = -D(t)\delta(\mathbf{q})\,. \tag{2.70}$$

The first-order Lagrangian solution, known as Zel'dovich approximation, already provides insights on Eulerian non-linearities in the density field at large scales, providing, for instance, a good description of the smoothing of the acoustic features present in the initial power spectrum due to nonlinear evolution.

The second-order correction (2LPT) [110] represents a great improvement over Zel'dovich solution, as it accounts for non-locality of the gravitation instability. In particular it provides an accurate prediction for the bispectrum at large scale.

The Lagrangian approach, providing predictions for particle displacements, is particularly useful for all applications requiring a numerical realisation of the matter density and velocity fields. These include the set-up of initial conditions in N-body simulations or the productions of approximate mock halo and galaxy catalogs, as we will see.

2.5 Bias

To translate predictions of matter clustering statistics into predictions of the galaxy distribution, galaxy bias must be considered. This accounts for the fact that galaxies could not be perfect tracers of matter and therefore, a non-linear relation, that can be described by a small set of parameters, is adopted to allow deviations from a one-to-one correspondence.

Since the observed scales are much larger than the characteristic scale of galaxy formation, where non-local phenomena are important, the simplest model theorises a local Eulerian, deterministic relation between matter and galaxy density contrasts. Deterministic bias assumes that although a scatter between δ and δ_g exists, this can be neglected, with biasing being described only by the mean relation between δ and δ_g. Perturbations in the galaxy number density δ_g are written as an expansion in the matter density profile δ, as

$$\delta_g(\mathbf{x}) = \sum_{j=1}^{\infty} \frac{b_j}{j!}\delta^j(\mathbf{x})\,, \tag{2.71}$$

where the coefficients b_j are the bias parameters. At first-order, $\delta_g \simeq b_1\delta$, so that $P_g(k) = b_1^2 P(k)$, with b_1 being the linear bias. Going beyond the linear bias model, i.e. breaking the series (2.71) at second-order, induces non-linearities in the correlation functions.

While non-linear, local biasing was historically motivated by being a simple generalisation

to linear biasing, the density perturbations in the non-linear regime receive contribution from different scales, as suggested by equation (2.53) and (2.54). This hints at a possible non-local nature of bias. Works as [13] and [33] showed that non-local corrections are needed to provide an accurate description of the halo power spectrum and bispectrum. This is done showing that local bias parameters b_1 and the second order bias b_2, vary with the smoothing scale of the density perturbations. Later, a major result came from [11], which realized that the *re-normalisation* of the bias parameters [107], adopted to remove the dependence from the smoothing scale from physical quantities, as δ, and possible divergences in the $\delta^{(n)}$ fields, requires non-local biasing.

Re-normalisation of the density field is achieved by adding counterterms $\mathcal{C}$

$$\delta_{\mathrm{R}}^{(n)}(\mathbf{x},\tau) = \delta^{(n)}(\mathbf{x},\tau) + \sum \mathcal{C}[\delta^{(n)}]\mathcal{F}(\mathbf{x},\tau)\,, \tag{2.72}$$

where additional fields $\mathcal{F}$ are required to account for these contributions. These terms can be effectively absorbed by bias, providing an *effective theory* in which the density contrast is given in terms of a re-normalized bias expansion $b_j^{(\mathrm{R})}$. At quadratic order the tidal tensor $(\nabla_i\nabla_j\phi_g)^2$ is added, ϕ_g being the gravitational potential. At cubic order, the velocity potential ϕ_v must be considered. In addition, some higher derivative terms can be added to account for sub-leading contributions in the smoothing scale.

Up to third order, the most general expansion considering both local and non-local corrections is

$$\begin{aligned}\delta_g = {} & b_1\delta + \frac{b_2}{2}\delta^2 + \frac{b_3}{6}\delta^3 + \\ & + b_{\mathcal{G}_2}\mathcal{G}_2 + b_{\mathcal{G}_3}\mathcal{G}_3 + b_{\mathcal{G}_2}\mathcal{G}_2\delta + b_{\Gamma_3}\Gamma_3\,,\end{aligned} \tag{2.73}$$

where b_3 is the third-order bias coefficient and $b_{\mathcal{G}_2}$ arises from re-normalizing the one-loop contribution of $\langle\delta^2(\mathbf{q})\delta_L(\mathbf{q}_1)\delta_L(\mathbf{q}_2)\rangle$. $\mathcal{G}_2$ is a non-local *Galileon*[3] operator made up from the second derivatives of the gravitational and velocity potentials. Up to second order there's no distinction between the two because, at this order, differences depend on squares of the linear potential and, in linear regime, $\delta_L = -\theta_L$. Differences appear only at third order, so now an additional degree of freedom must be considered, Γ_3. $\mathcal{G}_3$ is the cubic Galileon operator, analugous to $\mathcal{G}_2$. These operators are the only ones in the bias expansion which are not renormalized at first order in derivatives.

In addition, in order to account for the stochastic nature of galaxy formation, stochastic operators are usually introduced. These operators account for the shot-noise contributions in measurements of galaxy clustering coming from analysing a discrete distribution of points, and correspond to the two and three-point auto-correlation functions of galaxies. At third

[3]This kind of operators cannot be renormalized by terms with first order derivatives, but only through $\nabla^2\delta$ terms.

order these terms are

$$\delta_g^{\rm stoch} = \epsilon + \epsilon_\delta \delta + \epsilon_{\delta^2}\delta^2 + \epsilon_{\mathcal{G}_2}\mathcal{G}_2\,. \tag{2.74}$$

This description lead to a galaxy power spectrum model at one loop that can be written as

$$\begin{aligned} P_g(k) = & b_1^2[P_L(k) + P_{1-\rm loop}(k)] + b_1 b_2 P_{b_1 b_2}(k) + b_1 b_{\mathcal{G}_2} P_{b1\mathcal{G}_2}(k) + \\ & b_1 b_{\Gamma_3} P_{b_1 b_{\Gamma_3}}(k) + b_2^2 P_{b_2 b_2}(k) + b_2 b_{\mathcal{G}_2} P_{b_2 b_{\mathcal{G}_2}}(k) + b_{\mathcal{G}_2}^2 P_{b_{\mathcal{G}_2} b_{\mathcal{G}_2}}(k) + P_{\rm shot}(k)\,. \end{aligned} \tag{2.75}$$

The $P_{\alpha\beta}$ terms correspond to loop corrections arising from non-linearities from the biased tracer and include two types of mode-coupling integrals

$$P_{\alpha\beta}(k) = \int \mathrm{d}^3 q\, K(\mathbf{q}, \mathbf{k}-\mathbf{q}) P_L(\mathbf{q}) P_L(|\mathbf{k}-\mathbf{q}|) \tag{2.76}$$

$$P_{\alpha\beta}(k) = P_L(k) \int \mathrm{d}^3 q\, K(\mathbf{q}, \mathbf{k}-\mathbf{q}) P_L(\mathbf{q})\,. \tag{2.77}$$

The re-normalisation procedure subtracts from expressions (2.76) and (2.77) their large-scale limit [107, 11]. This enforces the requirement that bias parameters should not change when higher-order terms are added in the analysis. If this was not the case, this extra contribution would be absorbed by other parameters providing biased estimates of their posterior probability.

The analogue expression to equation (2.75) can be written for the tree-level galaxy bispectrum as

$$\begin{aligned} B_g(k_1, k_2, k_3) = & b_1^2[2 b_1 F_2(\mathbf{k}_1, \mathbf{k}_2) + b_2 - 2 b_{\mathcal{G}_2} S(\mathbf{k}_1, \mathbf{k}_2)] P_L(k_1) P_L(k_2) + \text{cyc.} \\ & + b_1^2(1+\alpha_1)[P_L(k_1) + P_L(k_2) + P_L(k_3)] P_{\rm SN} + (1+\alpha_2) P_{\rm SN}^2 \end{aligned} \tag{2.78}$$

where α_1 and α_2 are free parameters introduced to account for possible deviations from Poisson shot-noise.

The same description can be extended to other type of objects sampling the matter distribution, yet we should expect that different families of tracers will show different values of bias parameters.

2.6 Redshift Space Distortions

Real galaxy surveys measure galaxy positions with a combination of angles and redshift. This quantity is related to the effect experienced by light emitted from a source when travelling in an expanding universe. As a result of the this expansion along the line-of-sight (LOS), electromagnetic radiation is shifted to longer wavelengths by a factor proportional to the distance between the observer and the source,

$$1 + z = \frac{a_0}{a(t_{\rm emission})}\,. \tag{2.79}$$

This quantity z, known as redshift, is consequently adopted as a measure of distance. The space parametrised by angles and z is referred to as redshift space. To complicate the picture, contributions to the observed redshift do not come from the coherent Hubble expansion alone,

$$z_{\rm obs} = H\mathbf{x} + \mathbf{v}\cdot\hat{n}\,. \tag{2.80}$$

Peculiar velocities $\mathbf{v}$ induce distortions in the observed galaxy distribution along the LOS $\hat{n}$. These distortions break the isotropy otherwise present in the correlation functions and are known as Redshift Space Distortions (RSD).

The observed position $\mathbf{s}$ in redshift space is then related to the real position $\mathbf{x}$ by

$$\mathbf{s} = \mathbf{x} + \frac{\mathbf{v}\cdot\hat{n}}{a\,H(a)}\hat{n}\,. \tag{2.81}$$

As a result, clustering properties estimated from real galaxy redshift surveys, as galaxy correlation functions, will depend on the local LOS and bear non-isotropic contributions due to $\mathbf{v}$, so that equations (2.32) and (2.36) become

$$\langle\delta^s(\mathbf{k}_1)\delta^s(\mathbf{k}_2)\rangle = \delta_{\rm D}(\mathbf{k}_{12})P^s(\mathbf{k}_1,\hat{n}), \tag{2.82}$$

$$\langle\delta^s(\mathbf{k}_1)\delta^s(\mathbf{k}_2)\delta^s(\mathbf{k}_3)\rangle = \delta_{\rm D}(\mathbf{k}_{123})B^s(\mathbf{k}_1,\mathbf{k}_2,\hat{n})\,, \tag{2.83}$$

where the superscript s refers to redshift-space quantities.

Throughout this work we will work under the assumption of a fixed line of sight $\hat{n} = \hat{z}$, which is a fair restriction as long as the survey footprint spans a sufficiently small sky area. Given (2.81), the Jacobian $\partial\mathbf{s}/\partial\mathbf{x}$ allows to compute the density contrast in redshift space

$$\delta^s(\mathbf{k}) = \int \frac{{\rm d}^3x}{(2\pi)^3}\left[\delta(\mathbf{x}) - \frac{\nabla_z v_z(\mathbf{x})}{aH(z)}\right] e^{-i\mathbf{k}\cdot\mathbf{x}} e^{-ik_z v_z(\mathbf{x})/H}\,. \tag{2.84}$$

The relative power spectrum is then

$$P^s(\mathbf{k}) = \int \frac{{\rm d}^3x}{(2\pi)^3}\, e^{-i\mathbf{k}\cdot\mathbf{x}}\langle e^{ifk_z\Delta u_z}[\delta(\mathbf{x}) + f\nabla_z u_z(\mathbf{x})][\delta(\mathbf{x}') + f\nabla_z u_z(\mathbf{x}')]\rangle\,, \tag{2.85}$$

where we have used $u_z = v_z/(aHf)$ with $f = \frac{{\rm d}\log D}{{\rm d}\log a}$ being the growth rate of matter perturbations. The linear limit of (2.85) was studied by Kaiser [94]. Using that $\nabla\cdot\mathbf{u} = \delta$ in linear dynamics, and assuming linear bias,

$$P^s_{\rm Kaiser}(\mathbf{k}) = P^s_{\rm Kaiser}(k,\mu) = (b_1 + f\mu^2)^2 P_L(k)\,, \tag{2.86}$$

where $\mu = \hat{\mathbf{k}}\cdot\hat{n}$, in our specific case $\mu = k_z/|\mathbf{k}|$. From this equation, it follows that the power spectrum amplitude in redshift space is enhanced on large scales (where linear theory can be assumed) by the peculiar velocities of the coherent motion of perturbations towards

high-density regions.

On small scales, the velocity dispersion of particles and galaxies inside a collapsed structure results in a distribution elongated along the LOS (the so-called Fingers-of-God) and the power spectrum is dampened. In the literature [146, 162], this effect is sometimes described by a Gaussian exponential factor

$$D_{\rm FoG} = \exp(-f^2 k_z^2 \sigma_v^2)\,, \tag{2.87}$$

where σ_v is the pairwise velocity dispertion of particles $\sigma_v^2 = \langle \Delta u_z^2 \rangle$, often treated as a free-parameter in model inference studies. The two effects are then combined separately

$$P^s(k,\mu) = D_{\rm FoG}[\sigma_v]\, P_{\rm Kaiser}(k,\mu)\,, \tag{2.88}$$

and several authors have explored different choices of the two effects. The first step taken to refine the accuracy of this prediction is to go beyond linear theory, and apply the factor in equation (2.86) to the non-linear power spectrum

$$P^{1-\rm loop}_{\rm Kaiser}(k,\mu) = P_{\delta\delta}(k) + 2f\mu^2 P_{\delta\theta}(k) + f^2\mu^4 P_{\theta\theta}(k)\,, \tag{2.89}$$

where $P_{\delta\delta}$, $P_{\delta\theta}$, $P_{\theta\theta}$ stand for the cross-spectra between $\delta(k)$, and $\theta(k)$ and the linear regime $P_{\delta\delta}(k) = P_{\delta\theta}(k) = P_{\theta\theta}(k)$. [146] gives a general derivation of the large-scale limit of the redshift space power spectrum, showing that it differs form (2.86) by terms that depend on the Gaussian and non-Gaussian contributions to the velocity dispersion of large-scale flows. Nonetheless, [162] adopted a model that differs from (2.88) in the fact that, while Kaiser and Finger-of-God operators are treated separately, they include corrections coming from the non-linear coupling between density and velocity-divergence fields, and performed a fit to N-body simulations with σ_v used as a free parameter. The deviation of the best-fit parameters measured from the model without these additional terms from their fiducial value is taken as a claim that expression (2.88) is missing additional terms, $A(k,\mu)$ and $B(k,\mu)$, that arise form this non-linear coupling, so that

$$P(k,\mu) = D_{\rm FoG}[P_{\delta\delta}(k) + 2f\mu^2 P_{\delta\theta}(k) + f^2\mu^4 P_{\theta\theta}(k) + A(k,\mu) + B(k,\mu)]\,. \tag{2.90}$$

A and B have the form

$$A(k,\mu) = j_1 \int \frac{d^3x}{(2\pi)^3}\, e^{-i\mathbf{k}\cdot\mathbf{x}}\, \langle A_1 A_2 A_3 \rangle \tag{2.91}$$

$$B(k,\mu) = j_1^2 \int \frac{d^3x}{(2\pi)^3}\, e^{-i\mathbf{k}\cdot\mathbf{x}}\, \langle A_1 A_2 \rangle \langle A_1 A_3 \rangle \tag{2.92}$$

where

$$A_1 = v_z(\mathbf{x}) - v_z(\mathbf{x}')\,, \tag{2.93}$$

$$A_2 = \delta(\mathbf{x}) + f\nabla_z u_z(\mathbf{x})\,, \tag{2.94}$$

$$A_3 = \delta(\mathbf{x}') + f\nabla_z u_z(\mathbf{x}')\,. \tag{2.95}$$

The A-term contributions show oscillatory features and are tipically larger than those coming from B which are smooth and slightly lower. A fit performed on a volume $V_{\rm eff} = 20\,{\rm Gpc}^{-3}\,h^3$ considering these additional terms, shows a better agreement to the fiducial parameters f, H, D wrt the one missing these components, where the correspondent best-fit parameters are slightly biased.

The theoretical description of redshift-space correlation function predictions is usually given in terms of kernels analogous to those of equations (2.55) and (2.56), Z_n, which encode our predictions about this additional form of non-linearities. The expressions of those entering the 1-loop prediction for the power spectrum and tree-level bispectrum are

$$Z_1(\mathbf{k}) = b_1 + f\mu^2\,, \tag{2.96}$$

$$Z_2(\mathbf{k}_1,\mathbf{k}_2) = \frac{b_2}{2} + b_1 F(\mathbf{k}_1,\mathbf{k}_2) + f\mu^2 G_2(\mathbf{k}_1,\mathbf{k}_2) + \frac{f\mu k}{2}\left[\frac{\mu_1}{k_1}(b_1 + f\mu_2^2) + \frac{\mu_2}{k_2}(b_1 + f\mu_1^2)\right], \tag{2.97}$$

$$\begin{aligned} Z_3(\mathbf{k}_1,\mathbf{k}_2,\mathbf{k}_3) = {} & \frac{b_3}{6} + b_1 F_3(\mathbf{k}_1,\mathbf{k}_2,\mathbf{k}_3) + f\mu^2 G_3(\mathbf{k}_1,\mathbf{k}_2,\mathbf{k}_3) \\ & + f\mu k[b_1 F_2(\mathbf{k}_1,\mathbf{k}_2) + f\mu_{12}^2 G_2(\mathbf{k}_1,\mathbf{k}_2)]\frac{\mu_3}{k_3} \\ & + f\mu k Z_1(\mathbf{k}_1)\frac{\mu_{23}}{k_{23}} G_2(\mathbf{k}_2,\mathbf{k}_3) \\ & + \frac{(f\mu k)^2}{2} Z_1(\mathbf{k}_1)\frac{\mu_2}{k_2}\frac{\mu_3}{k_3} + 3b_2 F_2(\mathbf{k}_1,\mathbf{k}_2)\,, \end{aligned} \tag{2.98}$$

where $k = |\sum \mathbf{k}_i|$, $\mu = \hat{k}\cdot\hat{n}$, $\mu_i = \hat{k}_i\cdot\hat{n}$, F_2 and G_2 are the second-order real-space density and velocity divergence kernels, and F_3 and G_3 are the corresponding third-order real-space kernels. Once symmetrized with respect to all Fourier wavelengths, the 1-loop power spectrum can be written as

$$P_g^{(s)}(\mathbf{k}) = Z_1^2(\mathbf{k})P_L(k) + 2\int d^3q\,[Z_2(\mathbf{q},\mathbf{k}-\mathbf{q})]^2 P_L(q)P_L(|\mathbf{k}-\mathbf{q}|) + \tag{2.99}$$

$$+ 6Z_1(\mathbf{k})P_L(k)\int d^3q\, Z_3(\mathbf{k},\mathbf{q},-\mathbf{q}) + P_{\rm shot}^{(s)}(k) \tag{2.100}$$

where $P_{\rm shot}^{(s)}(k)$ represent the shot-noise contribution. Historically, working with $P(\mathbf{k})$ can be a nuisance given how large the datavector can be, in particular for numerical analyses, where the accessible memory of the computing infrastructure is finite. This shortcoming can

be avoided by projecting the anisotropic signal on a basis of Legendre polynomials

$$P(\mathbf{k}, \hat{n}) = \sum_{\ell} P_{\ell}(k)\mathcal{L}_{\ell}(\hat{k} \cdot \hat{n}) \,, \tag{2.101}$$

where $\hat{n}$ is the LOS, here given in the most general case without assuming any approximation, and

$$P_{\ell}(k) = \frac{(2\ell + 1)}{2} \int \mathrm{d}\mu \, P(\mathbf{k}, \hat{n})\mathcal{L}_{\ell}(\mu) \,, \tag{2.102}$$

where μ is the cosine of the angle between $\mathbf{k}$ and $\hat{n}$.

Early analyses were limited to the monopole $P_0(k)$, i.e. to the signal averaged over the LOS and much of the information encoded in the anisotropic power spectrum was thrown away. Today $P(\mathbf{k})$ is now routinely expanded in multipoles according to equation (2.102) and their power to determine cosmological parameters, as the cosmic growth factor f, or combinations of b_1/f, is recognized.

While many studies exist in which power spectrum analyses take full advantage of this multipoles expansion [4] [139], in the past bispectrum analyses have always been limited to the monopole. Nonetheless, as in the power spectrum case, the anisotropic signal carries additional information [61, 28] and a complete analysis should take advantage of this contribution. We will come back to this topic in Chapter 5 as we will discuss the assessment of the constraining power of the information content present in the redshift-space anisotropic bispectrum on best-fit model parameters inferred from likelihood analyses. This is the primary focus of my work and Chapter 5 is dedicated to the description of this analysis.

2.7 Baryonic Acoustic Oscillations

Baryonic Acoustic Oscillations, hereafter BAOs, arise from density variations in the baryon-photon fluid before photon decoupling. These perturbations, which were previously driven by the huge number of high energy photons coupled with high Thomson scattering interaction rate, freeze in the matter distribution after decoupling. This process left an imprint in the density distribution around $110\,\mathrm{Mpc}\,h^{-1}$ from primordial overdensities, which corredsponds to the distance travelled by density perturbations in primordial baryon-photon plasma prior to decoupling.

Imprints from BAOs in galaxy correlation functions have been first detected as a bump in the 2PCF in [53] or as an oscillatory feature in the power spectrum at the same scales. This signal constitutes a feature that can be used as a standard ruler which, observed at different redshifts, allows to measure robustly the cosmic expansion rate through the Hubble parameter. Luckily, many systematic effects targeting the power spectrum affect the broadband component without affecting the position of the peak [156] and are marginalized out when fitting the BAO signal. This allows to measure cosmological parameters with good

precision.

Bulk flows from long-wavelength modes, however, produce small deviations on short-wavelength due to the coupling effect coming from non-linear evolution. In other words, this long modes shift randomly particles positions closer and further away from each other, moving away power from the characteristic BAO scale. This results in a broadening of the peak in the two-point correlation function and to a damped oscillatory feature in the power spectrum.

Several strategies can be taken to handle this problem. One way is to measure these long wavelength modes and use them to *reconstruct* particle positions at smaller scales.

2.8 Galaxy Redshift Surveys

LSS analyses through galaxy redshift surveys allow to probe with exceptional accuracy many cosmological parameters of the ΛCDM model. Baryonic Acoustic Oscillations, arising from perturbations in the density field, frozen in the matter distribution after decoupling from radiation, allow to measure expansion and DE parameters [153]. The anisotropic signal due to Redshift Space Distortions encodes information about the growth rate of structures. Full Shape analysis of the two-point correlation function and power spectrum [90] [39], and power spectrum plus bispectrum joint analysis [40], fully exploit the information content encoded in the measured observables, allowing to constrain simultaneously cosmological and bias parameters. The amplitude of the bispectrum over specific triangle configurations allows to put constraints on primordial non-Gaussianity models predicted by many inflation prescriptions [40]. To further shrink joint parameter posterior contours from maximum likelihood analyses, different datasets can be combined together as happens for BAO and RSD information in [22] or for different surveys [152], in many data analyses of the BOSS collaboration.

I will now introduce the SDSS-III Baryon Oscillation Spectroscopic Survey, one of the most recent galaxy redshift surveys that has been thoroughly analysed by a large number of papers [141, 142, 71, 66] that represent the state-of-the-art for galaxy clustering analyses. The power of these methods has received much attention in these days and future missions are planned to provide increasingly accurate measurements. Two are the reasons to seek these new data. First, as we already addressed in this chapter, the nature of DE and DM is still poorly understood, the second is that new data start to display deviations from Planck results. In particular, local measurement of the Hubble constant through distance-ladder measurements of Cepheids and SNe Ia [135] show a 5σ deviation from the value predicted by Planck, while weak lensing data [42] systematically undershoot the amplitude of the matter power spectrum σ_8 from Planck. Euclid is a space-born mission that is expected to fly in 2023, which provide exceptional measurements for almost ~ 30 million spectrscopic redshifts for galaxy clustering studies. A particular feature of the Euclid mission will be the possibility

to perform simultaneous photometric and spectroscopic measurements that will allow to have overlapping catalogs for weak lensing and galaxy clustering. Cross-correlating these datasets will allow to place further constraints on cosmological and bias parameters up to an accuracy that would match current constraints on CMB.

2.8.1 BOSS

The SDSS-III Baryon Oscillation Spectroscopic Survey (BOSS) is a ground-based mission that has measured the spectroscopic redshifts af almost 1 million galaxies using two targeting algorithms, LOWZ and CMASS, providing two samples covering complementary redshift bins over the range $0.15 \leq z \leq 0.70$. The total, effective volume of the sample is $V_{\text{eff}} \sim 7.4\,\text{Gpc}^3$.

Over the years, several papers were produced by the collaboration and I will provide hereby some references, although without aiming to give a complete picture of the whole scientifiic production. Most early works focused on measurement of the Hubble parameter by BAO extraction from two-point correlation and power spectrum [6], from power spectum multipoles in the twelfth and final data release [66], and from the three-point correlation function [155] and galaxy bispectrum [121].

A lot more papers focused instead on the exploitation of the anisotropic signal present in RSD using power spectrum multipoles, [22] on DR11 sample, and [65] focusing on the full DR12, while the joint power spectrum and bispectrum analysis is addressed in [67].

Progress in the theory of EFTofLSS allowed to apply full shape analysis to power spectrum multipoles measurements [39] fitting a one-loop model in EFT and scanning over different cosmologies with $m_\mu \neq 0$ [90]. Finally [127] provides constraint on ΛCDM cosmological parameters from the joint analysis of power spectrum and bispectrum monopole.

It is worth pointing out that all ΛCDM cosmological parameters have been measured from the BOSS DRs. More recent analyses focus instead on the retrieval of limits on primordial non-Gaussianies through the bispectrum of galaxies [40].

Despite the large number of galaxies observed by BOSS and the exceptional measurements provided to the scientific community, future surveys are planned to provide data on complementary redshift ranges and on large sky areas, as DESI [100] and Euclid [96].

2.8.2 Euclid

Euclid is a Medium Class mission of the European Space Agency (ESA) Cosmic Vision 2015-2025 program, with the goal of studying:

- DE models, in particular the cosmological constat interpretation, by putting constraints on the parameter of state w in different redshift bins;
- Modified Gravity models, through the growth factor $f(z) = \Omega_m(z)^\gamma$;

Figure 2.1: Structural and thermal model of the Euclid satellite. Picture taken from https://sci.esa.int/web/euclid/multimedia-gallery.

- DM models, by putting constraints on the total neutrino mass m_ν;
- Initlial condition models, setting limits to primordial condition parametrisations, by constraining $f_{\rm NL}$.

To accomplish this goals a space mission is needed in order to survey a large fraction of the sky with exquisitely precise measurements. The spacecraft will host a 1.2 m Korsch telescope and two scientific instruments, a VISual imager (VIS) and a Near-Infrared Spectrometer and Photometer (NISP). These instruments will be used to map the distribution of matter and galaxies in the Universe and feed this informations to two main cosmological probes, Weak Lensing (WL) and Galaxy Clustering (GC). The Euclid mission will last at least 6 years and will perform a wide field survey, designed to cover an area of $15000\,\mathrm{deg}^2$. This wide survey will be coupled with two additional deep field surveys located close to the ecliptic poles and covering $20\,\mathrm{deg}^2$.

The work that I will describe in the following chapter can be very much considered as aimed at fully exploiting data that will be available with this mission. In fact, during my Ph.D. I was part of a work force in Euclid for the implementation, development, integration and validation of estimator codes, named Processing Functions (PFs), for GC. In particular, I was in charge of the power spectrum and bispectrum codes named *LE3_GC_PowerSpectrum* and *LE3_GC_Bispectrum* that will be used to provide official measurements of the Euclid survey. The next chapter will be devoted to the description of the state-of-the-art power spectrum and bispectrum estimators, and will particularly refer to the experience achieved working inside of the Euclid collaboration.

Chapter 3

Estimators of Correlation Functions in Fourier-Space

I shall now describe the power spectrum and bispectrum estimators commonly used in Large-Scale Structure studies. My experience with this topic relates to the activity I have carried out during my Ph.D. as a member of the Level3 Organisation Unit (OU-LE3) of the Euclid mission for Galaxy Clustering (GC).

In this regard, I worked as developer of the power spectrum and bispectrum estimator codes. These software units, hereafter named Processing Functions (PFs), need to be thoroughly tested against simulations and a meticulous assessment of the impact of observational systematics must be carried out in order to meet Euclid exceptional requirements. This requires to plan a dedicated validation campaign and produce a detailed documentation of the software design, accuracy and computing-performance for each PF.

In the following I will describe my implementation that has been adopted for the Euclid official data analysis and the tests defined to assess their maturity status. Moreover, I will provide a thorough description of the estimators commonly used in literature and of the ingredients that can help mitigate some of their inherent casualties.

3.1 Theory

3.1.1 Simple Estimator

Power Spectrum

A simple estimator for the power spectrum of the continuous, random density field $\delta(\mathbf{x})$ can be written as

$$\hat{P}(k) = \frac{1}{N_k} \int_k \mathrm{d}^3 q \, |\delta(\mathbf{q})|^2 \,, \tag{3.1}$$

where the integration is assumed to cover the shell of radius k and size Δk, so that $k - \Delta k/2 \leq q \leq k + \Delta k/2$, and where

$$N_k \equiv \frac{(2\pi)^3}{V} \int_k \mathrm{d}^3 q \tag{3.2}$$

is the number of modes $\mathbf{q}$ in the shell for a finite cubic volume $V = L^3$ with $k_f = 2\pi/L$ being the fundamental frequency of the box. While for a FT of a continuous field defined over a finite volume, the modes in Fourier space are discretised in units of k_f, we will keep, for simplicity, the integral notation through-out this thesis. It is easy to see that, given our definition of the power spectrum, eq. (2.33) we have $\langle \hat{P}(k) \rangle = P(k)$.

Bispectrum

For the bispectrum, the simple estimator of a random density field $\delta(\mathbf{x})$ can be written as

$$\hat{B}(k_1, k_2, k_3) = \frac{1}{N_T(k_1, k_2, k_3)} \int_{k_1} \mathrm{d}^3 q_1 \int_{k_2} \mathrm{d}^3 q_2 \int_{k_3} \mathrm{d}^3 q_3 \, \delta_{\mathrm{D}}(\mathbf{q}_{123}) \delta(\mathbf{q}_1) \delta(\mathbf{q}_2) \delta(\mathbf{q}_3) \,, \tag{3.3}$$

where the δ_{D} ensures that the integrals are computed over the wavenumber triplets $(\mathbf{q}_1, \mathbf{q}_2, \mathbf{q}_3)$ forming closed triangles that lie in the triangle bin defined by (k_1, k_2, k_3), and where

$$N_T(k_1, k_2, k_3) \equiv \frac{(2\pi)^3}{V} \int_{k_1} \mathrm{d}^3 q_1 \int_{k_2} \mathrm{d}^3 q_2 \int_{k_3} \mathrm{d}^3 q_3 \, \delta_{\mathrm{D}}(\mathbf{q})_{123} \tag{3.4}$$

is the number of triangular configurations in a given $\{k_1, k_2, k_3\}$ bin.

3.1.2 Direct Summation Approach

In the case of a discrete distribution of objects, the most trivial way to compute the density $n_g(\mathbf{x})$ is through a sum over the position $\mathbf{x}_i$ of all the objects in the sample

$$n_g(\mathbf{x}) = \frac{1}{N_p} \sum_{i=1}^{N_p} \delta_{\mathrm{D}}(\mathbf{x} - \mathbf{x}_i) \,, \tag{3.5}$$

with N_p being the number of particles of the input distribution. The Fourier space density required to evaluate the power spectrum and bispectrum of equation (3.1) and (3.3) results from applying the FT to this equation, giving

$$\delta(\mathbf{k}) = \frac{1}{N_p} \sum_{i=1}^{N_p} n_g(\mathbf{x}_i) e^{-i\mathbf{k}\cdot\mathbf{x}_i} \,. \tag{3.6}$$

This is known as the Direct Summation approach. Its shortcomings relate to the fact that the sum of the equations above are evaluated over the particle number, so that it can get very expensive to compute the FT for distributions with a large number of objects and a large Fourier data-vector. In particular, if N_k is the dimension of the Fourier wavelength domain on which we want to compute eq. (3.5), the scaling of this approach is $N_k \times N_p$. Usually, to speed-up the calculation, a regular grid of equispaced points is adopted to evaluate the FT above. If the linear dimension of the grid is N_{G}, the scaling for a cubic grid is $N_{\mathrm{G}} \times N_{\mathrm{G}} \times N_{\mathrm{G}}$, independent from the number of object. The introduction of the grid,

however, introduces some shortcomings due to the finite size of the grid that are not present in the Direct Summation approach. We will discuss these additional source of noise later on in this chapter, in section 3.2.4.

3.1.3 Yamamoto estimator

Departure from homogeneity and isotropy in the density field $\delta(\mathbf{x})$ introduces an additional dependence on the LOS in the power spectrum. Following the reasoning of the Simple Estimator, we can define a general estimator that takes into account this fact,

$$\hat{P}(\mathbf{k},\hat{n}) = \int d^3q\, \delta(\mathbf{k}+\mathbf{q}/2)\, \delta(-\mathbf{k}+\mathbf{q}/2)\, e^{i\hat{\mathbf{q}}\cdot\hat{\mathbf{n}}}\,, \tag{3.7}$$

where $\hat{n}$ is the LOS direction to the midpoint of the galaxy pair $\mathbf{x} = (\mathbf{x}_1+\mathbf{x}_2)/2$. The anisotropic power spectrum then, can be expanded in multipoles $P_\ell(k)$ as

$$\begin{aligned}\hat{P}_\ell(k) &= (2\ell+1)\int\frac{d\Omega}{4\pi}\int\frac{d^3x}{(2\pi)^3}\,P(\mathbf{k},\hat{n})\mathcal{L}_\ell(\hat{\mathbf{k}}\cdot\hat{n}) \\ &= (2\ell+1)\int\frac{d\Omega}{4\pi}\int\frac{d^3x_1}{(2\pi)^3}\frac{d^3x_2}{(2\pi)^3}\,\delta(\mathbf{x}_1)\delta(\mathbf{x}_2)e^{i\mathbf{k}\cdot(\mathbf{x}_1-\mathbf{x}_2)}\,\mathcal{L}_\ell(\hat{\mathbf{k}}\cdot\hat{n})\,.\end{aligned} \tag{3.8}$$

This is the Yamamoto estimator [169]. The discretisation step required to translate (3.8) into a code implementation, results in a double sum over space, giving a bottleneck of order N^2, N being related to the grid[1] dimension needed to compute Discrete Fourier Trasforms (DFTs).

Early works adopt a constant LOS, traditionally $\hat{n} = \hat{z}$, so that

$$\hat{P}_\ell(k) = (2\ell+1)\int\frac{d\Omega}{4\pi}\,P(\mathbf{k})\mathcal{L}_\ell(k_z)\,. \tag{3.9}$$

While this may work fairly well for pencil-beam surveys with a narrow sky aperture, upcoming space-missions as Euclid will cover a sky area of almost $15,000\ \mathrm{deg}^2$ so that $\hat{n}\simeq\hat{z}$ might not hold for galaxies with large angular separations. [23] proposes to choose the LOS definition in the Legendre term as $\hat{n}\to\hat{x}_1$. This allows us to split equation (3.8) in the product of two separate integrals:

$$\hat{P}_\ell(k) = (2\ell+1)\int\frac{d\Omega}{4\pi}\left(\int\frac{d^3x_1}{(2\pi)^3}\,\delta(\mathbf{x}_1)\,e^{i\mathbf{k}\cdot\mathbf{x}_1}\,\mathcal{L}_\ell(\hat{\mathbf{k}}\cdot\hat{\mathbf{x}}_1)\right)\left(\int\frac{d^3x_2}{(2\pi)^3}\,\delta(\mathbf{x}_2)\,e^{-i\mathbf{k}\cdot\mathbf{x}_2}\right), \tag{3.10}$$

and to define

$$\delta_\ell(k) = \int\frac{d^3x}{(2\pi)^3}\,\delta(\mathbf{x})\,e^{i\mathbf{q}\cdot\mathbf{x}}\,\mathcal{L}_\ell(\hat{\mathbf{k}}\cdot\hat{\mathbf{x}}) \tag{3.11}$$

[1] In Signal Theory regular grids of equally spaced points are required to apply Discrete Fourier Transforms formalism.

so that:

$$\hat{P}_\ell(k) = (2\ell+1)\int \frac{\mathrm{d}\Omega}{4\pi}\,\delta_\ell(\mathbf{k})\delta_0(-\mathbf{k}). \tag{3.12}$$

The estimator resulting from the approximation $\hat{n} = \hat{x}_1$ is known as end-point estimator. The advantage brought by (3.11) is easily recognized if the $\hat{\mathbf{k}}$ dependence is taken out of the integral, by writing the explicit expression for the Legendre term. For for $\ell = 2,\, 4$, equation (3.11) reads

$$\delta_2(\mathbf{k}) = \frac{3}{2}\hat{k}_i\hat{k}_j Q_{ij}(\mathbf{k}) - \frac{1}{2}\delta_0(\mathbf{k}) \tag{3.13}$$

$$\delta_4(\mathbf{k}) = \frac{35}{8}\hat{k}_i\hat{k}_j\hat{k}_l\hat{k}_k Q_{ijlk}(\mathbf{k}) - \frac{5}{2}\delta_2(\mathbf{k}) - \frac{7}{8}\delta_0(\mathbf{k}) \tag{3.14}$$

with

$$Q_{ij}(\mathbf{k}) = \int \frac{\mathrm{d}^3x}{(2\pi)^3}\, e^{-i\mathbf{k}\cdot\mathbf{x}}\,\delta(\mathbf{x})\,\hat{x}_i\hat{x}_j\,, \tag{3.15}$$

and

$$Q_{ijkl}(\mathbf{k}) = \int \frac{\mathrm{d}^3x}{(2\pi)^3}\, e^{-i\mathbf{k}\cdot\mathbf{x}}\,\delta(\mathbf{x})\,\hat{x}_i\hat{x}_j\hat{x}_l\hat{x}_k\,. \tag{3.16}$$

The Q operators are fully symmetric, so only 6 DFTs are needed to compute the quadrupole and 15 for the hexadecapole. In order to measure all multipoles then, 22 DFTs are needed to measure $\ell = 0, 2, 4$ multipoles moments. Reference [147] expands this reasoning questioning whether it would be possible to reduce further computing complexity for the hexadecapole, showing that, taking

$$\mathcal{L}_4(\hat{\mathbf{k}}\cdot\hat{\mathbf{x}}) = \frac{35}{8}[\mathcal{L}_2(\hat{k}\cdot\hat{x})]^2 - \frac{5}{9}\mathcal{L}_2(\hat{k}\cdot\hat{x}) - \frac{7}{18}\,, \tag{3.17}$$

the first term can be splitted as $[\mathcal{L}_2(\hat{k}\cdot\hat{x})]^2 = \mathcal{L}_2(\hat{k}\cdot\hat{x}_1)\mathcal{L}_2(\hat{k}\cdot\hat{x}_2)$, so that

$$\hat{P}_4(k) = \frac{35}{2}\int \frac{d\Omega}{4\pi}|\delta_2(\mathbf{k})|^2 - \hat{P}_2(k) - \frac{7}{2}\hat{P}_0(k)\,. \tag{3.18}$$

To compute (3.18) no additional DFTs with respect to those computed for $\ell = 0, 2$ are required and the total nuber of DFTs is just 7 (1+6), leading to additional computational savings. In [140] the authors find a small bias in the end-point estimator P_4 compared to the full anisotropic signal and [147] finds that it is slightly favoured with respect to the one of (3.18) due to lower cosmic variance.

We can understand the origin of the end-point estimator bias by geometrical arguments, comparing it to equation (3.8). First we note that as long as we only consider the monopole, the two estimators return the same prediction, therefore any bias is induced by higer order multipoles, $\ell = 2, 4$. In particular, the approximation $\hat{n} \to \hat{x}_1$ has two major consequences: 1) it introduces an error in the measured multipoles; 2) it breaks the symmetry between galaxy pairs, so that odd-multipoles will became non-vanishing. We restrict to point 1) as the information present in odd-multipoles is purely due to this symmetry breaking and thus purely geometrical. Reference [140] quantified the difference of the end-point estimator

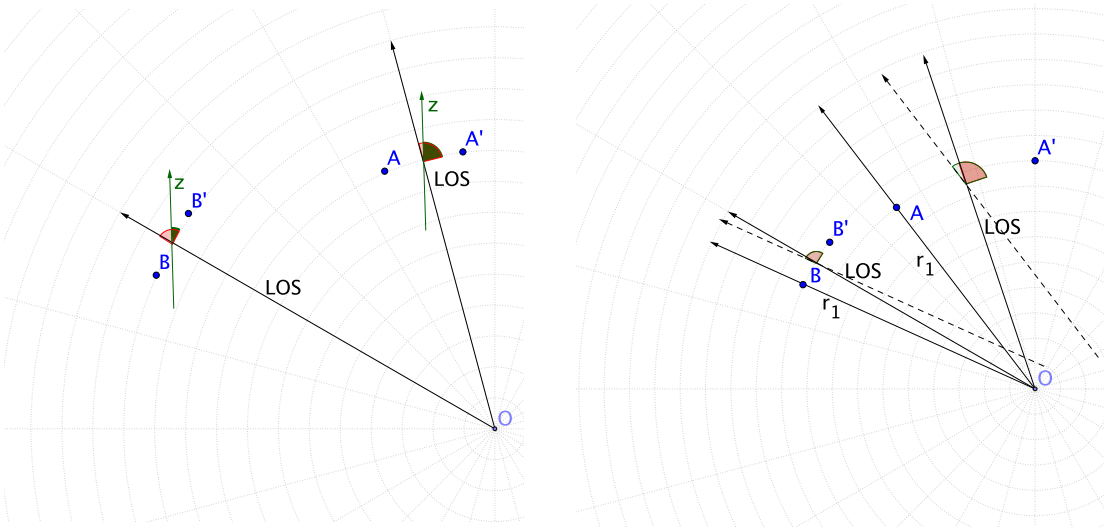

Figure 3.1: *Left:* Angles between the vector $y = \mathbf{x}_2 - \mathbf{x}_1$ connecting the galaxy pair and the LOS in the case of a constant LOS $\hat{z}$ (green), in the case of the mid-point LOS (red). *Right:* Angles between the vector connecting the galaxy pair and the LOS in the case of the end-point LOS approximation $\hat{n} = \hat{\mathbf{x}}_1$ (green), in the case of the mid-point LOS (red).

with respect to the Yamamoto estimator, where a pairwise LOS direction is originally considered and show by geometrical arguments that the situation in which the end-point approximation returns the largest difference with this reference is for pairs with large angular separations. On the other hand, the fixed LOS breaks already for galaxy pairs for which the mid-point direction departs from the fixed LOS, even for small pair separations. This result is schematically summarized by figure 3.1, taken from reference [140].

The same LOS hack can be arranged for the Bispectrum multipoles. We will adopt the definition of the redshift-space multipoles of the bispectrum introduced by [148], and assumed as well by [147] and [61], where $B_s(\mathbf{k}_1, \mathbf{k}_2, \hat{n})$ is given in terms of the variables k_1, k_2, k_3, $\mu_1 = \cos(\theta_1)$ and ξ, with θ being the angle between k_1 and the LOS $\hat{n}$ while ξ is the azimuthal angle describing a rotation of k_2 around k_1. Nonetheless, for the moment being, we stick to [147] definition of the local bispectrum at $\mathbf{x}$, so that angular coordinates are given with respect to the real-space position $\mathbf{x}$. In what follows, we start from the most generic description of a varying LOS, $\hat{n} = \hat{x}$, without any initial approximation. According to these choices, the local estimator is

$$\hat{B}^{\rm local}(\mathbf{k}_1, \mathbf{k}_2, \mathbf{x}) = \int \frac{\mathrm{d}^3 x_{13}}{(2\pi)^3} \frac{\mathrm{d}^3 x_{23}}{(2\pi)^3} \, e^{-i(\mathbf{k}_1 \cdot \mathbf{x}_{13} + \mathbf{k}_2 \cdot \mathbf{x}_{23})} \prod_{i=1}^{3} \delta(\mathbf{x} + \mathbf{w}_i) \,, \tag{3.19}$$

where $\mathbf{x} = (\mathbf{x}_1 + \mathbf{x}_2 + \mathbf{x}_3)/3$, $\mathbf{x}_i = \mathbf{x} + \mathbf{w}_i$ and $\mathbf{w}_{ij} = \mathbf{x}_i - \mathbf{x}_j$. We can expand the local bispectrum on the angular variables $\mu_1 = \hat{\mathbf{q}}_1 \cdot \hat{\mathbf{x}}$ and ξ, being the azimuthal angle of $\mathbf{q}_1$

around $\mathbf{q}_2$, with spherical harmonics

$$\hat{B}_{\ell m}(k_1,k_2,k_3) = \frac{(2\ell+1)}{N_T(k_1,k_2,k_3)} \prod \int_{k_i} \mathrm{d}^3 q_i \, \delta_{\mathrm{D}}(\mathbf{q}_{123}) \int \frac{\mathrm{d}^3 x}{(2\pi)^3} \, B(\mathbf{q}_1,\mathbf{q}_2,\mathbf{x}) Y_{\ell m}(\mu_1,\xi) \,, \tag{3.20}$$

where integrals are computed over k_i bins. For $m = 0$ multipoles, the ξ-dependence is dropped and

$$\hat{B}_{\ell}(k_1,k_2,k_3) = \frac{(2\ell+1)}{N_T(k_1,k_2,k_3)} \prod_{i=1,2,3} \int_{k_i} d^3 q_i \, \delta_{\mathrm{D}}(\mathbf{q})_{123} \int \frac{d^3 x_i}{(2\pi)^3} \, \delta(\mathbf{x}_i) e^{-i\mathbf{q}_i\cdot\mathbf{x}_i} \mathcal{L}_\ell(\mathbf{q}_1\cdot\hat{n}) \,, \tag{3.21}$$

where we have substituted $\hat{n} = \hat{x} = \frac{\widehat{(\mathbf{x}_1+\mathbf{x}_2+\mathbf{x}_3)}}{3}$ to emphasize the LOS dependence of the equation, which is the analogous of equation (3.12) for the bispectrum. Note that, in the most general form, the LOS corresponds to the direction of the geometrical center of the triangle. Taking the limit $\hat{n} \to \hat{\mathbf{x}}_1$, the integrals over the spatial coordinates are separable and the quadrupole and hexadecapole are:

$$\hat{B}_2(k_1,k_2,k_3) = 5 \int_{k_1} d^3 q_1 \int_{k_2} d^3 q_2 \int_{k_3} d^3 q_3 \, \frac{\delta_{\mathrm{D}}(\mathbf{q}_{123})}{N_T(k_1,k_2,k_3)} \, \delta_2(\mathbf{q}_1)\delta_0(\mathbf{q}_2)\delta_0(\mathbf{q}_3) \tag{3.22}$$

$$\hat{B}_4(k_1,k_2,k_3) = 9 \int_{k_1} d^3 q_1 \int_{k_2} d^3 q_2 \int_{k_3} d^3 q_3 \, \frac{\delta_{\mathrm{D}}(\mathbf{q}_{123})}{N_T(k_1,k_2,k_3)} \, \delta_4(\mathbf{q}_1)\delta_0(\mathbf{q}_2)\delta_0(\mathbf{q}_3) \tag{3.23}$$

As for the Power Spectrum case, one can decompose the 4-th order Legendre term and write an alternative expression for the hexadecapole which doesn't need δ_4:

$$\begin{aligned} \hat{B}_4(k_1,k_2,k_3) =& \frac{35}{2} \int_{k_1} d^3 q_1 \int_{k_2} d^3 q_2 \int_{k_3} d^3 q_3 \, \frac{\delta_{\mathrm{D}}(\mathbf{q}_{123})}{(2\pi)^3} \delta_2(\mathbf{q}_2)\delta_2(\hat{q}_1,\mathbf{q}_2)\delta_0(\mathbf{q}_3) \\ & - \hat{B}_2(k_1,k_2,k_3) - \frac{7}{2}\hat{B}_0(k_1,k_2,k_3) \end{aligned} \tag{3.24}$$

where

$$\delta_2(\hat{q}_1,\mathbf{q}_2) = \frac{3}{2}\hat{q}_i\hat{q}_j Q_{ij}(\mathbf{q}) - \frac{1}{2}\delta_0 \,. \tag{3.25}$$

The additional $\hat{q}_1$ dependence makes much harder to evaluate this term, so that in general (3.23) is used.

The evaluation the bispectrum multipoles suffers from an additional complication due to the Dirac delta function ensuring that $\mathbf{q}_1, \mathbf{q}_2, \mathbf{q}_3$ form a closed triangle. A possibility is to expand δ_{D} in plane waves and factorize the estimator as

$$\hat{B}_{\ell}(k_1,k_2,k_3) = \frac{(2\ell+1)}{N_T(k_1,k_2,k_3)} \int \frac{\mathrm{d}^3 x}{(2\pi)^3} \delta_\ell^{(k_1)}(\mathbf{x})\delta_0^{(k_2)}(\mathbf{x})\delta_0^{(k_3)}(\mathbf{x}) + \mathrm{cyc.} \,, \tag{3.26}$$

where

$$\delta_\ell^{(k_i)}(\mathbf{x}) = \int_{k_i} \mathrm{d}^3 q \, e^{i\mathbf{q}\cdot\mathbf{x}} \delta_\ell(\mathbf{q}) \,, \tag{3.27}$$

and cyc. stands for cyclic permutations in ℓ terms.

Bispectrum shot noise

Estimating the auto-correlation term for the bispectrum multipoles $B_{\rm shot}$ is a hard task. Referfence [147] provides an expression with some internal bug so, to derive our own expression, we start from

$$\begin{aligned}\langle\delta(\mathbf{x}_1)\delta(\mathbf{x}_2)\delta(\mathbf{x}_3)\rangle =& \,\delta_1\delta_2\delta_3 \\ &+ \frac{1}{\bar{n}}[\delta_1(1+\delta_2)\delta_{\rm D}(\mathbf{x}_{23}) + \delta_2(1+\delta_3)\delta_{\rm D}(\mathbf{x}_{13}) + \delta_3(1+\delta_2)\delta_{\rm D}(\mathbf{x}_{12})] \\ &+ \frac{1}{\bar{n}^2}(1+\delta_1)\delta_{\rm D}(\mathbf{x}_{12})\delta_{\rm D}(\mathbf{x}_{23})\,.\end{aligned} \tag{3.28}$$

Substituting the noise terms in the estimator, gives

$$\begin{aligned}\hat{B}_\ell^{SN}(k_1,k_2,k_3) =& \frac{(2\ell+1)}{N_T(k_1,k_2,k_3)}\prod_{i=1,2,3}\int_{k_i} d^3q_i\,\delta(\mathbf{q}_{123})\left[\frac{1}{\bar{n}^2}\left(\int\frac{{\rm d}^3x}{(2\pi)^3}(1+\delta(\mathbf{x}))\mathcal{L}_\ell(\hat{\mathbf{q}}_1\cdot\hat{\mathbf{x}}_1)\right)\right. \\ &\left. + \frac{1}{\bar{n}}\big(\delta_\ell(\mathbf{q}_1)\delta_0(-\mathbf{q}_1) + \delta_0(\mathbf{q}_2)\delta_\ell(\hat{\mathbf{q}}_1,\mathbf{q}_2) + \delta_0(\mathbf{q}_3)\delta_\ell(\hat{\mathbf{q}}_1,\mathbf{q}_3)\big)\right],\end{aligned} \tag{3.29}$$

where

$$\delta_\ell^w(\hat{\mathbf{q}}_1,\mathbf{q}) = \int\frac{{\rm d}^3x}{(2\pi)^3}\,e^{-i\mathbf{q}\cdot\mathbf{x}}\big(1+\delta(\mathbf{x})\big)\mathcal{L}_\ell(\hat{\mathbf{q}}_1\cdot\hat{\mathbf{x}})\,. \tag{3.30}$$

To compute this term, one can factor out the dependence on $\hat{\mathbf{q}}_1$ by expanding the Legendre polynomial, such that (for $l=2$)

$$\delta_2(\hat{\mathbf{q}}_1,\mathbf{q}_2) = \frac{3}{2}\hat{\mathbf{q}}_{1i}\hat{\mathbf{q}}_{1j}Q_{ij}^w(\mathbf{q}_2) - \frac{1}{2}\delta_0(\mathbf{q}_2)\,, \tag{3.31}$$

where Q_{ij}^w has a similar form to Q_{ij}. Then one can adopt once more the Dirac delta expansion trick to get the terms in (3.27). Each of these terms needs to be integrated over $\mathbf{q}_1$, $\mathbf{q}_2$, $\mathbf{q}_3$, so one has to keep these fields separately in memory when the shot-noise term is evaluated. Being each of these a symmetric tensor, 6 fields must be allocated for the quadrupole. Going to $\ell=4$, makes the problem even worse: instead of rank 2 tensors, you get rank 4 tensors, with 15 independent components each.For this reason, thin-shell approximation is often adopted and this allows to reduce the number of auxiliary fields to be computed to 2.

Beyond-Yamamoto Power Spectrum estimator

The approximation to the end-point estimator leads to differences with respect to the Yamamoto estimator that can biases two-point observables on BAO scales on a level of $0.1-1.0\%$, although being still smaller than the cosmic variance error for a typical survey

observing a large fraction of the sky [32], [21]. A recent paper, [128], questions the possibility to reach an efficient implementation of the Yamamoto estimator, adopting mid-point $\hat{n} = \widehat{\frac{\mathbf{x}_1+\mathbf{x}_2}{2}}$ and bisector $\theta = \frac{1}{2}\cos(\hat{\mathbf{x}}_1 \cdot \hat{\mathbf{x}}_2)$ definitions. The authors find that a series expansion of the angular dependence in the opening angle can do the trick, providing an algorithm that scales as $\mathcal{O}[N_g \log N_g]$ and allows in the meantime to use the FFT libraries.

3.1.4 The Feldman-Kaiser-Peacock (FKP) estimator

Historically, one of the milestones in power spectrum measurements from galaxy redshift surveys is the Feldman Kaiser Peacock (FKP) paper [55]. The authors develop an optimal weighting scheme for the estimator just described, according to which each galaxy is assigned a weight to reduce the variance of measurements on the scale of interest. This provides an optimal estimation in the case that

- the scale $1/k$ is small compared to the size of the survey,
- galaxy density fluctuations are Gaussian.

The estimators defined so far assumed an homogeneous distribution in a finite volume. This can be a box with periodic boundary conditions as in the case of N-body simulations. The estimation of the power spectrum (and bispectrum) in an actual galaxy survey must account for an irregular footprint geometry and the evolution of the mean number density with redshift, $\bar{n}(z)$. Therefore, galaxy perturbations must be evaluated from a comparison of the observed distribution against a simulated catalog with a uniform distribution of objects, constructed over the same survey footprint. Such mock allows us to incorporate observational systematic effects that affect the survey so that the comparison between the two datasets is consistent. This comparison is then described by the auxiliary field F measuring the excess of particles in each point against the simulated catalog of N_r objects, where typically $N_r \gg N_d$, N_d being the total number of observed objects. In this work we will swap sometimes from δ to F and viceversa depending on what we want to highlight in our discussion. We shall use δ when we prefer to put the accent on the physical interpretation of the fluctuations, hiding unnecessary implementation technicalities present in F. On the other hand, we shall use F when we want to discuss the algorithm used and show details.

This auxiliary field is given by

$$F(\mathbf{x}) = \frac{w(\mathbf{x})[n_{\rm d}(\mathbf{x}) - \alpha n_{\rm r}(\mathbf{x})]}{[\int d^3x\, \bar{n}^2(\mathbf{x}) w^2(\mathbf{x})]^{1/2}}\,. \tag{3.32}$$

where w is the FKP weight, given by

$$w = \frac{1}{1 + \bar{n}(z)P(k)}\,, \tag{3.33}$$

α is a factor needed to rescale the total number of particles in the random catalog to the

number density observed in the data,

$$\alpha = \frac{\int d^3x\, w(\mathbf{x})\, \bar{n}_{\rm g}(\mathbf{x})}{\int d^3x\, w(\mathbf{x})\, n_r(\mathbf{x})}\,, \tag{3.34}$$

and the denominator ensures that the power spectrum is dimensionless. One might question whether measuring the power spectrum with a weight that depends on $P(k)$ is a circular argument. This is a legitimate question. However, the application of a k-dependent weight is an even more cumbersone one. Usually, the solution to his problem is to use a single number for this term, corresponding to the order-of-magnitude amplitude of $P(k)$ at the wavenumber where we want the variance to be reduced. Taking the FT of equation (3.32) $F(\mathbf{k})$, the volume average of the signal is

$$\langle |F(\mathbf{k})|^2 \rangle = \int d^3k' P(k') |W(\mathbf{k}-\mathbf{k}')|^2 + (1+\alpha) \frac{\int \mathrm{d}^3x\, \bar{n}(\mathbf{x}) w^2(\mathbf{x})}{\int \mathrm{d}^3x\, \bar{n}^2(\mathbf{x}) w^2(\mathbf{x})}\,, \tag{3.35}$$

with the second term being the shot noise contribution $P_{\rm shot}$, and

$$W(\mathbf{k}) = \frac{\int d^3x\, \bar{n}(\mathbf{x}) w(\mathbf{x}) e^{i\mathbf{k}\cdot\mathbf{r}}}{[\int d^3x\, \bar{n}^2(\mathbf{x}) w^2(\mathbf{x})]^{1/2}} \tag{3.36}$$

being the window function of the random distribution, holding information on the survey geometry and on the galaxy weights. The FKP estimator is then defined as

$$\hat{P}_{\rm FKP}(k) = \langle |F(\mathbf{k})|^2 \rangle - \hat{P}_{\rm shot}(k)\,. \tag{3.37}$$

Note that the FKP estimator does not provide a direct evaluation of the power spectrum of a given distribution, but rather a convolution of the true power spectrum with the survey window function. In order to make a proper comparison with the theory, predictions must be convolved with the measured survey window. However, the broad extent of $W(\mathbf{k})$ in Fourier space makes the convolution computationally expensive. We will come back to this later on, when we discuss future extensions of this work to lightcone measurements. For the time being, let us just say that some smart shortcuts to deal with this issue exist [168, 24].

3.2 Implementation

Figure 3.2 and 3.3 provide the flow charts of the power spectrum and bispectrum codes that I developed during my PhD and that have eventually been adopted for the Euclid LE3_GC_PowerSpectrum and LE3_GC_Bispectrum codes. A former version of the code computing the bispectrum was used to provide measurements of N-body simulations and approximate mock catalogs of Chapter 4 and 5.

In this section we provide a description of the major steps that are needed to compute the power spectra and bispectra of a given particle distribution, starting from their positions

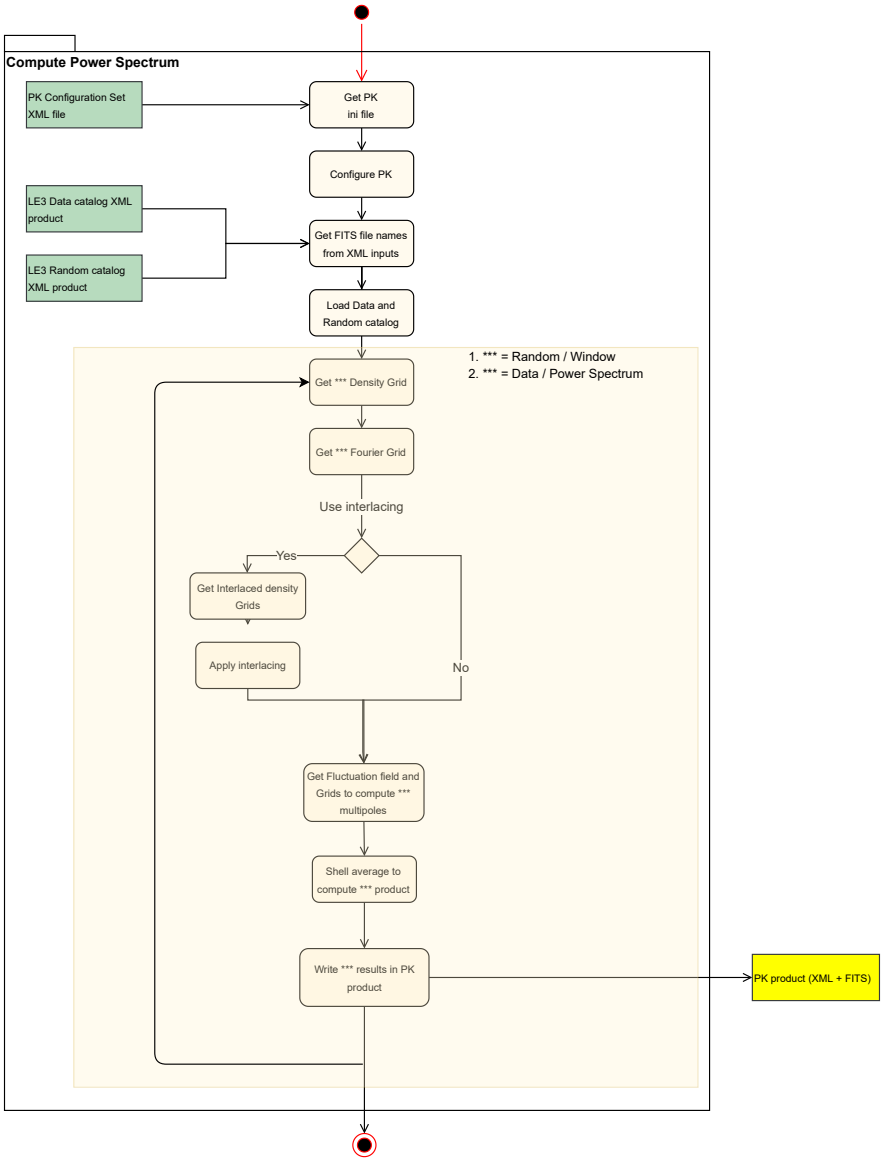

Figure 3.2: Flow Chart for Power Spectrum code

in configuration space. We will now describe the general behavior and major steps, while a more detailed description of each procedure will be given in a dedicated section.

After setting-up the options for the run, completely configurable by the user, the data catalog and the random catalog required to evaluate the FKP density field are loaded and stored into memory. The data catalog consists of the spectroscopic galaxy catalog whereas the random catalog corresponds to a synthetic mock populated by a uniform distribution of objects, which accounts for the systematic observational effects present in the data.

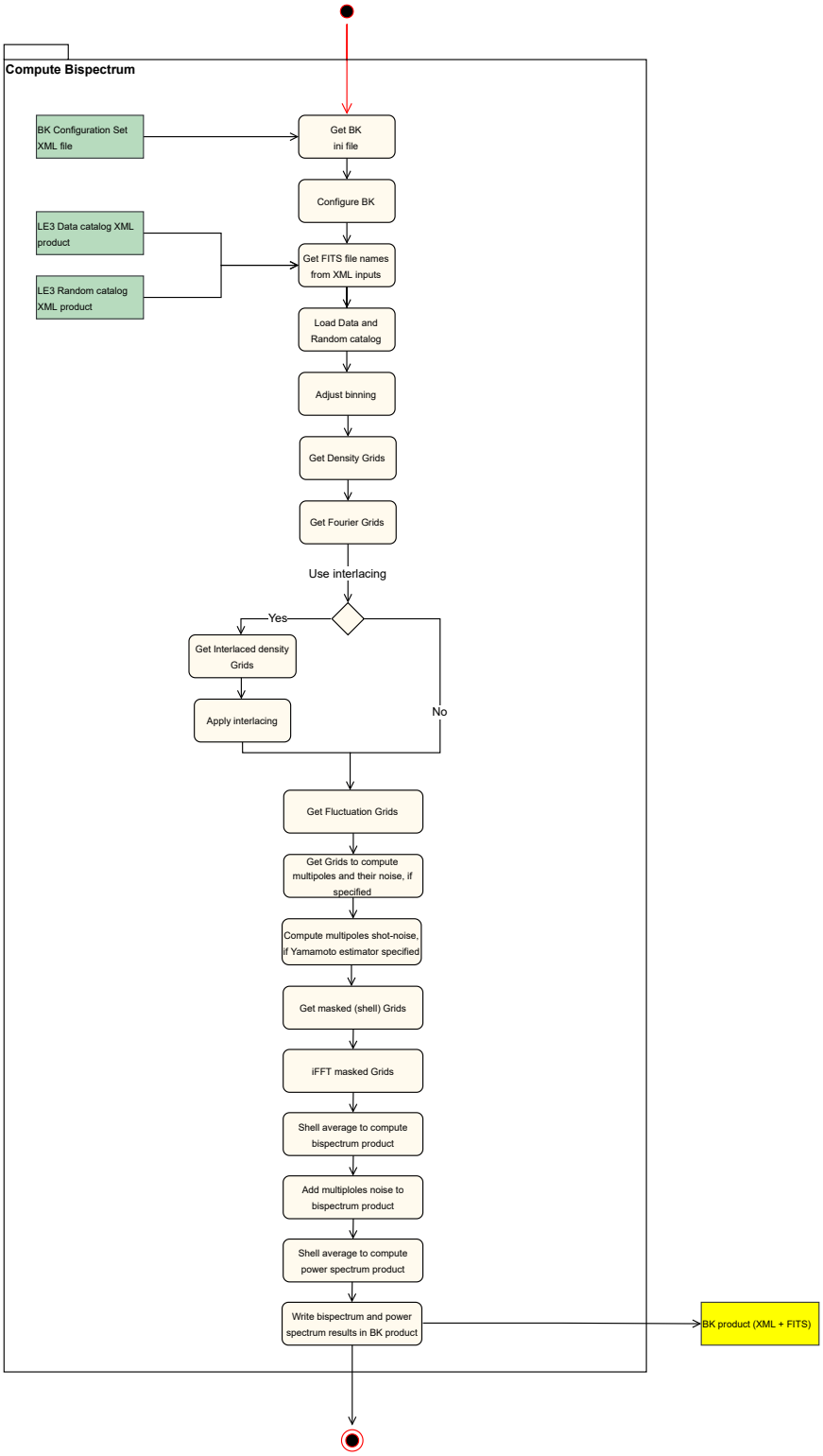

Figure 3.3: Flow Chart for Bispectrum code

Binning parameters are then computed, based on the user choices, specified in the configuration file. The catalogs are then run through and the density field is computed

over a grid for the data $n_d(\mathbf{x}^{\rm G})$ and random $n_r(\mathbf{x}^{\rm G})$ samples. The size of the grid $N_{\rm G}$ is a parameter that can be tuned in the configuration file according to the needs. The subscript G in the equations that follow, indicates that the coordinates are evaluated on a grid. We will address the need of introducing this object in the next section, Section 3.2.1.

The densities are then Fourier transformed to the wavelength domain where some procedures are adopted to mitigate some odd noise introduced by previous steps, ascribable to the finite size of the grid. These noise contributions relate to the convolution process inherent to the evaluation of the density on a grid of finite size and to the fact that small scale-modes not supported by the grid are mistakenly identified as large-scale supported modes. At this point, the data and random densities are combined together to compute the FKP fluctuation field $F(\mathbf{k}^{\rm G})$. Depending on the estimator chosen, specified in the configuration file, additional fields of equation (3.13) and (3.14) are computed.

Up to this moment, both power spectrum and bispectrum estimators share the same procedures. The power spectrum code, then, evaluates the first $\ell = 0, 1, 2, 3, 4$ multipoles of the power spectrum and of the window function, by averaging the signal $F_0(\mathbf{k})F_\ell(\mathbf{k})$ over Fourier-space shells according to the binning choices specified in the configuration file. In this section we adopt the notation implying the fluctuation field F, as we want to highlight the details of the code implementation.

The bispectrum code, on the other side, must consider some additional steps in order to evaluate the $\delta_\ell^{(k)}(\mathbf{x}^{\rm G})$ fields of equation (3.27), which we will call $F_\ell^{(k)}(\mathbf{x}^{\rm G})$ to highlight their derivation from $F(\mathbf{x}^{\rm G})$. We will address the details of their computation in section 3.2.5. Once computed, the code evaluates the bispectrum and its $\ell = 0, 2, 4$ multipoles at different triangle bins (k_1, k_2, k_3) by taking the real-space average of $F_\ell^{(k_1)}(\mathbf{x}^{\rm G})F_0^{(k_2)}(\mathbf{x}^{\rm G})F_0^{(k_3)}(\mathbf{x}^{\rm G})$.

In the following paragraphs we focus on some major steps that require particular care.

3.2.1 Discretisation of estimators on a Grid

The code reads a particle distribution and provides, in the first place, an estimate of the Fourier-space density of a distribution of N_g particles with given weight. The DFT step needed to move from configuration to Fourier space requires the density field $n(\mathbf{x})$ to be sampled on regular intervals. It is common practice to introduce a finite grid of equally-spaced points $\mathbf{x}_i^{\rm G}$ of size $N_{\rm G}$ such that

$$\mathbf{x}^{\rm G} = h\,\mathbf{m} = h\,(m_x, m_y, m_z)\,,\ \text{with}\ m_x, m_y, m_z \in (0, \ldots, N_{\rm G} - 1)\,, \tag{3.38}$$

h being the grid cell linear size, such that $h = L_{\rm box}/N_{\rm G}$. The particle distribution is then sampled on the grid by means of an interpolation on the grid points. As a consequence, discrete sampling drives equations (3.32)-(3.25) towards discrete notation. We show how this is performed for a generic integral $I_{\alpha\beta}$, which is just generalizing the normalisation term

in (3.32),

$$\begin{aligned} I_{\alpha,\beta} &= \frac{1}{V}\int d^3x\, \bar{n}^{\alpha}(\mathbf{x}) w^{\beta}(\mathbf{x}) \\ &= \frac{\alpha}{V}\int d^3x\, \bar{n}^{\alpha-1}(\mathbf{x}) w^{\beta}(\mathbf{x}) \sum_{i=1}^{N_{\rm r}} \delta_{\rm D}(\mathbf{x}-\mathbf{x}_i) \\ &= \frac{\alpha}{V}\sum_{i=1}^{N_{\rm r}} \bar{n}^{\alpha-1}(\mathbf{x}_i) w^{\beta}(\mathbf{x}_i)\,, \end{aligned} \tag{3.39}$$

but we do not rewrite the equations already specified above.

3.2.2 Density interpolation on a grid

The sampling of the density distribution on the grid is performed by means of an interpolating procedure which assigns particle contributions from the given catalog to nearby grid points. At each grid point $\mathbf{x}^{\rm G}$, the density is evaluated by summing the contributions provided by all particles

$$n_W(\mathbf{x}^{\rm G}) = \sum_{i=1}^{N_p} w_i\, W^{(\ell)}(\mathbf{x}^{\rm G}-\mathbf{x}_i) \tag{3.40}$$

where N_p is the number of particles in the catalog, and $W^{(\ell)}$ is the interpolating kernel. Explicitly,

$$W^{(\ell)}(\mathbf{x}^{\rm G}-\mathbf{x}_i) = W^{(\ell)}_{1-{\rm Dim}}\left(\mathbf{x}^{\rm G}-\frac{x_i}{h}\right) W^{(\ell)}_{1-{\rm Dim}}\left(\mathbf{x}^{\rm G}-\frac{y_i}{h}\right) W^{(\ell)}_{1-{\rm Dim}}\left(\mathbf{x}^{\rm G}-\frac{z_i}{h}\right)\,, \tag{3.41}$$

where $W_{1-{\rm Dim}}$ is the one dimensional Kernel of order ℓ. The first orders are:

- Nearest Grid Point (NGP)

$$W^{(1)}_{1-{\rm Dim}}(s) = \begin{cases} 1 & \text{for } |s| < \frac{1}{2} \\ 0 & \text{otherwise} \end{cases} \tag{3.42}$$

- Cloud In Cell (CIC)

$$W^{(2)}_{1-{\rm Dim}}(s) = \begin{cases} 1-|s| & \text{for } |s| < 1 \\ 0 & \text{otherwise} \end{cases} \tag{3.43}$$

- Triangular Shaped Cloud (TSC)

$$W^{(3)}_{1-\mathrm{Dim}}(s) = \begin{cases} \frac{3}{4} - s^2 & \text{for } |s| < \frac{1}{2} \\ \frac{1}{2}\left(\frac{3}{2} - |s|\right)^2 & \text{for } \frac{1}{2} \leq |s| < \frac{3}{2} \\ 0 & \text{otherwise} \end{cases} \tag{3.44}$$

- Piecewise Cubic Spline (PCS)

$$W^{(4)}_{1\mathrm{D}}(s) = \begin{cases} (2 - |s|)^3 & \text{for } 1 \leq |s| < 2 \\ 0 & \text{otherwise} \end{cases} \tag{3.45}$$

The order of the interpolating-kernel indicates the number of points which receive contribution from a given particle, so that if NGP is chosen, a galaxy contribution is attributed to a single point, its nearest neighbour, while CIC assigns non-zero contribution to the nearest two and so on and so forth. Note that the total contribution of a particle does not depend on the order of the interpolating kernel, and it is always equal to 1. As the catalog is run through, the code computes the contribution of each particle and assigns it to the correspondent grid points according to the scheme above.

Mass assignment correction

In practice, the result of the Density Interpolation step is a convolution of the configuration-space density with the Mass Assignment Scheme (MAS) kernel $W^{(\ell)}$ therefore, it needs to be corrected. Taking advantage of the fact that convolutions in configuration space become products in Fourier space and viceversa, this step is taken after DFT are applied to $n(\mathbf{x}^{\mathrm{G}})$. For a given MAS, the corrected density then becomes,

$$n(\mathbf{k}^{\mathrm{G}}) = \frac{n_W(\mathbf{k}^{\mathrm{G}})}{W^{(\ell)}(\mathbf{k}^{\mathrm{G}})}\,, \tag{3.46}$$

where, for a given MAS order ℓ, the kernel is

$$W^{(\ell)}(\mathbf{k}^{\mathrm{G}}) = \left[\frac{\sin(k_x h/2)}{k_x h/2}\right]^{\ell}\left[\frac{\sin(k_y h/2)}{k_y h/2}\right]^{\ell}\left[\frac{\sin(k_z h/2)}{k_z h/2}\right]^{\ell}. \tag{3.47}$$

3.2.3 Fourier Transform

Fourier Transforms are needed to translate the configuration-space estimate of the density to the Fourier domain. Be $n(\mathbf{x}^{\mathrm{G}})$ the density field, already interpolated on the grid - the density grid. The Fourier Transform is performed taking advantage of the FFTW library

[58]. This gives

$$\begin{aligned} n(\mathbf{k}^{\mathrm{G}}) &= \sum_{\mathbf{x}^{\mathrm{G}}} n(\mathbf{x}^{\mathrm{G}})\, e^{-i\mathbf{k}^{\mathrm{G}}\cdot\mathbf{x}^{\mathrm{G}}} \\ &= \sum_{\mathbf{m}} n\left(\frac{L_{\mathrm{box}}}{N_{\mathrm{G}}}\mathbf{m}\right)\, e^{-2\pi i\, \mathbf{n}\cdot\mathbf{m}/N_{\mathrm{FFT}}} \end{aligned} \tag{3.48}$$

The code takes full advantage of the time-optimization of this library, which allows parallel computation on multiple OpenMP threads. The scaling with respect to an increasing number of threads is not ideal, but the speed-up is anyway crucial.

3.2.4 Aliasing

It is broadly recognized that power spectrum estimator implementations relying on FFTs suffer from limitations. In particular, the Sampling Theorem guarantees that a lossless sampling of a given band-width limited signal is achieved only in the case when the sampling frequency is twice the frequency at the cut-off. Of course, these conditions are not met in the case of cosmological density perturbations, which are defined over the whole Universe. A poor matching of the Sampling Theorem's hypothesis is responsible for small scale modes, unresolvable for the given grid resolution, being erroneously identified as supported, long-wavelength modes, spoiling the Fourier space density and thus biasing the resulting power spectrum and bispectrum, specially at small scales.

The sampling in configuration space given by eq. (3.40) can be mathematically described in terms of the sampling function

$$\text{Ш}(\mathbf{x}) = \sum_{\mathbf{n}} \delta_D(\mathbf{x} - \mathbf{n})\,, \tag{3.49}$$

where $\mathbf{n}$ is an integer vector identifying each point of the grid, so that equation (3.40) can be re-written as

$$n^{\mathrm{G}}(\mathbf{x}) = \text{Ш}(\mathbf{x}/h) n_W(\mathbf{x})\,, \tag{3.50}$$

and the Fourier Transform of this product is

$$\delta^{\mathrm{G}}(\mathbf{k}) = k_f^3 \sum_{\mathbf{k}'} \text{Ш}(\mathbf{k}')\delta_W(\mathbf{k} - \mathbf{k}')\,, \tag{3.51}$$

where k_f is the fundamental frequency of the box $2\pi/L_{\mathrm{box}}$. As the Dirac delta function becomes a Kronecker delta in Fourier space, the transform of the sampling function gives

$$\delta^{\mathrm{G}}(\mathbf{k}) = \sum_{\mathbf{m}} \delta_W\left(\mathbf{k} - \frac{2\pi}{H}\mathbf{m}\right) \tag{3.52}$$

where $m \neq 0$ terms represent the spourious aliasing contribution due to small-scales unresolved modes.

Reference [91] computes the prediction of the aliasing contribution to the power spectrum. This is given by

$$\langle|\delta^{\mathrm{G}}(\mathbf{k})|^2\rangle = \sum_{\mathbf{n}} P(\mathbf{k}+2k_N\mathbf{n})|W(\mathbf{k}+2k_N\mathbf{n})|^2 + \frac{1}{N}\sum_{\mathbf{n}}|W(\mathbf{k}-2k_N\mathbf{n})|^2\,, \tag{3.53}$$

where $k_N = \pi/h$ is the largest wavenumber accessible, i.e.Nyquist frequency of the grid, and the second term represents the aliasing contribution to the shot-noise. This function connects the true power spectrum $P(k)$ to the one estimated on the grid $\langle|\delta^{\mathrm{G}}(\mathbf{k})|^2\rangle$. Two are the effects that enter in this equation. One is the convolution of the density with the MAS-window-function that returns the multiplication of the true power spectrum with $W(\mathbf{k})$, the other comes from the finite size of the grid which translates in a sum over the aliasing images.

Interlacing

The *Interlacing* technique, taking place right after the Fourier Transform one in 3.3 in order to reduce the memory budget, requires to estimate the density field $\delta_{\mathrm{G}}(\mathbf{k})$ on two, equal grids displaced by half of the cell size. Be $\delta_{\mathrm{G}_1}(\mathbf{k})$ the first density grid, the displaced density is

$$n_{\mathrm{G}_2}(\mathbf{k}) = \text{Ш}\left(\frac{\mathbf{x}}{H}+\frac{\mathbf{1}}{2}\right) n_W(\mathbf{x})\,, \tag{3.54}$$

where $\mathbf{1}$ is the unit vector. The Fourier transform is

$$n_{\mathrm{G}_2}(\mathbf{k}) = \frac{1}{2}\sum_{\mathbf{m}}(-1)^{m_x+m_y+m_z}\, n_W\left(\mathbf{k}-\frac{2\pi}{H}\mathbf{m}\right) \tag{3.55}$$

Taking the proper weighted average between $n_W(\mathbf{k}^{\mathrm{G}_1})$ and $n_W(\mathbf{k}^{\mathrm{G}_2})$ we get

$$n_{\mathrm{G}}(\mathbf{k}) = \frac{1}{2}\sum_{\mathbf{m}}\left[1+(-1)^{m_x+m_y+m_z}\right] n_W\left(\mathbf{k}-\frac{2\pi}{H}\mathbf{m}\right)\,. \tag{3.56}$$

The term between square brackets vanishes for odd values of $m_x+m_y+m_z$, therefore odd aliasing contributions can be completely removed by this technique. Note that higher-order interpolating schemes and MAS correction act to minimize the aliasing effect and can be coupled to interlacing to limit it to the frequencies above Nyquist and make it practically irrelevant for the scales of interest. In the case of the Euclid mission, which is the main target of this work, these are $0.005 - 0.5\,h\,\mathrm{Mpc}^{-1}$.

3.2.5 Shell average

Power Spectrum

Once that the density has been interpolated over the grid and Fourier transformed for both the data catalog $n_d(\mathbf{k}^{\mathrm{G}})$ and the random one $n_r(\mathbf{k}^{\mathrm{G}})$, the FKP auxiliary field $F(\mathbf{k}^{\mathrm{G}})$ is

computed as

$$F(\mathbf{k}^{\mathrm{G}}) = n_d(\mathbf{k}^{\mathrm{G}}) - \alpha\, n_r(\mathbf{k}^{\mathrm{G}})\,. \tag{3.57}$$

Note that the normalisation factor is not considered in the equation above and that normalisation is only applied after the shell-average has been performed. The reason for this choice is that this auxiliary field is shared by both the power spectrum and bispectrum codes, which, however, retain different normalisation factors, I_{22} and I_{33}. If the Yamamoto estimator is chosen in the configuration file, $F_2(\mathbf{k}^{\mathrm{G}})$ and $F_4(\mathbf{k}^{\mathrm{G}})$ are computed.

The power spectrum and its multipoles can then be evaluated by averaging over the Fourier space shells defined by the binning scheme. In the case of the distant observer approximation, this becomes

$$\hat{P}_\ell(k) = \frac{(2\ell+1)}{N_{\mathrm{modes}}}\frac{1}{I_{22}} \sum_{k-\mathrm{d}k\leq\mathbf{k}^{\mathrm{G}}\leq k+\mathrm{d}k} |F(\mathbf{k}^{\mathrm{G}})|^2 \mathcal{L}_\ell(\hat{k}\cdot\hat{n})\,. \tag{3.58}$$

On the other hand, according to [147] [26], the Yamamoto estimators are given by

$$\hat{P}_\ell(k) = \frac{(2\ell+1)}{N_{\mathrm{modes}}}\frac{1}{I_{22}} \sum_{k-\mathrm{d}k\leq\mathbf{k}^{\mathrm{G}}\leq k+\mathrm{d}k} F_0(\mathbf{k}^{\mathrm{G}})F_\ell(\mathbf{k}^{\mathrm{G}})\,, \tag{3.59}$$

where F_2 and F_4 are given by (3.13) and (3.14), and I_{22} takes care of the normalisation.

Bispectrum

As previously mentioned, the bispectrum code requires some additional steps after $F_0(\mathbf{k}^{\mathrm{G}})$, $F_2(\mathbf{k}^{\mathrm{G}})$, $F_4(\mathbf{k}^{\mathrm{G}})$ have been computed, before being able to return the final product. In particular, masked shells $F_\ell^{(k)}(\mathbf{k}^{\mathrm{G}})$ for each of these fields must be constructed. This procedure is schematically presented in Figure 3.4, where a filter is applied to $F_\ell(\mathbf{k}^{\mathrm{G}})$ according to the binning scheme selected for the wavenumbers k_1, k_2, k_3. The filter operates in such a way that Fourier modes lying outside of the bin k are set equal to 0 whereas modes contained within the bin remain unchanged. An additional set of masked binary-valued grids being equal to 1 over the given shell and 0 outside, $I^{(k)}(\mathbf{k}^{\mathrm{G}})$, are also generated to compute $N_T(k_1, k_2, k_3)$. Inverse FFTs are then computed for all masked shells $F_\ell^{(k)}(\mathbf{k}^{\mathrm{G}})$, giving $F_\ell^{(k)}(\mathbf{x}^{\mathrm{G}})$ and $I^{(k)}(\mathbf{x}^{\mathrm{G}})$ as output. Finally, shell-averaged measurements of the monopole, quadrupole, hexadecapole, and number of fundamental triangles are computed from summations of products of the real-space fields.

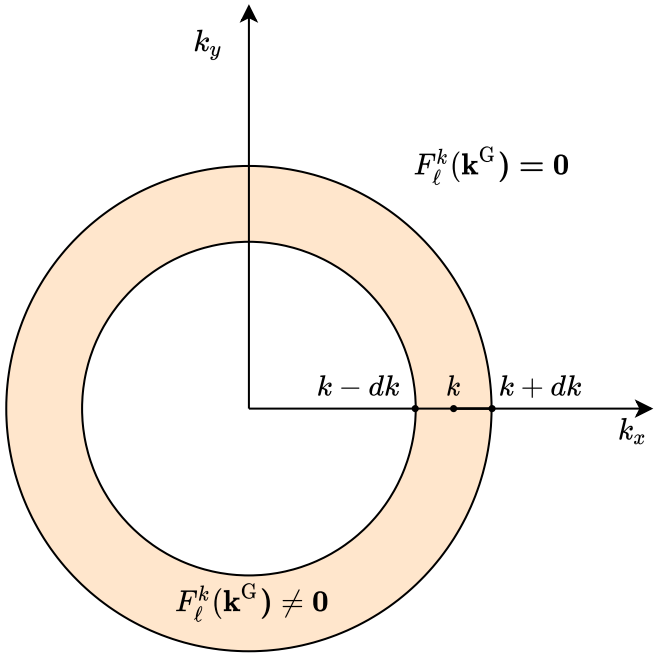

Figure 3.4: Visual rendering of the masked-field objects $F_\ell^{(k)}(\mathbf{k}^{\rm G})$. The *colored area* identifies the shell k in 2D. The masked field vanishes outside the shell and retains the correspondent value of $F_\ell(\mathbf{k}^{\rm G})$ inside it.

The bispectrum is given by

$$\hat{B}_\ell(k_1, k_2, k_3) = \frac{2\ell+1}{N_T(k_1, k_2, k_3)} \frac{1}{I_{33}} \sum_{\mathbf{x}^{\rm G}} F_\ell^{k_1}\big(\mathbf{x}^{\rm G}\big) F_0^{k_2}\big(\mathbf{x}^{\rm G}\big) F_0^{k_3}\big(\mathbf{x}^{\rm G}\big)\,, \tag{3.60}$$

where

$$N_T(k_1, k_2, k_3) = \sum_{\mathbf{x}^{\rm G}} I^{k_1}\big(\mathbf{x}^{\rm G}\big) I^{k_2}\big(\mathbf{x}^{\rm G}\big) I^{k_3}\big(\mathbf{x}^{\rm G}\big)\,, \tag{3.61}$$

and the normalisation factor is

$$I_{33} = \Big[\int \frac{\mathrm{d}^3x}{(2\pi)^3}\, \bar{n}^3(\mathbf{x}) w^3(\mathbf{x})\Big]^{1/3} \to \Big[\sum_{i=1}^{N_r} \bar{n}^2(\mathbf{x}_i) w^3(\mathbf{x}_i)\Big]^{1/3}. \tag{3.62}$$

Note that the arrow in this last expression follows from equation (3.39).

3.3 Contributions to Euclid Code

A large part of my Ph.D. work was carried out within the Euclid collaboration, where I was in charge of the development of the official data analysis software that will be used to provide measurements of the power spectrum and bispectrum of the spectroscopic Wide Survey sample. The development of such software is a complex duty as a meticulous assessment of its accuracy and computing performances is required to ensure that the mission requirements

are achieved and that the software execution proceeds flawlessly from the beginning to the end of the data reduction pipeline.

Each of the PFs (as the PK-GC and BK-GC) must possess a dedicated documentation describing the implemented algorithm, consisting of the Software Design Document (SDD), a Validation Plan document (VP-STS) describing the test developed to assess the scientific accuracy, a Software User Manual (SUM) providing the generic installation and usage instructions, and Software Release Notes (SRN) describing features of each new release. Consequently, each PF must take on a rigorous test campaign made by Maturity Assessment (MA) where a designated reviewer is expected to verify the quality of the code, the status of the PF with respect to the validation tests defined in the VP, and that the overall requirements are met. Each MA triggers the production of a new version of the documents and a new instance of the test execution, therefore, they must be prepared in advance with particular care.

Validation is intended to be an end-to-end testing. In practice, we run the PF using as inputs mock catalogs (produced by the validation team in collaboration with the Galaxy Clustering Science Working Group, who defines the science validation criteria) and compare the results to some benchmark measurements. As an output we obtain a pass/fail and/or a percentage of fulfilment of the scientific requirements. Requirement criteria for Euclid PK-GC and BK-GC codes usually require that the numerical systematic errors between the computed output and the reference values are smaller than 10% of the predicted Gaussian sample variance errors for the Euclid Wide Survey (as defined in the Euclid SGS LE3 Requirement Specification Document), on a bin-by-bin basis, in the range for which the input PF is expected to be recovered (binning and k-ranges are also specified in the Requirement Spscification Document). Since assessing that these requirements are actually met is not feasible for the time being, we assume that Euclid requirements are met if the same residuals are below 0.1%. In the following, we assume that Euclid requirements match with this threshold.

I will now briefly describe each test that is part of the validation campaign for the power spectrum PF, PK-GC ,and bispectrum PF, BK-GC. For each test I will identify the section of the code under review, the data-set used, and the purpose of the given analysis. No explicit results will be provided of these test, even if already completed, as they will be part of an official Euclid publication, currently in preparation.

3.3.1 Power Spectrum Validation Tests

Mass Assignment test by Direct Summation

This test focuses on the Mass Assignment Scheme (MAS) that interpolates the density field on a grid and the FFT that provides the Fourier-space density. The objective is to validate

the PK-GC code against the results obtained by direct summation from the `PowerI4` code[2]. This tests adopts as dataset the publicly available `POWMES` N-body simulation, provided in the package of the `POWMES` code of [36] for testing purposes. It consists of a simulation of 1283 particles in a $L_{\rm box} = 50 Mpc/h$ box run to $z = 0$. We will refer to this simulation as the `POWMES` N-body simulation or `POWMES` for short. The particle distribution is isotropic and therefore only the monopole of the matter power spectrum is considered for the test. Direct summation, at a great computational cost, provides an aliasing-free estimate of the Fourier-space density since it does not require an estimate of the configuration-space density on a grid. The comparison therefore allows us to estimate the aliasing contribution introduced by the FFT-based approach assumed by the PK-GC code.

Mass Assignment test by comparison with an external code

With this test we still focus on the MAS and FFT steps already analysed in the previous test, yet, this time we compare the results against an estimator of `PowerI4` that shares the same Mass Assignment Schemes (MAS) and interlacing technique implemented in the PK-GC code. Using the same options in both cases the codes are run on the same `POWMES` simulation already introduced, the difference between the outputs provided by the two codes should amount to the aliasing contribution expected for the given MAS and should therefore be within the accuracy limits of Euclid, stated in the Euclid SGS LE3 Requirements Specification Document.

Power spectrum multipole comparison against external code

This test goal is to check that our estimator products agree with results from a well-known and reliable software. We validate our results against the power spectrum multipoles obtained from the external code `Nbodykit` [82] which is a well-tested software in the scientific community for computing the power spectrum multipoles. The test is performed both for a simulation snapshot with periodic boundary conditions and a lightcone catalog. The snapshot corresponds to a realisation of the Minerva simulation [74] suite at redshift z=1 with box size $L_{\rm box} = 1500\,{\rm Mpc}\,h^{-1}$ (a more detailed description of these simulations is given in Chapter 4). The second is a lightcone coming from the Euclid Flagship Simulation, spanning a redshift range from 0.9 to 1.1. The Euclid Flagship Simulation [130] is made by 2 trillion DM haloes on a box with side $L_{\rm box} \sim 3780\,{\rm Mpc}\,h^{-1}$, populated by galaxies through the application of an empirical Halo Occupation Distribution model following the reference [131].

[2] https://github.com/sefusatti/PowerI4

Random phase mocks test on multipoles computation

This test focuses on the Yamamoto estimator. It is performed on realizations of a density field which has a given power spectrum following the linear Kaiser prediction for redshift space distortions, so that its monopole, quadrupole and hexadecapole are all known exactly. The PowerSpectrum reads directly the density field in Fourier space, so that only the shell-average procedure is performed. Results are then compared to expected results and a check is performed to assess that accuracy expectations are met.

Test of the Yamamoto estimator in the distant observer limit

FFT-based Yamamoto estimators of the power spectrum moments can speed up the estimate of the same quantities computed using the rigorous but impractically slow Yamamoto estimator [169] at the cost of introducing a "wide-angle" bias (whose magnitude and correction have been investigated by the Euclid SWG-GC Systematic Error Tiger Team). The objective of the test is to validate the FFT-based Yamamoto estimator in the limit of a distant observer. For this test we use a catalog with a sky area of 500deg^2 and a thickness $0.95 \leq z \leq 1.05$ in redshift. We consider a distribution of objects very far away (to the limit of infinitely far away) so that the FFT-based Yamamoto estimator is expected to measure the same power spectrum as the standard Distant Observer Approximation power spectrum estimator of eq. (3.58). Consequently, the catalog is moved $1 \cdot 10^8\,\text{Mpc}\,h^{-1}$ away from the coordinate center so that the DOA approximation is valid. A check is run to see that measurements computed with Yamamoto-like estimators recover the Distant Observer Approximation results with residuals below percent level.

Ideal window test

A requirement on the power spectrum code is to compute the power spectrum of the random distribution. This test checks that the code correctly computes and outputs the window power spectum when a random mock catalog is provided as input, and it validates its accuracy. The measured power spectrum is compared to a known analytical window function. For the test, a random catalog that represents a sphere of volume $700^3[\text{Mpc}\,h^{-1}]^3$ is adopted. This allows to write a simple analytic expression for the expected window function which is used for comparison.

Test on the output file

Euclid data-processing analysis is composed of multiple tasks that are planned to run in close sequence. In order to assure that no conflicts between inputs and outputs from different tasks are met, I/O products must match a predefined structure, i.e. a Data Model. The objective of this test is to check that the PowerSpectrum code produces output files in the expected format. A representative galaxy mock catalog from the Euclid Flagship simulation is provided as input into the PowerSpectrum code. This test then seeks to confirm that an

`xml`-file is produced containing a `fits`-file for each power spectrum and window function, with the right output templates.

Test on the capability for processing the full spectroscopic catalog

The objective of the test is to verify that the PowerSpectrum code is capable to process the full spectroscopic catalog of Euclid or fractions of it, meeting the k-binning and time-limit requirements imposed by the Requirement Specification Document. In particular, this test verifies that power spectrum output file covers a wavenumber range from 0.001 to $0.5\,\mathrm{Mpc}^{-1}\,h$ with a bin width of $0.001\,\mathrm{Mpc}^{-1}\,h$. Together with this test, other checks are performed, aiming at validating the requirement on the maximum computation time and RAM usage for the full spectroscopic catalog. These are satisfied if the code successfully processes the provided catalog within the required time limit of 8 CPU hours and within the required memory limit of 120 GB.

3.3.2 Bispectrum Validation Tests

In addition to the test on the density estimation common to the PK-GC and BK-GC codes, a few test are specific to the bispectrum estimator.

Comparison with a brute-force estimator

The objective of this test is to validate the Bispectrum software with an estimate from a brute-force approach from an external software for a realistic distribution of points in a given volume, extracted from cosmological simulations. The data come from a catalog whose objects populate a cubic box of sidelength $200\,\mathrm{Mpc}\,h^{-1}$. Because the computational cost of the brute-force approach is extremely high ($\mathcal{O} \sim N_\mathrm{G}^6$), a grid of size 32^3 will be used to compute the Fourier transform of the galaxy density field. The residuals between the monopole computed from the Bispectrum code and the expected output, acquired from the brute-force approach, are computed, and a check is performed to verify that they are below Euclid requirements.

Comparison with an external code

The test mirrors the first one introduced for the PowerSpectrum code and focuses on the Mass Assignment Scheme that interpolates the density field on a grid and the FFT that provide the Fourier-space density. It validates the code against the results obtained by direct summation through the PowerI4 code on the POWMES N-body simulation. Although computationally expensive, the direct summation approach provides an aliasing-free estimate of the Fourier-space density since it does not require an estimate of the configuration-space density on a grid. The comparison, therefore, provides an estimate of the aliasing contribution introduced by the FFT-based approach implemented within the Bispectrum software.

Test on the input-output products

This test verifies that the Bispectrum code is able to process a simple mock catalog, matching the DataModel structure for the Bispectrum code, and outputs the galaxy bispectrum products according to the Data Model Definitions of Euclid, in all the cases allowed for the parameter file options.

Binning test

The objective of the test is to verify that the code is able to process a representative mock catalog of the Euclid Wide Survey providing measurements that satisfy the binning requirements imposed by the Requirement Specification Document. The bispectrum binning is given in terms of the three wavenumbers k_1, k_2, and k_3. The minimum wavenumber is set equal to the binning in k which must span the range from $[0.005, 0.2]\,h\,\mathrm{Mpc}^{-1}$ with separation $0.005\,h\,\mathrm{Mpc}^{-1}$.

Triangle modes test

The objective of the test is to verify that the output file of the Bispectrum code provides results for at least 6530 unique triangle configurations $\{k_1, k_2, k_3\}$ when run on a representative mock catalog of the Euclid Wide Survey, providing measurements that satisfy the binning requirements imposed by the Requirement Specification Document.

Increasing Fraction test

The objective of the test is to verify that the Bispectrum code can execute successfully with input catalogs which are one-sixth, one-half, and one times the full spectroscopic catalog, while providing measurements that satisfy the binning requirements. For such test, we built a representative mock catalog of the Euclid Wide Survey consisting of $3 \cdot 10^7$ galaxies and random catalog of $1.5 \cdot 10^9$ objects which will be partitioned into the three fractions defined above which are provided as sequential inputs to the Bispectrum code. This test checks that the output products provide the right binning, given in terms of the three wavenumbers k_1, k_2, and k_3. The minimum wavenumber is set equal to the binning in k which must span the range $[0.005, 0.2]\mathrm{Mpc}^{-1}\,h$ with separation $0.005\,\mathrm{Mpc}^{-1}\,h$. Two additional checks are performed to verify that the code successfully processes the full catalog within the required time limit of 200 CPU hours and within the required RAM usage limit of 1.1 TB of memory. This last test is crucial for the Bispectrum code, as memory is the main challenge that hampers an accurate, dense estimation of the bispectrum on a large wavenumber range. I will briefly address this issue in the next paragraph.

The bispectrum estimation algorithm employs FFTs of the density grid of linear size N_G, where the CPU usage scales as $N_\mathrm{G} \log N_\mathrm{G}$. Given the large number of grids required at the same time, the memory budget is the most challenging requirement for the Bispectrum,

and it is driven by the girds size. For this reason, the main parameter to consider is $N_{\rm G}$. The peak of memory usage occurs when the four grids $F_0(\mathbf{k})$, $F_2(\mathbf{k})$, $F_4(\mathbf{k})$ and $F_0^w(\mathbf{k})$ are loaded in memory together with the masked shells. Then, the memory peak is

$$\mathrm{MEM} = N_{\rm grids}\, N_{\rm G}^3 + (N_{\rm grids}+1)\, N_{\rm bins}\, (N_{\rm G}^{mask})^3 \tag{3.63}$$

where $N_{\rm G}$ is the number of grid points (per dimension) of the original grids, $N_{\rm G}^{\rm mask}$ is the number of grid points of each shell (per dimension), $N_{\rm bins}$ is the number of Fourier-bins required by the binning scheme adopted and $N_{\rm grids}$ is the number of fields required to estimate the products, i.e. 4 if we want to compute the $\ell = 0, 2, 4$ multipoles as well as the shot-noise of the monopole. From these grids, masked fields are built, giving a number of $N_{\rm bins}$ shell fields per grid. In order to optimize the use of memory, the grid on which these fields are computed is allowed to have a lower linear dimension than the original one and a mapping procedure between the two grids takes care of evaluating the quantities on the new one. In addition to the masked fields corresponding to the $F_0(\mathbf{k})$, $F_0(\mathbf{k})$, $F_0(\mathbf{k})$, $F_0^w(\mathbf{k})$ grids, identity masked fields are built (which are responsible for the "+1" term in the square brackets). Each of these masked identity fields is 1 on the particular shell, identified by the given bin, and zero outside. It is important to highlight that the amount of memory required for a given run of the code depends mainly on the chosen binning $N_{\rm bins}$ and on the number of fields $N_{\rm grids}$, that need to be computed.

Chapter 4

Toward a robust inference method for LSS observables

The following chapters are dedicated to the work done in the context of an end-to-end data analysis pipeline to extract cosmological information from LSS catalogs. This project has been a shared effort by a relatively small group of people in Trieste which began with [119]. This paper presents the results from the likelihood analysis of the real-space bispectrum computed from N-body simulations using the new code PBJ, developed by A. Oddo (paper in preparation). In this analysis the authors address the consequences of different choices routinely made on binning schemas, theoretical models, covariance estimation and likelihood function on bias parameter constraints. In doing so, they take advantage of a precise estimate of the full anisotropic covariance of a large set of mock catalogs in order to make unbiased determination of model parameters.

The present chapter describes the natural continuation of [119], hereafter named Paper I. In this project we investigate the consequences of several assumptions that can be made on the joint likelihood analysis of the galaxy power spectrum and bispectrum in real-space, and their effects on the constraints of bias and cosmological parameters. We also apply the Bayesian model selection methods considered there to evaluate theoretically or numerically derived relations among the bias parameters that can reduce the parameter space and speed-up the likelihood evaluation. We make use of the same set of Minerva simulations of Paper I, allowing, due to the small sample variance, not only an assessment of the systematic errors in the theoretical model, but also an evaluation of the effects related to technical details of the likelihood analysis. In addition, we estimate the full covariance, including cross-correlations between power spectrum and bispectrum, from measurements of the Pinocchio mocks already adopted in Paper I.

We fit the data with a one-loop PT model for the power spectrum similar to those tested in the blinded challenge presented in [117] (here limited to real space), including a counterterm to account for the dynamics of short-scale perturbations [132, 17, 31], higher-derivative bias [44, 108, 45, 46] and including the infrared (IR) resummation procedure to describe the non-linear evolution of the BAO features [12, 89]. Finally, we also consider a possible scale-dependent correction to the constant shot-noise contribution induced by halo

exclusion [157, 14]. For the bispectrum we limit the prediction to the tree-level contribution, testing the possible effect of including higher-derivative bias and IR resummation.

We explore the consequences of an improper treatment of Fourier-space discretization effects in the theoretical predictions on the estimate of the parameters, and study different criteria for the selection of the triangular configurations of the bispectrum. In addition, we investigate common approximations to the covariance matrix. Finally, we present the results of a full likelihood analysis of the combination of the galaxy power spectrum and bispectrum in real space where cosmological parameters are allowed to vary, using the full simulation volume.

This study has ended up in a published paper [118] at the beginning of 2021.

My contribution to this work consisted in investigating the validity of the real-space bispectrum model not only, as routinely done, in terms of a range of scales but also accounting for the shape of the triangular bispectrum configuration. The aim is to more fully exploit available data-sets. Typically, these type of analyses consider all triangles with sides equal or lower than a given $k_{\rm max}$. However, there exist several triangular configurations, past this limit, for which our model still works to good extent. I devised various options to include these configurations by choosing a different way to define the triangular configuration limit, which is no more imposed by setting the largest k-vector smaller than $k_{\rm max}$, as, for instance, by limiting the sum between two k-vectors to higher values of k. All such options are then tested in terms of the constraints on galaxy bias parameters they provide, after running a full likelihood analysis of a synthetic data-set.

This chapter is organised as follows. We introduce all numerical data in section 4.1 and the theoretical model and the likelihood functions in section 4.2. Our results are discussed in section 4.3. Finally, we present our conclusions in section 4.4.

4.1 Data

For this analysis the authors adopt two datasets. The first is composed by 298 N-body simulations that comprise a volume of almost 1000 $\mathrm{Gpc}^3\,h^{-3}$, so large that it allows to reduce the statistical error associated to the measurements and grant the opportunity to investigate the effect of different choices often made in these analyses with high accuracy. Whereas, for the sake of a precise estimation of the covariance, a series of 10,000 mocks allows us to limit the noise affecting the inverse of the covariance matrix, which propagates to model parameter posteriors. Requirements for future surveys as Euclid demand that the precision matrix be determined with sufficient accuracy such that the bias introduced in the cosmological parameter errors does not exceed 10%. The problem of precise covariance estimation is well-known in the literature and it is particularly relevant in maximum likelihood analyses that use a numerical estimation from simulations and seek to vary the assumed cosmology,

as the number of required mocks quickly explodes. Methods to control this additional source of error exist, but the ultimate target would be to produce an analytic covariance sufficiently precise to mimic the measured one, which would allow to rapidly compute the covariance matrix in different cosmological models.

4.1.1 N-body simulations and measurements

N-body simulations have seen renewed interest since since the early 2000. This enthusiasm is due to the fact that not only they can be used for a direct comparison with observed data, but also because they provide precise calibration for clustering estimators. As upcoming surveys like Euclid and DESI will reach exceptional level of accuracy in their clustering measurements, reaching sub-percent level from linear to strongly non-linear scales, extreme simulations are needed to match these requirements.

The main bottleneck in the production of large N-body simulations is the computation of the displacement on each particle due to the gravitational effect of the distribution. However, as the costly direct-summation approach has been outperformed by new algorithms, simulations with an exceptional number of objects have become accessible. Moreover, an important role was also played by the hardware evolution and, currently, the most extreme simulations are able to reproduce cosmological boxes with almost a trillions of particles. An example is the *flagship* wide field simulation which is set-up for the Euclid mission and comprise 4.1 trillion DM particles in boxes of size $L \sim 3600\,\mathrm{Mpc}\,h^{-1}$.

Following Paper I, for this series of works we have used the MINERVA N-body simulations developed by [74, 103] , where they have been used to validate their model of the analytic covariance prediction for the anisotropic signal of galaxy clustering two-point statistics. These simulations were produced using GADGET-2[1] [160], and contain positions and velocities of 1000^3 DM particles of mass $2.67 \cdot 10^{12}\,M_\odot\,h^{-1}$ simulated in boxes of 1500 $\mathrm{Mpc}\,h^{-1}$ with periodic boundary conditions, assuming a flat ΛCDM model with $h = 0.695$, $\Omega_m = 0.285$, $\Omega_b = 0.046$, as suggested by the combined anaylis of WMAP and BOSS DR9. The initial particle distribution is taken at $z = 63$ and evolved to $z = 1$ adopting second-order Lagrangian Perturbation Theory (2LPT). The transfer function is taken from CAMB [102] assuming $n_s = 0.9632$ and a r.m.s. matter density fluctuation, averaged over spheres of radius equal to $8\,h^{-1}\,\mathrm{Mpc}$, of $\sigma_8 = 0.828$.
Unlike [74], which populate halos with galaxies according to a suitable Halo Occupation Distribution (HOD) model, [119] directly focus on the halo catalog, with the additional constraint of considering only halos above a certain mass threshold, $1.12 \cdot 10^{13}\,M_\odot\,h^{-1}$.

Measurements of matter and halo power spectra are obtained from the PowerSpectrum

[1] http://www.gadgetcode.org/

code, using the estimator presented in Chapter 3 (3.1),

$$\hat{P}(k) \equiv \frac{1}{N_P(k)\, L^3_{\rm box}} \sum_{\mathbf{q}\in k} |\delta(\mathbf{q})|^2 \,, \tag{4.1}$$

where $V = L^3_{\rm box}$ and the Fourier-space density $\delta(\mathbf{k})$ is the result of fourth-order interpolation and the interlacing technique [150] described in Chapter 3. The sum runs over all discrete vectors $\mathbf{q}$ in a bin of size Δk with $k - \Delta k/2 \leq |\mathbf{q}| < k + \Delta k/2$, and $N_P(k) = \sum_{\mathbf{q}\in k} 1$ represents their total number.

The bispectrum is computed through the simple estimator of Chapter 3

$$\hat{B}(k_1, k_2, k_3) \equiv \frac{1}{N_B(k_1, k_2, k_3)\, L^3} \sum_{\mathbf{q}_1\in k_1} \sum_{\mathbf{q}_2\in k_2} \sum_{\mathbf{q}_3\in k_3} \delta_K(\mathbf{q}_{123})\delta(\mathbf{q}_1)\delta(\mathbf{q}_2)\delta(\mathbf{q}_3) \,, \tag{4.2}$$

where $\delta_K(\mathbf{k})$ denotes the Kronecker delta function (equal to 1 for $\mathbf{k} = 0$ and 0 otherwise) and $\mathbf{q}_{i_1\ldots i_n} \equiv \mathbf{q}_{i_1} + \cdots + \mathbf{q}_{i_n}$. The normalisation factor

$$N_B(k_1, k_2, k_3) \equiv \sum_{\mathbf{q}_1\in k_1} \sum_{\mathbf{q}_2\in k_2} \sum_{\mathbf{q}_3\in k_3} \delta_K(\mathbf{q}_{123}) \,, \tag{4.3}$$

corresponds to the total number of wavenumber triplets $(\mathbf{q}_1, \mathbf{q}_2, \mathbf{q}_3)$ forming closed triangles that lie in the "triangle bin" defined by the triplet (k_1, k_2, k_3), with the k_i's being the bin centers, and where each bin has a width Δk. In the rest of the chapter we refer to the triplets $(\mathbf{q}_1, \mathbf{q}_2, \mathbf{q}_3)$ formed by wavevectors on the original density grid as "fundamental triangles" to distinguish them from the "triangle bin" (k_1, k_2, k_3).

Following the notation adopted in Paper I, we denote with $s = \Delta k/k_f$ the k-bin size and with c the center of the first bin, both in units of the fundamental frequency. We focus on the power spectrum and bispectrum measurements with the binning scheme given by $(s, c) = (2, 2.5)$. Imposing a maximum wavenumber $k_{\rm max} = 0.09\, h\,{\rm Mpc}^{-1}$, the range of validity (also known as the reach) for the tree-level model found in Paper I for the whole Minerva data-set, an $s = 2$ binning leads to a total of 170 triangle bins.

The left panels of figure 4.1 show the total halo power spectrum (i.e. including shot-noise), averaged over the full set of 298 N-body simulations (top panel) and the relative error on the mean (bottom panel). Measurements of the cross halo-matter power spectrum (not shown) have also been performed and used for cross-checks and independent estimates of some of the model parameters. The right panels of figure 4.1 show instead the average total halo bispectrum (top panel) and the relative error on the mean (bottom panel). We show all triangle bins with increasing values for the sides subject to the constraint $k_1 \geq k_2 \geq k_3$. The gray vertical lines and the numbers mark those configurations where the value of k_1 changes.

We should notice that the statistical uncertainty on the halo power spectrum is below the percent level even at the largest scales considered, while for the bispectrum it is below the

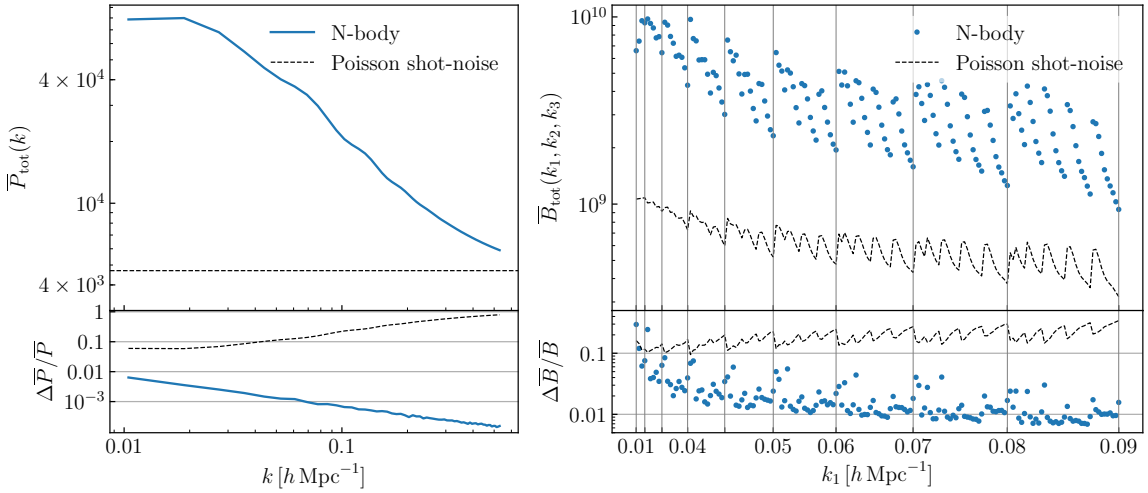

Figure 4.1: The upper panels show the mean of the measurements of the halo power spectrum (left) and bispectrum (right) extracted from the N-body simulations; the dashed lines represent the Poisson prediction for the shot-noise contributions of the corresponding statistics. The lower panels show the relative standard error on the mean of the power spectrum (left) and the bispectrum (right); the dashed lines show the relative contribution of the Poisson prediction of the shot-noise to the total statistics. In the panels for the bispectrum measurements, we show triangles with increasing values of the sides subject to the constraint $k_1 \geq k_2 \geq k_3$, with gray vertical lines marking the last configuration sharing the corresponding value of k_1.

10 percent level for most of the triangles considered, and in some cases is even sub-percent. It is natural to expect that systematic errors related to the approximations assumed by the N-body solver might then be larger and relevant. We refer the reader to [5] for a study of how systematic errors affect the determination of the reach of PT models on the matter power spectrum and bispectrum. Based on that work, we expect systematics to affect to some extent the determination of the bias and cosmological parameters, but we assume their effect to be overall negligible. For this reason, we are not accounting for them in our results.

4.1.2 Mock halo catalogs and covariance

The production of a high number of simulations to limit the noise in the estimate of the precision matrix, in particular when aiming at properly sampling the cosmological parameter space, poses a strong challenge also for current N-body simulation techniques. This reason brought interest to *approximate methods*, algorithms that favour speed at the expense of accuracy in the small-scale regime [113, 112, 111, 114] . The PINpointing Orbit Crossing Collapsed HIerarchical Objects (Pinocchio) developed by Monaco et al. starts from a Gaussian smoothed field and adopts 3LPT to evolve halos whose collapsing history is described by ellipsoidal collapse.

In addition to the Minerva set of N-body simulations, we also employ a much larger set of

10 000 mock halo catalogs, generated with the PINOCCHIO code. These mocks are produced with the same characteristic and the same cosmological model as the one used for the MINERVA simulations. Furthermore, the first 300 realizations of both samples share the same random seeds, i.e. the same initial conditions and particle positions, with the result of the comparison of the two samples not being affected by sample variance.

We use the mock halo catalogs to estimate the covariance matrix for the joint power spectrum and bispectrum measurements. For both the power spectrum and bispectrum, the leading Gaussian contribution to the covariance matrix depends on the amplitude of the total halo power spectrum. Therefore, we require the total halo power spectrum of the mock catalogs to match the one of the N-body simulations at large scales, by adjusting the mass threshold in the PINOCCHIO mocks. This is done in order to minimize the systematic differences between the covariance matrices extracted from the mocks and the ones from the N-body simulations, and thus to allow for an assessment of the goodness of the fit of the theoretical models we study. The relative difference between the power spectrum variance from the simulation and the one recovered from the PINOCCHIO mocks is within a few percent while for the bispectrum variance the difference is at the 5% level (see Paper I for further details).

In a fitting problem with N_p free parameters, approximating the $N_b \times N_b$ covariance matrix $\mathbb{C}$ of the data with the sample covariance $\widetilde{\mathbb{C}}$ measured from a finite number N_m of mock catalogs leads to spuriously enlarged errors for the model parameters. According to [164, 124], the actual parameter covariance is multiplied by the factor

$$f = 1 + \frac{(N_m - N_b - 2)(N_b - N_p)}{(N_m - N_b - 1)(N_m - N_b - 4)} \,. \tag{4.4}$$

In our case, setting $N_m = 10\,000$, a maximum of $N_b = 233$, and assuming $N_p = 10$, gives $f = 1.023$. We thus expect that our error estimates for the model parameters are accurate to percent level.

Figure 4.2 shows the correlation matrix

$$r_{ij} = \frac{\widetilde{C}_{ij}}{\sqrt{\widetilde{C}_{ii}\widetilde{C}_{jj}}} \tag{4.5}$$

for the power spectrum and bispectrum measurements estimated from the set of 10 000 mock halo catalogs. Specifically, the upper left and the lower right quadrants show the correlations of power spectrum and bispectrum respectively, with maximum wavenumbers $k_{\mathrm{max,P}} = 0.53\,h\,\mathrm{Mpc}^{-1}$ for the power spectrum and $k_{\mathrm{max,B}} = 0.09\,h\,\mathrm{Mpc}^{-1}$ for the bispectrum; the other two quadrants show the cross-correlations between power spectrum and bispectrum measurements. Off-diagonal correlations in the power spectrum are of the order of a few percent, and tend to increase up to 15-20 % at smaller scales due to the relative importance

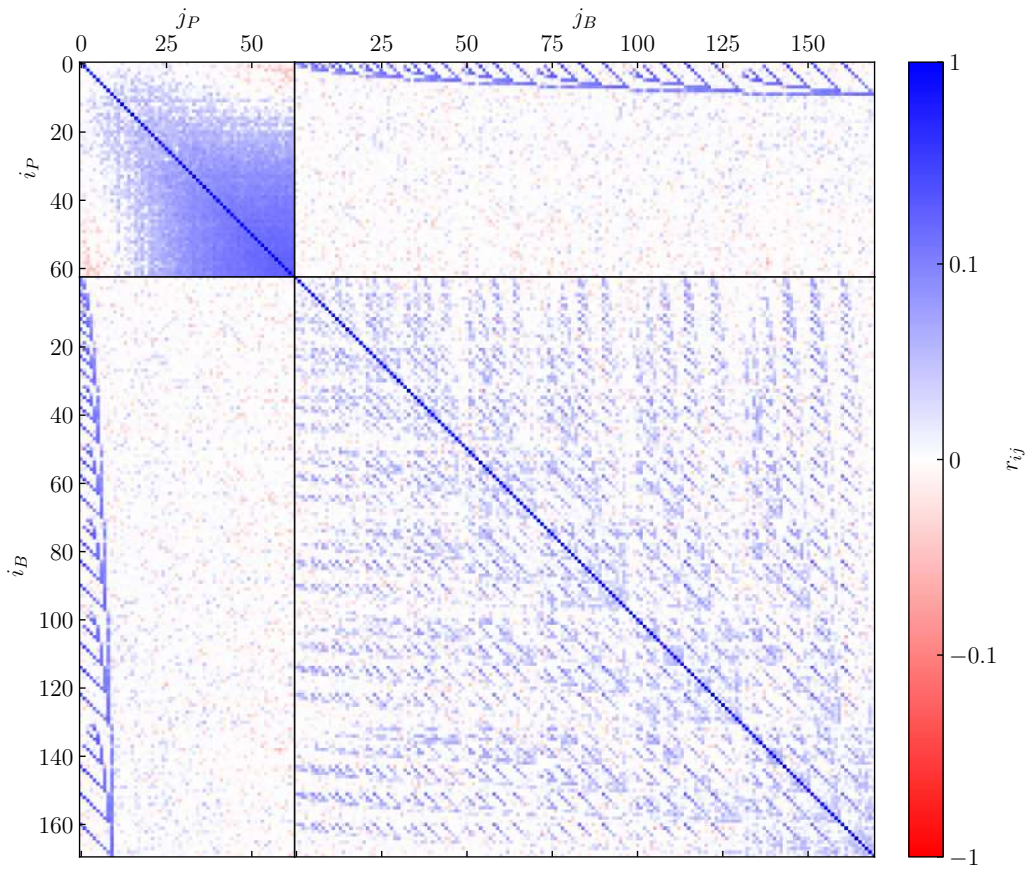

Figure 4.2: Correlation matrix for the power spectrum and bispectrum measurements of the mock halo catalogs generated with the code PINOCCHIO. The upper-left quadrant shows the power spectrum correlations between the measurements in the 63 Fourier bins from $k_{\mathrm{min,P}} \simeq 0.0063\,h\,\mathrm{Mpc}^{-1}$ to $k_{\mathrm{max,P}} \simeq 0.53\,h\,\mathrm{Mpc}^{-1}$; the lower-left quadrant shows the bispectrum correlations between the measurements in the 170 triangle bins from $k_{\mathrm{min,B}} \simeq 0.0063\,h\,\mathrm{Mpc}^{-1}$ to $k_{\mathrm{max,B}} \simeq 0.09\,h\,\mathrm{Mpc}^{-1}$. The other two quadrants show the cross-correlations between the power spectrum and the bispectrum measurements.

of non-linearities and of the shot-noise in that regime. In the bispectrum, off-diagonal correlations reach 10-20 %, while cross-correlations between power spectrum and bispectrum can reach 30-40% for those triangular configurations where, as one can expect, one of the sides coincides with the power spectrum bin. Therefore, neglecting these correlations could in principle lead to inconsistent results in a likelihood analysis. We explore the effects of possible approximations to this covariance matrix on parameters determination in section 4.3.5.

4.2 Model inference

4.2.1 Theoretical model

The theoretical model we consider for the halo power spectrum is essentially equivalent to the one employed for the recent analyses of the BOSS data in [90, 39] and tested in the challenge paper [116], albeit limited to real space. This assumes for the matter power spectrum the one-loop expression in Standard Perturbation Theory (SPT) (see, *e.g.* [19]) with the addition of a counterterm contribution accounting for the dynamics of short-scale perturbations as proposed in the Effective Field Theory of the Large Scale Structure (EFTofLSS) [31]. The galaxy power spectrum expression includes galaxy bias one-loop corrections, arising from local and non-local bias operators, and taking into account bias renormalization (see [46] for a recent review). The bispectrum model is limited to the tree-level expression, the leading contribution in SPT. In addition, we account for the damping of the oscillatory features in the power spectrum and the bispectrum following the IR resummation approach of [12, 27, 89]. In the following, we write explicitly the expressions we assume for both the power spectrum and the bispectrum.

We consider the bias expansion for the galaxy overdensity δ_g given by

$$\delta_g = b_1\delta + \frac{b_2}{2}\delta^2 + b_{\mathcal{G}_2}\mathcal{G}_2 + b_{\Gamma_3}\Gamma_3 + b_{\nabla^2\delta}\nabla^2\delta + \epsilon + \epsilon_\delta\delta, \tag{4.6}$$

where δ is the matter overdensity, while $\mathcal{G}_2$ and Γ_3 are the relevant non-local operators, up to third order, that can be written as a function of the gravitational and velocity potentials Φ and Φ_v as

$$\mathcal{G}_2 \equiv \left[(\partial_i\partial_j\Phi)^2 - (\nabla^2\Phi)^2\right] \tag{4.7}$$

$$\Gamma_3 \equiv \mathcal{G}_2(\Phi) - \mathcal{G}_2(\Phi_v). \tag{4.8}$$

The bias expansion in eq. (4.6) includes as well the $\nabla^2\delta$ higher-derivative operator [108] (that could be particularly relevant for massive halos [60, 115]), while ϵ and $\epsilon_\delta\delta$ are stochastic contributions to the galaxy density field [41, 106, 163]. We are not considering those third order operators that only provide scale-independent corrections contributing to the renormalization of linear bias [107, 11, 50].

The expression for the one-loop galaxy power spectrum in real space can be written as the sum of the SPT model plus contributions due to the higher-derivative bias corrections, the counterterm of the matter power spectrum, and stochasticity

$$P_{gg}(k) = P_{\rm SPT}(k) + P_{\rm h.d.}(k) + P_{\rm ct}(k) + P_{\rm stoch}(k). \tag{4.9}$$

The SPT model is explicitly given by

$$\begin{aligned} P_{\rm SPT}(k)(k) &= b_1^2\, P_{\rm L}(k) + 2\int {\rm d}^3\mathbf{q}\, \left[K_2(\mathbf{q},\mathbf{k}-\mathbf{q})\right]^2 P_{\rm L}(q) P_{\rm L}(|\mathbf{k}-\mathbf{q}|) + \\ &+ 6\, b_1\, P_{\rm L}(k) \int {\rm d}^3\mathbf{q}\, K_3(\mathbf{k},\mathbf{q},-\mathbf{q}) P_{\rm L}(q)\,. \end{aligned} \tag{4.10}$$

with $P_{\rm L}(k)$ being the linear matter power spectrum, and the K_n kernels defined (in analogy to the redshift-space kernels Z_n adopted, e.g., in [19]) as

$$K_2(\mathbf{k}_1,\mathbf{k}_2) = b_1 F_2(\mathbf{k}_1,\mathbf{k}_2) + \frac{b_2}{2} + b_{\mathcal{G}_2} S(\mathbf{k}_1,\mathbf{k}_2) \tag{4.11}$$

$$\begin{aligned} K_3(\mathbf{k}_1,\mathbf{k}_2,\mathbf{k}_3) &= b_1 F_3(\mathbf{k}_1,\mathbf{k}_2,\mathbf{k}_3) + \frac{b_2}{3}\left[F_2(\mathbf{k}_1,\mathbf{k}_2) + \text{cyc.}\right] + \\ &+ \frac{2}{3} b_{\mathcal{G}_2}\left[S(\mathbf{k}_1,\mathbf{k}_{23}) F_2(\mathbf{k}_2,\mathbf{k}_3) + \text{cyc.}\right] - \frac{4}{21} b_{\Gamma_3}\left[S(\mathbf{k}_1,\mathbf{k}_{23}) S(\mathbf{k}_2,\mathbf{k}_3) + \text{cyc.}\right], \end{aligned} \tag{4.12}$$

where $F_2(\mathbf{k}_1,\mathbf{k}_2)$ is the usual second-order kernel of the matter expansion in the Eistein-de Sitter approximation of equation 2.55, while

$$S(\mathbf{k}_1,\mathbf{k}_2) = \left(\hat{\mathbf{k}}_1\cdot\hat{\mathbf{k}}_2\right)^2 - 1, \tag{4.13}$$

provides the tidal term at second order. We refer the reader to, *e.g.* , [73] for an explicit expression of the third order kernel $F_3(\mathbf{k}_1,\mathbf{k}_2,\mathbf{k}_3)$ of the matter density SPT solution. The higher-derivative bias corrections lead to the galaxy power spectrum contribution

$$P_{\rm h.d.}(k) = -2 b_1 b_{\nabla^2\delta} k^2 P_{\rm L}(k) \tag{4.14}$$

while the EFT counterterm leads to

$$P_{\rm ct}(k) = -2 b_1^2 c_s^2 k^2 P_{\rm L}(k)\,, \tag{4.15}$$

with c_s^2 representing the effective sound speed of the matter fluid. Finally, we write the stochastic contribution as

$$P_{\rm stoch}(k) = \left(1 + \alpha_P + \epsilon_{k^2} k^2\right) \bar{n}^{-1} \tag{4.16}$$

where the two free parameters α_P and ϵ_{k^2} describe, respectively, constant and scale-dependent corrections to the Poisson shot-noise term $\bar{n}^{-1}$. The integrals include loop-corrections to the matter power spectrum $\Delta P^m_{1-\rm loop}(k)$, as well as other contributions coming from the galaxy bias expansion.

We can expand equation (4.9) to obtain

$$P_{gg}(k) = b_1^2 P_{mm}(k) + b_1 b_2 P_{b_1 b_2}(k) + b_1 b_{\mathcal{G}_2} P_{b_1 b_{\mathcal{G}_2}}(k) + b_1 b_{\Gamma_3} P_{b_1 b_{\Gamma_3}}(k) + \tag{4.17}$$

$$+ b_2^2 P_{b_2 b_2}(k) + b_2 b_{\mathcal{G}_2} P_{b_2 b_{\mathcal{G}_2}}(k) + b_{\mathcal{G}_2}^2 P_{b_{\mathcal{G}_2} b_{\mathcal{G}_2}}(k) - 2 b_1 b_{\nabla^2\delta} k^2 P_{\rm L}(k) + \tag{4.18}$$

$$+ \quad \left(1 + \alpha_P + \epsilon_{k^2} k^2\right) \bar{n}^{-1}, \tag{4.19}$$

where

$$P_{mm}(k) = P_{\rm L}(k) + \Delta P^m_{1-\rm loop}(k) - 2c_s^2 k^2 P_{\rm L}(k) \tag{4.20}$$

is the one-loop model for the matter power spectrum, and where we have introduced the individual contributions

$$\begin{aligned}
\Delta P^m_{1-\rm loop}(k) &= 2\int \mathrm{d}^3\mathbf{q}\, [F_2(\mathbf{q}, \mathbf{k}-\mathbf{q})]^2\, P_{\rm L}(q) P_{\rm L}(|\mathbf{k}-\mathbf{q}|) + \\
&\qquad +6\, P_{\rm L}(k) \int \mathrm{d}^3\mathbf{q}\, F_3(\mathbf{k}, \mathbf{q}, -\mathbf{q}) P_{\rm L}(q)\,, && (4.21)\\
P_{b_1 b_2}(k) &= 2\int \mathrm{d}^3\mathbf{q}\, F_2(\mathbf{q}, \mathbf{k}-\mathbf{q}) P_{\rm L}(q) P_{\rm L}(|\mathbf{k}-\mathbf{q}|)\,, && (4.22)\\
P_{b_1 b_{\mathcal{G}_2}}(k) &= 4\int \mathrm{d}^3\mathbf{q}\, F_2(\mathbf{q}, \mathbf{k}-\mathbf{q}) S(\mathbf{q}, \mathbf{k}-\mathbf{q}) P_{\rm L}(q) P_{\rm L}(|\mathbf{k}-\mathbf{q}|) + \\
&\qquad +8 P_{\rm L}(k) \int \mathrm{d}^3\mathbf{q}\, F_2(\mathbf{k}, -\mathbf{q}) S(\mathbf{q}, \mathbf{k}-\mathbf{q}) P_{\rm L}(q)\,, && (4.23)\\
P_{b_1 b_{\Gamma_3}}(k) &= -\frac{16}{7} P_{\rm L}(k) \int \mathrm{d}^3\mathbf{q}\, S(\mathbf{q}, \mathbf{k}-\mathbf{q}) S(\mathbf{k}, \mathbf{q}) P_{\rm L}(q)\,, && (4.24)\\
P_{b_2 b_2}(k) &= \frac{1}{2}\int \mathrm{d}^3\mathbf{q}\, P_{\rm L}(q) P_{\rm L}(|\mathbf{k}-\mathbf{q}|) - \frac{1}{2}\int P^2_{\rm L}(q) \mathrm{d}^3 q\,, && (4.25)\\
P_{b_2 b_{\mathcal{G}_2}}(k) &= 2\int \mathrm{d}^3\mathbf{q}\, S(\mathbf{q}, \mathbf{k}-\mathbf{q}) P_{\rm L}(q) P_{\rm L}(|\mathbf{k}-\mathbf{q}|)\,, && (4.26)\\
P_{b_{\mathcal{G}_2} b_{\mathcal{G}_2}}(k) &= 2\int \mathrm{d}^3\mathbf{q}\, S^2(\mathbf{q}, \mathbf{k}-\mathbf{q}) P_{\rm L}(q) P_{\rm L}(|\mathbf{k}-\mathbf{q}|)\,. && (4.27)
\end{aligned}$$

The constant subtracted to $P_{b_2 b_2}(k)$ in equation (4.25) ensures that all loop-corrections converge to zero in the large-scale limit, and allows for the renormalization of the constant shot-noise parameter α_P. Notice that, whenever this model is used without any additional information on its parameters, the EFT counterterm and the higher-derivative contribution are perfectly degenerate. When this is the case, we can define the combination

$$\tilde{c}_0 = b_1^2 c_s^2 + b_1 b_{\nabla^2\delta}\,, \tag{4.28}$$

reducing the dimensionality of the parameter space.

We account for the smoothing of the acoustic features due to the bulk flow by implementing the IR resummation [12, 27] in the power spectrum model. The starting point to this is to split the linear power spectrum into a smooth, no-wiggle part $P_{\rm nw}(k)$, capturing the broadband shape of the power spectrum, and a wiggly part $P_{\rm w}(k)$, describing the baryon acoustic oscillations,

$$P_{\rm L}(k) = P_{\rm nw}(k) + P_{\rm w}(k)\,. \tag{4.29}$$

We obtain this split by applying the 1D Gaussian filter method described in the appendix of

[166]. Following [12], the wiggly part is then suppressed by a damping factor, $e^{-k^2\Sigma^2}$, with

$$\Sigma^2 = \frac{1}{6\pi^2}\int_0^{k_S} \mathrm{d}q\, P_{\rm nw}(q)\left[1 - j_0\left(\frac{q}{k_{\rm osc}}\right) + 2j_2\left(\frac{q}{k_{\rm osc}}\right)\right], \tag{4.30}$$

where the $j_n(x)$ are the spherical Bessel functions, $k_{\rm osc}$ is the BAO wavenumber, with $1/k_{\rm osc} \simeq 103\,h^{-1}\,$Mpc for the MINERVA cosmology, and $k_S = 0.2\,h\,\mathrm{Mpc}^{-1}$ is an arbitrary cut-off scale that separates the short and long modes; note that Σ^2 is only weakly dependent on the choice of k_S (see [12]). The leading order galaxy power spectrum in real space reads then

$$P_{\rm LO}(k) = b_1^2\left[P_{\rm nw}(k) + e^{-k^2\Sigma^2}P_{\rm w}(k)\right]. \tag{4.31}$$

Finally, all loop corrections are computed replacing $P_{\rm L}(k)$ with the leading-order power spectrum for the matter perturbations (obtained by setting $b_1 = 1$ in eq. 4.31) in eqs. (4.21)-(4.27). These are then multiplied by the respective bias parameters, and finally summed to obtain the IR-resummed loop correction $\Delta P_{\rm IR}^{1-\rm loop}$. This leads to the next-to-leading order galaxy power spectrum

$$P_{\rm NLO}(k) = b_1^2\left[P_{\rm nw}(k) + e^{-k^2\Sigma^2}\left(1 + k^2\Sigma^2\right)P_{\rm w}(k)\right] + \Delta P_{\rm IR}^{1-\rm loop}(k). \tag{4.32}$$

The tree-level galaxy bispectrum in real space can be written as

$$B_{ggg}(\mathbf{k}_1,\mathbf{k}_2,\mathbf{k}_3) = B_{\rm SPT}(\mathbf{k}_1,\mathbf{k}_2,\mathbf{k}_3) + B_{\rm h.d.}(\mathbf{k}_1,\mathbf{k}_2,\mathbf{k}_3) + B_{\rm stoch}(k_1,k_2,k_3)\,, \tag{4.33}$$

where

$$\begin{aligned} B_{\rm SPT}(\mathbf{k}_1,\mathbf{k}_2,\mathbf{k}_3) &= 2\,b_1^2\,K_2(\mathbf{k}_1,\mathbf{k}_2)P_{\rm L}(k_1)P_{\rm L}(k_2) + \text{cyc.} \\ &= 2b_1^2\left[b_1F_2(\mathbf{k}_1,\mathbf{k}_2) + \frac{b_2}{2} + b_{\mathcal{G}_2}S(\mathbf{k}_1,\mathbf{k}_2)\right]P_{\rm L}(k_1)P_{\rm L}(k_2) + \text{cyc.}, \end{aligned} \tag{4.34}$$

while the contributions coming from the higher-derivative operator in the bias expansion (limited to the correction to linear bias) are given by

$$\begin{aligned} B_{\rm h.d.}(\mathbf{k}_1,\mathbf{k}_2,\mathbf{k}_3) = &- 2b_1^2b_{\nabla^2}(k_1^2+k_2^2+k_3^3)F_2(\mathbf{k}_1,\mathbf{k}_2)P_{\rm L}(k_1)P_{\rm L}(k_2) + \text{cyc.} \\ &- b_1b_{\nabla^2}(k_1^2+k_2^2)\left[b_2 + 2b_{\mathcal{G}_2}S(\mathbf{k}_1,\mathbf{k}_2)\right]P_{\rm L}(k_1)P_{\rm L}(k_2) + \text{cyc.}\,. \end{aligned} \tag{4.35}$$

Although these contributions are often included only in one-loop corrections [50], we still decide to include them because, since they depend on the same $b_{\nabla^2\delta}$ appearing also in the power spectrum model, they can potentially break the degeneracy between the higher-derivative bias and the effective sound speed in the EFT counterterm. Other higher-derivative contributions could be included in the bispectrum model due to further operators (see e.g. [51]). However, as shown in Paper I, the bispectrum model at tree-level is able to describe our measurements in terms of the parameters b_1, b_2, and $b_{\mathcal{G}_2}$ at the scales we consider.

Therefore, while including for the moment the contributions in eq. 4.35, we neglect possible contributions from these extra higher-derivative operators.

Finally, the stochastic contribution to the galaxy bispectrum is given by

$$B_{\rm stoch}(k_1,k_2,k_3) = \frac{1+\alpha_1}{\bar{n}}\, b_1^2\, [P_{\rm L}(k_1)+P_{\rm L}(k_2)+P_{\rm L}(k_3)] + \frac{1+\alpha_2}{\bar{n}^2}, \tag{4.36}$$

with α_1 and α_2 representing corrections to the Poisson prediction.

As with the power spectrum, we perform here the IR resummation by replacing any instance of the linear matter power spectrum $P_{\rm L}(k)$ with its IR-resummed counterpart, the leading order power spectrum $P_{\rm LO}(k)$. Notice that, with respect to e.g. [89], for simplicity we do not subtract the contribution proportional to $\mathrm{e}^{-2k^2\Sigma^2}P_w^2$, since it is negligible at the scales we consider.

4.2.2 Fourier-space grid effects

While the theoretical models for matter or halo correlators are functions of Fourier wavevectors defined over an infinite volume, measurements from N-body simulations in boxes with periodic boundary conditions are not. Therefore, care must be taken when comparing the two, especially in our case where statistical uncertainties are significantly small due to the large volume available.

The most consistent approach requires to average exactly the theoretical model over each Fourier bin. In the power spectrum case this amounts to compute

$$P_{gg}^{\rm bin}(k) = \frac{1}{N_P(k)}\sum_{\mathbf{q}\in k} P_{gg}^{\rm th}(q), \tag{4.37}$$

where in practice we replaced the term $|\delta_{\mathbf{q}}|^2/L^3$ with its expected theoretical mean $P_{gg}(q)$ in the expression for the power spectrum estimator (4.1). In this way the theory is evaluated on the wavenumbers available on the discrete grid characterising the simulation we want to compare with. Similarly for the bispectrum model, we replace $\delta_{\mathbf{q}_1}\delta_{\mathbf{q}_2}\delta_{\mathbf{q}_3}/L^3$ with $B_{ggg}(\mathbf{q}_1,\mathbf{q}_2,\mathbf{q}_3)$ to obtain

$$B_{ggg}^{\rm bin}(k_1,k_2,k_3) = \frac{1}{N_B(k_1,k_2,k_3)}\sum_{\mathbf{q}_1\in k_1}\sum_{\mathbf{q}_2\in k_2}\sum_{\mathbf{q}_3\in k_3}\delta_K(\mathbf{q}_{123})B_{ggg}^{\rm th}(\mathbf{q}_1,\mathbf{q}_2,\mathbf{q}_3). \tag{4.38}$$

Clearly this approach is numerically demanding, particularly in a likelihood analysis that requires this evaluation at each step of the Markov chain. One common alternative is to evaluate the theoretical model at "effective" values of the Fourier wavenumbers, often computed as averages over the bin, both for the power spectrum and the bispectrum. For

the power spectrum this definition is unambiguous and unique for any bin of center k,

$$k_{\rm eff}(k) = \frac{1}{N_P(k)} \sum_{\mathbf{q}\in k} |\mathbf{q}|, \tag{4.39}$$

and allows for a fast evaluation of the theoretical model as

$$P_{gg}^{\rm eff}(k) = P_{gg}^{\rm th}(k_{\rm eff}). \tag{4.40}$$

However, for the bispectrum the definition of average Fourier wavenumbers is not unique. Among a couple of possible choices tested in Paper I, the one performing best is the one defined on sorted Fourier wavevectors and defined as follows

$$\begin{aligned}
k_{\rm eff,l}(k_1,k_2,k_3) &= \frac{1}{N_B(k_1,k_2,k_3)} \sum_{\mathbf{q}_1\in k_1} \sum_{\mathbf{q}_2\in k_2} \sum_{\mathbf{q}_3\in k_3} \delta_K(\mathbf{q}_{123}) \max(q_1,q_2,q_3) \\
k_{\rm eff,m}(k_1,k_2,k_3) &= \frac{1}{N_B(k_1,k_2,k_3)} \sum_{\mathbf{q}_1\in k_1} \sum_{\mathbf{q}_2\in k_2} \sum_{\mathbf{q}_3\in k_3} \delta_K(\mathbf{q}_{123}) \,{\rm med}(q_1,q_2,q_3) \\
k_{\rm eff,s}(k_1,k_2,k_3) &= \frac{1}{N_B(k_1,k_2,k_3)} \sum_{\mathbf{q}_1\in k_1} \sum_{\mathbf{q}_2\in k_2} \sum_{\mathbf{q}_3\in k_3} \delta_K(\mathbf{q}_{123}) \min(q_1,q_2,q_3).
\end{aligned} \tag{4.41}$$

In real space, the effective wavenumbers provide a fast evaluation of the theoretical prediction as

$$B_{ggg}^{\rm eff}(k_1,k_2,k_3) = B_{ggg}^{\rm th}\left(k_{\rm eff,l}, k_{\rm eff,m}, k_{\rm eff,s}\right). \tag{4.42}$$

We also consider, as an additional approach, an extension to the effective wavenumbers prescription based on a Taylor expansion of the theoretical model. For the power spectrum we can write, for instance,

$$P_{\rm bin}(k) = \frac{1}{N_P(k)} \sum_{\mathbf{q}\in k} \sum_{n=0}^{\infty} \frac{1}{n!} P^{(n)}(k_{\rm eff})(q-k_{\rm eff})^n \simeq P(k_{\rm eff}) + \frac{1}{2} P''(k_{\rm eff})\mu_2(k) \equiv P_{\rm exp}(k) \tag{4.43}$$

where the Taylor series has been truncated to include up to the second-order term and where

$$\mu_2(k) \equiv \frac{1}{N_P(k)} \sum_{\mathbf{q}\in k} (q-k_{\rm eff})^2. \tag{4.44}$$

We refer to this approach as an "expansion" to the effective approach. Details of its implementation to the bispectrum tree-level predictions can be found in Appendix A.1.

Differences between these approximations and the bin-average of the theoretical model are typically larger for small values of the wavenumbers, and in the bispectrum case, particularly pronounced for squeezed triangular configurations. In general, a larger bin width also leads to a worse agreement with the case involving the full bin-average.

An alternative approach to account for grid effects employs the same expressions in eqs. (4.37) and (4.38), but where the sums over Fourier wavevectors are replaced by integrals (see [51] for a fast implementation for the bispectrum). However, we do not consider this approach in our analysis, since this introduces systematic errors comparable to the statistical uncertainties of our datasets on a wide range of scales, as well to the systematics of the effective wavenumbers approach, see Appendix A.1.

4.2.3 Bias relations

In our analysis we consider some relations between the bias parameters in order to reduce the dimensionality of the parameter space. These relations are helpful in the analysis of the real-space power spectrum alone since large degeneracies between $b_{\mathcal{G}_2}$ and b_{Γ_3} make the determination of both bias and cosmological parameters difficult. As shown in section 4.3.7, this is less of a problem in the joint fit of power spectrum and bispectrum, since the latter provides useful constraints on $b_{\mathcal{G}_2}$. Still, reducing the dimensionality of the bias parameter space can in general provide tighter constraints on the cosmological parameters, as long as it does not introduce systematic errors relevant for the level of statistical uncertainty that characterises our measurements.

We test the following relations between bias parameters with joint fits of power spectrum and bispectrum:

- the relation $b_2(b_1, b_{\mathcal{G}_2})$ from [98], given by

$$b_2 = 0.412 - 2.143\, b_1 + 0.929\, b_1^2 + 0.008\, b_1^3 + \frac{4}{3}\, b_{\mathcal{G}_2}; \tag{4.45}$$

  this is a fitting formula from measurements in separate universe simulations, obtained for values of b_1 in the range $(1, 10)$; notice that the $4/3$ $b_{\mathcal{G}_2}$ term in the equation accounts for the different definition of the bias expansion adopted in [98];

- the relation $b_{\mathcal{G}_2}(b_1)$ from [49],

$$b_{\mathcal{G}_2} = 0.524 - 0.547\, b_1 + 0.046\, b_1^2\,, \tag{4.46}$$

  obtained as a quadratic fit to the excursion set prediction of the tidal bias in [154];

- the relation $b_{\Gamma_3}(b_1, b_{\mathcal{G}_2})$ derived in [50, 49] assuming conserved evolution of the galaxies after formation (co-evolution), that in our basis becomes

$$b_{\Gamma_3} = -\frac{1}{6}(b_1 - 1) - \frac{3}{2} b_{\mathcal{G}_2}\,. \tag{4.47}$$

While this is not a comprehensive list of all possible relations proposed in the literature, they represent a starting point of possible relations to explore. We do not consider the local-Lagrangian relation between $b_{\mathcal{G}_2}$ and b_1 [33, 13] since different studies have shown its

limits [97, 2]; moreover, in the bispectrum-only analysis of Paper I, it is shown to lead to systematic errors in the constraints on the bias parameters, at least when the full simulation volume is considered.

All these bias relations have been derived and studied in the context of distributions of dark matter halos. While their validity is expected to extend as well, to some degree, to galaxy measurements (see, e.g. [16, 172]), we will leave the quantitative exploration of such topic to future work.

4.2.4 Likelihood function

As for the analysis in Paper I, we fit all power spectrum and bispectrum measurements from the MINERVA simulations together, assuming that they are independent. This means that the total log-likelihood we use to sample the parameter space is given by

$$\log \mathcal{L}_{\rm tot}(\boldsymbol{\theta}) = \sum_{\alpha} \log \mathcal{L}_{\alpha}(\boldsymbol{\theta}|\mathbf{X}_{\alpha}), \tag{4.48}$$

where the subscript α runs over all realizations, $\boldsymbol{\theta}$ is the parameter vector, and $\mathbf{X}_{\alpha}$ is the dataset of realization α. The dataset $\mathbf{X}_{\alpha}$ represents either the data vector for the power spectrum, the one for the bispectrum, or the combination of the two. For the individual $\log \mathcal{L}_{\alpha}$, we use two different likelihood functions, depending on the type of covariance used. When the covariance is chosen as the sample covariance of the measurements from the mock catalogs, we assume the Sellentin & Heavens likelihood [151] to account for the residual uncertainties in the numerical estimation of the precision matrix due to the finite number of mocks. The adoption of Sellentin & Heavens likelihood model reduces the broadening of the posteriors which is largely overestimated by the Gaussian approximation when the Hartlap factor (4.4) is applied, and when the length of the datavector becomes comparable to the dimension of measurement sample. In the case of a theoretical prediction for the covariance (diagonal assuming Gaussianity), we assume the usual Gaussian likelihood. In both cases, the individual likelihood $\mathcal{L}_{\alpha}$ can be written as a function of the chi-square of the model for each single realization α. This allows for a fast evaluation of the likelihood when only bias parameters are varied.

4.2.5 Likelihood evaluation

We perform two types of analyses: in the first, the cosmological parameters are fixed to the values used to run the N-body simulations and we perform tests of the different implementations and approximations of the theoretical model; in the second, we also vary three cosmological parameters in order to assess if possible model systematics can bias the recovered cosmological information.

When the cosmological parameters are fixed, the parameter space is given by the set of 10 parameters $\{b_1, b_2, b_{\mathcal{G}_2}, b_{\Gamma_3}, c_s^2, b_{\nabla^2\delta}, \alpha_P, \alpha_1, \alpha_2, \epsilon_{k^2}\}$. We refer to this choice as the "maximal

Parameter		Prior (uniform)
b_1		$[0.9, 3.5]$
b_2		$[0, 4]$
$b_{\mathcal{G}_2}$		$[-4, 4]$
b_{Γ_3}		$[-10, 10]$
$\tilde{c}_0$	$[h^{-2}\,\mathrm{Mpc}^2]$	$[-100, 100]$
$b_{\nabla^2\delta}$	$[h^{-2}\,\mathrm{Mpc}^2]$	$[-100, 100]$
ϵ_{k^2}	$[h^{-2}\,\mathrm{Mpc}^2]$	$[-10, 10]$
α_P		$[-1, 1]$
α_1		$[-1, 1]$
α_2		$[-1, 1]$
A_s/A_s^{fid}		$[0.0004, 4.]$
h		$[0.4, 1.]$
$\Omega_m h^2$		$[0.07224, 0.2224]$

Table 4.1: Uniform prior intervals of the model parameters.

model", since we explore the possibility of reducing the number of parameters by setting some of them to zero, or by imposing the relations described in section 4.2.3. The priors on these parameters are assumed to be uniform, and are given in table 4.1. In addition, we consider varying the power spectrum amplitude parameter A_s, the Hubble parameter h, and the relative matter density parameter $\omega_m = \Omega_m h^2$. Including these cosmological parameters, and in particular A_s, introduces degeneracies that can hamper the estimation of the posterior with Monte Carlo Markov Chains (MCMC). For this reason, we define the relative amplitude parameter $A \equiv A_s/A_s^{\mathrm{fid}}$. Any n-th order operator $\mathcal{O}$ scales proportionally to $A^{n/2}$. In order to reduce the degeneracies between the bias parameters and the amplitude of the scalar perturbations, we redefine the coefficients $b_{\mathcal{O}}$ as follows:

$$\tilde{b}_1 = A^{1/2}\, b_1, \quad \tilde{b}_2 = A\, b_2, \quad \tilde{b}_{\mathcal{G}_2} = A\, b_{\mathcal{G}_2}, \quad \tilde{b}_{\Gamma_3} = A^{3/2}\, b_{\Gamma_3}\,, \tag{4.49}$$

adopting the same uniform priors. We keep the tilt of the scalar power spectrum n_s and the baryon content Ω_b fixed, as these parameters are very well constrained by CMB experiments.

We evaluate posterior distributions by means of MCMC using the code `emcee` [57]. With fixed cosmological parameters, we evaluate the posterior distribution by simulating 100 dependent walkers; moves are performed using the affine invariant "stretch move" ensemble

method from [72] with parallelization, as described in [57]. We run chains for a number of steps equal to $\min(50\,000, 100\tau)$, where τ is the integrated autocorrelation time. With our setup, we can run chains of this type in approximately 5 minutes on a single core of a laptop. When we include cosmological parameters, we evaluate the posterior distribution by simulating independent chains; moves are performed using a Metropolis-Hastings sampler with steps defined by a Gaussian proposal function, with the parameters covariance determined iteratively running chains a few times. MCMC simulations are run until convergence defined by the Gelman-Rubin diagnostic [63], assuming a precision $\epsilon = 0.05$ and a confidence percentile of 95%. The change in sampling method is due to the longer running times when including cosmological parameters. At each step, we call the Boltzmann solver `CAMB` [102] to compute the linear power spectrum, we compute loop corrections to the power spectrum using a custom implementation based on the `FAST-PT` code [109], and perform our IR-resummation routine. Grid effects for both power spectrum and bispectrum are accounted for by adopting the approximated approach outlined in appendix A.1. This allows us to have a likelihood evaluation (and thus one MCMC step) in $\sim 1.5\,\mathrm{s}$, and therefore to reach convergence in a relatively short time, of the order of 10 hours (running each independent chain on a separate core at the same time). Marginalized one-dimensional and two-dimensional posterior distributions are shown in triangle density plots generated through the code `GetDist` [101].

4.2.6 Goodness of fit and model selection

As a way to compare the quality of the fits we perform, we compute the posterior predictive p-value ppp and the posterior-averaged reduced chi-square $\langle\chi^2_\nu\rangle_{\rm post}$. For details on the particular choice of these diagnostics, we redirect the reader to Paper I; for the purposes of the present work, it suffices to say that we consider a value of ppp ≥ 0.95 to signal a failure of the model in reproducing a good fit to the data. We compare instead $\langle\chi^2_\nu\rangle_{\rm post}$ to the corresponding 95 percent (upper) confidence limit associated to a number of degrees of freedom equal to the total number of data points fitted: when $\langle\chi^2_\nu\rangle_{\rm post}$ is greater than this value, the model fails to describe the data.

However, our main goal is to extract *unbiased* values of the fitted parameters. For the cosmological sector, the systematic shift can be easily quantified by comparing the results of the fit to the input values used in the N-body simulations. Conversely, this procedure cannot be followed for the bias parameters as we do not know their values *a priori*. For the sake of understanding whether our analysis leads to biased estimates for the bias sector, we thus attempt to measure b_1 from the ratio between the halo-matter cross-power spectrum $P_{hm}(k)$ and the matter auto-power spectrum $P_{mm}(k)$. In order to obtain an estimate of b_1 which is independent of our likelihood pipeline, we fit the large-scale behaviour of the ratio $P_{hm}(k)/P_{mm}(k)$ assuming for the cross-power spectrum the model

$$P_{hm}(k) = (b_1 + ck^2)P_{mm}(k) \tag{4.50}$$

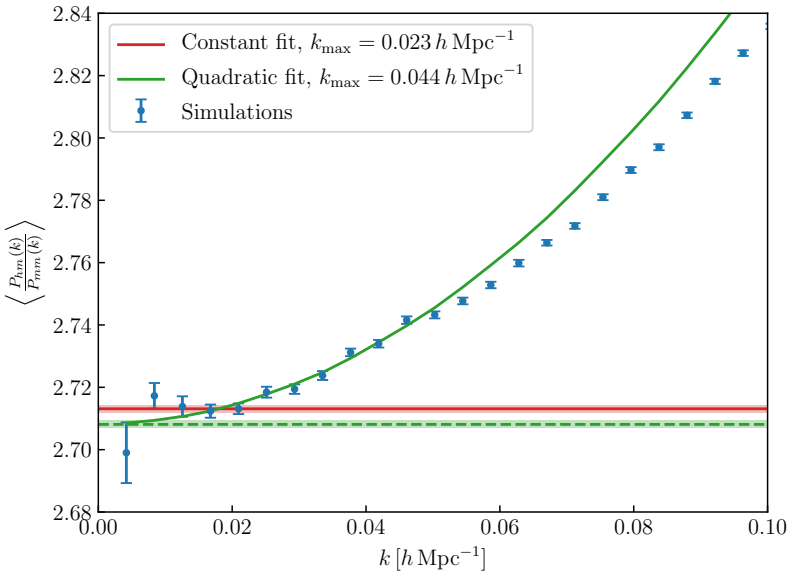

Figure 4.3: Average of the ratios between the cross halo-matter power spectrum and the matter power spectrum over the full set of MINERVA simulations. The red line is the best fit of the data up to $k_{\rm max} = 0.023\,h\,{\rm Mpc}^{-1}$ with a constant function; the solid green line is the best fit of the data up to $k_{\rm max} = 0.044\,h\,{\rm Mpc}^{-1}$ with a constant plus a k^2-dependent term. The green dashed line shows the best-fit value for b_1 with this second fit function. Shaded regions show the errors on the best-fit values for b_1.

where c is a constant and the k^2-correction is a way to partially account for non-linearities detectable even at the largest scales, see figure 4.3. In what follows, we refer to the estimate of b_1 derived assuming this model as $b_1^\times$. Using chi-square minimization, we find $b_1^\times = 2.7081 \pm 0.0012$, which we use as a reference value[2] to draw conclusions about the unbiasedness of the posterior distributions extracted from the MCMC runs discussed in section 4.3. In practice, we use $b_1^\times$ as if it was the true value for b_1.

A note is in order concerning this test. Eq. (4.50) is not equivalent to the full one-loop expression in perturbation theory, given the bias expansion in eq. (4.6). While the two models share the same large-scale limit, they describe non-linearities in different ways, which could lead to a slightly different value of the linear bias. For this reason, we will not conclude that the results of our main analysis are biased unless they lie more than two standard deviations away from the best-fitting value for $b_1^\times$. Note that our estimate for $b_1^\times$ is only used to measure the bias of our fits and does not enter our fitting procedure as a prior.

[2]It is worth stressing that a different fit for $b_1^\times$ was used in Paper I, where we fit a constant linear bias coefficient to the ratio $P_{hm}(k)/P_{mm}(k)$ up to $k_{\rm max} = 0.023\,h\,{\rm Mpc}^{-1}$. This leads to a best-fit value almost 3σ away from (and thus inconsistent with) our reference $b_1^\times$. In any case, due to the larger relative uncertainties in Paper I, the posteriors of the bispectrum-only analysis are compatible with both values in the same range of validity of the model.

An alternative approach in order to test for the consistency of our results with $P_{hm}(k)$ would be to include the cross-power spectrum in the data vector for the likelihood analysis (see, e.g. [49]). However, this would require the full covariance for all correlators, including all cross-covariances, and in our case this is not available.

For the comparison between different models and different assumptions on the bias parameters, we take advantage of the Deviance Information Criterion (DIC) computed from the MCMC simulations as a model-selection statistic. Again, we refer the reader to Paper I for a brief introduction to the DIC and a description of our implementation.

4.3 Results

We now present the results of our analysis of the halo power spectrum and bispectrum measurements using, unless otherwise stated, the full volume of the combined MINERVA simulations of about $1000\,h^{-3}\,\mathrm{Gpc}^3$. We stress that, while clearly out of reach for even future surveys, such large volume is still useful to explore and quantify systematic errors from both the model and the methodology.

4.3.1 Selecting the fiducial model

We first perform a joint analysis of power spectrum and bispectrum adopting the models in equations (4.19) and (4.33) as a function of 10 free parameters: 5 bias coefficients, one EFT counterterm, two stochastic parameters for the power spectrum, and two for the bispectrum. This is what we introduced as the maximal model. Figure 4.4 shows the corresponding 1D and 2D marginalized posteriors with different values of the maximum wavenumber for the power spectrum, $k_{\mathrm{max,P}} = 0.15$, 0.20, 0.25 and $0.30\,h\,\mathrm{Mpc}^{-1}$, while for the bispectrum we consider the fixed maximum wavenumber of $k_{\mathrm{max,B}} = 0.09\,h\,\mathrm{Mpc}^{-1}$, this being the reach for the tree-level bispectrum model as shown in Paper I. In the rest of this chapter, unless otherwise stated, we keep $k_{\mathrm{max,B}}$ fixed to this value. The recovered value of b_1 is consistent, well within the 95% credibility regions, with the reference value from the cross-power spectrum $b_1^{\times}$, shown with its own uncertainty by the vertical gray band. We observe that the credible regions for the parameters b_{Γ_3}, c_s^2, α_P, and ϵ_{k^2} shrink as a function of $k_{\mathrm{max,P}}$. Note that these parameters do not appear in the bispectrum model, and thus are constrained by the power spectrum alone, so that their constraints improve with larger $k_{\mathrm{max,P}}$. On the other hand, the constraints on the parameters b_2, $b_{\mathcal{G}_2}$, $b_{\nabla^2\delta}$, α_1, and α_2 do not improve as a function of $k_{\mathrm{max,P}}$. The two shot-noise parameters are in fact only present in the bispectrum model (and as such their constraints do not improve with increasing $k_{\mathrm{max,P}}$, since $k_{\mathrm{max,B}}$ is kept fixed), while the others appear in the models for both power spectrum and bispectrum, suggesting that they are mostly constrained by the bispectrum.

Just like in the bispectrum-only analysis of Paper I, α_2 is completely unconstrained inside the prior, and α_1 is consistent with zero at 1σ level. Moreover, while the bispectrum appears

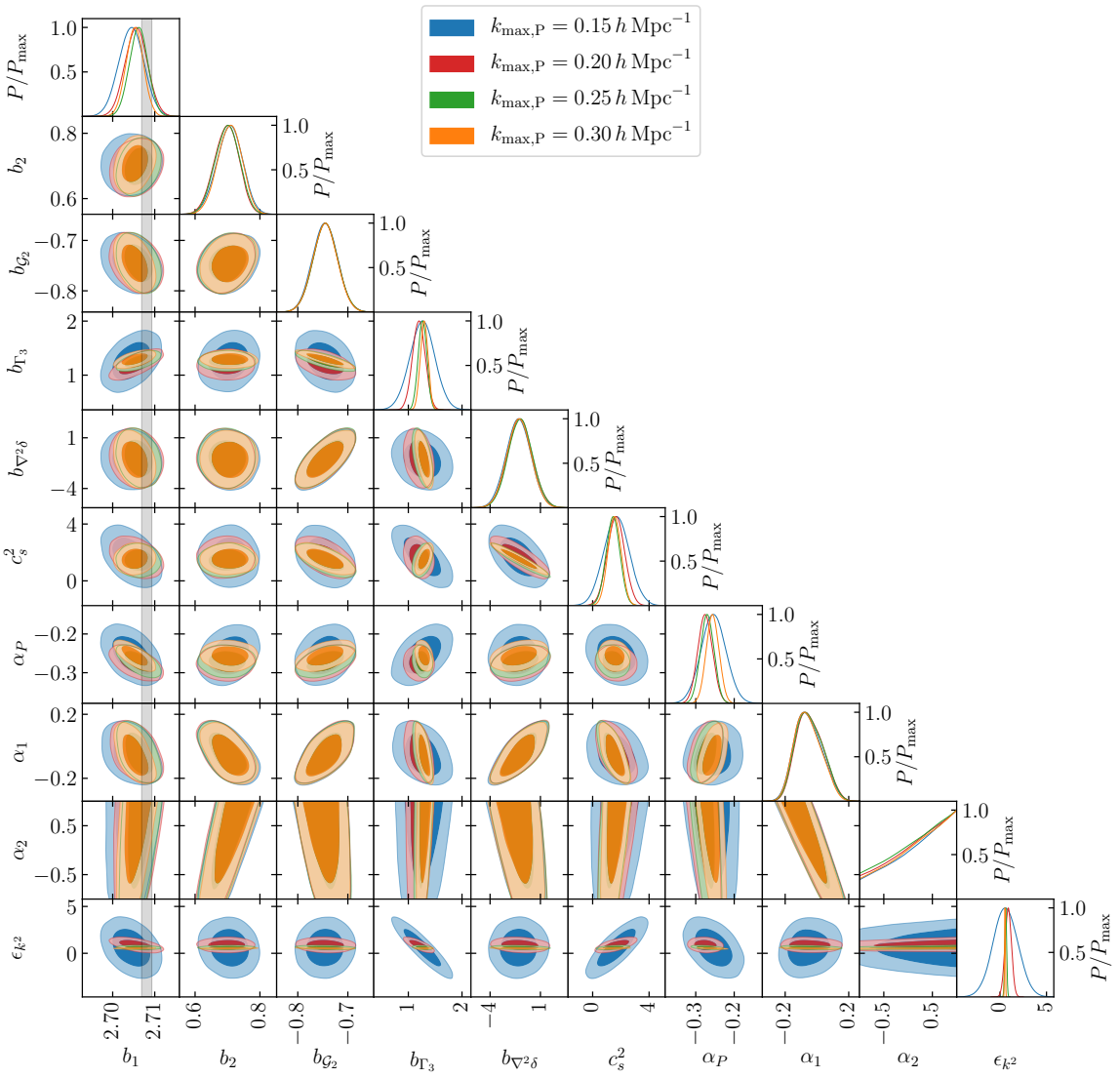

Figure 4.4: 1D and 2D marginalized posteriors for the parameters of the maximal model, obtained through a joint analysis of the halo power spectrum and bispectrum in real space measured from the full set of N-body simulations. The value for $k_{\rm max,B}$ is fixed to be $k_{\rm max,B} = 0.09\,h\,{\rm Mpc}^{-1}$, while the value of $k_{\rm max,P}$ is varied; here we show four different values of $k_{\rm max,P} = 0.15\,h\,{\rm Mpc}^{-1}, 0.20\,h\,{\rm Mpc}^{-1}, 0.25\,h\,{\rm Mpc}^{-1}, 0.30\,h\,{\rm Mpc}^{-1}$ respectively in blue, red, green, and orange. The gray band shows the value of b_1 measured from the halo-matter cross-power spectrum, along with its error bar.

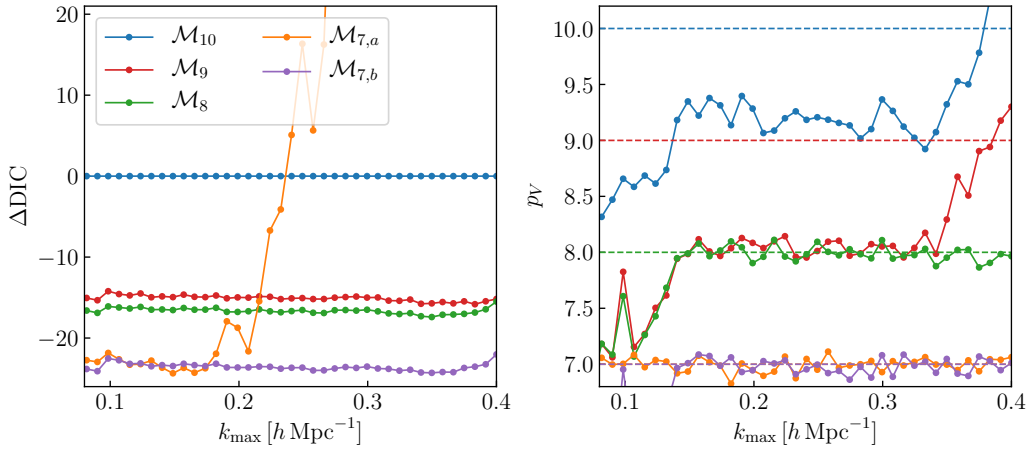

Figure 4.5: Left panel: difference in DIC of the models considered in the comparison with respect to the maximal model, as a function of $k_{\rm max,P}$. Right panel: number of effective parameters p_V constrained by the data for each model, as a function of $k_{\rm max,P}$; dashed lines show the actual number of free parameters in the model indicated with the corresponding color (the orange and the purple dashed lines are on top of each other).

to be able to partially break the degeneracy between $b_{\nabla^2\delta}$ and c_s^2, $b_{\nabla^2\delta}$ is still consistent with zero. Finally, also the k^2 correction to the power spectrum stochasticity is consistent with zero within the 95 percent credibility regions, although only for $k_{\rm max,P} = 0.15\,h\,{\rm Mpc}^{-1}$. All of the other parameters are either required by the data, or significantly different from zero.

In order to explore the possibility of a smaller parameter space, we use the DIC to assess the performances of a number of different reductions of the maximal model where a subset of the parameters is set to zero. Figure 4.5 shows the results of the comparison of the following cases:

- the maximal model, $\mathcal{M}_{10}$, with all 10 parameters left free to vary;
- the maximal model, $\mathcal{M}_9$, where $b_{\nabla^2\delta}$ has been set to zero;
- the maximal model, $\mathcal{M}_8$, where both $b_{\nabla^2\delta}$ and α_2 have been set to zero;
- the maximal model, $\mathcal{M}_{7,a}$, where $b_{\nabla^2\delta}$, α_2 and ϵ_{k^2} have been set to zero;
- the maximal model, $\mathcal{M}_{7,b}$, where $b_{\nabla^2\delta}$, α_1 and α_2 have been set to zero.

In the left panel, we show the difference in DIC between each model and the maximal model as a function of the $k_{\rm max}$ of the power spectrum ($k_{\rm max,B}$ being fixed at $0.09\,h\,{\rm Mpc}^{-1}$). The right panel shows the number of effective parameters p_V constrained by each model, defined as half of the posterior variance of the deviance $D = -2\log\mathcal{L}_{\rm tot}$ [62], again as a function of $k_{\rm max,P}$.

The large degeneracy between the higher-derivative bias $b_{\nabla^2\delta}$ and the EFT counterterm

amplitude c_s^2 is such that setting $b_{\nabla^2\delta} = 0$ allows for a large reduction of the DIC by ~ 15 at all values of $k_{\rm max}$ considered. For this reason, in all subsequent analysis we set $b_{\nabla^2\delta} = 0$, and thus ignore the higher-derivative bias correction in the bispectrum model, while in the power spectrum model it remains as degenerate with the EFT counterterm. In the following, we consider the combination in eq. (4.28). Setting α_2 to zero does not improve by much the DIC, however, since α_2 is unconstrained and prior dominated, it allows for the number of effective parameters p_V to be consistent with the number of model parameters.

A further reduction to a seven-parameters model can be achieved by setting either α_1 or ϵ_{k^2} to zero, in addition to $b_{\nabla^2\delta} = \alpha_2 = 0$. While $\alpha_1 = 0$ decreases the DIC by ~ 5 at all values of $k_{\rm max,P}$ considered, setting $\epsilon_{k^2} = 0$ leads to a comparable improvement only for $k_{\rm max,P} < 0.2\,h\,{\rm Mpc}^{-1}$, but this improvement is rapidly lost for larger Fourier modes. In fact, at small scales the k^2 stochastic term turns out to be relevant, perhaps accounting as well for additional corrections beyond the one-loop model we assumed.

In what follows we consider $\mathcal{M}_{7,b}$ as the reference bias model, being the one defined by the seven parameters

$$\boldsymbol{\theta}_{\rm reference} = \{b_1, b_2, b_{\mathcal{G}_2}, b_{\Gamma_3}, \tilde{c}_0, \alpha_P, \epsilon_{k^2}\}, \tag{4.51}$$

with $b_{\nabla^2\delta}$, α_1, and α_2 set to zero in the bispectrum model. For this case the number of effective parameters shown in the right panel of figure 4.5 matches the number of free parameters over the entire $k_{\rm max,P}$ interval explored.

4.3.2 Analysis with the reference model

Figure 4.6 shows the results obtained fitting the reference model to the power spectrum data and to the combination of power spectrum and bispectrum data. The left column of panels shows the mean of the posteriors of the model parameters as a function of $k_{\rm max,P}$ ($k_{\rm max,B}$ is again set to $0.09\,h\,{\rm Mpc}^{-1}$). Darker shaded regions correspond to the central 68 and 95 percent ranges.

The two outcomes are in general agreement, for the most part because of the large uncertainties characterising the posteriors from the power spectrum-only analysis. When fitting the power spectrum alone, we notice that some of the priors turn out to be informative, with b_2 being unconstrained from below, and with ϵ_{k^2} being basically unconstrained at small values of $k_{\rm max,P}$, where the k-dependent stochastic contribution is expected to be negligible. Moreover, the recovered value of b_1 mildly runs as a function of $k_{\rm max,P}$, but this feature is not present in the joint analysis. In any case, the posteriors of b_1 in the two fits are in general agreement with each other, and they also agree with the value of $b_1^\times$ from the cross halo-matter power spectrum, albeit at 2σ in the case of the joint-fit. However, considering the method used to fit $b_1^\times$ (see section 5.4.3), we do not deem this deviation to be significant.

The top-right panels show the goodness-of-fit for the power spectrum only (in blue) and for the combination of power spectrum and bispectrum (in red). Both the posterior-averaged

reduced chi-square and the ppp agree in assessing that the power spectrum model provides a good fit to the data up to $k_{\rm max,P} \sim 0.30\,h\,{\rm Mpc}^{-1}$, while in the case of the joint fit the model seems to provide a good fit of the data even beyond that. By direct inspection of the total posterior-averaged chi-squares, compared to the one of a bispectrum-only fit at $k_{\rm max,B} = 0.09\,h\,{\rm Mpc}^{-1}$, we suspect that this apparent inconsistency is likely due to the large number of triangles in the bispectrum, that reduce the relative weight of the power spectrum in the evaluation of the joint fit.

The bottom-right panels show 1D and 2D marginalized posteriors for the power spectrum-only fit and for the joint fit, with $k_{\rm max,P} = 0.30\,h\,{\rm Mpc}^{-1}$. A number of results are worth noticing. The addition of the bispectrum tightens the constraints on b_1 by a factor of ~ 3.4, and is able to break the degeneracies between b_2 and $b_{\mathcal{G}_2}$, and between $b_{\mathcal{G}_2}$ and b_{Γ_3}, thus providing a significant improvement in constraining higher-order bias parameters. The constraints on the effective counterterm $\tilde{c}_0$ are shrunk by almost a factor of two, while the ones on α_P and ϵ_{k^2} by almost a factor of 3.5.

Figure 4.7 shows the comparison between the model from the MCMC fit and the measured data of power spectrum and bispectrum. We compute the posterior-averaged models for both correlators, and then plot the mean residuals with the data, normalized by the standard deviation. The blue markers show points where the model is computed from the posterior of a power spectrum-only fit, while the red markers indicate that the model is computed as the average over the posterior of a joint fit of power spectrum and bispectrum; for the fits in this plot, we choose $k_{\rm max,P} = 0.30\,h\,{\rm Mpc}^{-1}$ and $k_{\rm max,B} = 0.09\,h\,{\rm Mpc}^{-1}$. In the plot showing the residuals for the bispectrum, we mark with empty squares the residuals computed with a posterior-averaged model from a bispectrum-only fit. The two cases relative to the power spectrum are consistent up to the $k_{\rm max,P}$ of the fit, which is as well close to the maximum Fourier wavenumber up to which the model is expected to work. As shown by the residuals in the lower panel of figure 4.7, a bispectrum model determined as the posterior-average of a power spectrum-only fit is visibly not able to reproduce the bispectrum data; notice however that the model from the joint fit is largely consistent with the model from a bispectrum-only fit. Since we average the models over the posterior of the MCMC runs, and the posterior from the joint fit is consistent with the posterior from the power spectrum-only fit, we suspect that the observed deviation is due to the additional information provided by the bispectrum on nonlinear bias.

4.3.3 Testing bias relations

We now turn to the performances of the bias relations in eq.s (4.45), (4.46), and (4.47). We take our reference model as a starting point and impose each of these relations to reduce to six the number of free parameters. We assume that all relevant halo bias coefficients are physical parameters, consistently describing nonlinear corrections in both the power spectrum and bispectrum, as opposed to simple nuisance parameters. Therefore, any valid

physical relation among them should not, in principle, introduce any significant deviation in their recovered values. The results are shown in figure 4.8. In general, all relations appear to fail, to some extent, in reproducing the values of the parameters obtained with the reference model. We should remember that this test takes advantage of the full simulation volume, well beyond the typical size even of future redshift surveys. It is interesting to notice how the $b_{\Gamma_3}(b_1, b_{\mathcal{G}_2})$ relation (4.47) introduces a notable dependence on $k_{\rm max,P}$ in the posteriors for parameters like b_1 and b_2. On the other hand, the $b_{\mathcal{G}_2}(b_1)$ relation (4.46) is recovering correctly the expected value of b_1, but leading to differences as large as 30% on parameters as b_2. These inconsistencies appear even more significant in the 2D marginalised posteriors in the bottom right inset obtained for $k_{\rm max,P} = 0.3\,h\,{\rm Mpc}^{-1}$.

In order to assess the relevance of the systematic errors induced by the bias relations in a more realistic context, we repeat the same analysis for a smaller effective volume of $V_{\rm eff} = 6\,h^{-3}\,{\rm Gpc}^3$. The effective volume of the full MINERVA dataset is given by (*e.g.* [153])

$$V_{\rm eff}^{\rm N-body}(k) = \left[\frac{\bar{n}P_{hh}(k)}{1+\bar{n}P_{hh}(k)}\right]^2 V_{\rm N-body}, \tag{4.52}$$

where $V_{\rm N-body} = 298 \times (1.5\,h^{-1}\,{\rm Gpc})^3 \simeq 1000\,h^{-3}\,{\rm Gpc}^3$. We then choose the reference $k_r = 0.1\,h\,{\rm Mpc}^{-1}$, and then compute the factor $\eta = V_{\rm eff}^{\rm N-body}(k_r)/6\,h^{-3}\,{\rm Gpc}^3$, that we use to rescale the covariance matrix. Finally, we rerun the analysis with the rescaled covariance matrix. The results are shown in figure 4.9. Notice that, in this case, the goodness-of-fit statistics we have defined cannot be used anymore to determine the range of validity of the model, because of the artificial rescaling of the covariance. For this reason, we simply assume the range of validity to be $k_{\rm max,P} = 0.30\,h\,{\rm Mpc}^{-1}$. With this smaller effective volume, all bias relations are consistent with the reference analysis and they all provide tighter constraints on one or more parameters, with the $b_2(b_1, b_{\mathcal{G}_2})$ fitting function, in particular, leading to the smaller uncertainty on the linear bias b_1.

In order to further compare the performance of the bias relations considered, we compute the difference in DIC with respect to the reference analysis, still using the smaller effective volume of $6\,h^{-3}\,{\rm Gpc}^3$, and show them in figure 4.10. In the range of validity of the model, all bias relations are favoured with respect to the reference model with the eq. (4.46) providing the largest improvement (largest negative difference ΔDIC) over the whole range in $k_{\rm max}$. The $b_{\Gamma_3}(b_1, b_{\mathcal{G}_2})$ relation (4.47), instead, appears to improve the fit only at the largest scales.

4.3.4 Effects of binning approximations

We now study how different ways to account for Fourier-space grid effects in the theoretical models impact parameter posteriors. Our reference case is the full bin-average of the theoretical predictions of both the power spectrum and the bispectrum, eq.s (4.37) and (4.38), which we compare to two, more efficient alternatives. We refer to the first as the "effective wavenumbers" approach, eq.s (4.40) and (4.42), where the theoretical predictions

are evaluated on the average Fourier wavenumbers, and to the second, based on a Taylor expansion about the effective method approximation, as the "expansion" approach, eq.s (4) and (9), both truncated to include up to second-order terms.

The comparison, which considers the full volume of all MINERVA simulations, is shown in figure 4.11. Even in this rather challenging test, the results for the expansion method (in green) are essentially indistinguishable from the results assuming the exact binning (in blue, but exactly underneath the green areas). The effective approach shows instead some significant discrepancies: the posterior of the linear bias b_1 is clearly inconsistent with the value measured from the cross-to-matter ratio at all values of $k_{\mathrm{max,P}}$, and moreover significant tensions are present for most of the parameters, particularly at larger scales. The 2D marginalized posteriors also show these strong deviations, with the $b_2 - b_{\mathcal{G}_2}$ contours being completely inconsistent in the two cases.

These differences are evident because of the large volume considered and the corresponding small statistical uncertainties in both the power spectrum and the bispectrum. Still, such effects are typically larger for higher-order multipoles in redshift space and it is interesting to explore alternative, efficient methods to deal with Fourier-space discreteness. The expansion method allows us to compute an excellent approximation of the full bin-average of theoretical predictions in a time of the same order of magnitude needed for an evaluation with the effective method: we use it in section 4.3.7 to run the MCMC simulations where the parameter space includes cosmological parameters, since in this case the exact binning approach for the bispectrum would be impracticable.

4.3.5 Covariance approximations

So far, all results assumed the covariance matrix for power spectrum and bispectrum, including the cross-covariance, estimated from the full set of 10 000 PINOCCHIO mocks. Such a large number of mocks is very often not available and it is necessary to resort to various approximations for the data covariance properties. We consider specifically three different cases in addition to our reference full covariance. In the first we exclude the cross-covariance between power spectrum and bispectrum, retaining the full individual covariance matrices for both statistics. The other two cases both consider the approximation that reduces the covariance matrix to its diagonal, requiring simply an estimate of the variance of power spectrum and bispectrum. In one case, this is estimated numerically from the mocks (and denoted as mock variance) while in the other we compute its Gaussian prediction from the power spectrum nonlinear, theoretical model assuming the bias parameters given by the best-fit values of the reference analysis (theoretical variance).

The comparison is shown in figure 4.12. All approximations are consistent with the reference case starting from the mildly non-linear regime, $k_{\mathrm{max,P}} \gtrsim 0.15\,h\,\mathrm{Mpc}^{-1}$. At larger scales, we notice some differences between the reference case and all approximations, including

the one excluding only the cross-covariance. This suggests that this contribution has some impact in the recovery of unbiased estimates of the model parameters, at least at the 1σ level. This is also consistent with the fact that these cross-correlations are expected to be quite large, with some of them being of the order of 40%. We remind the reader that the single-parameter posteriors are shown as a function of $k_{\rm max} \equiv k_{\rm max,P}$, denoting the power spectrum range only, while for the bispectrum we fixed $k_{\rm max,B} = 0.09\,h\,{\rm Mpc}^{-1}$. It is possible that if both statistics covered the same range of scales these effects would appear at larger values of k.

Looking at goodness-of-fit metrics, the covariance approximations determined from the mocks, including the case of the sole variance, provide estimates of the range of validity of the model quite close to our reference case. The theoretical Gaussian variance, however, does not provide a good fit at any of the scales shown in the plot. Since the reduced chi-square is nearly constant as a function of $k_{\rm max}$, one possible explanation might be that the Gaussian approximation provides a bad estimate of the full bispectrum variance. Indeed, by direct comparison, we observe that the theoretical Gaussian variance is a few percent lower with respect to the PINOCCHIO variance, and that differences reach 20% for some squeezed triangles, even at relatively large scales. It is possible that for such configurations the non-Gaussian contributions can be particularly large, but we leave this to future investigations.

4.3.6 Triangle selection criteria

In the power spectrum case, the range of validity of a given theoretical model is usually simply determined in terms of the largest wavenumber, $k_{\rm max,P}$, where the model provides a good fit to the data. In the bispectrum case, each value of $k_{\rm max,B}$ corresponds to a subset of triangles and we can expect a given theoretical model to perform more or less well on these configurations characterised by the same largest side but different shapes.

This is illustrated in figure 4.13, where we show the mean residuals with respect to the model, normalized to the standard error on the mean, of all the measured bispectrum bins up to the maximum wavenumber $k_{1,\rm max} = 0.174\,h\,{\rm Mpc}^{-1}$, assuming a posterior-averaged model from the reference joint fit. Each panel shows a subset of triangles characterised by the same value for the largest side k_1, shown as a function of the ratios k_2/k_1 and k_3/k_1 so that at the top-left we have squeezed configurations, at the top-right equilateral configurations, while at the bottom we have collinear, isosceles triangles ($k_1 \simeq 2\,k_2 \simeq 2\,k_3$). So far we assumed for all our analysis a $k_{\rm max,B} = 0.09\,h\,{\rm Mpc}^{-1}$. Including the whole subset of triangles with the next value of the largest side $k_1 > k_{\rm max,B}$ leads to the failure of the model to correctly describe the additional data, but we can expect this to happen first for nearly equilateral configurations, while a good fit can still be recovered for generic collinear configurations, i.e. with $k_1 \simeq k_2 + k_3$.

We want to check if different selection criteria based on other parameters than the sole $k_{\rm max,B}$ could lead to sensibly improved constraints on the model parameters. To this end we consider the following two triangle selection criteria:

- we choose only triangles satisfying the condition $k_1 + k_3 \leq \tilde{k}$ for a fixed value of $\tilde{k}$, and study parameter constraints as a function of k_1;
- we choose only triangles satisfying the condition $k_1 + k_2 \leq \tilde{k}$ for a fixed value of $\tilde{k}$, and study parameter constraints as a function of k_1;

Both choices, that always assume $k_1 \geq k_2 \geq k_3$, allow us to remove from the analysis nearly equilateral triangle bins, while keeping a subset of triangles with a different shape, as we include smaller scales by increasing k_1. This means that, when compared to the usual analysis, these selections lead to a smaller total number of triangles for the same value of $k_1 = k_{\rm max,B}$, but, at the same time, they should provide a good fit for larger values of $k_{\rm max,B}$.

Figure 4.14 shows (in blue) the results of the analysis of the bispectrum alone as a function of $k_{\rm max,B}$ as usually performed, compared with the same analysis where an additional condition is imposed to the combination $k_1 + k_3$, reducing the total number of triangles. In particular we consider $k_1 + k_3 \leq 0.14\,h\,{\rm Mpc}^{-1}$ (red) and $k_1 + k_3 \leq 0.18\,h\,{\rm Mpc}^{-1}$ (green). We notice that the stricter condition $k_1 + k_3 \leq 0.14\,h\,{\rm Mpc}^{-1}$ allows the inclusion of only a few more configurations w.r.t. those included in the standard result for $k_{\rm max} = 0.09\,h\,{\rm Mpc}^{-1}$. In fact, for $k_{\rm max} > 0.13\,h\,{\rm Mpc}^{-1}$ the posteriors do not change as no additional configuration can satisfy the condition and the quality of the fit remains acceptable for all the selected triangles. Comparing these results at $k_{\rm max} = 0.14\,h\,{\rm Mpc}^{-1}$ with the usual ones at $k_{\rm max} = 0.09\,h\,{\rm Mpc}^{-1}$ we find a non-negligible improvement on the parameters constraints of almost 50%. Imposing the condition on the sum $k_1 + k_3$ with the larger value $k_1 + k_3 \leq 0.18\,h\,{\rm Mpc}^{-1}$ allows for too many triangles not properly described by the model to be included, leading quickly to significant systematic errors on the recovered parameters.

In figure 4.15 we consider instead a condition on the sum $k_1 + k_2$. In this case, both $k_1 + k_2 < 0.14\,h\,{\rm Mpc}^{-1}$ and $k_1 + k_2 < 0.18\,h\,{\rm Mpc}^{-1}$ do not allow for any additional configurations for $k_{\rm max} > 0.12\,h\,{\rm Mpc}^{-1}$ and in both cases we retrieve constraints on b_1 consistent with the expected value $b_1^{\times}$. However, only the looser condition $k_1 + k_2 < 0.18\,h\,{\rm Mpc}^{-1}$ provides better constraints, of about 30%, than the standard case with $k_{\rm max} = 0.09\,h\,{\rm Mpc}^{-1}$.

We expect the introduction of selection criteria of this kind to be particularly relevant for constraining non-Gaussian initial conditions of the local type, where the signal peaks in the squeezed configurations [149]. We limit ourselves to remark, here, that the improvement, even when small, is obtained at no additional cost.

4.3.7 Inference of cosmological parameters

We finally present the results for the joint fit of the halo power spectrum and bispectrum in real space aimed at recovering unbiased estimates of the cosmological parameters. We use here the total volume of the MINERVA simulations. The theoretical model coincides with the reference model depending on the seven bias and shot-noise parameters in eq. (4.51). In this case, however, also the three cosmological parameters A_s, h, and ω_m are let free to vary within a range specified by uniform priors (see table 4.1). Notice that, in practice, the bias parameters that we vary are the ones defined in eq. (4.49) (but we show the original ones in the figure). This alleviates the strong degeneracy between *e.g.* b_1 and A_s, and thus speeds up the convergence of the MCMC runs. All parameters are varied consistently at each step of the MCMC runs, the theoretical model is recomputed fully, and Fourier-grid effects are accounted for by means of the expansion method described in appendix A.1. The covariance matrix is again the one estimated from the PINOCCHIO mocks.

Figure 4.16 shows the parameter constraints on the model parameters for four different values of $k_{\rm max,P} = 0.15, 0.20, 0.25, 0.30\,h\,{\rm Mpc}^{-1}$ (for the bispectrum, we still set $k_{\rm max,B} = 0.09\,h\,{\rm Mpc}^{-1}$). The posteriors for the cosmological parameters are nicely consistent with the input values used to run the N-body simulations, marked with gray lines, and the one for the linear bias b_1 again agrees with the value measured from the cross halo-matter power spectrum. This agreement is clearly visible in the 2D marginalized posteriors as well. Moreover, all the other parameters are still perfectly consistent with the values extracted from the reference analysis with fixed cosmological parameters. It is also worth noticing how, regardless of the degeneracies that might be present between bias and cosmological parameters, the posteriors for the bias parameters are still stable as a function of $k_{\rm max,P}$. Similar conclusions can also be drawn for the parameter $\tilde{c}_0$ and for the stochastic parameters.

In figure 4.17, we compare the constraints obtained fitting the power spectrum only (up to $k_{\rm max,P} = 0.30\,h\,{\rm Mpc}^{-1}$) and performing a joint fit of the power spectrum and the bispectrum (for the latter we use $k_{\rm max,B} = 0.09\,h\,{\rm Mpc}^{-1}$). The fiducial model discussed in section 4.3.2 is fitted to the data but, once again, we let the cosmological parameters A_s, h, and ω_m vary. Strong parameter degeneracies are present in the power spectrum-only fit and the Markov chains do not satisfy the formal convergence criterion we use even after very many steps. Therefore, it is possible that the size of the blue constraints in the figure are underestimated, although we suspect not by much (based on multiple MCMC chains). The inclusion of the bispectrum to the analysis, even at large scales, tightens the constraints on the cosmological parameters: constraints on A_s are reduced by a factor 3.3, while the ones on h and ω_m by a factor of roughly 2.

The data set we have analysed does not capture the full complexity of a galaxy redshift survey. Our setup, based on simulations within periodic boxes, at fixed redshift, and in real space, still lacks a proper modelling (in the observables, and possibly in the covariances) of

non-linearities arising from redshift-space distortions, and of mode-coupling effects due to the survey window function. To an extent, this might result in a minor improvement on the constraints of the model parameters when the bispectrum is included in a realistic data analysis. However, given the unprecedentedly large volume we considered ($1000\,h^{-3}\,\mathrm{Gpc}^3$, almost twice the volume analysed in the challenge paper of [117]), our results form a very stringent test of halo bias models, as well as a strong consistency check between perturbative models and the non-linear dynamics simulated by N-body solvers. They also provide strong evidence that the perturbative bias treatment and the counterterms do not distort the posterior distribution of the cosmological parameters, at least in real-space. We thus conclude that a joint likelihood analysis of the power spectrum and the bispectrum should be able to provide unbiased estimates for the cosmological parameters, including information on the accelerated expansion of the Universe.

4.4 Conclusions

We presented a joint likelihood analysis of the real-space halo power spectrum and bispectrum extracted from 298 N-body simulations covering a total volume of roughly $1000\,h^{-3}\,\mathrm{Gpc}^3$. We compared the data to a perturbative model at one-loop for the power spectrum and at tree-level for the bispectrum. The model implementation, limited here to real space, is essentially the same that has been recently applied to the analysis of the BOSS data in [90]. In order to estimate the full non-linear covariance matrix for both observables along with their cross-covariance, we used measurements from 10 000 mock halo catalogs generated with the PINOCCHIO code. We can summarize the main results of our analysis as follows.

- Using Bayesian model selection, we identify the optimal set of free parameters that can be constrained by the data (with a fixed background cosmological model), namely four bias parameters, one counterterm parameter, and two stochastic corrections to the power spectrum model.
- The theoretical model for the power spectrum nicely fits our numerical data up to $k_{\mathrm{max,P}} \sim 0.3\,h\,\mathrm{Mpc}^{-1}$. Considering the power spectrum along with the bispectrum (up to $k_{\mathrm{max,B}} = 0.09\,h\,\mathrm{Mpc}^{-1}$), the fit provides unbiased estimates of the linear bias parameter b_1 with sub-percent precision, as well as a good fit to the data as estimated both in terms of the χ^2 and ppp diagnostics – even when the full data set is considered.
- We explore the possibility of reducing the dimensionality of parameter space by assuming that not all the bias parameters are independent, as suggested by several numerical and theoretical studies. In all cases, fitting the simplified models to the full data set gives biased estimates of the parameters. However, when the probed volume is reduced to match those that will be covered by the upcoming surveys ($6\,h^{-3}\,\mathrm{Gpc}^3$), all the fits based on the bias relations provide consistent values of the free parameters with smaller uncertainties than the default case. In particular, the DIC indicates that

the data are best described by the $b_{\mathcal{G}_2}(b_1)$ relation proposed by [49].

- We investigate different methods to account for the discrete nature of measurements of Fourier-space correlators in the binning of the theoretical predictions. We find that, when the larger volume is considered, the evaluation of the model at a single effective triangle per bin leads to strongly biased parameter constraints. We propose a new method, discussed in appendix A.1, and we show that it is able to provide constraints consistent with our reference results (obtained by averaging exactly the model over the Fourier wavenumbers in each bin).

- We test several approximations to the covariance matrix. We find that neglecting the cross-correlations between power spectrum and bispectrum slightly biases the constraints on the model parameters. In addition, we show that the Gaussian (diagonal) approximation to the covariance matrix underestimates the errors by up to 20% on some triangular configurations, and fails to provide a proper estimate of the goodness-of-fit of the theoretical model.

- We explore different selection criteria to reduce the number of triangular configurations for the analysis of the bispectrum. We find that a selection of the triangular configurations accounting as well for their shape, rather than only the largest wavenumber $k_{\mathrm{max,B}}$, can lead to an improvement in the parameters constraints by up to 50%.

- Finally, we perform a likelihood analysis in which also three cosmological parameters are varied. In this case, we use the power spectrum and the bispectrum data extracted from the full simulation suite. The constraints on the cosmological parameters obtained with our default 7-parameter model are nicely consistent with the input values of the simulations, up to $k_{\mathrm{max,P}} = 0.3\,h\,\mathrm{Mpc}^{-1}$. Moreover, compared to a power spectrum-only analysis, the constraints on cosmological parameters in a joint analysis shrink significantly, by a factor of ~ 3 for the amplitude of scalar perturbations A_s and by a factor of ~ 2 for the Hubble parameter h and the relative abundance of matter ω_m. This major achievement demonstrates the feasibility of using perturbative models with free parameters in order to extract information on the underlying cosmological parameters from the joint analysis of the power spectrum and the bispectrum.

As already mentioned in the introduction, the likelihood analysis of three-point statistics is still a relatively poorly explored subject (particularly in order to set constraints on the cosmological parameters). While the ideal data set considered here does not have the complexity of a galaxy redshift survey, its large total simulation volume (combined with the 10,000 mock catalogs), allowed us to investigate the impact of several assumptions which are routinely made in this kind of studies. Upcoming observations will require a better quantification and control over possible systematic errors both in the theoretical modelling as in the methodology. For these reasons, we think that our work is a step towards more rigorous and thorough analysis of spectroscopic redshift surveys.

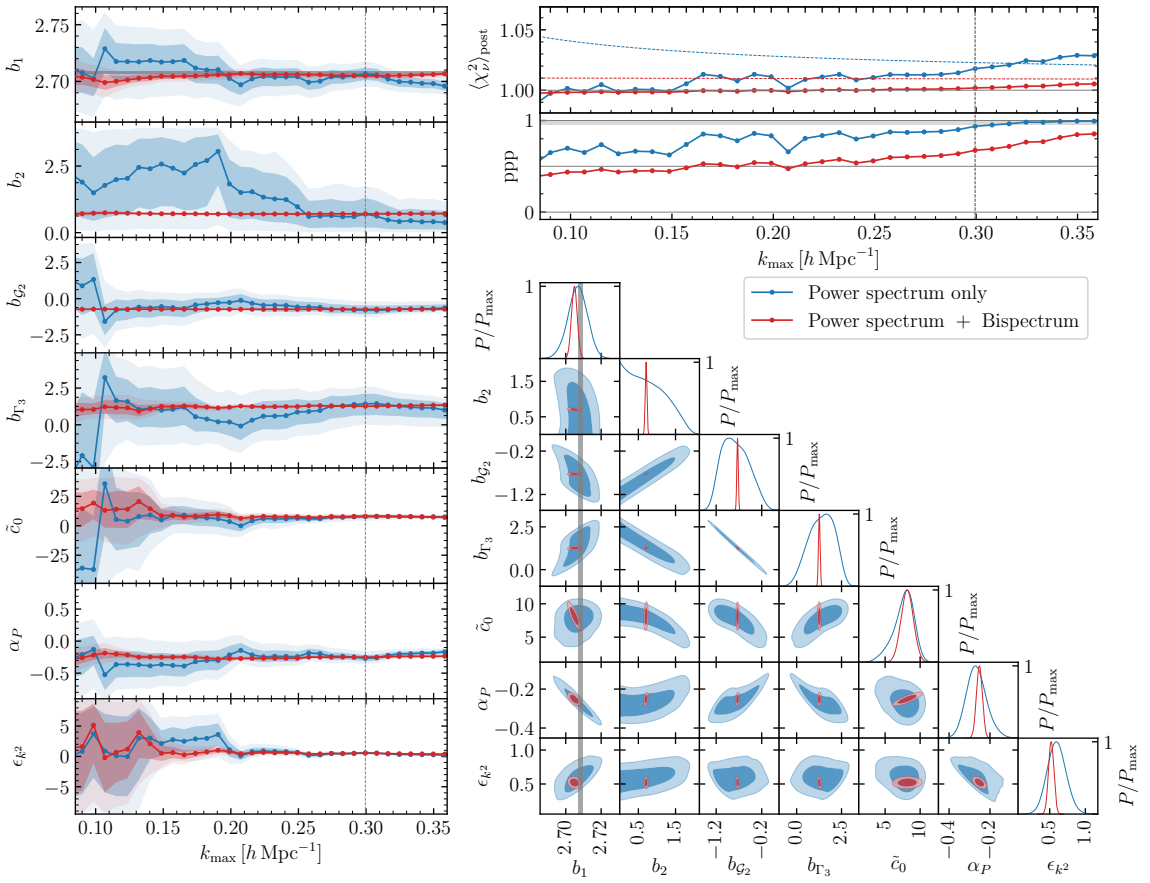

Figure 4.6: Comparison between the fit of the halo power spectrum and the joint fit of the halo power spectrum and bispectrum measured from the N-body simulations. The left panels show the posterior mean (solid lines), and central 68 and 95 percent ranges (darker and lighter shaded areas respectively) of the model parameters as a function of $k_{\rm max} \equiv k_{\rm max,P}$. The bispectrum data range is fixed by $k_{\rm max,B} = 0.09\,h\,{\rm Mpc}^{-1}$. The vertical dashed line highlights the reference scale of $k_{\rm max,P} = 0.30\,h\,{\rm Mpc}^{-1}$ for which we display contour plots for the joint posterior density of parameter pairs in the lower-right panel. Here, darker and lighter shaded areas represent the 68 and 95 percent joint credibility regions, respectively. The narrow gray bands indicate the constraints on the linear-bias parameter derived from the halo-matter cross power spectrum. Two goodness-of-fit diagnostics are displayed in the top-right panel as function of $k_{\rm max}$: the reduced χ^2 statistic averaged over the posterior (top inset) and the ppp (bottom inset). As a reference, the dashed curves in the top inset indicate the upper one-sided 95 percent confidence limit in a frequentist χ^2 test (note that the number of datapoints included in the fit varies with $k_{\rm max}$).

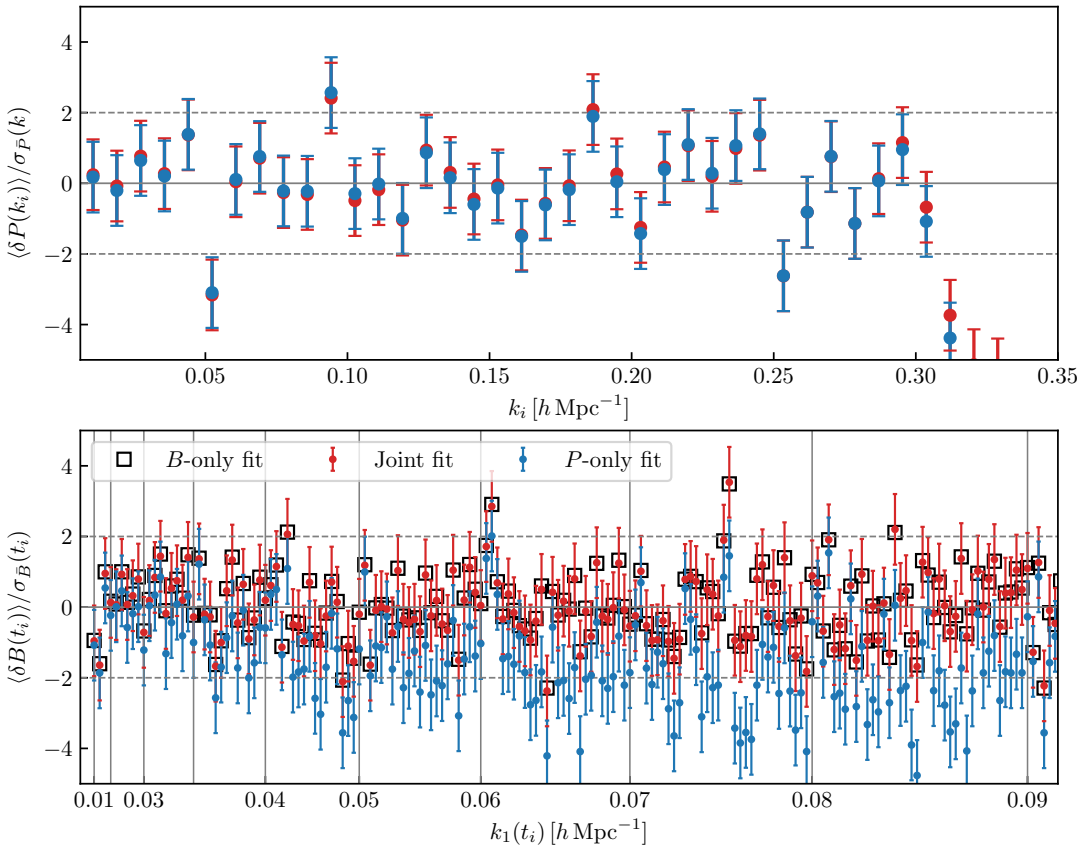

Figure 4.7: Top: mean residuals, normalized to the standard error on the mean, between the power spectrum measured from the N-body simulations and the posterior-averaged theoretical model from a power spectrum-only fit (blue) and from a joint fit (red), with $k_{\mathrm{max,P}} = 0.30\,h\,\mathrm{Mpc}^{-1}$ and $k_{\mathrm{max,B}} = 0.09\,h\,\mathrm{Mpc}^{-1}$. Bottom: same as the top panel, but for the bispectrum measurements; empty squares show the same quantity for the posterior-averaged theoretical model for a bispectrum-only fit with $k_{\mathrm{max,B}} = 0.09\,h\,\mathrm{Mpc}^{-1}$.

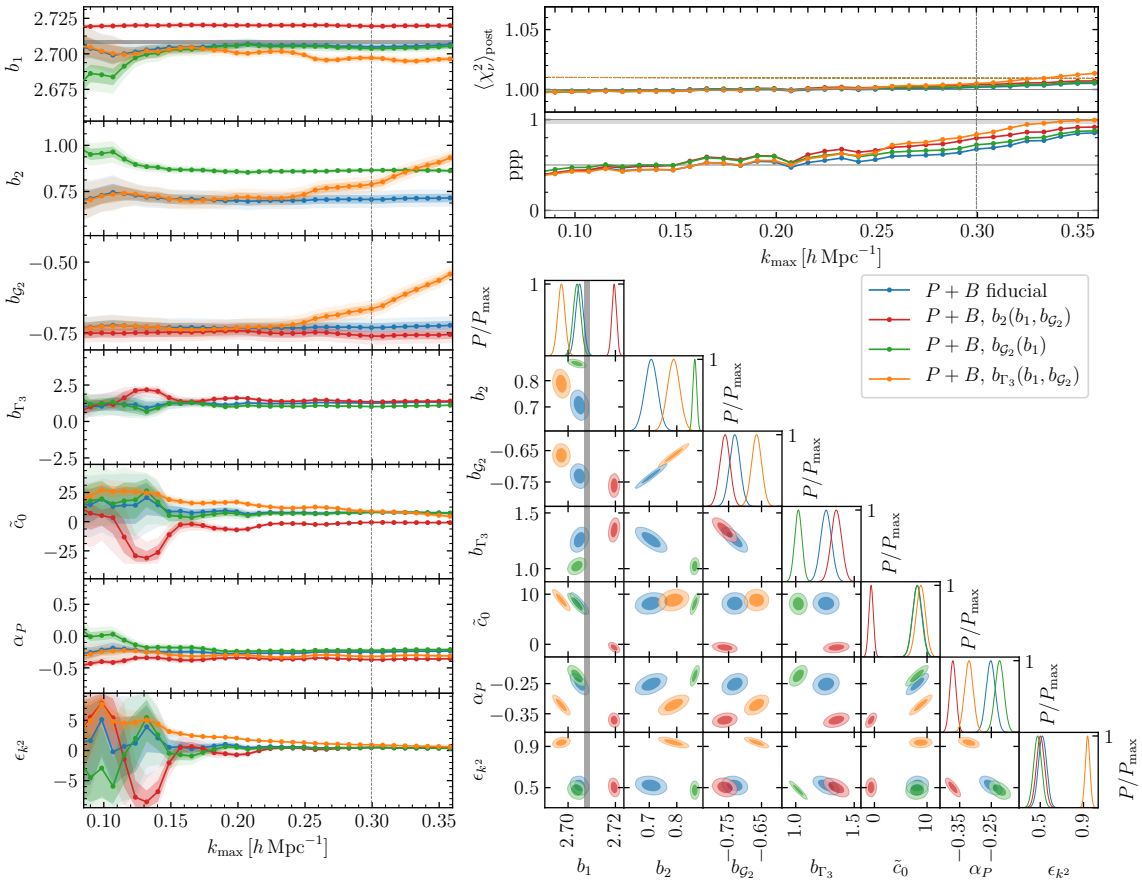

Figure 4.8: Same as figure 4.6, but comparing the fit performed with the fiducial model to models where different relations between bias parameters are assumed; in blue the reference case of the fiducial model, in red the case where equation (4.45) is assumed, in green the case where we set equation (4.46), and in orange the case with equation (4.47). The deviations in the 2D marginalised posteriors suggest that all relations fail in reproducing the values of the parameters obtained with the reference model. However, note that this test takes advantage of the full simulation volume, which is far beyond the usual size of a redshift survey.

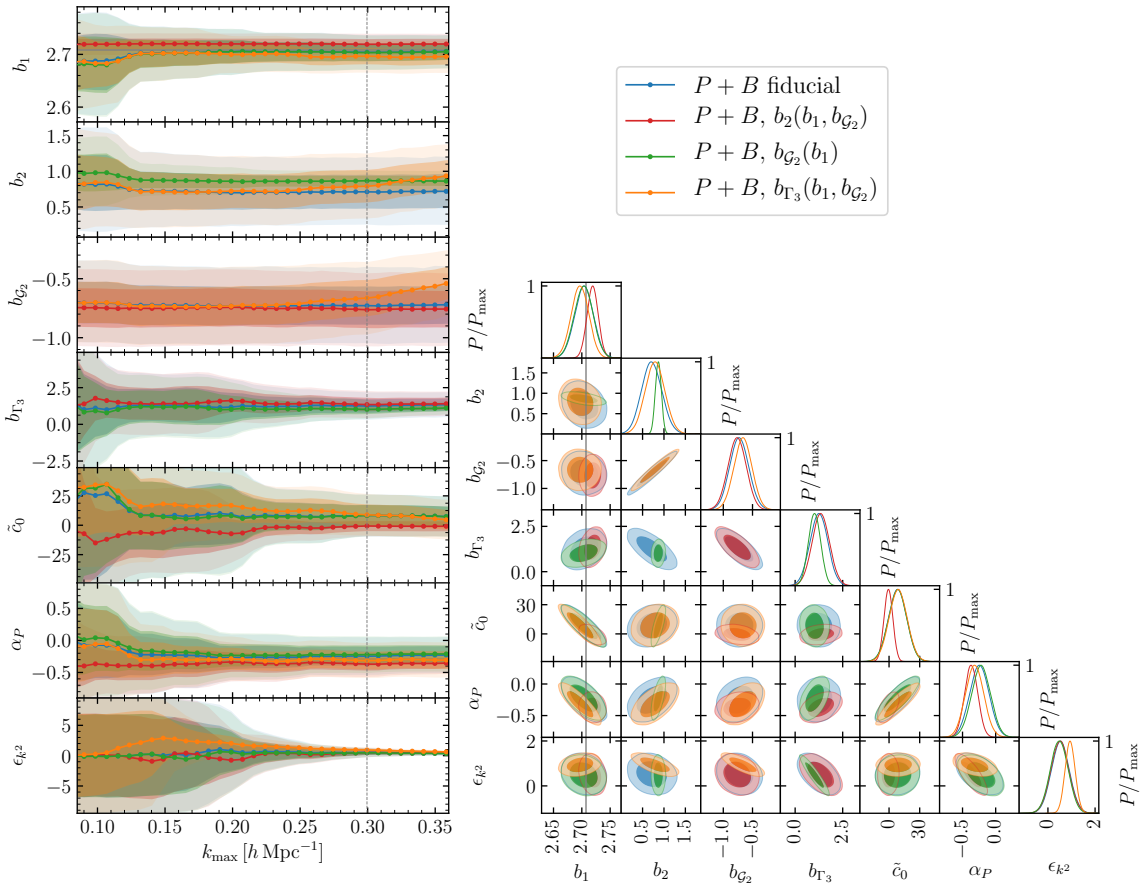

Figure 4.9: Same as figure 4.8, but for an effective volume of $6\,h^{-3}\,\mathrm{Gpc}^3$.

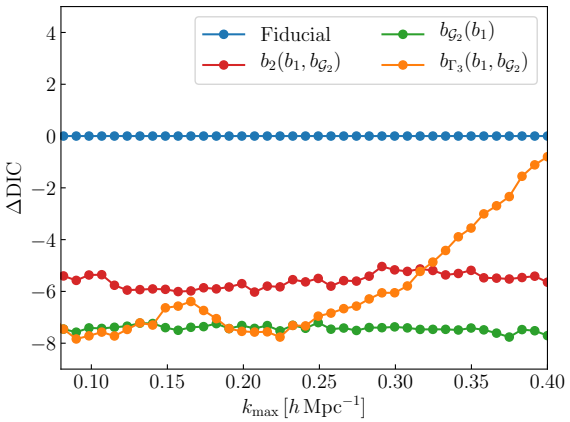

Figure 4.10: Difference in DIC, with respect to the fiducial case, of the alternative models that assume relations between bias parameters, as a function of $k_{\rm max}$, for an effective volume of $6\,h^{-3}\,\mathrm{Gpc}^3$.

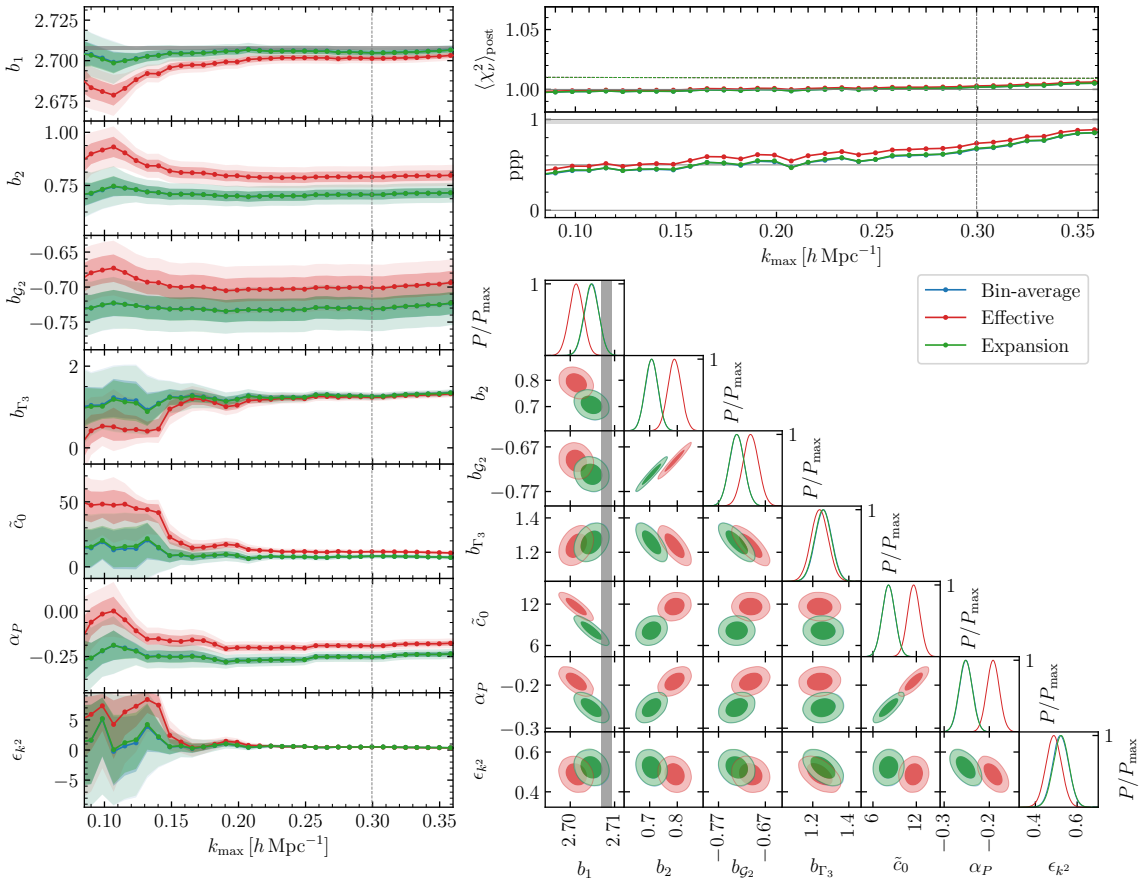

Figure 4.11: Same as figure 4.6, but now comparing different methods to evaluate the theoretical models for the power spectrum and the bispectrum. In blue, the reference case with the bin-average of the theoretical prediction, in red the case where the models are evaluated at effective wavenumbers, and in green the case where the expansion method, described in appendix A.1, is used. Blue and green lines and contours coincide almost exactly.

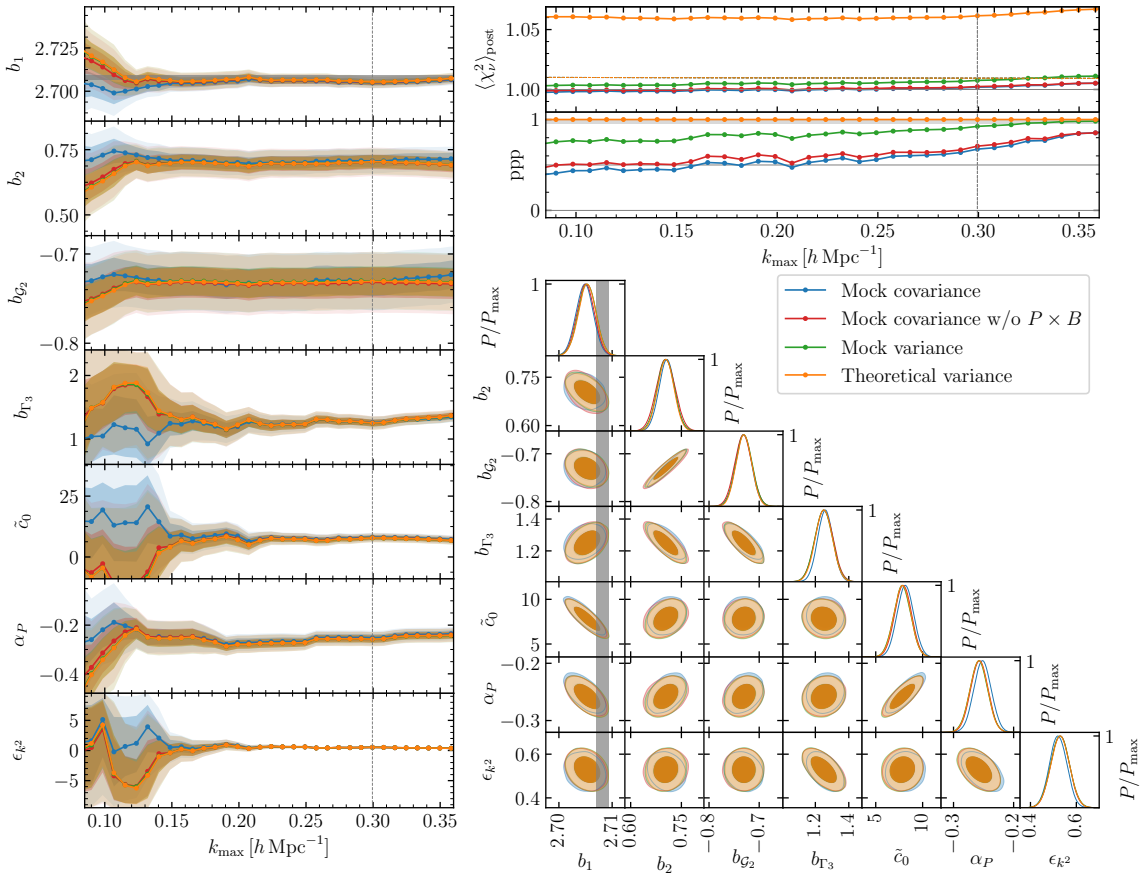

Figure 4.12: Same as figure 4.6, but now comparing different approximation to the covariance matrix. In blue, the reference case with the full mock covariance; in red, the case where cross-correlations between power spectrum and bispectrum are set to zero; in green, the case where only the mock variance is used; in orange, the case where a theoretical Gaussian covariance is assumed.

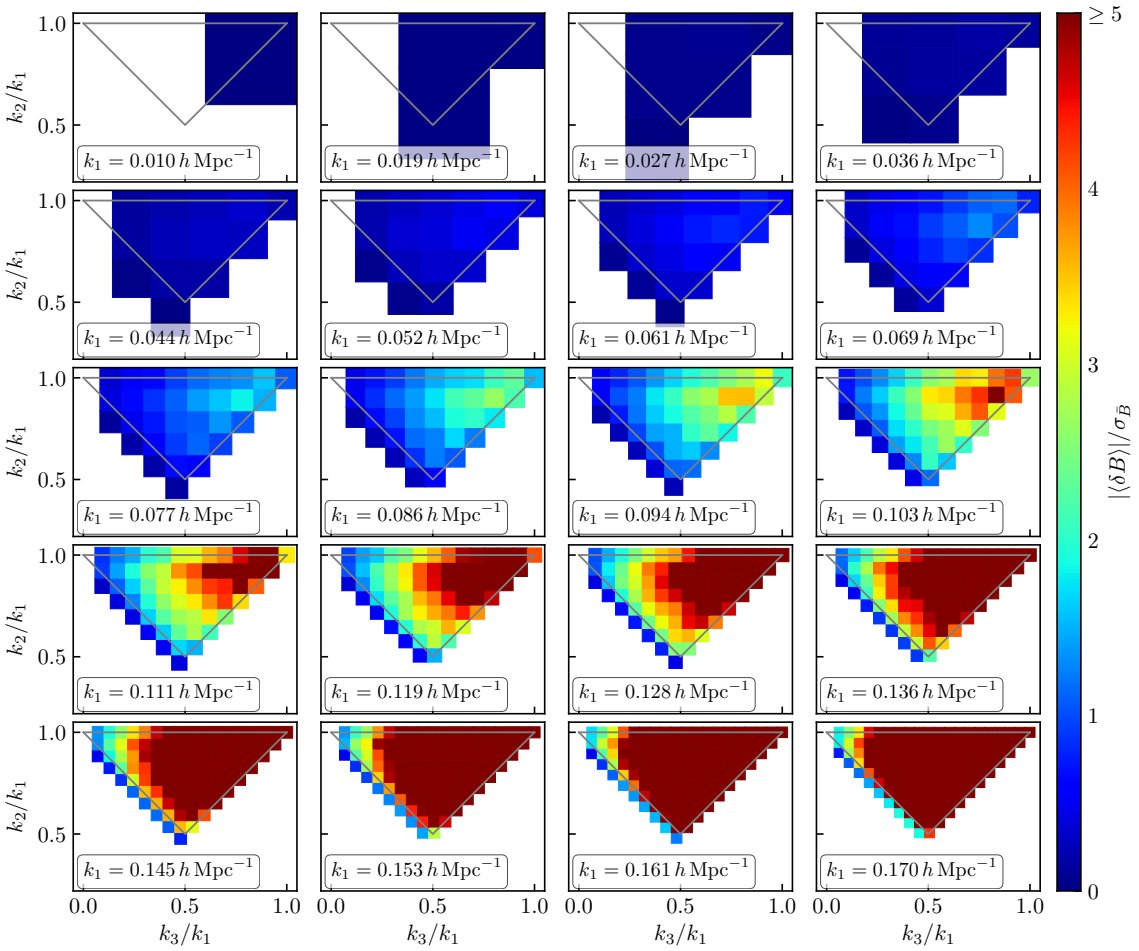

Figure 4.13: Mean residuals, normalized to the standard error on the mean, of all the measured bispectrum bins, with respect to the posterior-averaged tree-level model of the reference analysis, $k_{\mathrm{max,P}} = 0.30\,h\,\mathrm{Mpc}^{-1}$, $k_{\mathrm{max,B}} = 0.09\,h\,\mathrm{Mpc}^{-1}$. In each panel, we fix the value of k_1 and show all triangle bins according to their value of k_2 and k_3. As a reference, the gray triangle in each panel represents the border of allowed fundamental triangles with $|\mathbf{q}_1| = k_1$. Tiles in the upper-right corner represent triangles closer to equilateral ($k_1 \simeq k_2 \simeq k_3$), those in the lower corner represent collinear triangles ($k_1 \simeq 2k_2 \simeq 2k_3$) while those in the upper-left corner represent squeezed triangles ($k_3 \ll k_1$). A bluer color shows a better agreement between model and data, while a redder color shows a worse fit. We cutoff the scale at 5σ.

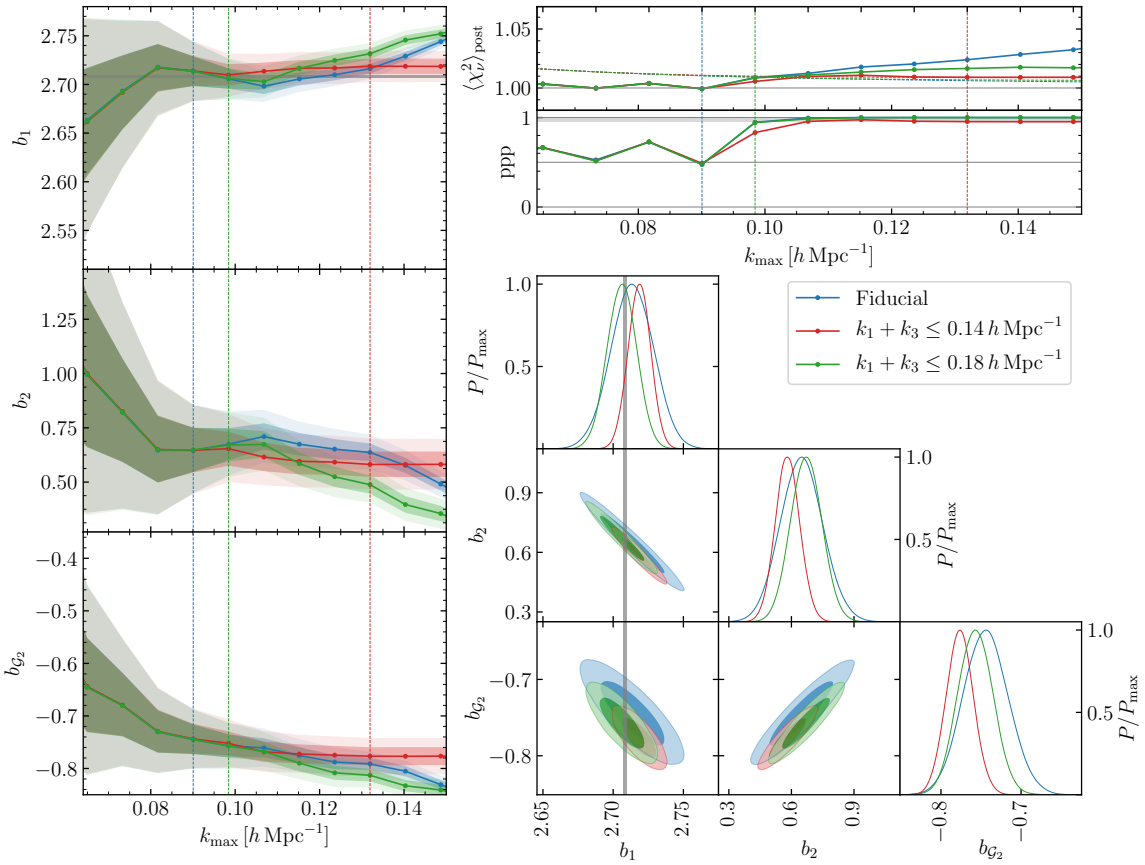

Figure 4.14: Comparison between the fits to the bispectrum-only data shown as a function of the largest wavenumber $k_{\max}$ included (blue) against the same analysis performed over data sets satisfying an additional condition of the maximum value of the combination k_1+k_3. We consider in particular $k_1+k_3\leq 0.14\,h\,\mathrm{Mpc}^{-1}$ (red) and $k_1+k_3\leq 0.18\,h\,\mathrm{Mpc}^{-1}$ (green). The 2D contour plots in this case correspond to different values of $k_{\max}$ defined as the largest values ensuring consistent results. They are marked with vertical lines of the corresponding colors in the left and top-right panels. In the contour plot, the number of triangles is 170, 222, 215 for the blue, red and green contours respectively.

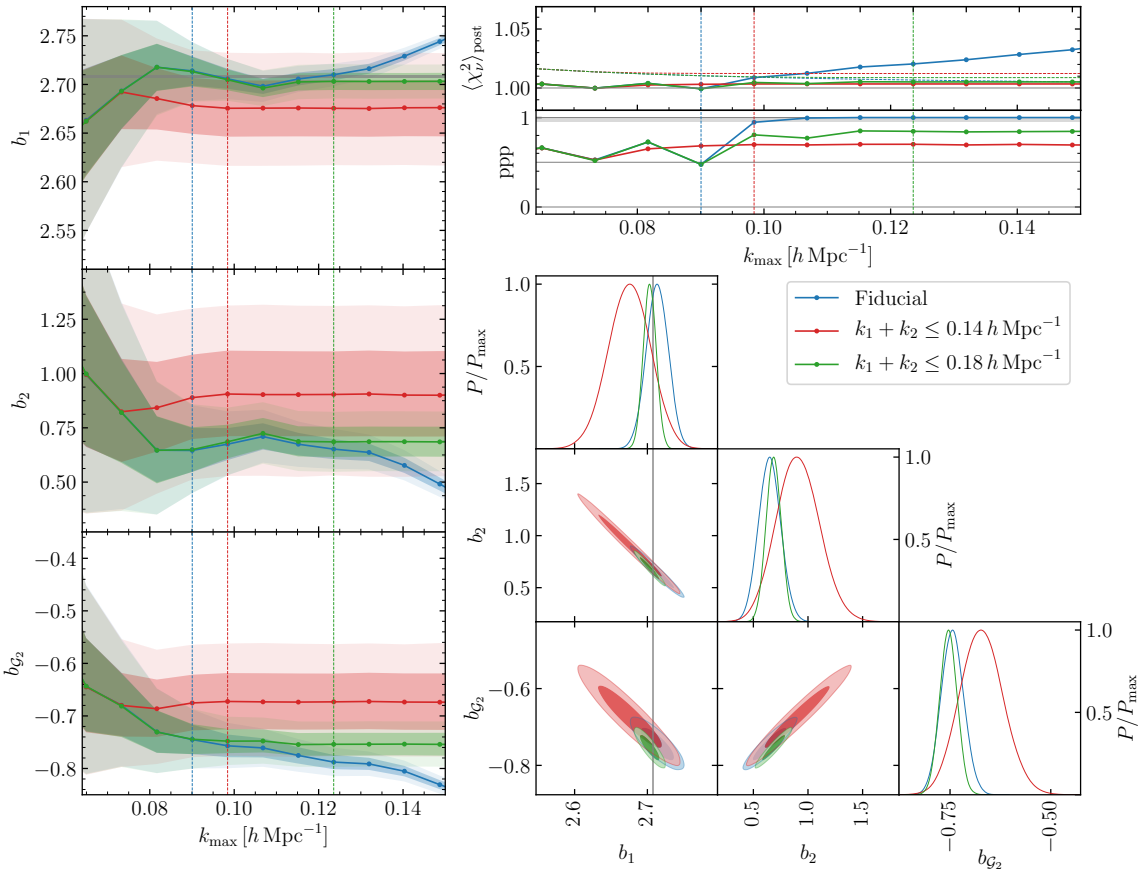

Figure 4.15: Same as fig. 4.14 but with the additional condition on the combination $k_1 + k_2$. We consider $k_1 + k_2 \leq 0.14\,h\,\mathrm{Mpc}^{-1}$ (red) and $k_1 + k_2 \leq 0.18\,h\,\mathrm{Mpc}^{-1}$ (green). This time, in the contour plot, the number of triangles is 170, 121, 236 for the blue, red and green contours respectively.

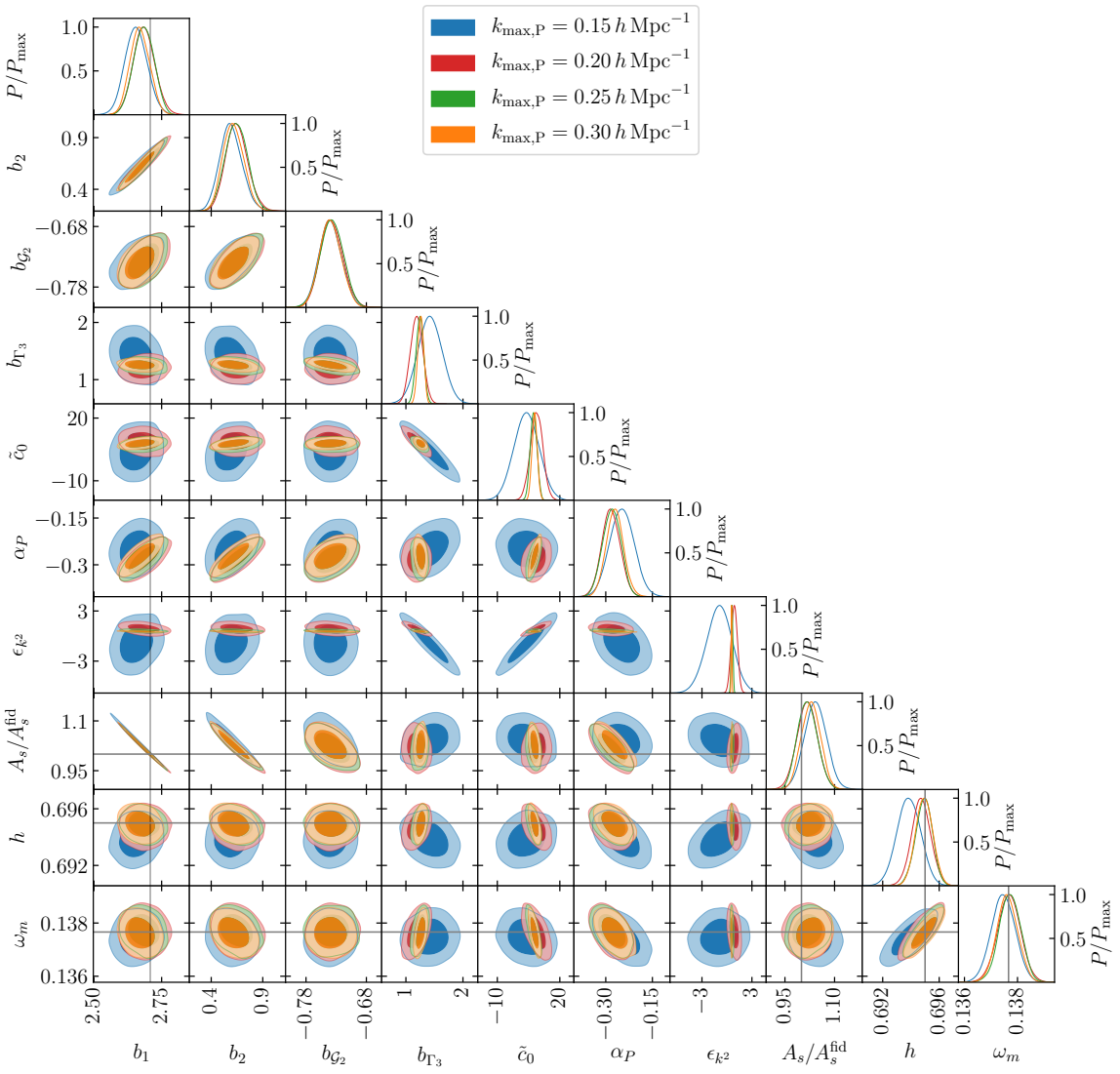

Figure 4.16: Triangle plot showing the 1D and 2D marginalized posteriors of the parameters of the fiducial model, where also three cosmological parameters are varied, from a joint fit of the halo power spectrum and bispectrum measured from the N-body simulations, for different values of $k_{\mathrm{max,P}} = 0.15, 0.20, 0.25, 0.30\,h\,\mathrm{Mpc}^{-1}$ (in blue, red, green, and orange respectively). Gray lines show the linear bias measured from the cross power spectrum and the input values of the cosmological parameters.

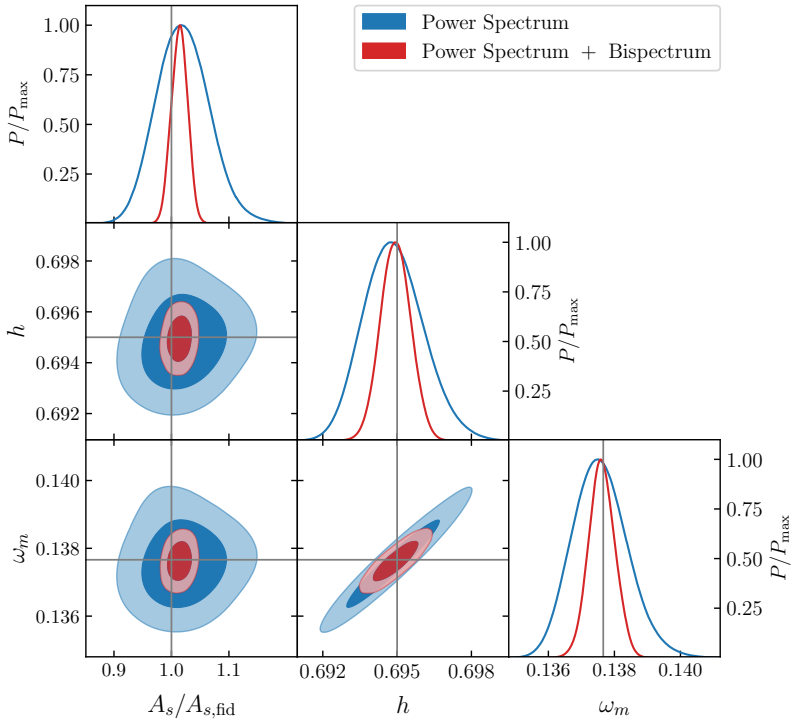

Figure 4.17: Triangle plot showing the 1D and 2D marginalized posteriors of the cosmological parameters inferred through a likelihood analysis of power spectrum (blue) and power spectrum and bispectrum (red) using the fiducial model. In this plot, we marginalize over all bias and stochastic parameters in order to highlight the impact that the inclusion of the bispectrum to the analysis has on the inference of cosmological parameters. For the power spectrum we set $k_{\rm max,P} = 0.30\,h\,{\rm Mpc}^{-1}$, while we set $k_{\rm max,B} = 0.09\,h\,{\rm Mpc}^{-1}$ for the bispectrum. Gray lines show the input values of the cosmological parameters.

Chapter 5

The Halo Bispectrum Multipoles in Redshift Space

While the analysis of the power spectrum takes full advantage of redshift-space distortions by means of a multipoles expansion with respect to the angle between the wavenumber $\mathbf{k}$ and the line-of-sight (see, e.g. [4, 139]), in the case of the bispectrum past data analyses have always been limited to the monopole. On the other hand, the potential offered by the galaxy bispectrum measured in future surveys to further constrain cosmological parameters has been explored in several papers [158, 61, 170, 34, 81, 77, 80, 3, 88]. A subset of these works specifically considered the relevance of the anisotropic bispectrum signal [158, 61, 170, 77, 3] remarking that we can expect additional information in the higher-order multipoles of the bispectrum, although the exact extent of the improvement on parameters constraints, typically of the order of tens of percents, highly depends on the assumptions on the observable, its covariance and the survey specifications.

A first theoretical modelling of the redshift-space bispectrum at tree-level in Perturbation Theory can be found in [86] (see [19] and references therein for earlier work on the matter and galaxy bispectrum in real space). Early comparisons against measurements of the bispectrum monopole in numerical simulations are presented in [165, 148, 144] with [148] including as well a first test of the quadrupole. The analysis of the BOSS data-set of [64, 68, 67] includes the bispectrum monopole and takes advantage of a phenomenological model [69], based on fits to simulations, to extend the validity of the tree-level expression to smaller scales, reaching $0.15\,h\,\mathrm{Mpc}^{-1}$ with a 5% accuracy on the halo bispectrum monopole at redshift $z = 0.55$ (to contrast $0.06\,h\,\mathrm{Mpc}^{-1}$ in the case of tree-level PT). A similar approach is adopted as well in [76] where the monopole and quadrupole of the power spectrum, bispectrum and integrated trispectrum are compared to simulations.

Ref. [84] goes beyond the tree-level expression presenting a one-loop PT model for the redshift-space *matter* bispectrum multipoles (but defined differently from [148]), including additional corrections along the lines of those introduced by [162] for the power spectrum. The comparison with numerical simulations shows an agreement up to $k \sim 0.15$ - $0.2\,h\,\mathrm{Mpc}^{-1}$ depending on redshift and configuration shape while the corresponding tree-level approximation typically fails already around $k \sim 0.07$ - $0.08\,h\,\mathrm{Mpc}^{-1}$ for both the monopole and the quadrupole.

More recently, [39] re-analysed the BOSS bispectrum monopole, adopting a tree-level model up to $0.1\,h\,\mathrm{Mpc}^{-1}$, although no comparison with simulations or details on model validation are provided. A further analysis, extending the model to include one-loop corrections and corrections due to primordial non-Gaussianity is presented in [40]. A comparison with large-volume simulations can be found instead, again for the monopole only, in [88] for measurements obtained from the very large simulation set already adopted for the challenge paper [117], corresponding to a cumulative volume of $566\,h^{-3}\,\mathrm{Gpc}^3$: in this case as well the reach of the tree-level expression is found to be $k_{\mathrm{max}} \sim 0.08\,h\,\mathrm{Mpc}^{-1}$. The same pipeline for the bispectrum monopole analysis is applied to the BOSS data in [127, 30, 29].

It appears that, despite the recent attention, tests of the redshift-space galaxy bispectrum model have been rather limited. In fact, current literature is for the most part focused on the bispectrum monopole with only partial assessments of higher-order multipoles predictions in PT.

The main goal of this chapter is to provide a rigorous and extensive comparison of the tree-level predictions for the halo bispectrum monopole, quadrupole and hexadecapole (as defined in [148]) against measurements in a very large set of numerical simulations ($\sim 1,000\,h^{-3}\,\mathrm{Gpc}^3$) while taking advantage of a robust estimate of their covariance properties from an even larger set of mock catalogs. It constitutes the natural continuation of a series of papers exploring in details the challenges of a joint analysis of the galaxy power spectrum and bispectrum, so far focused on real-space modelling [119, 5, 118]. We will refer, in particular as Paper I and Paper II respectively to [119] and [118] as this work shares with these references, to a large extent, both data-sets and methodology. We test the model by means of a likelihood analysis in terms of bias parameters along with the growth rate of perturbations f, using the simulation input and real-space results as reference values. For measurement uncertainties corresponding to the total combined volume of our simulations, we find that the model provides a valid description up to a maximum wavenumber of $0.08\,h\,\mathrm{Mpc}^{-1}$ for the monopole, $0.06\,h\,\mathrm{Mpc}^{-1}$ for the quadrupole, and $0.045\,h\,\mathrm{Mpc}^{-1}$ for the hexadecapole. We show that, as in the power spectrum case, the inclusion of the bispectrum quadrupole greatly improves the posteriors from the monopole alone.

This chapter is organised as follows. In section 5.1 we introduce the theoretical background for the tree-level prediction of the bispectrum multipoles in Perturbation Theory. Section 5.2 describes the numerical simulations and mock catalogs adopted and the bispectrum estimator. In Section 5.4 we present the set-up for our likelihood analyses and in Section 5.5 the relative results. We will present our conclusions in Section 5.6.

5.1 Theoretical background

5.1.1 Model

Given the halo number density contrast $\delta_h(\mathbf{x}) \equiv [n_h(\mathbf{x}) - \bar{n}_h]/\bar{n}_h$ defined in terms of the number density $n_h(\mathbf{x})$ and its expectation value $\bar{n} = \langle n_h(\mathbf{x})\rangle$, and its Fourier Transform[1] $\delta_h(\mathbf{k})$ we can define the halo power spectrum P_h and bispectrum B_h respectively as

$$\langle \delta_h(\mathbf{k}_1)\delta_h(\mathbf{k}_2)\rangle \equiv (2\pi)^3\delta_D(\mathbf{k}_{12})\, P_h(k_1) \tag{5.3}$$

$$\langle \delta_h(\mathbf{k}_1)\delta_h(\mathbf{k}_2)\delta_h(\mathbf{k}_3)\rangle \equiv (2\pi)^3\delta_D(\mathbf{k}_{123})\, B_h(k_1,k_2,k_3)\,, \tag{5.4}$$

where the Dirac deltas δ_D results from the assumed statistical homogeneity and isotropy. For the same reason $P_h(k_1)$ is a function of one variable, $k_1 = |\mathbf{k}_1|$ and $B_h(k_1,k_2,k_3)$ is a function of the three sides of the triangle formed by $\mathbf{k}_1$, $\mathbf{k}_2$ and $\mathbf{k}_3$ and independent of its orientation.

In redshift-space, peculiar velocities $\mathbf{v}$ induce distortions in the galaxy distribution along the line-of-sight (LOS) $\hat{n}$. The observed position $\mathbf{s}$ will then be related to real position $\mathbf{x}$ by 2.81. As a result clustering properties, and in particular galaxy correlation functions estimated in a given region of the sky, will depend on the local LOS. Since our focus is to test the modelling of the bispectrum based on measurements in simulation boxes with periodic boundary conditions, we will assume throughout this work the plane-parallel approximation for redshift-space distortions and therefore a global, constant LOS. The halo bispectrum will then be a function of the wavenumbers defining the triangular configuration $\mathbf{k}_1$, $\mathbf{k}_2$ and $\mathbf{k}_3$ plus the LOS $\hat{n}$, that is $B_s = B_s(\mathbf{k}_1,\mathbf{k}_2,\hat{n})$.

Our model for the redshift-space halo bispectrum is the sum of a deterministic and stochastic contribution, as

$$B_s(\mathbf{k}_1,\mathbf{k}_2,\mathbf{k}_3) = B_s^{(\mathrm{det})}(\mathbf{k}_1,\mathbf{k}_2,\mathbf{k}_3) + B_s^{(\mathrm{stoch})}(\mathbf{k}_1,\mathbf{k}_2,\mathbf{k}_3)\,, \tag{5.5}$$

corresponding to the tree-level expression in Perturbation Theory (PT) resulting from the halo density given, in turn, by the sum of a deterministic and a stochastic component

$$\delta_s = \delta_s^{(\mathrm{det})} + \delta_s^{(\mathrm{stoch})}\,. \tag{5.6}$$

[1] We adopt the convention for the Fourier Transform

$$\delta(\mathbf{k}) \equiv \int d^3x\, e^{-i\mathbf{k}\cdot\mathbf{x}}\,\delta(\mathbf{x})\,, \tag{5.1}$$

with the inverse given by

$$\delta(\mathbf{x}) \equiv \int \frac{d^3k}{(2\pi)^3}\, e^{i\mathbf{k}\cdot\mathbf{x}}\,\delta(\mathbf{k})\,. \tag{5.2}$$

In Fourier space and up to the relevant order the deterministic contributions are given by

$$\delta_s^{(\rm det)}(\mathbf{k}) = Z_1(\mathbf{k})\,\delta_L(\mathbf{k}) + \int d^3q_1 d^3q_2 \delta_D(\mathbf{k}-\mathbf{q}_{12}) Z_2(\mathbf{q}_1,\mathbf{q}_2)\,\delta_L(\mathbf{q}_1)\,\delta_L(\mathbf{q}_1)\,, \tag{5.7}$$

where δ_L is the linear matter density and the relevant Z_n redshift-space kernels are given in terms of the local (b_1, b_2) and tidal ($b_{\mathcal{G}_2}$) bias parameters and the linear growth rate f by [59, 86, 165, 148, 33, 13, 47]

$$\begin{aligned} Z_1(\mathbf{k}) &= b_1 + f\mu^2\,, & (5.8)\\ Z_2(\mathbf{k}_1,\mathbf{k}_2) &= \frac{b_2}{2} + b_1 F_2(\mathbf{k}_1,\mathbf{k}_2) + b_{\mathcal{G}_2} S(\mathbf{k}_1,\mathbf{k}_2) + f\mu_{12}^2 G_2(\mathbf{k}_1,\mathbf{k}_2) + \\ &\quad + \frac{f\mu_{12}k_{12}}{2}\left[\frac{\mu_1}{k_1}Z_1(\mathbf{k}_2) + \frac{\mu_2}{k_2}Z_1(\mathbf{k}_1)\right] & (5.9) \end{aligned}$$

with F_2 and G_2 representing the usual matter density and velocity quadratic kernels and

$$S(\mathbf{k}_1,\mathbf{k}_2) = \left(\hat{k}_1\cdot\hat{k}_2\right)^2 - 1 \tag{5.10}$$

while $\mu_i \equiv \mathbf{k}_i\cdot\hat{n}/k_i$ is the cosine of the angle formed by the wavenumber $\mathbf{k}_i$ with the LOS. We also adopt the short-hand notation for vector sums $\mathbf{k}_{12} = \mathbf{k}_1 + \mathbf{k}_2$ so that

$$\mu_{12} = \frac{\mathbf{k}_{12}\cdot\hat{n}}{k_{12}} = -\frac{\mathbf{k}_3\cdot\hat{n}}{k_3} = -\mu_3\,, \tag{5.11}$$

for a closed triangle with $\mathbf{k}_{123} = 0$. The expansions of eq. (5.7) leads to the tree-level prediction for the bispectrum

$$B_s^{(\rm det)}(\mathbf{k}_1,\mathbf{k}_2,\hat{n}) = 2\,Z_1(\mathbf{k}_1)\,Z_1(\mathbf{k}_2)Z_2(\mathbf{k}_1,\mathbf{k}_2)P_L(k_1)P_L(k_2) + 2\text{ perm.} \tag{5.12}$$

where $P_L(k)$ is the linear matter power spectrum.

The stochastic contribution to δ_s is given instead, following [47] and their notation, by

$$\delta_s^{(\rm stoch)}(\mathbf{x}) = \epsilon(\mathbf{x}) + \epsilon_\delta(\mathbf{x})\,\delta(\mathbf{x}) + \epsilon_\eta(\mathbf{x})\eta(\mathbf{x})\,, \tag{5.13}$$

where ϵ, ϵ_δ and ϵ_η are stochastic fields uncorrelated to the density perturbations. The composite terms are limited to those linear in the matter density δ and in the l.o.s. derivative of the l.o.s velocity component $\eta \equiv \partial_{\hat{n}}(\mathbf{v}\cdot\hat{n})$, as these are responsible for the leading order contributions to the bispectrum. We neglect any higher-derivative operator in the stochastic contribution and we note that the last term should appear only due to selection effects [47]. In the large k limit, we expect to recover the Poisson predictions for the power spectrum and bispectrum of the stochastic fields, that is [143]

$$\langle\epsilon(\mathbf{k}_1)\epsilon(\mathbf{k}_2)\rangle \to \delta_D(\mathbf{k}_{12})\,\frac{1}{\bar{n}}\,, \tag{5.14}$$

$$\langle \epsilon(\mathbf{k}_1)\epsilon(\mathbf{k}_2)\epsilon(\mathbf{k}_3)\rangle \to \delta_D(\mathbf{k}_{123})\,\frac{1}{\bar{n}^2}\,, \tag{5.15}$$

$$\langle \epsilon(\mathbf{k}_1)\epsilon_\delta(\mathbf{k}_2)\rangle \to \delta_D(\mathbf{k}_{123})\,\frac{b_1}{2\bar{n}}\,, \tag{5.16}$$

$$\langle \epsilon(\mathbf{k}_1)\epsilon_\eta(\mathbf{k}_2)\rangle \to \delta_D(\mathbf{k}_{123})\,\frac{1}{2\bar{n}}\,, \tag{5.17}$$

where the first only appears in the halo power spectrum, while the last three all contribute to the halo bispectrum. In principle we can expect independent departures from the Poisson prediction for all three terms, which in the large-scale limit can be described in terms of three constant parameters[2]

The corresponding stochastic contribution to the bispectrum at tree-level will then read

$$B_s^{(\mathrm{stoch})}(\mathbf{k}_1,\mathbf{k}_2,\hat{n}) = \frac{1}{\bar{n}}\left[(1+\alpha_1)\,b_1 + (1+\alpha_3)\,f\,\mu^2\right]\,Z_1(\mathbf{k}_1)\,P_L(k_1) + 2\text{ perm.} + \frac{1+\alpha_2}{\bar{n}^2}\,, \tag{5.19}$$

where α_i are all parameters vanishing in the Poisson limit[3].

In this work we do not consider any modelling of Finger-of-God effects as we expect them to be negligible at large scales and for a halo distribution.

5.1.2 Bispectrum multipoles

We adopt the definition of the redshift-space multipoles of the bispectrum introduced by [148] (and assumed as well by [147] and [61]) where the vector configurations comprising the domain of $B_s(\mathbf{k}_1\mathbf{k}_2,\hat{n})$ are given in terms of the variables k_1, k_2, k_3, $\mu_1 \equiv \cos(\theta_1)$ and ξ, with θ_1 being the angle between $\mathbf{k}_1$ and the LOS while ξ is the azimuthal angle describing a rotation of $\mathbf{k}_2$ around $\mathbf{k}_1$.

B_s is then expanded in spherical harmonics as

$$B_s(k_1,k_2,k_3,\theta,\xi) = \sum_\ell \sum_{m=-\ell}^{\ell} B_{\ell m}(k_1,k_2,k_3)\,Y_\ell^m(\theta,\xi) \tag{5.20}$$

---

[2] In [88] the authors follow [125] in the modelling of the stochastic contribution assuming

$$\delta_s^{(stoch)} = d_1\,\epsilon_P + d_2\,b_1\,\epsilon_P\,\delta + d_1\,\epsilon_P\,\eta\,, \tag{5.18}$$

where the coefficients d_1 and d_2 parameterize the corrections to the Poisson prediction represented by field ϵ_P (for which the limits (5.14) and (5.15) hold as equalities). The Poisson case is recovered for $d_1 = 2\,d_2 = 1$. This implies that $\langle\epsilon\epsilon\rangle = \langle\epsilon\epsilon_\eta\rangle$ and their corrections to Poisson are therefore described by a single degree of freedom. They also relate $\langle\epsilon\epsilon\rangle$ and $\langle\epsilon\epsilon\epsilon\rangle$ but it does not seem justified. Such relation also appears inconsistent with the expansion above and it does not seem to be supported by the halo model description of [70].

[3] The notation for the α_i parameters is chosen in order to be consistent with Paper I and Paper II, where α_2 already appeared as correction to the $1/\bar{n}^2$ term, while α_3 was not present.

with the coefficients of the expansion given by

$$B_{\ell m}(k_1,k_2,k_3) = \int_{-1}^{+1} d\cos\theta \int_0^{2\pi} d\xi B_s(k_1,k_2,k_3,\theta,\xi)\, Y_\ell^m(\theta,\xi)\,. \tag{5.21}$$

We only consider $m = 0$ multipoles as the loss of information coming from excluding the $m \neq 0$ terms is negligible [61]. In this case the spherical harmonics reduce to Legendre polynomials $\mathcal{L}_\ell$ and only depend on $\mu_1 \equiv \cos\theta_1$,

$$Y_\ell^0(\theta,\xi) = \sqrt{\frac{2\ell+1}{4\pi}}\mathcal{L}_\ell(\mu_1) \tag{5.22}$$

and the expansion of eq. 5.20 is replaced by

$$\frac{1}{2\pi}\int d\xi B_s(k_1,k_2,k_3,\theta,\xi) = \sum_\ell B_\ell(k_1,k_2,k_3)\,\mathcal{L}_\ell(\mu_1) \tag{5.23}$$

where

$$\begin{aligned} B_\ell(k_1,k_2,k_3) &= \sqrt{\frac{2\ell+1}{4\pi}}\, B_{\ell 0}(k_1,k_2,k_3) \\ &= (2\ell+1)\frac{1}{2}\int_{-1}^{+1} d\cos\theta \Big[\frac{1}{2\pi}\int_0^{2\pi} d\xi B_s(k_1,k_2,k_3,\theta,\xi)\Big]\,\mathcal{L}_\ell(\cos\theta)\,. \end{aligned} \tag{5.24}$$

5.2 Data

5.2.1 N-body simulations

The analysis is performed on redshift-space, halo bispectrum measurements from the set of 298 Minerva N-body simulations [74] whose real-space counterpart was already studied in Paper I and Paper II. These follow the evolution of 1000^3 dark matter particles in a cubic box of side $L = 1500\,h^{-1}$ Mpc and correspond to a total volume of about $1,000\,h^{-3}\,\mathrm{Gpc}^3$. Each halo catalog is defined by a minimal mass of $M \simeq 1.12 \times 10^{13}\ h^{-1}M_\odot$. We refer the reader to Paper I for a more detailed description of the simulations and of the halo catalog construction.

Paper II provides us with an estimate of the bias parameters characterising the halo population obtained as posteriors from the joint analysis of the halo power spectrum and bispectrum in real space. We will use these here as a reference for our redshift-space analysis, in addition to the value for the linear growth rate expected from the fiducial cosmology.

5.2.2 Bispectrum multipoles estimator

Our estimator of the bispectrum multipoles follow the definition of [148] for the $m = 0$ case and constitutes an implementation of the one described in [147] based on Fast-Fourier

Transforms. In our case, however, we assume a constant line-of-sight $\hat{n}$, corresponding to an exact realisation of the plane-parallel or distant observer approximation. The estimator reduces therefore to the following expression

$$\hat{B}_\ell = (2\ell+1)\frac{k_f^3}{N_B}\sum_{\mathbf{q}_1\in k_1}\sum_{\mathbf{q}_2\in k_2}\sum_{\mathbf{q}_3\in k_3}\delta_K(\mathbf{q}_{123})\,\delta_s(\mathbf{q}_1)\,\delta_s(\mathbf{q}_2)\,\delta_s(\mathbf{q}_3)\,\mathcal{L}_\ell(\hat{q}_1\cdot\hat{n})\,, \tag{5.25}$$

where the sums, accounting for the discrete nature of the Fourier Transform $\delta_s(\mathbf{q})$ of the halo density in a simulation box, are over all wavenumbers $\mathbf{q}_i$ falling into the bin centered at k_i of radial size Δk, that is, such that $k_i - \Delta k/2 \leq |\mathbf{q}_i| < k_i + \Delta k/2$. Also, $\delta_K(\mathbf{q})$ is a Kronecker symbol equal to unity for $\mathbf{q} = \mathbf{0}$ and vanishing otherwise, while the normalisation factor

$$N_B(k_1,k_2,k_3) = \sum_{\mathbf{q}_1\in k_1}\sum_{\mathbf{q}_2\in k_2}\sum_{\mathbf{q}_3\in k_3}\delta_K(\mathbf{q}_{123})\,, \tag{5.26}$$

provides the number of "fundamental triangles" $\{\mathbf{q}_1,\mathbf{q}_2,\mathbf{q}_3\}$ present in the "triangle bin" $\{k_1,k_2,k_3\}$. The grid-interpolation of the halo density $\delta_s(\mathbf{q})$ is obtained by means of a fourth-order mass assignment scheme and adopts the interlacing technique for aliasing reduction [150]. All bispectrum measurements, unless otherwise stated, assume a wavenumber bin size $\Delta k = k_f$, that is corresponding to the fundamental frequency characterising the simulation box, $k_f \equiv 2\pi/L$. This leads to the measurement of 1475 triangular configurations up to $k_{\rm max} = 0.1\,h\,{\rm Mpc}^{-1}$ for each multipole[4].

5.2.3 Measurements

Figure 5.1 shows the mean of the bispectrum multipoles measured from the 298 Minerva N-body simulations for all triangular configurations. In these type of plots, the ordering of the configurations is determined by increasing values of k_1, k_2, k_3 which obey the requirement, $k_1 \geq k_2 \geq k_3$ (see Paper I for a more detailed explanation). Vertical gray lines mark the triangle where the value of k_1 changes, so that all configurations on the left correspond to triangles made up with sides smaller or equal to such value of k_1. All measurements include shot-noise. The bottom half of each panel shows the relative error on the mean, along with the ratio between the expected Poisson shot-noise contribution and the overall signal (black, dashed lines).

We notice that the relative error on the mean for the bispectrum monopole is at the ten-percent level and just slightly smaller at smaller scales. The shot-noise level is comparable to the statistical error at large scales and it is larger at smaller scales, as it happens in real-space for this halo population (see Paper I). The relative error on the quadrupole

[4]We include "open triangle bins", that is those where the bin centers cannot form a closed triangle such as $\{k_1,k_2,k_3\} = \{6,3,2\}k_f$ but that nevertheless contain closed fundamental triplets $\{\mathbf{q}_1,\mathbf{q}_2,\mathbf{q}_3\}$. See section 2.2 of Paper I for a detailed description of the binning definition.

and hexadecapole mean is instead of the order of tens of percent and hundreds of percent, respectively. Because of the first term on the r.h.s. of equation (5.19), all multipoles receive a shot-noise contribution. This is comparable to the error on the mean for the quadrupole and lower by an order of magnitude for the hexadecapole.

5.3 Covariance

5.3.1 Numerical estimate

As for Paper I and Paper II, the covariance properties of our observables are estimated from a much larger set of 10,000 measurements from mock halo catalogs obtained with the PINOCCHIO code [113, 112, 114]. The mocks share the same cosmology, box size and resolution with the Minerva simulations and 298 realisations also adopt the same initial conditions. The mass threshold for the mocks is chosen to reproduce (below percent level) the amplitude of the large-scale halo power spectrum (including shot-noise) of the numerical simulations (see Paper I for details). This quantity, in fact, accounts for the Gaussian contribution to the bispectrum covariance, the leading one for most triangular configurations (see also [15, 25]).

The covariance matrix for each bispectrum multipole and their cross-covariance is defined as

$$C_{\ell_1\ell_2}(t_i, t_j) \equiv \langle \hat{B}_{\ell_1}(t_i)\, \hat{B}_{\ell_2}(t_j) \rangle - \langle \hat{B}_{\ell_1}(t_i) \rangle \langle \hat{B}_{\ell_2}(t_j) \rangle \,, \tag{5.27}$$

where $t_i = \{k_{1i}, k_{2i}, k_{3i}\}$ and $t_j = \{k_{1j}, k_{2j}, k_{3j}\}$ represent two triangle configurations. We will denote as $\hat{C}_{\ell_1\ell_2}(t_i, t_j)$ its estimate from the 10,000 mock catalogs.

The left column of figure 5.2 shows the ratio between the mean of each bispectrum multipole measured in the numerical simulations and the mean of the same quantity measured in the PINOCCHIO mocks, limited to the 298 mocks with matching initial conditions. We find for the monopole the same discrepancy, as large as 7-8% depending on the triangle shape, already encountered in real space (see Paper I). The noise in the measurements for the higher-order multipoles, on the other hand, does not allow to clearly identify systematic differences at the level of 10% or below. The right column of figure 5.2 shows instead the ratio between the variance $\Delta B_\ell(t_i) \equiv C_{\ell\ell}(t_i, t_i)$, estimated again from the numerical simulations and the one estimated from the PINOCCHIO mocks. Again, the PINOCCHIO set is limited here to the 298 realisations with matching seeds. Despite possible systematics on the observables, the variance is recovered by the PINOCCHIO mocks with an error below 10% and no apparent systematic difference for all multipoles. This is expected, given the close match of the power spectra and the fact that the leading contribution to the bispectrum covariance is fully determined by the power spectrum, see eq. (5.29).

5.3.2 Theoretical Gaussian covariance

In addition to the numerical estimate of the covariance we consider as well the analytical prediction in the Gaussian approximation. The Gaussian contribution is present for the variance of each multipole, $\Delta B_\ell \equiv C_{\ell\ell}(t_i, t_i)$, but also for the correlation $C_{\ell_1\ell_2}(t_i, t_i)$ between $\hat{B}_{\ell_1}(t_i)$ and $\hat{B}_{\ell_2}(t_i)$ with $\ell_1 \neq \ell_2$ but measured for the same triangle t_i.

From the definition of the multipoles estimators, eq. (5.25), we can write

$$\begin{aligned} C_{\ell_1\ell_2}(k_1,k_2,k_3) &\equiv \langle \hat{B}_{\ell_1}\hat{B}_{\ell_2}\rangle - \langle \hat{B}_{\ell_1}\rangle\langle \hat{B}_{\ell_2}\rangle \\ &= (2\ell_1+1)(2\ell_2+1)\frac{k_f^6}{N_B^2}\sum_{\mathbf{q}_1\in k_1}\sum_{\mathbf{q}_2\in k_2}\sum_{\mathbf{q}_3\in k_3}\delta_K(\mathbf{q}_{123})\sum_{\mathbf{p}_1\in k_1}\sum_{\mathbf{p}_2\in k_2}\sum_{\mathbf{p}_3\in k_3}\delta_K(\mathbf{p}_{123}) \\ &\times\ \mathcal{L}_{\ell_1}(\mu_{\mathbf{q}_1})\,\mathcal{L}_{\ell_2}(\mu_{\mathbf{p}_1})\left[\langle\delta_{\mathbf{q}_1}\,\delta_{\mathbf{q}_2}\,\delta_{\mathbf{q}_3}\delta_{\mathbf{p}_1}\,\delta_{\mathbf{p}_2}\,\delta_{\mathbf{p}_3}\rangle - \langle\delta_{\mathbf{q}_1}\,\delta_{\mathbf{q}_2}\,\delta_{\mathbf{q}_3}\rangle\langle\delta_{\mathbf{p}_1}\,\delta_{\mathbf{p}_2}\,\delta_{\mathbf{p}_3}\rangle\right]. \end{aligned} \tag{5.28}$$

In the Gaussian approximation, from the expectation values on the r.h.s. of the equation above, we retain only the contributions depending on the field power spectrum. Assuming (without loss of generality) that $k_1 \geq k_2 \geq k_3$, these are given by

$$\begin{aligned} C^G_{\ell_1\ell_2}(k_1,k_2,k_3) &= \frac{(2\ell_1+1)(2\ell_2+1)}{N_B^2\,k_f^3}\sum_{\mathbf{q}_1\in k_1}\sum_{\mathbf{q}_2\in k_2}\sum_{\mathbf{q}_3\in k_3}\delta_K(\mathbf{q}_{123})\,P_{tot}(\mathbf{q}_1)\,P_{tot}(\mathbf{q}_2)\,P_{tot}(\mathbf{q}_3) \\ &\times\left[(1+\delta^K_{k_2,k_3})\,\mathcal{L}_{\ell_1}(\mu_{\mathbf{q}_1})\mathcal{L}_{\ell_2}(-\mu_{\mathbf{q}_1}) + (\delta^K_{k_1,k_2}+\delta^K_{k_2,k_3})\,\mathcal{L}_{\ell_1}(\mu_{\mathbf{q}_1})\mathcal{L}_{\ell_2}(-\mu_{\mathbf{q}_2}) + \right. \\ &\left. +\,2\,\delta^K_{k_1,k_3}\,\mathcal{L}_{\ell_1}(\mu_{\mathbf{q}_1})\mathcal{L}_{\ell_2}(-\mu_{\mathbf{q}_3})\right], \end{aligned} \tag{5.29}$$

where $P_{tot}(\mathbf{q}_1) = P(\mathbf{q}_1) + P_{SN}$ is the anisotropic halo power spectrum including a shot-noise contribution while $\delta^K_{k_i,k_j}$ is the Kronecker symbol equal to one for $k_i = k_j$, and vanishing otherwise. Notice that the terms in the square brackets correspond, in the case $\ell_1 = \ell_2 = 0$, to the usual factor equal to 6, 2 and 1 respectively for equilateral, isosceles and scalene triangles.

Similarly to the power spectrum variance case, see e.g. [74], we can expand the anisotropic power spectra in multipoles to obtain

$$\begin{aligned} C^G_{\ell_1\ell_2} &= \frac{(2\ell_1+1)(2\ell_2+1)}{N_B^2\,k_f^3}\sum_{\ell_3,\ell_4,\ell_5}\sum_{\mathbf{q}_1\in k_1}\sum_{\mathbf{q}_2\in k_2}\sum_{\mathbf{q}_3\in k_3}\delta_K(\mathbf{q}_{123})\,P_{tot,\,\ell_3}(q_1)\,P_{tot,\,\ell_4}(q_2)\,P_{tot,\,\ell_5}(q_3) \\ &\times\left[(1+\delta^K_{k_2,k_3})\,\mathcal{L}_{\ell_1}(\mu_{\mathbf{q}_1})\mathcal{L}_{\ell_2}(-\mu_{\mathbf{q}_1}) + (\delta^K_{k_1,k_2}+\delta^K_{k_2,k_3})\,\mathcal{L}_{\ell_1}(\mu_{\mathbf{q}_1})\mathcal{L}_{\ell_2}(-\mu_{\mathbf{q}_2}) + \right. \\ &\left. +\,2\,\delta^K_{k_1,k_3}\,\mathcal{L}_{\ell_1}(\mu_{\mathbf{q}_1})\mathcal{L}_{\ell_2}(-\mu_{\mathbf{q}_3})\right]\mathcal{L}_{\ell_3}(\mu_1)\mathcal{L}_{\ell_4}(\mu_2)\mathcal{L}_{\ell_5}(\mu_3)\,. \end{aligned} \tag{5.30}$$

This is the expression we adopt in our evaluation of the Gaussian variance, with the sums over the k-shells performed exactly over the discrete wavenumbers $\mathbf{q}$ defining the Fourier-space

density grid[5].

The comparison between the numerical estimate and analytic prediction for these quantities is shown in figure 5.3. One can see how the Gaussian prediction for C_{00}, C_{22} and C_{44} is able to describe the measured ones at the level of 5%, with a slight deficit noticeable in the monopole and quadrupole case for squeezed triangles, due to the missing non-Gaussian contribution [15, 25]. The agreement in the case of the cross-covariance $C_{\ell_1\ell_2}(t_i, t_i)$ is also rather good, with the theory underestimating the measurements by an overall 10%. In these cases, the ratio can take large values when the denominator is close to zero, as it is the case particularly for $C_{0,4}$.

Finally, figure 5.4 shows a subset of the correlation matrix, defined as

$$r_{\ell_1\ell_2}(t_i, t_j) = \frac{C_{\ell_1\ell_2}(t_i, t_j)}{\sqrt{C_{\ell_1\ell_1}(t_i, t_i)\, C_{\ell_2\ell_2}(t_j, t_j)}}\,. \tag{5.36}$$

Each data-set $\hat{B}_\ell(t_i)$ is restricted, for illustration purposes, to its first 32 triangular configurations t_i, denoted in the figure in terms of the three sides in units of the fundamental

[5]It is possible to simplify further this expression in the thin-shell approximation so that

$$C^G_{\ell_1\ell_2} \simeq \frac{(2\ell_1+1)(2\ell_2+1)}{N_B\, k_f^3} \sum_{\ell_3,\ell_4,\ell_5} P_{tot,\,\ell_3}(k_1)\, P_{tot,\,\ell_4}(k_2)\, P_{tot,\,\ell_5}(k_3) R_{\ell_1,\ell_2;\ell_3\ell_4,\ell_5}(k_1,k_2,k_3)\,. \tag{5.31}$$

where we defined

$$\begin{aligned} R_{\ell_1,\ell_2;\ell_3\ell_4,\ell_5}(k_1,k_2,k_3) \equiv \frac{1}{N_B} \sum_{\mathbf{q}_1\in k_1} \sum_{\mathbf{q}_2\in k_2} \sum_{\mathbf{q}_3\in k_3} \delta_K(\mathbf{q}_{123}) \\ \times \Big[(1+\delta^K_{k_2,k_3})\, \mathcal{L}_{\ell_1}(\mu_{\mathbf{q}_1})\mathcal{L}_{\ell_2}(-\mu_{\mathbf{q}_1}) + (\delta^K_{k_1,k_2}+\delta^K_{k_2,k_3})\, \mathcal{L}_{\ell_1}(\mu_{\mathbf{q}_1})\mathcal{L}_{\ell_2}(-\mu_{\mathbf{q}_2}) + \\ + 2\,\delta^K_{k_1,k_3}\, \mathcal{L}_{\ell_1}(\mu_{\mathbf{q}_1})\mathcal{L}_{\ell_2}(-\mu_{\mathbf{q}_3})\Big] \mathcal{L}_{\ell_3}(\mu_1)\mathcal{L}_{\ell_4}(\mu_2)\mathcal{L}_{\ell_5}(\mu_3)\,. \end{aligned} \tag{5.32}$$

In the continuum limit, we can replace the sums over the shells with integrals and reduced them to a simple average over the orientation of the triangle $\{\mathbf{q}_1, \mathbf{q}_2, \mathbf{q}_3\}$, that is

$$\frac{1}{N_B} \sum_{\mathbf{q}_1\in k_1} \sum_{\mathbf{q}_2\in k_2} \sum_{\mathbf{q}_3\in k_3} \delta_K(\mathbf{q}_{123}) \simeq \frac{1}{N_B\, k_f^6} \prod_{i=1}^{3} \int_{k_i} d^3q_i\, \delta_D(\mathbf{q}_{123}) = \frac{1}{4\pi} \int_{-1}^{1} d\mu_1 \int d\xi\,, \tag{5.33}$$

with an integrand that is now only a function of powers of μ_1, μ_2 and μ_3. Then, assumming only even values for ℓ_3, ℓ_4 and ℓ_5 (and clearly for ℓ_1 and ℓ_2), we can use the expansion for the Legendre polynomials

$$\mathcal{L}(\mu) = \frac{1}{2^\ell} \sum_{n=1}^{\ell/2} \frac{(-1)^n (2\ell-2n)!}{n!(\ell-n)!(\ell-2n)!} \mu^{\ell-2n} \equiv \sum_{n=1}^{\ell/2} C_{\ell,n}\, \mu^{\ell-2n} \tag{5.34}$$

to get an expression that can be automatically evaluated with a software allowing for symbolic manipulation,

$$\begin{aligned} R_{\ell_1,\ell_2;\ell_3\ell_4,\ell_5}(k_1,k_2,k_3) \simeq \prod_{i=1}^{5} \sum_{n_i=1}^{\ell_i/2} C_{\ell_i,n_i} \Big[(1+\delta^K_{k_2,k_3})\mathcal{I}_{\ell_1+\ell_2+\ell_3-2(n_1+n_2+n_3),\,\ell_4-2n_4,\,\ell_5-2n_5} \\ + (\delta^K_{k_1,k_2}+\delta^K_{k_2,k_3})\mathcal{I}_{\ell_1+\ell_3-2(n_1+n_3),\,\ell_2+\ell_4-2(n_2+n_4),\,\ell_5-2n_5} \\ + 2\,\delta^K_{k_1,k_3}\,\mathcal{I}_{\ell_1+\ell_3-2(n_1+n_3),\,\ell_4-2n_4,\,\ell_2+\ell_5-2(n_2+n_5)}\Big]\,, \end{aligned} \tag{5.35}$$

, where the integrals $\mathcal{I}_{\alpha,\beta,\gamma}$ are defined in Appendix A.2.

frequency, that is $\{k_1, k_2, k_3\}/k_f$. It follows that while the block-diagonal matrices show the correlation coefficients $r_{\ell\ell}(t_i, t_j)$ for each multipoles, the off-diagonal matrices depict their relative cross-covariance $r_{\ell_1\ell_2}(t_i, t_j)$. In addition, the top-right half is estimated from the full set of 10,000 PINOCCHIO mocks, while the bottom-left half is the theoretical prediction in the Gaussian approximation, vanishing for all elements with $t_i \neq t_j$. The bottom panels compare in more detail the predicted and measured coefficients $r_{\ell_1\ell_2}(t_i, t_i)$ with $\ell_1 \neq \ell_2$ as a function of the selected triangles t_i. On these quantities the agreement between theory and numerical estimates is truly remarkable and extends up to $k_{\rm max} \sim 0.1\,h\,{\rm Mpc}^{-1}$, that is over the full range of scales that we will consider in the analysis described in the following sections.

Regarding the structure of the correlation coefficient, it is clear that only the elements corresponding to the expected Gaussian contributions appear to be relevant at these large scales. These, however, are not limited to the diagonal for the full data vector $D = \{B_0, B_2, B_4\}$, but obviously include all elements corresponding to the correlation between different multipoles sharing the same triangles.

5.4 Likelihood analysis

5.4.1 Likelihood function

Following Paper I and Paper II, we fit all measurements together assuming their independence. This means that our total log-likelihood function corresponds to the sum of the log-likelihood for each individual realisation,

$$\ln \mathcal{L}_{\rm tot} = \sum_{\alpha=1}^{N_R} \ln \mathcal{L}_\alpha \,, \tag{5.37}$$

where N_R is the total number of realisations considered.

We work under the assumption of Gaussianity for the individual likelihood $\mathcal{L}_\alpha$. However, we adopt the proposal of [151] to account for possible uncertainties in the determination of the precision matrix due to a limited number of mocks. The log-likelihood for a single realisation is then, modulo an additive, normalization constant,

$$\ln \mathcal{L}_\alpha = -\frac{N_M}{2} \ln \left[1 + \frac{\chi^2_\alpha}{N_M - 1}\right], \tag{5.38}$$

where N_M is the number of mock catalogs used for the numerical estimation of the covariance matrix (we refer the reader to Paper I for further details). In this expression χ^2_α represents the chi-square for the individual realisation, given by

$$\chi^2_\alpha = \sum_{i,j=1}^{N_D} \left[\hat{D}^{(\alpha)}_i - D^{(theory)}_i\right] C^{-1}_{ij} \left[\hat{D}^{(\alpha)}_j - D^{(theory)}_j\right] , \tag{5.39}$$

where, in the most general case, $\hat{D}^{(\alpha)} \equiv \left\{\hat{B}_0, \hat{B}_2, \hat{B}_4\right\}$ is the data vector, of size N_D, encompassing the three bispectrum multipoles while $D^{(theory)}$ and C_{ij} are, respectively, the corresponding theoretical model and covariance matrix.

We should notice that given the large number of 10,000 PINOCCHIO realisations, even for the largest data-set corresponding to the joint analysis of the three bispectrum multipoles up to $k_{\rm max,B} = 0.1\,h\,{\rm Mpc}^{-1}$, with a total of $1,475 \times 3 \simeq 4,425$ data-points, the difference w.r.t. the Gaussian case is in fact negligible. The alternative approach of re-scaling the inverse covariance, as suggested in [7, 83], gives rise to error bars up to 10% larger, although we have checked that these do not lead to any appreciable differences in the recovered parameter posteriors that we discuss below.

5.4.2 Model evaluation

Our main goal is assessing the validity and reach of the tree-level bispectrum model, eqs. (5.12) and (5.19) leaving the exploration of their potential to constrain cosmological parameters to a future work. For this reason, in our likelihood analyses we assume galaxy bias, shot-noise and the growth rate f as the only free parameters. The bispectrum multipoles defined in eq. (5.21) can be written as a linear combination of several contributions where the dependence on these parameters can be factorised, leading to a quick exploration of the likelihood function since each term only needs to be computed once for the fiducial cosmology.

This allows as well for an exact binning of the theoretical model, taking advantage of the discrete Fourier-space grid characterising numerical simulations in boxes with periodic boundary conditions. In this case we can sum $B_s(\mathbf{q}_1, \mathbf{q}_2, \mathbf{q}_3, \hat{n})$ over all discrete modes $\mathbf{q}_i$ forming a close triangle $\mathbf{q}_{123} = 0$ and belonging to the bin $\{k_1, k_2, k_3\}$. This leads to

$$B_\ell^{(\rm binned)}(k_1, k_2, k_3) = \frac{2\ell+1}{N_B} \sum_{\mathbf{q}_1 \in k_1} \sum_{\mathbf{q}_2 \in k_2} \sum_{\mathbf{q}_3 \in k_3} \delta_K(\mathbf{q}_{123}) B_s(\mathbf{q}_1, \mathbf{q}_2, \mathbf{q}_3, \hat{n}) \mathcal{L}_\ell(\hat{q}_1 \cdot \hat{n}), \quad (5.40)$$

where the sums account for the angle-average defining the bispectrum multipoles.

This approach requires the evaluation of the bispectrum model over a very large number of triangular configurations, making it unfeasible in a likelihood analysis where cosmological parameters are explored. An approximate solution would be to evaluate the model B_ℓ on a single triangle defined by effective values of the wavenumbers. This approach, that takes advantage of the analytical evaluation of the angle integrals in (5.24) described in Appendix A.2, is presented in Appendix 5.5.6 along with a quantification of the systematic errors resulting in the parameter determination.

5.4.3 Goodness of fit and model selection

We will assess the goodness of the fits that we will perform in terms of the posterior predictive p-value (ppp) and the posterior-averaged reduced chi-square $\langle \chi^2_\nu \rangle_{\rm post}$. The ppp is defined in

Parameter	Prior (uniform)
b_1	$[0.9, 3.5]$
b_2	$[-4, 4]$
$b_{\mathcal{G}_2}$	$[-4, 4]$
α_1	$[-1, 2]$
α_2	$[-1, 2]$
α_3	$[-1, 2]$
f	$[0.1, 1]$

Table 5.1: Uniform prior intervals of the model parameters.

the interval 0 to 1 with values of ppp ≥ 0.95 signaling a failure of the model. The $\langle\chi^2_\nu\rangle_{\rm post}$ is compared to the 95 percent (upper) confidence limit associated to a number of degrees of freedom equal to the total number of data points fitted: when $\langle\chi^2_\nu\rangle_{\rm post}$ is greater than this value, the model fails to describe the data. For the comparison between different models and assumptions on the bias parameters, we use the Deviance Information Criterion (DIC) computed from the MCMC simulations. For details on the choice of these diagnostics, we redirect the reader to Paper I.

5.5 Results

5.5.1 Maximal model

We start with a test of the full model with all seven bias and shot-noise parameters free. We compare the fit to the bispectrum monopole to the joint analysis of monopole and higher-order multipoles, assuming the full volume of the 298 Minerva simulations. The first goal is to identify the set of parameters that can effectively be determined by our data-set, and the relative importance of the different multipoles in their constraints. We assume uniform priors on all parameters, with bounds specified in table 5.1.

The main results are shown in figure 5.5. The left panels show the marginalised, 1-σ posteriors for the model parameters as a function of the maximum wavenumber included in the triangle selection. Two-dimensional marginalised contours are shown in the bottom-right panel for the $k_{\rm max} = 0.06\,h\,{\rm Mpc}^{-1}$ case (indicated as the vertical, dotted line in the other two sub-panels). Finally, the top-right panel shows the posterior-averaged, reduced chi-square, $\langle\chi^2_\nu\rangle$ and the posterior predictive p-value.

The tree-level model described in section 5.1.1 provides a good fit to the data up to a $k_{\rm max} \simeq 0.08\,h\,{\rm Mpc}^{-1}$ for the monopole, while the reach is restricted to 0.06 and $0.045\,h\,{\rm Mpc}^{-1}$,

respectively, when B_2 and B_4 are also considered.

For $k_{\rm max} = 0.06\,h\,{\rm Mpc}^{-1}$, the combination $B_0 + B_2$ properly recovers the best-fit values of the bias parameters obtained from the joint analysis of the real-space power spectrum and bispectrum, given by the horizontal solid line in the marginalised, 1-σ posteriors, along with the fiducial value of the linear growth rate f, which are shown by the gray, dashed lines in the bottom-right panel.

The addition of the quadrupole B_2 greatly reduces the large degeneracy between the linear bias b_1 and the growth rate f, as well as with the quadratic bias parameters, characterising the monopole-only constraints. This qualitatively confirms the expectation that the bispectrum monopole does not fully capture the information potentially present in the anisotropic, redshift-space bispectrum [170, 75]. On the other hand, including as well the hexadecapole leads to no significant improvement for any parameter and we will drop it from all results that will follow.

5.5.2 Shot-noise

It is clear that, despite the large total simulation volume, the data set is not able to provide meaningful constraints on all shot-noise parameters. This was true as well, for the same halo catalogs, in real space, even including power spectrum information (see Paper II).

In this section we compare different options to reduce the shot-noise parameters to a single one. In addition to the maximal model, characterised by seven parameters in total, we will consider the following models

- $\alpha_2 = 0$ (6 parameters); this is justified by the posteriors obtained for the maximal model, which show that this parameter is simply not constrained by the data and can therefore be set to zero without affecting the overall fit;
- $\alpha_3 = -1$ (6 parameters); this corresponds to setting $\epsilon_\eta = 0$, as expected under the assumption of no velocity bias and no selection effects.

Another option is to set $\alpha_1 = \alpha_3$. This is implicit in the Poisson prediction for the shot-noise of a generic distribution in redshift space, where *both* corrections vanish. This prediction is also the outcome of a count-in-cell estimate of the shot-noise contributions to the bispectrum [122, 105] and corresponds to the standard shot-noise correction often implemented in bispectrum estimators [147, 161] and implicitly assumed in some data analysis [64, 67]. We will therefore consider the two, additional 5-parameters models (both assuming $\alpha_2 = 0$):

- $\alpha_3 = \alpha_1$ *and* $\alpha_2 = 0$ (5 parameters);
- $\alpha_3 = -1$ *and* $\alpha_2 = 0$ (5 parameters).

The top left panel in figure 5.6 shows a general comparison between all the models described in the bullet points above in terms of the difference in their DIC w.r.t. the maximal

model with seven parameters, as a function of the maximum wavenumber $k_{\rm max}$, again for the monopole and quadrupole analysis. Differences larger than 5 are usually considered relevant. The top right panel of the same figure shows instead the effective number of parameters we are able to constrain from the data also as a function of $k_{\rm max}$. For a value of $k_{\rm max} < 0.05\,h\,{\rm Mpc}^{-1}$, we do not have enough information to determine even the least number of parameters and the ΔDIC simply favours the simplest models. These are still favoured up to $k_{\rm max} \sim 0.08\,h\,{\rm Mpc}^{-1}$, where the additional degrees of freedom of more complex models are probably accounting for missing nonlinear corrections. The test does not clearly indicate a preference for the 5-parameters model with $\alpha_3 = \alpha_1$ model over the one one with $\alpha_3 = -1$, except for $k_{\rm max} > 0.08\,h\,{\rm Mpc}^{-1}$, where we know that none of the models provides a good overall fit anymore. A comparison of the 2D marginalised posteriors from the monopole and quadrupole analysis at $k_{\rm max} = 0.06\,h\,{\rm Mpc}^{-1}$ is shown for the two 5-parameters models and the maximal one in the bottom panel of figure 5.6. Both models improve the constraints on the growth rate, with minimal differences on the posteriors for the other parameters. The $\alpha_3 = -1$ case provides a slightly better agreement with the fiducial value of f and the real-space estimate of b_1.

We will assume the $\alpha_3 = -1$ (i.e. $\epsilon_\eta = 0$) and $\alpha_2 = 0$ case as our default model in all following tests. This implies the expression for the shot-noise contribution

$$B_s^{(\rm stoch)}(\mathbf{k}_1, \mathbf{k}_2, \hat{n}) = \frac{1+\alpha_1}{\bar{n}}\, b_1\, Z_1(\mathbf{k}_1)\, P_L(k_1) + 2 \text{ perm.} + \frac{1}{\bar{n}^2}\,, \tag{5.41}$$

only depending on the parameter α_1. We assume that this model provides an accurate description of the stochastic contribution to the bispectrum, consistent with the large-scale expectation, in a relatively restricted range ($k \lesssim 0.08\,h\,{\rm Mpc}^{-1}$) where the Poisson limit ($\alpha_1 = \alpha_3 = 0$) does not apply.

5.5.3 Bias relations

The parameter space can be further reduced by introducing relations among the bias parameters. In Paper I and Paper II we considered a few of such relations, either theoretically motivated or from results of numerical simulations [154, 98, 97, 49, 51]. Of those, we select the two that provide the best improvement to the fit of the power spectrum and bispectrum in real space and test them again here in redshift space. The first is the fitting function for $b_2(b_1, b_{\mathcal{G}_2})$ obtained in [98] from separate universe simulations. The second is the fit to the excursion set prediction for the tidal bias parameter $b_{\mathcal{G}_2}(b_1)$ proposed in [49, 51]. For convenience we reproduce these two relations here:

$$b_2(b_1, b_{\mathcal{G}_2}) = 0.412 - 2.142\,b_1 + 0.929\,b_1^2 + 0.008\,b_1^3 + \frac{4}{3} b_{\mathcal{G}_2}\,, \tag{5.42}$$

$$b_{\mathcal{G}_2}(b_1) = 0.524 - 0.547\,b_1 + 0.046\,b_1^2\,. \tag{5.43}$$

In figure 5.7 we compare three cases with our reference 5-parameter model: applying each of the bias relations $b_2(b_1, b_{\mathcal{G}_2})$ and $b_{\mathcal{G}_2}(b_1)$ individually, as well as the two of them combined. In the top-left panel we show their difference in the DIC with respect to the reference model, as a function of the largest wavenumber $k_{\rm max}$ for the analysis of the monopole plus quadrupole. The top-right panel shows instead the effective numbers of parameters, again as a function of $k_{\rm max}$ and for $B_0 + B_2$. The DIC shows a marginal preference for the $b_{\mathcal{G}_2}(b_1)$ relation, for values of $k_{\rm max}$ close to $0.06\,h\,{\rm Mpc}^{-1}$, whereas the combination of the two relations quickly becomes disfavoured beyond $k_{\rm max} = 0.05\,h\,{\rm Mpc}^{-1}$.

In the bottom panel of figure 5.7 we show the contour plots from the analysis at $k_{\rm max} = 0.06\,h\,{\rm Mpc}^{-1}$, showing the 1- and 2-$\sigma$ 2D constraints on the bias and shot-noise parameters for the three models. All three cases lead to a reduction in the marginalised posterior constraints, however, we notice how the application of the tidal bias relation leads to constraints on b_1 and f that are systematically offset from the fiducial values, while the other two cases involving the $b_2(b_1)$ relation significantly reduce any potential tension. We caution that this outcome might in fact be fortuitous since the $b_2(b_1)$ relation crosses the b_1 - b_2 contour of the reference model close to the fiducial value of b_1 recovered from the real-space analysis of Paper II. We should stress, in any event, that these systematic differences are only evident due to the very large cumulative simulation volume: we leave for future work an assessment for a more realistic volume (Moretti et al., in preparation).

5.5.4 Scale cuts

In section 5.5.1 we have seen that for higher-order multipoles, the range of validity of the tree-level model is more limited than for the monopole. This suggests that it could be convenient to consider different values of $k_{\rm max}$ for the different multipoles.

We illustrate this point in figure 5.8 where we compare the contour plots for the $B_0 + B_2$ analysis under the following assumptions:

- $k_{\rm max}^{B_0} = k_{\rm max}^{B_2} = 0.06\,h\,{\rm Mpc}^{-1}$ (blue);
- $k_{\rm max}^{B_0} = 0.08\,h\,{\rm Mpc}^{-1}$ and $k_{\rm max}^{B_2} = 0.06\,h\,{\rm Mpc}^{-1}$ (yellow);
- $k_{\rm max}^{B_0} = k_{\rm max}^{B_2} = 0.08\,h\,{\rm Mpc}^{-1}$ (magenta).

In all cases we adopt the reference, 5-parameter model.

We find that extending $k_{\rm max}^{B_0}$ to $0.08\,h\,{\rm Mpc}^{-1}$ can significantly reduce the error, in particular on the bias parameters. However, for the $k_{\rm max}^{B_0} = k_{\rm max}^{B_2} = 0.08\,h\,{\rm Mpc}^{-1}$ case, where the χ^2 for the fit is already above the 95% C.L., we notice that the f-b_1 contour already shows a discrepancy with the expected values at more than 2-σ. We will adopt the scale cuts defined by $k_{\rm max}^{B_0} = 0.08\,h\,{\rm Mpc}^{-1}$ and $k_{\rm max}^{B_2} = 0.06\,h\,{\rm Mpc}^{-1}$ as our reference choice for most of the tests in the following sections.

5.5.5 Covariance approximations

In section 5.3 we directly compared the Gaussian prediction for the bispectrum covariance with the numerical estimate from the PINOCCHIO mocks, finding a remarkable agreement both in the variance $C_{\ell_1\ell_2}(t_i,t_i)$ as in the correlation coefficients $r_{\ell_1\ell_2}(t_i,t_i)$.

Here we check if any residual difference could affect the parameters determination. The comparison is shown in figure 5.9 in terms of the contour plots for the reference analysis of B_0 and B_2 assuming, respectively, $k_{\rm max}^{B_0} = 0.08\,h\,{\rm Mpc}^{-1}$ and $k_{\rm max}^{B_2} = 0.06\,h\,{\rm Mpc}^{-1}$. The full numerical covariance, $\hat{C}_{\ell_1,\ell_2}(t_i,t_j)$ (blue contours) is compared to the numerical variance $\hat{C}_{\ell_1,\ell_2}(t_i,t_i)$ (orange) and to the Gaussian prediction (magenta). In the last two cases, all elements with $t_i \neq t_j$ are set to zero. We notice that the inclusion of such elements is responsible for constraints only slightly larger, while the Gaussian prediction reproduces the results from the numerical variance case almost exactly, with no appreciable differences in the 1D or 2D marginalised posteriors. This is perhaps not too surprising given that the analysis is restricted to relatively large-scales.

5.5.6 Effective binning of the theoretical model

All of our results assumed an evaluation of the theory predictions implementing the exact scheme of eq. (5.40). Since this approach can be numerically quite demanding, particularly in likelihood evaluations extended to several cosmological parameters, it is worth exploring the systematic errors induced on the parameter posteriors by the more efficient choice of a single bispectrum evaluation at the effective wavenumbers, after the analytical integration over the angles described in Appendix A.2.

In this case, the theoretical prediction is given by

$$B_\ell^{\rm eff}(k_1,k_2,k_3) \equiv B_\ell(k_{\rm eff,l}, k_{\rm eff,m}, k_{\rm eff,s}), \tag{5.44}$$

where the computation of the multiples assumes the analytical integration over the angles described in Appendix A.2 and where the definition of the effective triplet, in general not unique, is based on "sorted" $\{q_1,q_2,q_3\}$ triplets as (see Paper I)[6].

$$\begin{aligned}
k_{\rm eff,l}(k_1,k_2,k_3) &= \frac{1}{N_B}\sum_{\mathbf{q}_1\in k_1}\sum_{\mathbf{q}_2\in k_2}\sum_{\mathbf{q}_3\in k_3}\delta_K(\mathbf{q}_{123})\max(q_1,q_2,q_3)\,,\\
k_{\rm eff,m}(k_1,k_2,k_3) &= \frac{1}{N_B}\sum_{\mathbf{q}_1\in k_1}\sum_{\mathbf{q}_2\in k_2}\sum_{\mathbf{q}_3\in k_3}\delta_K(\mathbf{q}_{123})\mathrm{med}(q_1,q_2,q_3)\,,\\
k_{\rm eff,s}(k_1,k_2,k_3) &= \frac{1}{N_B}\sum_{\mathbf{q}_1\in k_1}\sum_{\mathbf{q}_2\in k_2}\sum_{\mathbf{q}_3\in k_3}\delta_K(\mathbf{q}_{123})\min(q_1,q_2,q_3)\,.
\end{aligned} \tag{5.45}$$

[6] See also [51] and [88] for alternative proposals.

For the choice of the bin size $\Delta k = k_f$ adopted in our result, the difference between the two approaches, estimated in terms of the posteriors on the bias and shot-noise parameters, is completely negligible. For a larger size of the bin Δk, useful to reduce the overall size of the data vector, however, we can find some systematic effect on parameters determination. This is shown in fig. 5.10, where we plot the 2D marginalised posteriors for different choices of the binning scheme and evaluations of the theoretical prediction. In particular, there is a significant shift in the 1D marginalised posterior for f (shown in orange in fig. 5.10) for the case $\Delta k = 3\ k_f$ when we compute the theoretical prediction at the effective wavenumbers. We notice as well how the larger bin size leads to larger contours, even in the exact binning case, due to the reduced shape-dependence of the bispectrum measurements.

5.6 Conclusions

This work presents a test of the tree-level prediction in Perturbation Theory for the halo bispectrum in redshift space with particular attention to its anisotropic signal as described by higher-order multipoles such as the quadrupole and hexadecapole. It extends previous results in real space (Paper I and Paper II), taking advantage of a very large set of 298 N-body simulations corresponding to a cumulative volume of about $1{,}000\,h^{-3}\,\mathrm{Gpc}^3$ and an even larger set of PINOCCHIO mocks. The latter provides a robust estimate of the covariance properties for the full data vector given by the three bispectrum multipoles. We explore different assumptions on the observables and related covariance models and assess them in terms of constraints on bias parameters and the fiducial linear growth rate.

We summarise below our main findings.

- The PINOCCHIO mocks provide a very good description of the variance estimated from full numerical simulations with a residual scatter below the 10% level and no apparent shape-dependence (Fig. 5.2), for all bispectrum multipoles, extending previous assessments in real-space (Paper I, [35]).
- The comparison of the likelihood analysis based on the monopole alone with the joint analyses of $B_0 + B_2$ and $B_0 + B_2 + B_4$ (Fig. 5.5), using the full covariance from the mocks, indicates that the addition of the quadrupole alone greatly improves the determination of bias parameters and, perhaps not surprisingly, allows to properly constrain the growth rate f; the further addition of the hexadecapole, instead, leads to no appreaciable improvement.
- For our full simulation volume, the tree-level model provides a good fit for the bispectrum monopole up to $k_{\mathrm{max}} = 0.08\,h\,\mathrm{Mpc}^{-1}$ while the inclusion of the quadrupole and of the hexadecapole reduce significantly this range to 0.06 and $0.045\,h\,\mathrm{Mpc}^{-1}$, respectively. Indeed, an optimal configuration for the joint $B_0 + B_2$ analysis should assume distinct values for k_{max}. We tested that better constraints on the model parameters

are obtained assuming $k_{\rm max}^{B_0} = 0.08\,h\,{\rm Mpc}^{-1}$ and $k_{\rm max}^{B_2} = 0.06\,h\,{\rm Mpc}^{-1}$ with respect to the case where a single, lower value of $k_{\rm max}^{B_0} = k_{\rm max}^{B_2} = 0.06\,h\,{\rm Mpc}^{-1}$ is adopted to keep within the model validity range (Fig. 5.8).

- In general our data, despite the large volume, cannot fully determine all constant shot-noise parameters describing different departures from the Poisson expectation. It appears, however, that the stochastic velocity contribution $\epsilon_\eta \eta$ to the halo density, that one can expect when selection effects are present [46], is indeed disfavoured in our ideal set-up, at least at the large scales we are exploring (Fig. 5.6).

- Both the fitting function for the quadratic local bias parameter $b_2(b_1, b_{\mathcal{G}_2})$ of [98] as the relation for the tidal bias parameter $b_{\mathcal{G}_2}(b_1)$ proposed in [49, 51] (and their combination) appear to significantly improve the posteriors on b_1 and f (Fig. 5.7); the first, however, appears to introduce some bias in the determination of b_1, although relevant only because of the large cumulative volume of our simulations set.

- For our ideal measurements in a simulation box with periodic boundary conditions, the Gaussian model for the bispectrum multipoles covariance provides a very good approximation to the numerical estimate. A small underestimate is noticeable (and expected [15, 25]) for the squeezed configurations of the bispectrum monopole (Fig. 5.3). On the other hand a quite remarkable agreement is obtained in the comparison with the cross-correlation coefficients (Fig. 5.4). In terms of the posteriors on bias parameters and f we find no noticeable difference between the Gaussian theory variance and the numerical variance, while a very small difference is present when compared to the full numerical covariance (Fig. 5.9).

- All our main results assumed an exact binning of the theoretical prediction. When a single evaluation on a triplet of effective wavenumbers is assumed we notice a negligible difference only if the bin size is small (equal to the box fundamental frequency). For a larger bin size, in addition to somehow larger posteriors, this approximation can lead to significant systematic differences, particularly on the growth rate f.

As mentioned in the introduction, not many works explored the modelling and the potential information of the anisotropic bispectrum. Our results qualitatively confirm earlier Fisher-matrix forecasts [158, 61, 170, 3] in remarking on the importance of going beyond the analysis of the bispectrum monopole. The same can be said for [77] and [76], both based instead on a full likelihood analysis and therefore closer, in principle, to our work. For these last two references, however, many differences in methodology do not allow a rigorous, quantitative comparison with our results, in addition to the fact, of course, that we do not include power spectrum measurements in our data-vector. We will present a joint analysis of the Minerva-set power spectrum and bispectrum in redshift space elsewhere (Moretti et al. in preparation). For the time being we limit ourselves to observe that the inclusion of full anisotropic bispectrum information will likely be an important step toward a complete

exploitation of cosmological information in spectroscopic galaxy surveys.

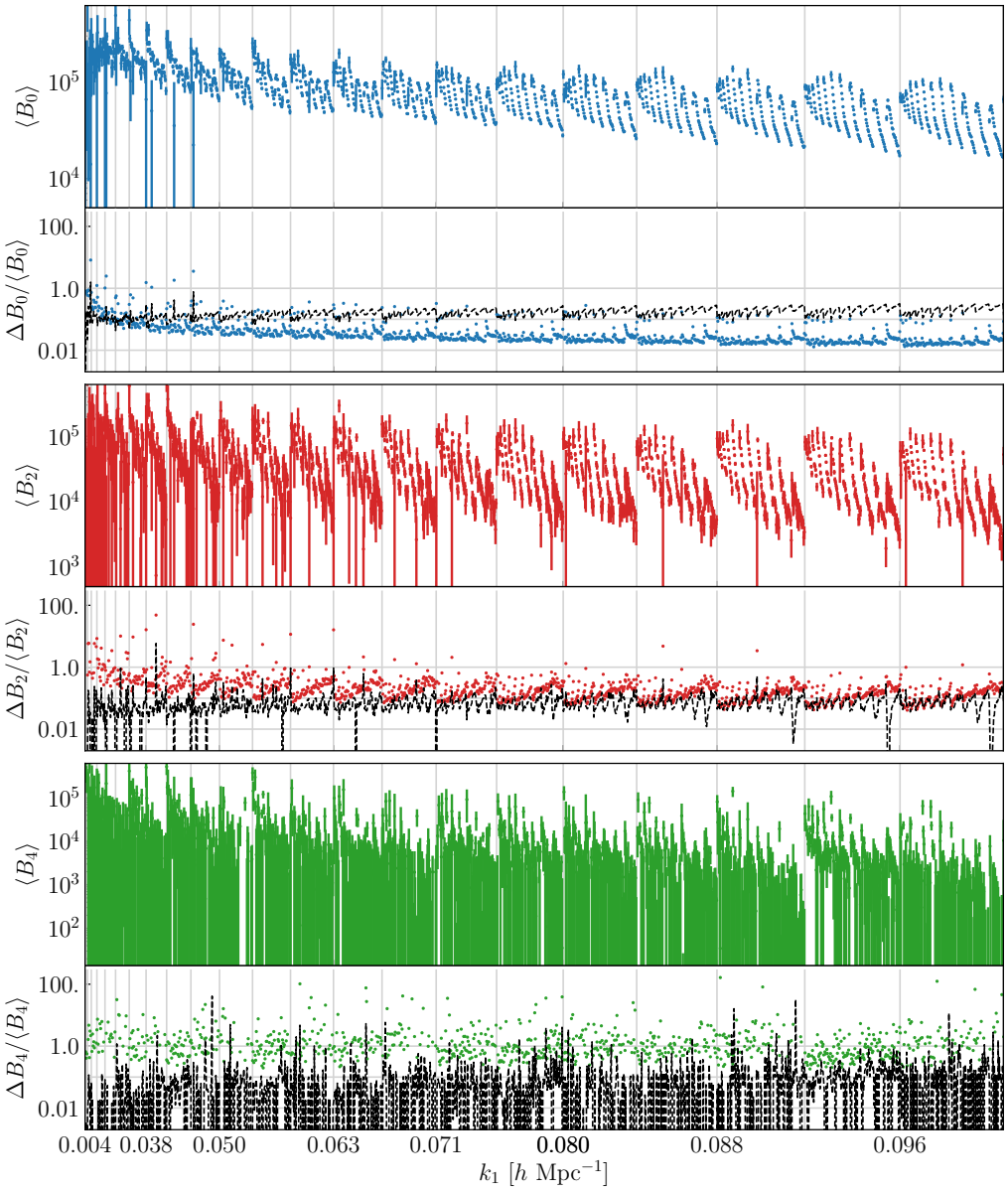

Figure 5.1: Mean of the halo bispectrum multipoles measurements (including shot-noise) from the 298 N-body Minerva simulations, shown for all triangular configurations. For each multipole moment, the bottom half of each panel shows the relative error on the mean (in color) along with the relative (Poisson) shot-noise contribution (in black).

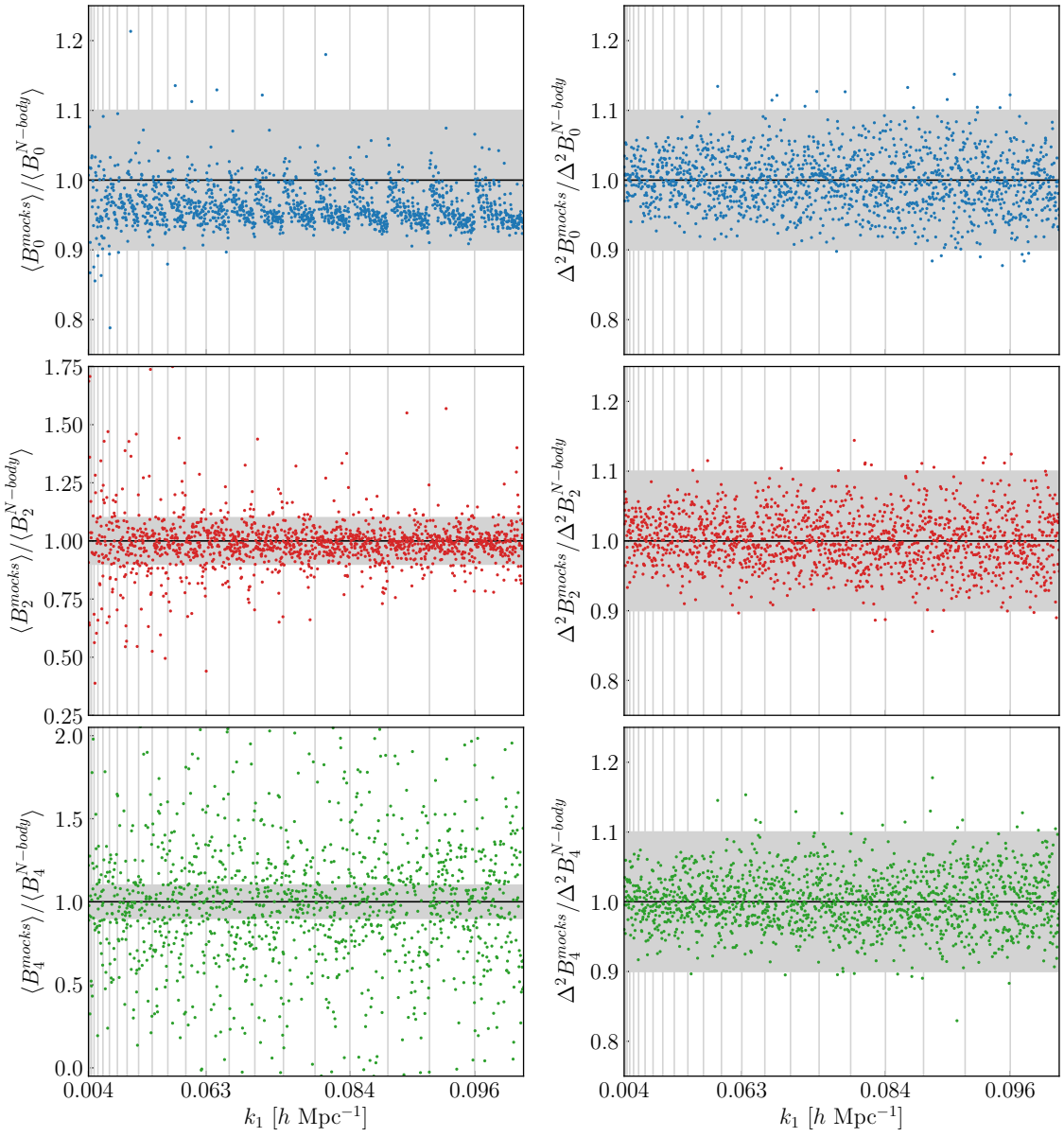

Figure 5.2: Left column: ratio between the mean bispectrum multipoles from the 298 N-body simulations and the mean of the same quantity from the corresponding PINOCCHIO mocks with matching initial conditions. Right column: ratio between the bispectrum multipoles variance estimated from the simulations and the one estimated from the corresponding mocks.

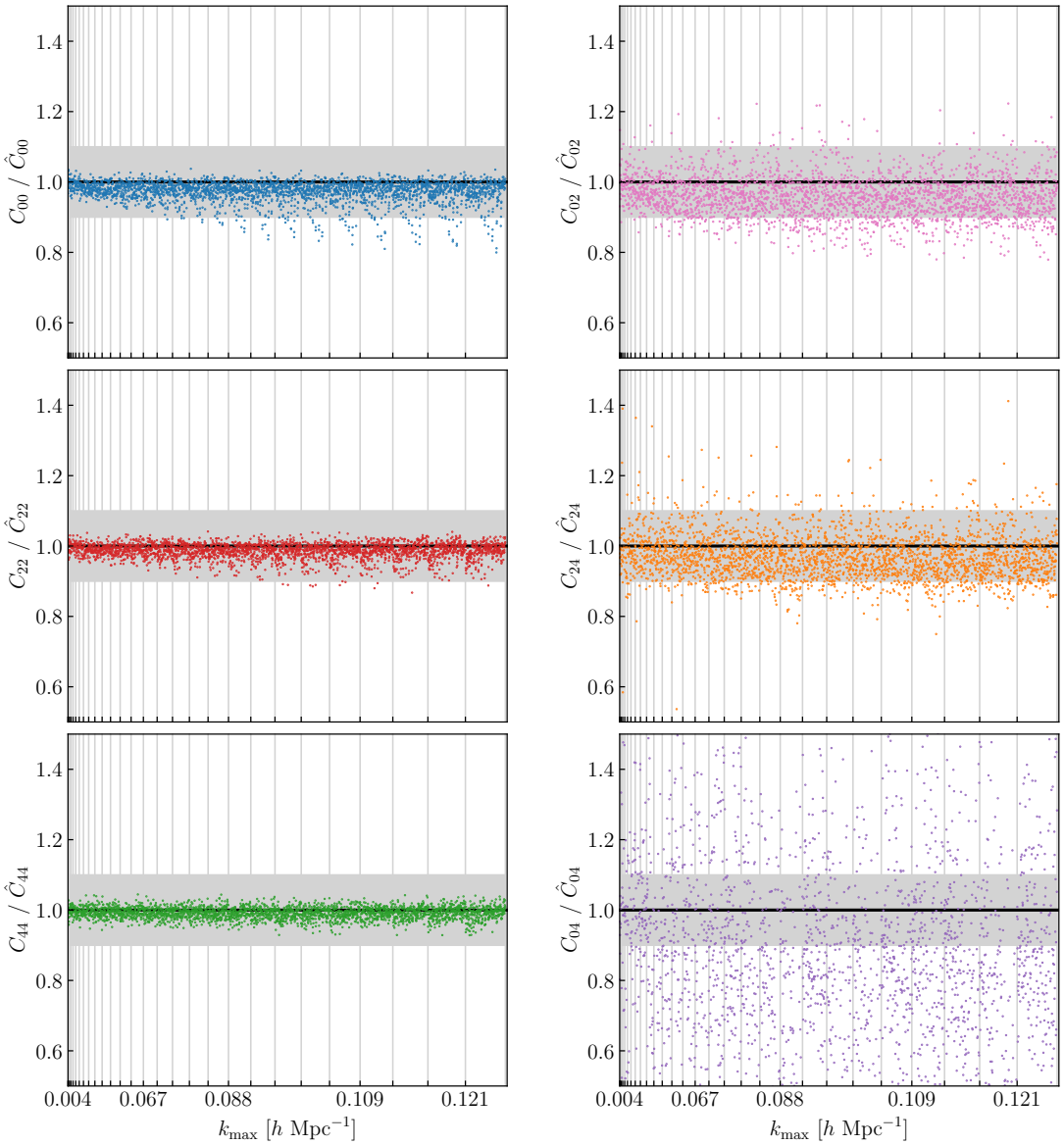

Figure 5.3: Ratio between the theoretical prediction of the multipoles covariance $C_{\ell_1\ell_2}(t_i, t_i)$ in the Gaussian approximation and its numerical estimate from the PINOCCHIO mocks.

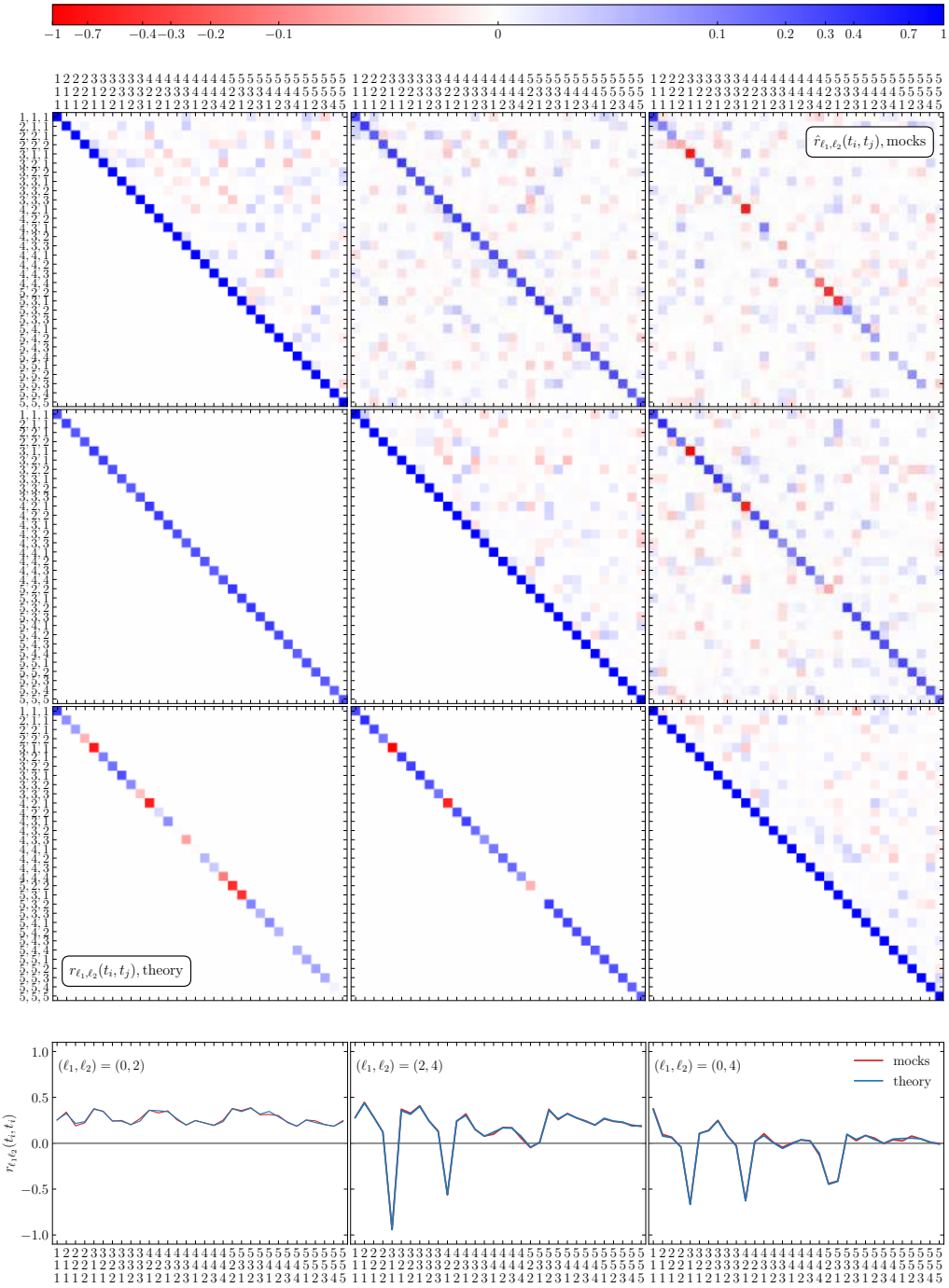

Figure 5.4: Subset of the correlation matrix $r_{\ell_1\ell_2}(t_i,t_j)$, defined in eq. (5.36) for $\ell = 0, 2$ and 4, restricted to the first 32 triangular configurations t_i. The top-right half is estimated from the full set of 10,000 PINOCCHIO mocks, while the bottom-left half is the theoretical prediction in the Gaussian approximation. The bottom panels compare the predicted (blue) and measured (red) coefficients $r_{\ell_1\ell_2}(t_i,t_i)$ with $\ell_1 \neq \ell_2$ as a function of the selected triangles t_i. The two estimates overlap almost exactly.

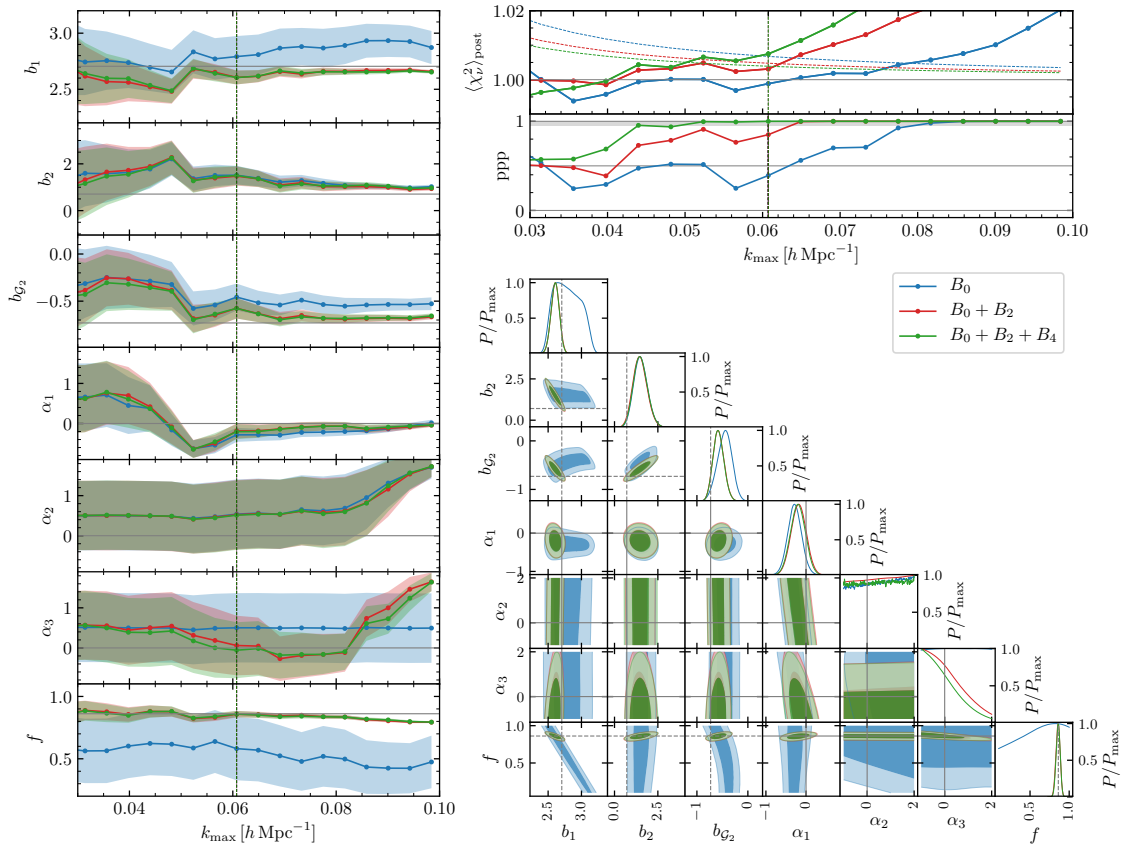

Figure 5.5: Results for the analysis of the whole 298 Minerva simulations data-set in terms of the full, seven-parameters model. Left panels: marginalised, 1-σ posteriors for each parameter as a function of $k_{\rm max}$. Top-right panels: posterior-averaged, reduced chi-square, $\langle\chi^2_\nu\rangle$ and the posterior predictive p-value (ppp) as a function of $k_{\rm max}$. The blue, red and green dashed lines in the $\langle\chi^2_\nu\rangle$ panel represent the 95% confidence limits for the three combinations of multipoles considered. Bottom-right panel: two-dimensional, marginalised 1-σ contours for $k_{\rm max} = 0.06\,h\,{\rm Mpc}^{-1}$ case (corresponding to the vertical line in the other panels). In all panels, the B_0-only analysis (blue) is compared to the joint $B_0 + B_2$ (red) and $B_0 + B_2 + B_4$ (green). All posteriors are compared with the results from the joint analysis of the real-space power spectrum and bispectrum derived in Paper II, whose best-fit values are shown by the gray, dashed lines.

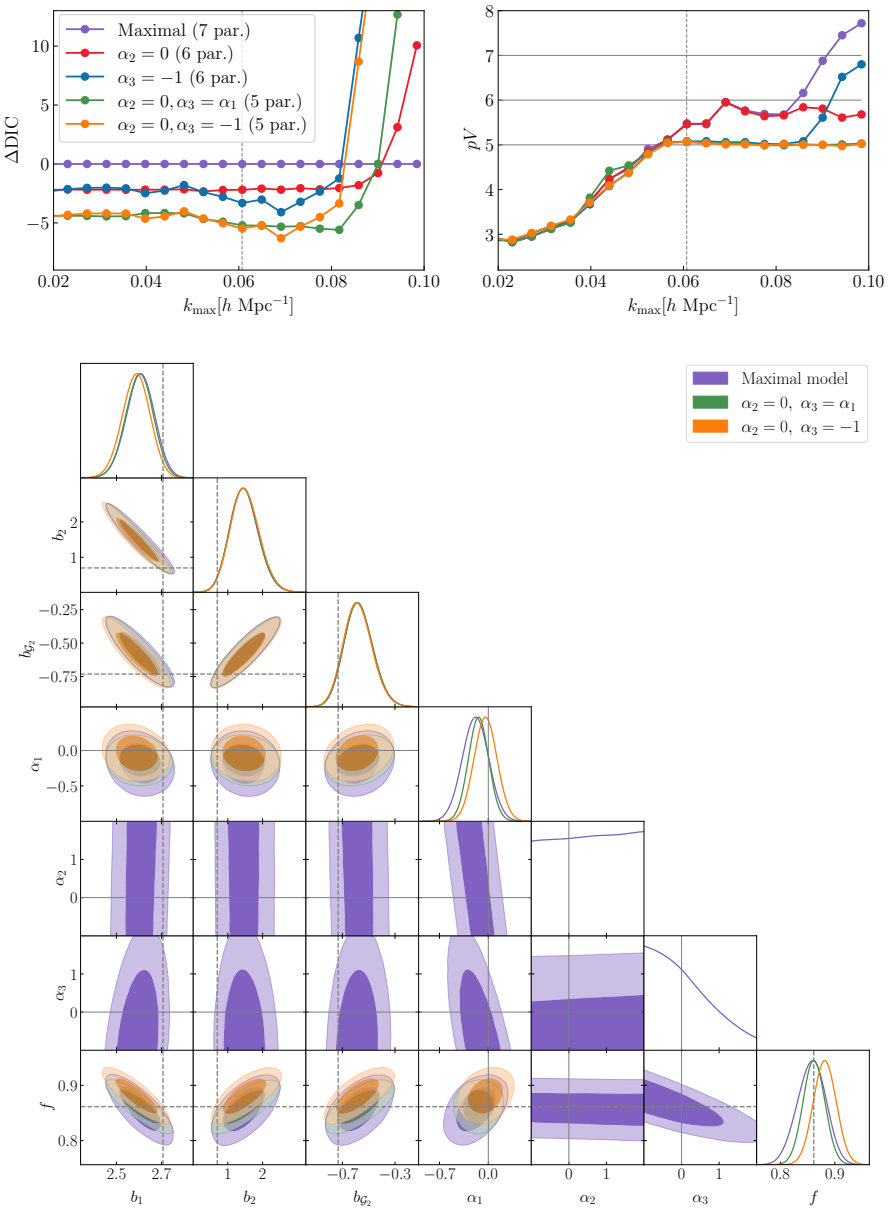

Figure 5.6: Top left panel: difference in the DIC of the various shot-noise models with respect to the maximal one with seven free parameters, as a function of the largest wavenumber $k_{\rm max}$ for the analysis of the monopole plus quadrupole. Top right panel: effective numbers of parameters as a function of $k_{\rm max}$ for the same shot-noise models and the same dataset, $B_0 + B_2$. Bottom panel: contour plots for $B_0 + B_2$ at $k_{\rm max} = 0.06\,h\,{\rm Mpc}^{-1}$, showing the 1- and 2-$\sigma$ 2D constraints on the bias and shot-noise parameters for the maximal model compared to the two 5-parameters models defined by setting $\alpha_3 = \alpha_1$ and $\alpha_3 = -1$ (both with $\alpha_2 = 0$). Dashed lines represent the fiducial value of growth rate f and the best-fit values for the bias parameters obtained in real space in Paper II.

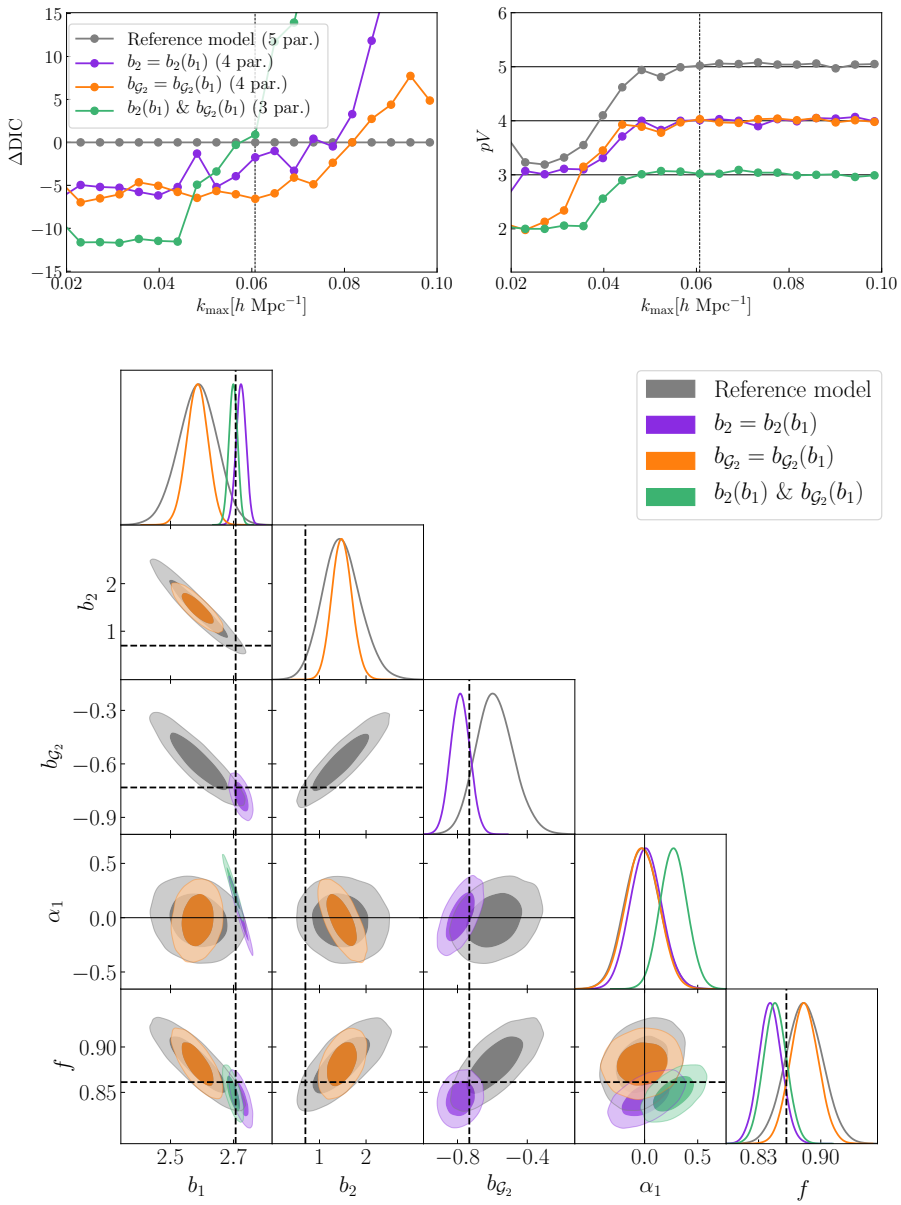

Figure 5.7: Top left panel: difference in the DIC of the two model adopting the bias relations $b_2(b_1, b_{\mathcal{G}_2})$ and $b_{\mathcal{G}_2}(b_1)$ with respect to the reference, 5-parameter model, as a function of the largest wavenumber $k_{\rm max}$ for the analysis of the monopole plus quadrupole. Top right panel: effective numbers of parameters as a function of $k_{\rm max}$ for the same models and datasets, $B_0 + B_2$. Bottom panel: contour plots for $B_0 + B_2$ at $k_{\rm max} = 0.06\,h\,{\rm Mpc}^{-1}$, showing the 1- and 2-$\sigma$ 2D constraints on the bias and shot-noise parameters for the three models. Dashed lines represent the fiducial value of growth rate f and the best-fit values for the bias parameters obtained in real space in Paper II.

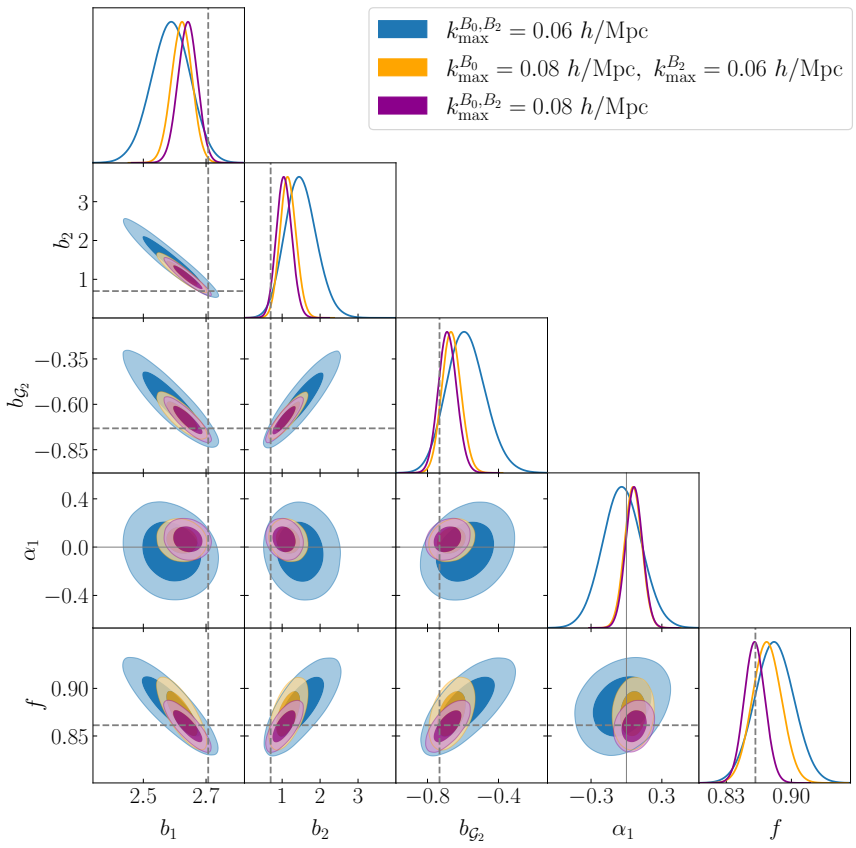

Figure 5.8: Contour plots for the $B_0 + B_2$ analysis assuming $k_{\rm max}^{B_0} = k_{\rm max}^{B_2} = 0.06\,h\,{\rm Mpc}^{-1}$ (blue) compared to the cases with $k_{\rm max}^{B_0} = 0.08\,h\,{\rm Mpc}^{-1}$ and $k_{\rm max}^{B_2} = 0.06\,h\,{\rm Mpc}^{-1}$ (yellow) and $k_{\rm max}^{B_0} = k_{\rm max}^{B_2} = 0.08\,h\,{\rm Mpc}^{-1}$ (magenta). The gray, dashed mark the best-fit values from the real-space, joint analysis of power spectrum and bispectrum of Paper II.

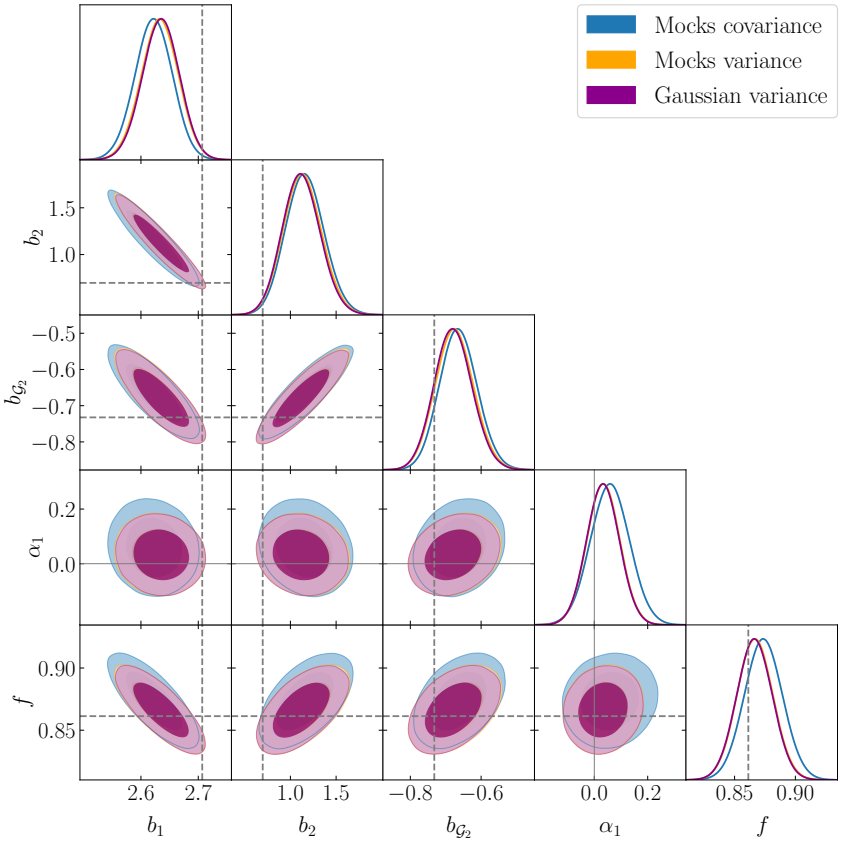

Figure 5.9: Contour plots for the $B_0 + B_2$ reference analysis under different assumptions for the covariance. The case of the full covariance, $C_{\ell_1\ell_2}(t_i, t_j)$, estimated from the mocks (blue contours) is compared to the variance $C_{\ell_1\ell_2}(t_i, t_i)$ estimated from the mocks (orange) and from the Gaussian theory prediction (magenta). The last two cases overlap almost exactly. The analysis assumes $k^{B_0}_{\rm max} = 0.08\,h\,{\rm Mpc}^{-1}$ and $k^{B_2}_{\rm max} = 0.06\,h\,{\rm Mpc}^{-1}$.

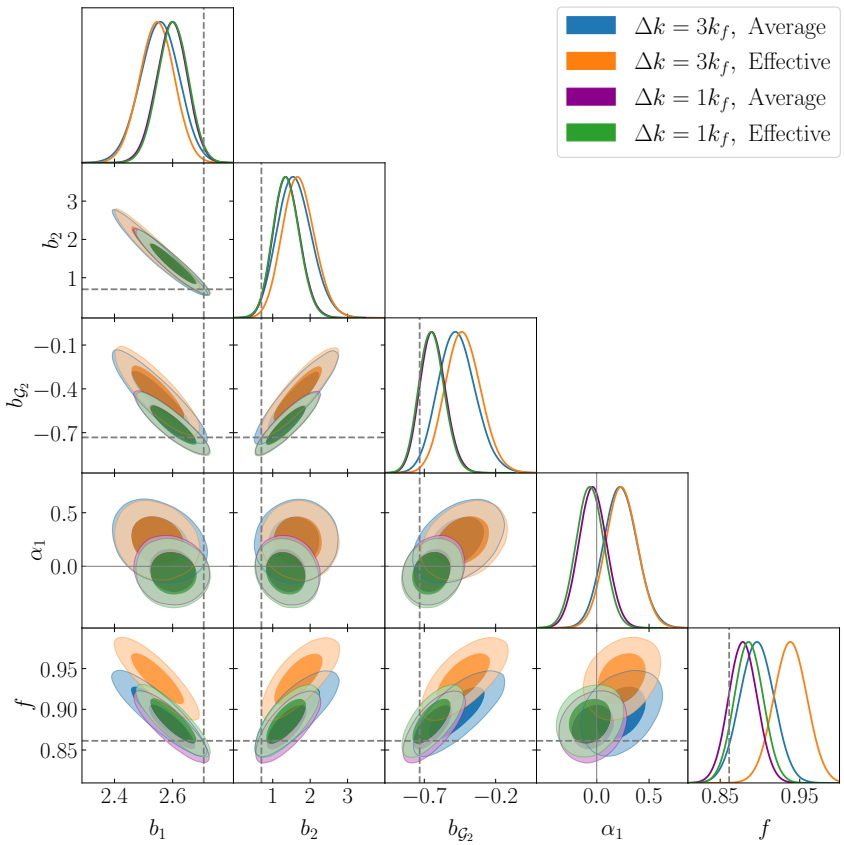

Figure 5.10: Contour plots for the $B_0 + B_2$ reference analysis for $k_{\rm max}^{B_0} = k_{\rm max}^{B_2} = 0.06\,h\,{\rm Mpc}^{-1}$, under different assumptions for the binning scheme and evaluation of the theoretical prediction: $\Delta k = k_f$ with exact binning (magenta), $\Delta k = k_f$ with effective prediction (green), $\Delta k = 3\ k_f$ with exact binning (blue) and $\Delta k = 3\ k_f$ with effective prediction (orange).

Chapter 6

Current and future developments

In this chapter I will briefly summarize two projects to whom I have provided a minor contribution.

The former [120] is the derivation of an exact expression for the analytical convolution of the bispectrum prediction with the window function, developed for the standard FKP estimator. This is crucial to exploit bispectrum measurements in upcoming redshift surveys accurately, accounting for all measurable scales.

The second project, currently being completed, constitutes the natural extension of [136] as it considers the constraining power of the bispectrum multipoles in the natural context of a joint analysis of power spectrum and bispectrum in redshift space.

6.1 Bispectrum Window Convolution

6.1.1 Theory

Conventional FKP-like estimators [148, 145, 147] provide as output measurements of the true galaxy bispectrum which are convolved with the survey window function, just as happens for the FKP power spectrum. Consequently, theoretical predictions for the matter bispectrum $B(\mathbf{k}_1, \mathbf{k}_2)$ must be convolved with the window $B_W(\mathbf{k}_1, \mathbf{k}_2) \equiv W(\mathbf{k}_1)W(\mathbf{k}_2)W^*(\mathbf{k}_1 + \mathbf{k}_2)$ to obtain

$$\hat{B}(\mathbf{k}_1, \mathbf{k}_2) = \int \frac{d^3p_1}{(2\pi)^3} \int \frac{d^3p_2}{(2\pi)^3} B_W(\mathbf{k}_1 - \mathbf{p}_1, \mathbf{k}_2 - \mathbf{p}_2) B(\mathbf{p}_1, \mathbf{p}_2)\,. \tag{6.1}$$

A similar computation is now routinely evaluated for power spectra by means of one-dimensional Hankel transforms [168], especially by implementing the so-called mixing matrix form $\tilde{P}_\ell(\mathbf{k}) = \mathcal{W}_{\ell\ell'}(\mathbf{k}, \mathbf{p}) P_{\ell'}(\mathbf{p})$ [39, 22] which allows to pre-compute $\mathcal{W}_{\ell\ell'}(\mathbf{k}, \mathbf{p})$ and use it for optimized likelihood analysis when cosmological parameters are changed at each step.

For the bispectrum, the exact convolution was often bypassed by ignoring the effect on the non-linear kernel characterizing the tree-level prediction, as in BOSS bispectrum analyses [64, 68, 67]. While this approach works quite well on most triangle shapes, squeezed configurations give somehow a worse agreement. This could lead to discarding potentially valuable information on large scales and bias results for local primordial non-Gaussianity

related to this triangle shape [149]. Alternatives to this method exist, however they adopt a different coordinate system then the one routinely adopted in most and our analyses [136] or, a completely different estimator [126].

In [120] we provide a method to compute (6.1) for the redshift-space bispectrum multipoles estimator of [147], presented in Chapter 3. The main result is equation (6.2) where the convolved bispectrum is given in a form of matrix multiplication, as happens for the Power Spectrum in [168]. In the following we will not provide the full derivation of these equations as the mathematical details, consisting of spherical harmonics expansions, contractions, and integrations over angular variables, do not add much information to the final result and their description is beyond our purpose here which is just to declare that, in the broader picture of a full likelihood pipeline, we are able to address the effect of convolution with a realistic survey window function. Therefore we directly provide the final result, given by

$$\hat{B}_L(k_1,k_2,k_3) = \int \frac{dp_1}{2\pi^2}p_1^2 \int \frac{dp_2}{2\pi^2}p_2^2 \int \frac{dp_3}{2\pi^2}p_3^2 \sum_{L'M'} B_{L'M'}(p_1,p_2,p_3) \times \sum_{\ell} I_{\ell\ell 0}(p_1,p_2,p_3)\mathcal{Q}^L_{L',-M',\ell}(k_1,k_2,k_3;p_1,p_2)\,. \tag{6.2}$$

The matrix, represented by the second row of this equation, is defined on the usual wavelength triplet $\{p_1,p_2,p_3\}$ and is written in terms of the $I_{\ell\ell 0}(p_1,p_2,p_3)$ function, enforcing the triangle condition on $\{p_1,p_2,p_3\}$, and a second term accounting for the window function contribution,

$$\mathcal{Q}^L_{L'M'\ell}(k_1,k_2,k_3;p_1,p_2) \equiv \sum_{\ell_1,\ell_2,\ell'} \frac{128\pi^2}{V_B}\int_{k_1} dq_1 q_1^2 \int_{k_2} dq_2 q_2^2 \int_{k_3} dq_3 q_3^2\; I_{\ell_2\ell_2 0}(q_1,q_2,q_3) \times \mathcal{W}^L_{L'M'\ell\ell'\ell_1\ell_2}(q_1,q_2;p_1,p_2)\,, \tag{6.3}$$

that can be evaluated as a two-dimensional Hankel Transform of the product of two spherical Bessel functions with the 3PCF multipoles of the window function,

$$\begin{aligned} Q^L_{L'M'\ell\ell'\ell_1\ell_2}(x_{13},x_{23}) \equiv &(-1)^{M'} \sum_{\tilde{\ell}_1,\tilde{\ell}_2} \sum_{\substack{M,m_1,m_2\\ m,m',\tilde{m}_1,\tilde{m}_2}} 4\pi i^{\ell'-\ell+\ell_2-\ell_1}\, \mathcal{G}^{Mm_1m_2}_{L\ell_1\ell_2}\, \mathcal{G}^{M'mm'}_{L'\ell\ell'}\, \mathcal{G}^{m_1m'\tilde{m}_1}_{\ell_1\ell'\tilde{\ell}_1}\, \mathcal{G}^{m_2m\tilde{m}_2}_{\ell_2\ell\tilde{\ell}_2} \\ &\times \int d^3x_3 \int \frac{d^2\hat{x}_{13}}{4\pi}\int \frac{d^2\hat{x}_{23}}{4\pi} Y^*_{LM}(\hat{x}_3) Y_{\tilde{\ell}_1\tilde{m}_1}(\hat{x}_{13}) Y_{\tilde{\ell}_2\tilde{m}_2}(\hat{x}_{23}) \\ &\times W(\mathbf{x}_3+\mathbf{x}_{13})W(\mathbf{x}_3+\mathbf{x}_{23})W(\mathbf{x}_3). \end{aligned} \tag{6.4}$$

6.1.2 Results

We test this method by applying it to the MINERVA and PINOCCHIO mocks already used in previous papers. In this work, I provided measurements for the bispectrum monopole in real-space, on periodic boxes which do not account for the effect of the survey footprint, and on spheres of radius $400\,\mathrm{Mpc}\,h^{-1}$ carved inside each realisation of the MINERVA and

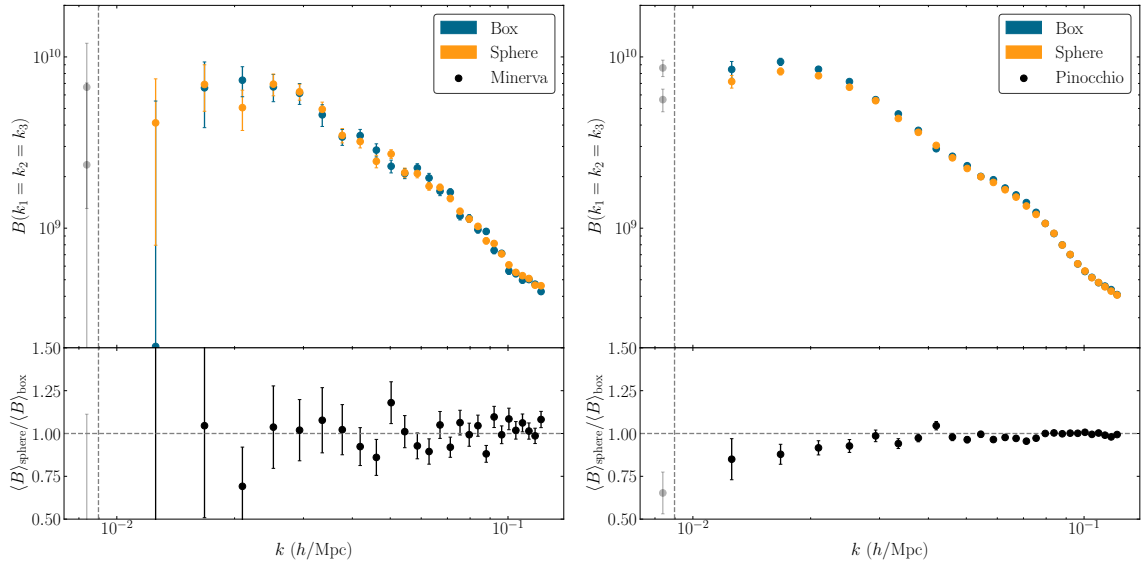

Figure 6.1: *Top panels:* mean of the bispectrum equilateral configurations, $\hat{B}_0(k,k,k)$, as a function of k for both the box (blue) and spherical window (orange) measurements and for both the Minerva simulations (*left*) and PINOCCHIO box (*right*). *Bottom panels:* ratio of the sphere to box measurements for simulations and mocks. The vertical dashed line indicates the effective fundamental frequency of the sphere $k_f^{\rm sphere} = 2\pi/V_{\rm sphere}^{1/3}$.

PINOCCHIO mocks. This last set of data simulate measurements on an ideal footprint, in this case taken as a simple sphere of $V_{\rm eff} \sim 700\,{\rm Mpc}^3\,h^{-3}$. The choice of the spherical footprint relates to the fact that for such a geometry it is possible to give an analytic description of the corresponding window function.

To perform these measurements, I used the bispectrum code described in Chapter 3, where the auxiliary field was computed from the spherical mock catalogs and from a random mock catalog accounting for the same footprint. This means that the densities $n_d^{\rm sphere}$ and $n_r^{\rm sphere}$ correspond to $n_d^{Minervabox}$ and $n_r^{\rm box}$ over the volume of the sphere, and vanish outside. I produced these mocks by populating cosmological boxes with the same characteristics of MINERVA and PINOCCHIO ones with a uniform distribution of objects, with $N_r^{\rm box} = 50 \times N_d^{\rm box}$. Out of these, I extracted a spherical volume, of same geometry as the one specified above, to mimic a random mock accounting for the survey footprint of the corresponding measurements.

We first check the effect of the ideal footprint on the bispectrum measurements by comparing the mean of the periodic box to the one of the sphere. Results, shown in Figure 6.2, suggest that the typical suppression induced by the window on large scales is very difficult to detect, if not for very large surveys for which statistical noise is extremely small. In fact, the total effective volume of MINERVA spheres, $V \sim 2.1 \times 10^{-4}\,{\rm Gpc}^3\,h^{-3}$, is not sufficient and the effect is only observable in the case of PINOCCHIO spherical mocks.

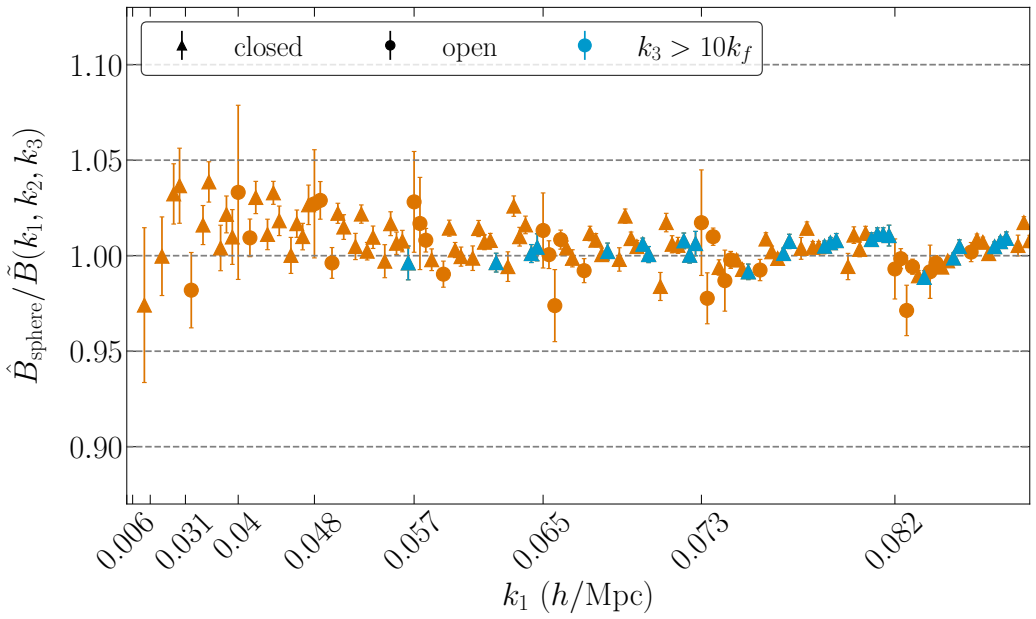

Figure 6.2: *Top panels:* mean of the bispectrum equilateral configurations, $\hat{B}_0(k, k, k)$, as a function of k for both the box (blue) and spherical window (orange) measurements and for both the Minerva simulations (*left*) and PINOCCHIO box (*right*). *Bottom panels:* ratio of the sphere to box measurements for simulations and mocks. The vertical dashed line indicates the effective fundamental frequency of the sphere $k_f^{\rm sphere} = 2\pi/V_{\rm sphere}^{1/3}$.

A check of the accuracy of our convolution model to correctly reproduce bispectrum measurements on the PINOCCHIO spherical mocks is shown in Figure 6.2. In this picture, our theoretical model for the bispectrum is evaluated using the model parameters determined from a likelihood analysis run over the 10000 PINOCCHIO boxes, and is convolved through our mixing matrix approach using an analytical estimate of three-point correlation function of the footprint. The convolution step makes use of the the 2DFFTLog algorithm[1] [54] to compute the two-dimensional Hankel transform needed to evaluate the $\mathcal{W}$ term inside of equation (6.3). Figure 6.2 shows the ratio of the measurements on the ideal volume to the convolved model for all configurations up to $k_{\rm max} = 0.09\,{\rm Mpc}^{-1}\,h$. The error bars correspond to the error on the mean of the 10000 PINOCCHIO mocks, while the blue dots highlight specific configurations, as those with $k_3 > 10\,k_f$, selected and analysed in the analysis of [64]. From this plot, we notice that our method recovers quite well the measurement on the spherical mocks. The agreement is of the order $\leq$2-3% and the result shows a marginal residual dependence on shape.

The application of this method for convolving theoretical predictions of the bispectrum was also applied to a full likelihood analysis. Results were obtained by using two different

[1] github.com/xfangcosmo/2DFFTLog

methods to evaluate the $\mathcal{W}$ term inside of equation (6.3). The two, however, give differences of the order of 2σ in the determimation of local bias parameters, suggesting that further investigation is required.

Despite this fact, we want to emphasize that the main result of this work was to show that our mixing matrix method allows for a fast treatment of convolution inside likelihood analyses such that does not significantly change the run-time for a typical Markov chain. This is a major result and will have great impact on future analyses, especially those aiming at studying the redshift space bispectrum multipoles, for which the effect of the survey window function is expected to be more relevant.

6.2 Joint analysis of power spectrum and bispectrum in redshift-space

This project corresponds to the natural extension of the work carried out in paper [136] which is the main focus of this dissertaion. At present, we are already involved in the development of this analysis whose results will be published by the end of 2022. In principle, most of the tools are already there. The model for the one-loop power spectrum multipoles has been implemented this year in the PBJ code. As it is the case in real space, a full consistent analysis in redshift space, including cosmological parameters, requires the computation of all loop-corrections at every step of the MCMC. Computing 28 loop integrals using standard numerical integration can become numerically expensive, and for this reason an efficient implementation is required. This can be obtained by the approach of [109], where all mode-coupling type integrals can be written as a function of just seven "building-blocks" integrals, linearly combined using some numerical coefficients, and where the propagator type integrals can be written with some fast Fourier convolution implementation. The tree-level bispectrum multipoles were already implemented and tested by myself in this work. However, some problems must still be solved. In particular, we want to perform this analysis changing, during each step of the MCMC chain, not only the bias and stochastic parameters but also cosmological ones. This introduces a new bottleneck in the computing time of our likelihood code, the evaluation of the linear power spectrum used to compute predictions. In order to alleviate this problem we are now implementing an emulator recipe, which is a fast method to produce linear power spectra through neural network-based numerical interpolators that usually need some kind of training based on N-body simulations. These kind of tools allow to speed-up the whole computation of the likelihood by two orders of magnitude compared to most typical Boltzmann solvers as CAMB [102] or CLASS [99] which typically require $\mathcal{O} \sim$ sec to solve cosmological equations and compute a linear power spectrum. This advantage comes at expense of a small downgrade in accuracy and of a restriction in the parameter space which is limited by the training set values. Our specific implementation is based on the Bacco emulator [8], which can compute a linear power

spectrum in about one millisecond with 0.2% (0.5%) accuracy over redshifts $z \leq 3$ ($z \leq 9$), and scales $10^{-4}\,\mathrm{Mpc}^{-1}\,h \leq k \leq 50\,\mathrm{Mpc}^{-1}\,h$.

In figure 6.3 we show a preliminary result from this analysis. Here, we put on the spotlight the effect of adding one-at-a-time the bispectrum monopole and quadrupole to the power spectrum multipoles analysis. I do not aim at commenting the full picture, however I just want to focus the attention of the reader on the contour of the joint b_1 and f posteriors. The bispectrum-only contours related to these two parameters were barely consistent with the combined, expected values of f and $b_1^{\times}$. We note that the addition of the power spectrum multipoles in this case, alleviates this tension. Naively, we can say that such result does not come as a surprise since the value of b_1 should be much more sensitive to the amplitude of the power spectrum on large scales than to the bispectrum. Indeed, if we look at the power-spectrum-only contours, we note that the area comprised in the purple lines is perfectly centered on the expected value for the linear bias. On the other hand, the bispectrum contours of Chapter 5 appeared to be much more sensitive to the value of the linear growth rate. Further investigations are naturally needed, and we expect the result of this analysis to appear in a dedicated paper which will be submitted by the end of 2022.

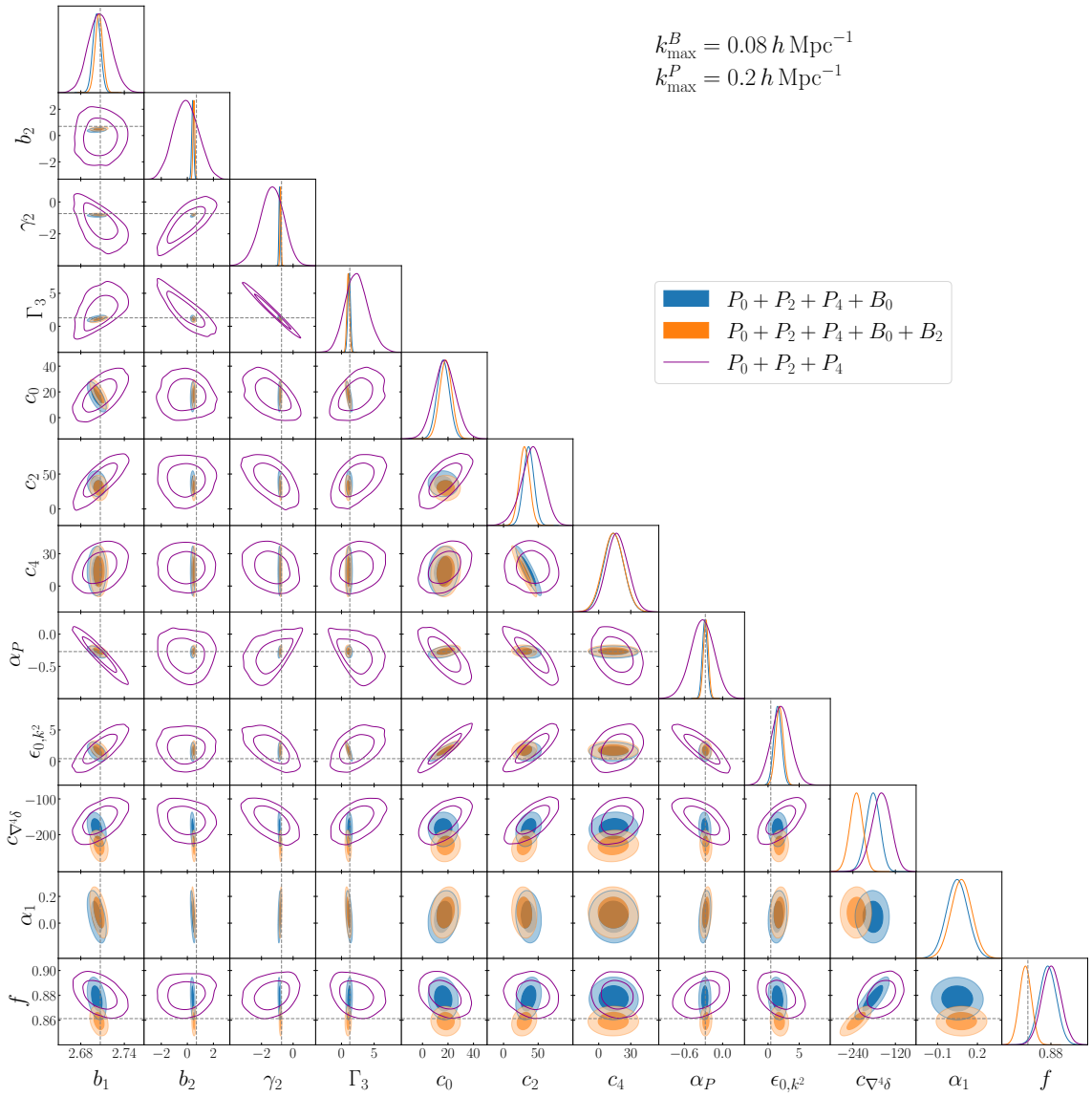

Figure 6.3: Two-dimensional marginalised $1-\sigma$ contours for $k^P_{\rm max} = 0.2\,{\rm Mpc}^{-1}\,h$ and $k^B_{\rm max} = 0.08\,{\rm Mpc}^{-1}\,h$. $P_0+P_2+P_4$ analysis (purple) is compared to the joint $P_0+P_2+P_4+B_0$ (blue) and $P_0+P_2+P_4+B_0+B_2$ (orange). All posteriors are compared with the results from the joint analysis of the real-space power specturm and bispectrum derived in Paper II, whose best-fit values are shown by the gray dashed lines.

Chapter 7

Conclusions

The work presented in this dissertation relates to the current effort from the scientific community to improve the methods to exploit the information content encoded in the observed large-scale structure distribution of matter in the Universe. This information is extracted from spetroscopic galaxy redshift surveys through measurements of correlation functions of some type of tracer assumed to sample the matter distribution through some physically-motivated model, characterized by bias. These measurements, are usually fed to a likelihood code along with theoretical predictions, developed in the context of perturbation theory. Joint posteriors between model parameters, resulting from likelihood analyses, describe the confidence regions for these quantities and allow us to constrain their value. This approach is broadly used by the scientific community, as shown at the end of Chapter 2, and in Chapter 4 and 5, to evaluate cosmological and bias parameters. We now feel impelled to highlight once more the novelty of our work and its importance in this panorama.

The main focus of this dissertation has been the estimate and the analysis of the galaxy bispectrum in spectroscopic redshift surveys, and the study of the impact of the information encoded in its multipoles on likelihood analyses aiming at extracting constraints on bias $b_1, b_2, b_{\mathcal{G}_2}$ and cosmological parameters f from halo N-body simulations. The advance of this work is that it is one of the first studies about the constraining power of the bispectrum multipoles in redshift space in which a direct comparison with real measurements of N-body simulations is made, with previous works being mostly limited to forecast studies or to the use of synthetic measurements built through analytical templates [77]. A major result is the fact that our analysis confirms the results from these pioneering works [61, 28] in the importance of going beyond the analysis of the bispectrum monopole. In particular, we find that the model at tree-level in PT provides a valid description of the measurements, within the errors defined by the full volume of our simulations, up to a maximum wavenumber of $0.08\,\mathrm{Mpc}^{-1}\,h$ for the monopole, $0.06\,\mathrm{Mpc}^{-1}\,h$ for the quadrupole, and $0.045\,\mathrm{Mpc}^{-1}\,h$ for the hexadecapole. As in the power spectrum case, the inclusion of the bispectrum quadrupole greatly improves the posteriors from the monopole alone, while the addition of the hexadecapole leaves the contours almost untouched. The robustness of this outcome relies on the exceptional cumulative volume of the simulations we analysed and on the large number of mocks utilized to compute the numerical covariance matrix. In this regard, another

major result is that the Gaussian covariance model for the cross-multipoles bispectrum provides a good approximation to the numerical estimate we used. We tested the variance of the Gaussian covariance model in terms of likelihood results, showing that contours for joint parameter posteriors do not show any appreciable difference with the variance of the numerical estimate. Moreover, the subsequent comparison with the full numerical covariance run does only display a small variation. This work resulted in a paper that has been submitted on April 26^{th}. Its results will be key to interpret the analysis of the joint analysis of the power spectrum and bispectrum in redshift-space which will study the constraining power that the bispectrum multipoles add on top of the anisotropic power spectrum information content. This project is just started and will end up in a publication which will be likely submitted by the end of this year.

These studies, together with Paper I and Paper II, are applied to boxes with periodic boundary conditions. This represents an ideal set-up that singles-out the complications introduced by observational systematics affecting real spectroscopic surveys. In this sense, the relevance of this work will extend also to the possibility of using our results as reference for studying the impact of these systematics all the way down to their ripercussion on bias and cosmological parameter constraints. This will be achievable thanks to the complete data analysis pipeline that we built over these years within the Trieste group. This pipeline is now partecipating to a challenge within the Euclid Higher-Order Statistics Working Group. Purpose of the challenge is to compare constraints on model parameters for a variety of likelihood codes, in order to provide a robust analysis of current codes and models used by the scientific community. The results of this project will be published in a dedicated study.

Last but not least, this type of test was also particularly important for the bispectrum multipoles estimator itself: the code I am developing is now being used as an official code of the Euclid collaboration, of which I am a member. The low number of bispectrum estimator implementations does not allow for a comprehensive validation against eternal codes, as it happens for the monopole or for the power spectrum multipoles. Therefore, our results can be considered as a further validation of the code against theoretical tree-level multipoles predictions. The work I have been doing in the Euclid Collaboration about the implementation and validation of the power spectrum and bispectrum codes will be part of a dedicated official publication of the Euclid Consortium, to be published at the end of this year.

Having explained the relevance of our work in the context of LSS studies, I conclude by clarifying the role that these topics will play in the near future. In particular, their importance is soon justified in light of future surveys as Euclid [96] or DESI (Dark Energy Spectroscopic Instrument) [43] which will provide a large amount of data that needs to be exploited to the best of our capabilities. These data will allow us to study DE and DM, the two dominant energy components whose nature in still poorly understood, and shed light on the recent deviations of cosmological parameters measured from local observations from

Type 1a supernovae and weak lensing measurements from the Planck cosmology.

Appendix

A.1 Approximations for the bin-averaged theoretical predictions

A.1.1 Power spectrum

Within a Fourier bin, the theoretical model for the power spectrum can be expanded in Taylor series around some wavenumber q_0 included in the same bin as

$$P(q) = \sum_{n=0}^{\infty} \frac{1}{n!} P^{(n)}(q_0)(q - q_0)^n, \tag{1}$$

so that its bin-average can be written as

$$P_{\rm bin}(k) = \frac{1}{N_P(k)} \sum_{\mathbf{q}\in k} \sum_{n=0}^{\infty} \frac{1}{n!} P^{(n)}(q_0)(q - q_0)^n = \frac{1}{N_P(k)} \sum_{n=0}^{\infty} \frac{1}{n!} P^{(n)}(q_0) \sum_{\mathbf{q}\in k} (q - q_0)^n \,. \tag{2}$$

By defining the quantities

$$\mu_n(k) = \frac{1}{N_P(k)} \sum_{\mathbf{q}\in k} (q - q_0)^n, \tag{3}$$

we can write the bin-average of the power spectrum as

$$P_{\rm bin}(k) = \sum_{n=0}^{\infty} \frac{1}{n!} P^{(n)}(q_0)\mu_n(k) \,. \tag{4}$$

This expression does not involve the evaluation of the power spectrum and its derivatives at each value of $q = |\mathbf{q}|$, and the quantities $\mu_n(k)$ can be pre-computed.

If we choose for q_0 the effective wavenumber $k_{\rm eff}$ defined in eq. (4.39), the generic $\mu_n(k)$ reduces to the central n-th moment of the discrete distribution of Fourier wavenumbers in the bin. The zero-th order term in the infinite expansion eq. (4), reduces to the standard effective power spectrum of eq. (4.40), since $\mu_0(k) = 1$. The first order contribution vanishes since $\mu_1(k) = 0$. The first, non-vanishing correction to the zero-th order term is then given by the second-derivative term, with $\mu_2(k)$ being the variance of the distribution of Fourier wavenumbers inside the bin. Therefore, we can approximate the bin-averaged power spectrum, truncating the expansion to include up to the second order, as

$$P^{(2)}_{\rm bin}(k) \simeq P(k_{\rm eff}) + \frac{1}{2} P''(k_{\rm eff})\mu_2(k). \tag{5}$$

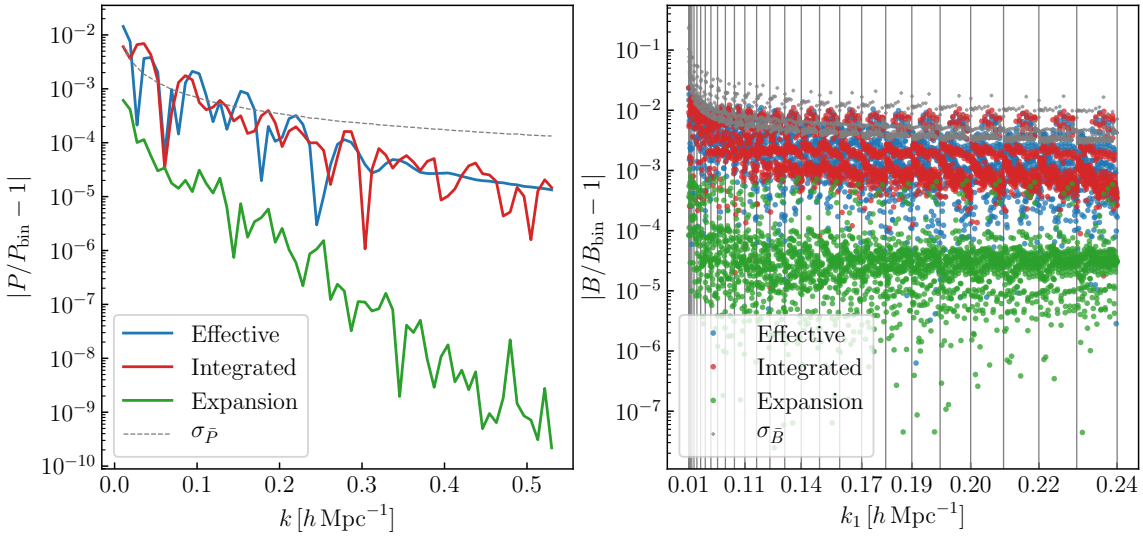

Figure 1: Left panel: relative difference between the bin-averaged theoretical model of the halo power spectrum and the model evaluated at the effective wavenumbers $k_{\rm eff}$ (in blue), the model evaluated using eq. (5) based on a Taylor expansion about $k_{\rm eff}$ (in green), and the model averaged approximating the discrete sums with continuous integrals (in red); in gray, the relative standard error on the mean (estimated from the mocks) of the full dataset of 298 N-body simulations. Right panel: same comparison for the bispectrum case.

In order to have a well-behaved, continuous n-th derivative, it is required that the starting power spectrum is interpolated with at least an $(n+1)$-th order spline. This means that a cubic spline interpolation of the theoretical model of the power spectrum is sufficient for our purposes. The quantities $k_{\rm eff}$ and $\mu_2(k)$ are evaluated only once, and therefore the computational cost of this approach is of the same order of the usual effective approach, while providing a great improvement in accuracy. This is shown in the left panel of figure 1, where the relative difference with the fully bin-averaged power spectrum is compared with the one of the effective prediction. As a reference, we also compare it with the integral approximation of the exact bin-average, and with the relative statistical uncertainty of our dataset.

A.1.2 Bispectrum

In the case of the bispectrum, due to its shape-dependence, the Taylor expansion approach is model dependent. For this reason, in the following it is more convenient to assume explicitly the structure of the tree-level model, eq. (4.34), that we adopted for the galaxy bispectrum. Introducing the generic kernel $\widetilde{K}$, we can write the model in the form

$$B(\mathbf{q}_1,\mathbf{q}_2,\mathbf{q}_3) = \widetilde{K}(\mathbf{q}_1,\mathbf{q}_2)P_{\rm L}(q_1)P_{\rm L}(q_2) + \text{cyc.}\,. \tag{6}$$

We also make use of the following notation for averages over the triangular bin with sides (k_1, k_2, k_3)

$$\langle f(\mathbf{q}_1, \mathbf{q}_2, \mathbf{q}_3)\rangle_\triangle \equiv \frac{1}{N_B(k_1, k_2, k_3)} \sum_{\mathbf{q}_1\in k_1} \sum_{\mathbf{q}_2\in k_2} \sum_{\mathbf{q}_3\in k_3} \delta_K(\mathbf{q}_{123}) f(\mathbf{q}_1, \mathbf{q}_2, \mathbf{q}_3)\,. \tag{7}$$

Then, inside the triangle bin, we can expand the product of the power spectra in Taylor series around the sorted effective wavenumbers defined in eq.s (4.41)

$$P_{\rm L}(q_l)P_{\rm L}(q_m) = \sum_{u=0}^{\infty}\sum_{v=0}^{\infty} \frac{1}{u!\,v!} P_{\rm L}^{(u)}(k_{{\rm eff},l}) P_{\rm L}^{(v)}(k_{{\rm eff},m})(q_l - k_{{\rm eff},l})^u (q_m - k_{{\rm eff},m})^v, \tag{8}$$

where $(\mathbf{q}_1, \mathbf{q}_2, \mathbf{q}_3)$ are relabeled as $(\mathbf{q}_l, \mathbf{q}_m, \mathbf{q}_s)$ (ordered from the longest to the shortest), and the full expression for the bin-average of the bispectrum model becomes

$$B_{\rm bin}(k_1, k_2, k_3) = \sum_{u=0}^{\infty}\sum_{v=0}^{\infty} \frac{1}{u!\,v!} P_{\rm L}^{(u)}(k_{{\rm eff},l}) P_{\rm L}^{(v)}(k_{{\rm eff},m}) \left\langle \widetilde{K}(\mathbf{q}_l, \mathbf{q}_m)(q_l - k_{{\rm eff},l})^u (q_m - k_{{\rm eff},m})^v \right\rangle_\triangle + \text{cyc.} \tag{9}$$

At zero-th order, we have that the approximation to the full bin-average of the bispectrum is simply

$$B^{(0)}_{\rm bin}(k_1, k_2, k_3) \simeq \left\langle \widetilde{K}(\mathbf{q}_l, \mathbf{q}_m) \right\rangle_\triangle P_{\rm L}(k_{{\rm eff},l}) P_{\rm L}(k_{{\rm eff},m}) + \text{cyc.}\,. \tag{10}$$

Notice that this expression does not reduce to the bispectrum evaluated at effective wavenumbers, since it includes the exact bin-average of the kernel. At higher order, new terms appear, where the bin-average now applies to the product of the kernel with powers of Fourier wavenumbers. Truncating the full expansion, retaining terms up to $u + v = 2$, this approximation requires to precompute 18 averages for each kernel, in addition to the three effective wavenumbers.

The shot-noise contribution does not require the computation of any extra term, since the averages appearing are already computed for the constant kernel relative to the quadratic bias operator,

$$B^{\rm bin}_{\rm shot-noise}(k_1, k_2, k_3) \simeq \frac{1+\alpha_1}{\bar{n}} b_1^2 \left[P_{\rm L}(k_{{\rm eff},l}) + \frac{1}{2} P''_{\rm L}(k_{{\rm eff},l}) \left\langle (q_l - k_{{\rm eff},l})^2 \right\rangle_\triangle \right] + \text{cyc.} + \frac{1+\alpha_2}{\bar{n}^2}\,. \tag{11}$$

As shown in the right panel of figure 1, this method provides generally a better accuracy (of at least one order of magnitude) compared to the standard effective method with sorted wavenumbers and to the integral approximation of the exact bin-average.

A.2 Analytical evaluation of the bispectrum multipoles

The orientation of the $\{\mathbf{k}_1, \mathbf{k}_2, \mathbf{k}_3\}$ triangle w.r.t. the LOS in the model for the redshift-space bispectrum $B_s(\mathbf{k}_1, \mathbf{k}_2, \mathbf{k}_3, \hat{n})$, eq. (5.5), is expressed entirely in terms of products of powers

of the cosines $\mu_i \equiv \hat{k}_i \cdot \hat{n}$ that can be factorised in each contribution.

The integrals defining the bispectrum multipoles in eq. (5.24) are therefore limited to angle-averages of such combinations, with the additional factors from the Legendre polynomials corresponding to additional powers of μ_1. We denote these integrals as

$$\mathcal{I}_{\alpha\beta\gamma} = \frac{1}{4\pi}\int_{-1}^{+1} d\mu_1 \int_0^{2\pi} d\xi\, \mu_1^\alpha\, \mu_2^\beta(\mu_1,\xi)\, \mu_3^\gamma(\mu_1,\xi)\,, \tag{12}$$

where

$$\mu_2(\mu_1,\xi) = \mu_1\mu_{12} - \sqrt{1-\mu_1^2}\sqrt{1-\mu_{12}^2}\cos\xi \tag{13}$$

and

$$\mu_3(\mu_1,\xi) = -\frac{k_1\mu_1 + k_2\mu_2(\mu_1,\xi)}{k_3}\,, \tag{14}$$

having introduced $\mu_{12} \equiv \hat{k}_1 \cdot \hat{k_2}$. Since the angle integration of eq. (12) is to be intended as a generic integration over all orientations, it is easy to see that it should satisfy the following property

$$\mathcal{I}_{\alpha,\beta,\gamma}(k_1,k_2,k_3) = \mathcal{I}_{\sigma(\alpha,\beta,\gamma)}[\sigma(k_1,k_2,k_3)]\,, \tag{15}$$

where $\sigma(...)$ represents a generic permutation applied, *at the same time*, to its indices *and* arguments[1] We write, for illustration purposes the first few as

$$\mathcal{I}_{\alpha 00} = \frac{1}{1+\alpha} \text{ for } \alpha \text{ even (vanishing otherwise)}\,, \tag{16}$$

$$\mathcal{I}_{\alpha 01} = -\frac{k_1^2+k_3^2-k_2^2}{2(2+\alpha)\,k_1\,k_3} \text{ for } \alpha \text{ odd (vanishing otherwise)}\,, \tag{17}$$

$$\mathcal{I}_{\alpha 11} = \frac{(2+\alpha)\,k_1^4 - \alpha\,(k_2^2-k_3^2)^2 - 2\,k_1^2\,(k_2^2+k_3^2)}{4(1+\alpha)(3+\alpha)k_1^2\,k_2\,k_3} \text{ for } \alpha \text{ even (vanishing otherwise)}\,, \tag{18}$$

$$\mathcal{I}_{\alpha 02} = \frac{4\,k_1^2\,k_3^2 + \alpha\,(k_1^2+k_3^2-k_2^2)^2}{4(1+\alpha)(3+\alpha)k_1^2\,k_3^2} \text{ for } \alpha \text{ even (vanishing otherwise)}\,. \tag{19}$$

We can group all contributions to the bispectrum multipoles according to the source of quadratic nonlinearity, that is

$$B_\ell(k_1,k_2,k_3) = B_\ell^{(F_2)} + B_\ell^{(b_2)} + B_\ell^{(S_2)} + B_\ell^{(G_2)} + B_\ell^{(\text{mixed})}\,. \tag{20}$$

These contributions can be expressed in terms of the $\mathcal{I}_{\alpha\beta\gamma}$

$$\begin{aligned} B_0^{(F_2)} &= 2\,b_1^3\,\mathcal{I}_{000}\,F_2(k_1,k_2;k_3)\,P_L(k_1)\,P_L(k_2) + 2 \text{ perm.}+ \\ &\quad + 2\,b_1^2\,f\,(\mathcal{I}_{200}+\mathcal{I}_{020})\,F_2(k_1,k_2;k_3)\,P_L(k_1)\,P_L(k_2) + 2 \text{ perm.}+ \end{aligned}$$

[1]Notice that in general is not true that $\mathcal{I}_{\alpha,\beta,\gamma}(k_1,k_2,k_3) = \mathcal{I}_{\sigma(\alpha,\beta,\gamma)}(k_1,k_2,k_3)$, so if we write, e.g., $\mathcal{I}_{200}+\mathcal{I}_{020}$ we implicitly mean $\mathcal{I}_{200}(k_1,k_2,k_3)+\mathcal{I}_{020}(k_1,k_2,k_3)$ corresponding to the sum of two different quantities.

$$+ 2\,b_1\,f^2\,\mathcal{I}_{220}\,F_2(k_1,k_2;k_3)\,P_L(k_1)\,P_L(k_2) + 2\text{ perm.}\,, \tag{21}$$

$$\begin{aligned} B_0^{(b2)} &= b_1^2\,b_2\,\mathcal{I}_{000}\,P_L(k_1)\,P_L(k_2) + 2\text{ perm.}+ \\ &+ b_1\,b_2\,f\,(\mathcal{I}_{200}+\mathcal{I}_{020})\,P_L(k_1)\,P_L(k_2) + 2\text{ perm.}+ \\ &+ b_2\,f^2\,\mathcal{I}_{220}P_L(k_1)P_L(k_2) + 2\text{ perm.}\,, \end{aligned} \tag{22}$$

$$\begin{aligned} B_0^{(S_2)} &= 2\,b_1^2\,b_{\mathcal{G}_2}\,\mathcal{I}_{000}\,S(k_1,k_2;k_3)\,P_L(k_1)\,P_L(k_2) + 2\text{ perm.}+ \\ &+ 2\,b_1\,b_{\mathcal{G}_2}\,f\,(\mathcal{I}_{200}+\mathcal{I}_{020})\,S(k_1,k_2;k_3)\,P_L(k_1)\,P_L(k_2) + 2\text{ perm.}+ \\ &+ 2\,b_{\mathcal{G}_2}\,f^2\,\mathcal{I}_{220}\,S(k_1,k_2;k_3)\,P_L(k_1)\,P_L(k_2) + 2\text{ perm.}\,, \end{aligned} \tag{23}$$

$$\begin{aligned} B_0^{(G_2)} &= 2\,b_1^2\,f\,\mathcal{I}_{002}\,G_2(k_1,k_2;k_3)\,P_L(k_1)\,P_L(k_2) + 2\text{ perm.}+ \\ &+ 2\,b_1\,f^2\,(\mathcal{I}_{202}+\mathcal{I}_{022})\,G_2(k_1,k_2;k_3)\,P_L(k_1)\,P_L(k_2) + 2\text{ perm.}+ \\ &+ 2\,f^3\,\mathcal{I}_{222}\,G_2(k_1,k_2;k_3)\,P_L(k_1)\,P_L(k_2) + 2\text{ perm.}\,, \end{aligned} \tag{24}$$

$$\begin{aligned} B_0^{(\text{mixed})} &= -b_1^3\,f\left(\frac{k_3}{k_1}\mathcal{I}_{101}+\frac{k_3}{k_2}\mathcal{I}_{011}\right)P_L(k_1)\,P_L(k_2) + 2\text{ perm.}- \\ &- b_1^2\,f^2\left[\frac{k_3}{k_1}(\mathcal{I}_{301}+2\mathcal{I}_{121})+\frac{k_3}{k_2}(\mathcal{I}_{031}+2\mathcal{I}_{211})\right]P_L(k_1)\,P_L(k_2) + 2\text{ perm.}- \\ &- b_1\,f^3\left[\frac{k_3}{k_1}(\mathcal{I}_{141}+2\mathcal{I}_{321})+\frac{k_3}{k_2}(\mathcal{I}_{411}+2\mathcal{I}_{231})\right]P_L(k_1)\,P_L(k_2) + 2\text{ perm.}- \\ &- f^4\left(\frac{k_3}{k_1}\mathcal{I}_{341}+\frac{k_3}{k_2}\mathcal{I}_{431}\right)P_L(k_1)\,P_L(k_2) + 2\text{ perm.}\,. \end{aligned} \tag{25}$$

Here the permutations are intended to apply as well on the $\mathcal{I}_{\alpha\beta\gamma}$ integrals. The shot-noise contribution to the monopole is given by

$$\begin{aligned} B_0^{(\text{shot-noise})} &= \frac{1}{\tilde{n}}\Big\{b_1^2\,\mathcal{I}_{000}\Big[P_L(k_1)+P_L(k_2)+P_L(k_3)\Big]+ \\ &+ b_1 f\Big[\mathcal{I}_{200}\,P(k_1)+\mathcal{I}_{020}\,P(k_2)+\mathcal{I}_{002}\,P(k_3)\Big]+ \\ &+ f^2\Big[\mathcal{I}_{400}P(k_1)+\mathcal{I}_{040}P(k_2)P+\mathcal{I}_{004}P(k_3)\Big]\Big\}+\frac{\mathcal{I}_{000}}{\bar{n}^2} \end{aligned} \tag{26}$$

Then the quadrupole and hexadecapole, defined as

$$B_2(k_1,k_2,k_3) = \int_{-1}^{+1} d\mu_1 \int_0^{2\pi} d\xi B(k_1,k_2,k_2,\mu_1,\xi)\Big[\frac{1}{4}\sqrt{\frac{5}{\pi}}(3\mu_1^2-1)\Big] \tag{27}$$

$$B_4(k_1,k_2,k_3) = \int_{-1}^{+1} d\mu_1 \int_0^{2\pi} d\xi B(k_1,k_2,k_2,\mu_1,\xi)\Big[\frac{3}{16}\sqrt{\frac{1}{\pi}}(35\mu_1^4-30\mu_1^2+3)\Big] \tag{28}$$

can be readily written starting from eq.s (21)-(25), replacing the $\mathcal{I}_{\alpha\beta\gamma}$ integrals with the quantities

$$\mathcal{J}^{(2)}_{\alpha\beta\gamma} \equiv \frac{1}{4}\sqrt{\frac{5}{\pi}}\,(3\,\mathcal{I}_{\alpha+2\,\beta\,\gamma}-\mathcal{I}_{\alpha\,\beta\,\gamma})\,, \tag{29}$$

in the quadrupole case and with

$$\mathcal{J}^{(4)}_{\alpha\beta\gamma} \equiv \frac{3}{16\sqrt{\pi}}\,(35\,\mathcal{I}_{\alpha+4\,\beta\,\gamma}-30\mathcal{I}_{\alpha+2\,\beta\,\gamma}+3\mathcal{I}_{\alpha\,\beta\,\gamma})\,, \tag{30}$$

for the hexadecapole.

References

[1] B. P. Abbott, R. Abbott, T. D. Abbott, M. R. Abernathy, F. Acernese, K. Ackley, C. Adams, T. Adams, P. Addesso, R. X. Adhikari, and et al. Observation of Gravitational Waves from a Binary Black Hole Merger. *Physical Review Letters*, 116(6):061102, Feb. 2016.

[2] M. M. Abidi and T. Baldauf. Cubic halo bias in Eulerian and Lagrangian space. *Journal of Cosmology and Astro-Particle Physics*, 2018(7):029, Jul 2018.

[3] N. Agarwal, V. Desjacques, D. Jeong, and F. Schmidt. Information content in the redshift-space galaxy power spectrum and bispectrum. *Journal of Cosmology and Astro-Particle Physics*, 2021(3):021, Mar. 2021.

[4] S. Alam, M. Ata, S. Bailey, F. Beutler, D. Bizyaev, J. A. Blazek, A. S. Bolton, J. R. Brownstein, A. Burden, C.-H. Chuang, J. Comparat, A. J. Cuesta, K. S. Dawson, D. J. Eisenstein, S. Escoffier, H. Gil-Marín, J. N. Grieb, N. Hand, S. Ho, K. Kinemuchi, D. Kirkby, F. Kitaura, E. Malanushenko, V. Malanushenko, C. Maraston, C. K. McBride, R. C. Nichol, M. D. Olmstead, D. Oravetz, N. Padmanabhan, N. Palanque-Delabrouille, K. Pan, M. Pellejero-Ibanez, W. J. Percival, P. Petitjean, F. Prada, A. M. Price-Whelan, B. A. Reid, S. A. Rodríguez-Torres, N. A. Roe, A. J. Ross, N. P. Ross, G. Rossi, J. A. Rubiño-Martín, S. Saito, S. Salazar-Albornoz, L. Samushia, A. G. Sánchez, S. Satpathy, D. J. Schlegel, D. P. Schneider, C. G. Scóccola, H.-J. Seo, E. S. Sheldon, A. Simmons, A. Slosar, M. A. Strauss, M. E. C. Swanson, D. Thomas, J. L. Tinker, R. Tojeiro, M. V. Magaña, J. A. Vazquez, L. Verde, D. A. Wake, Y. Wang, D. H. Weinberg, M. White, W. M. Wood-Vasey, C. Yèche, I. Zehavi, Z. Zhai, and G.-B. Zhao. The clustering of galaxies in the completed SDSS-III Baryon Oscillation Spectroscopic Survey: cosmological analysis of the DR12 galaxy sample. *Mon. Not. R. Astron. Soc.* , 470:2617–2652, Sept. 2017.

[5] D. Alkhanishvili, C. Porciani, E. Sefusatti, M. Biagetti, A. Lazanu, A. Oddo, and V. Yankelevich. The reach of next-to-leading-order perturbation theory for the matter bispectrum. *arXiv e-prints*, page arXiv:2107.08054, July 2021.

[6] L. Anderson, É. Aubourg, S. Bailey, F. Beutler, V. Bhardwaj, M. Blanton, A. S. Bolton, J. Brinkmann, J. R. Brownstein, A. Burden, C.-H. Chuang, A. J. Cuesta, K. S. Dawson, D. J. Eisenstein, S. Escoffier, J. E. Gunn, H. Guo, S. Ho, K. Honscheid, C. Howlett, D. Kirkby, R. H. Lupton, M. Manera, C. Maraston, C. K. McBride, O. Mena, F. Montesano, R. C. Nichol, S. E. Nuza, M. D. Olmstead, N. Padmanabhan, N. Palanque-Delabrouille, J. Parejko, W. J. Percival, P. Petitjean, F. Prada, A. M.

Price-Whelan, B. Reid, N. A. Roe, A. J. Ross, N. P. Ross, C. G. Sabiu, S. Saito, L. Samushia, A. G. Sánchez, D. J. Schlegel, D. P. Schneider, C. G. Scoccola, H.-J. Seo, R. A. Skibba, M. A. Strauss, M. E. C. Swanson, D. Thomas, J. L. Tinker, R. Tojeiro, M. V. Magaña, L. Verde, D. A. Wake, B. A. Weaver, D. H. Weinberg, M. White, X. Xu, C. Yèche, I. Zehavi, and G.-B. Zhao. The clustering of galaxies in the SDSS-III Baryon Oscillation Spectroscopic Survey: baryon acoustic oscillations in the Data Releases 10 and 11 Galaxy samples. *Mon. Not. R. Astron. Soc.* , 441:24–62, June 2014.

[7] T. W. Anderson. *An introduction to multivariate statistical analysis*. Wiley New York, 1958.

[8] G. Aricò, R. E. Angulo, and M. Zennaro. Accelerating Large-Scale-Structure data analyses by emulating Boltzmann solvers and Lagrangian Perturbation Theory. *arXiv e-prints*, page arXiv:2104.14568, Apr. 2021.

[9] N. Arkani-Hamed, P. Creminelli, S. Mukohyama, and M. Zaldarriaga. Ghost inflation. *Journal of Cosmology and Astro-Particle Physics*, 4:1–+, Apr. 2004.

[10] C. Armendariz-Picon and J. T. Neelakanta. How Cold is Cold Dark Matter? *ArXiv e-prints*, Sept. 2013.

[11] V. Assassi, D. Baumann, D. Green, and M. Zaldarriaga. Renormalized halo bias. *Journal of Cosmology and Astro-Particle Physics*, 8:056, Aug. 2014.

[12] T. Baldauf, M. Mirbabayi, M. Simonović, and M. Zaldarriaga. Equivalence principle and the baryon acoustic peak. *Phys. Rev. D* , 92(4):043514, Aug. 2015.

[13] T. Baldauf, U. Seljak, V. Desjacques, and P. McDonald. Evidence for quadratic tidal tensor bias from the halo bispectrum. *Phys. Rev. D* , 86(8):083540, Oct. 2012.

[14] T. Baldauf, U. Seljak, R. E. Smith, N. Hamaus, and V. Desjacques. Halo stochasticity from exclusion and nonlinear clustering. *Phys. Rev. D* , 88(8):083507, Oct. 2013.

[15] A. Barreira. The squeezed matter bispectrum covariance with responses. *Journal of Cosmology and Astro-Particle Physics*, 2019(3):008, Mar. 2019.

[16] A. Barreira, T. Lazeyras, and F. Schmidt. Galaxy bias from forward models: linear and second-order bias of IllustrisTNG galaxies. *Journal of Cosmology and Astro-Particle Physics*, 2021(8):029, Aug. 2021.

[17] D. Baumann, A. Nicolis, L. Senatore, and M. Zaldarriaga. Cosmological non-linearities as an effective fluid. *Journal of Cosmology and Astro-Particle Physics*, 2012(7):051, July 2012.

[18] D. J. Baumgart and J. N. Fry. Fourier spectra of three-dimensional data. *Astrophys. J.* , 375:25–34, July 1991.

[19] F. Bernardeau, S. Colombi, E. Gaztañaga, and R. Scoccimarro. Large-scale structure of the universe and cosmological perturbation theory. Phys. Rep., 367:1–3, Sept. 2002.

[20] F. Bernardeau and J.-P. Uzan. Non-Gaussianity in multifield inflation. *Phys. Rev. D* , 66(10):103506, Nov. 2002.

[21] F. Beutler, E. Castorina, and P. Zhang. Interpreting measurements of the anisotropic galaxy power spectrum. *Journal of Cosmology and Astro-Particle Physics*, 3:040, Mar. 2019.

[22] F. Beutler, S. Saito, H.-J. Seo, J. Brinkmann, K. S. Dawson, D. J. Eisenstein, A. Font-Ribera, S. Ho, C. K. McBride, F. Montesano, W. J. Percival, A. J. Ross, N. P. Ross, L. Samushia, D. J. Schlegel, A. G. Sánchez, J. L. Tinker, and B. A. Weaver. The clustering of galaxies in the SDSS-III Baryon Oscillation Spectroscopic Survey: testing gravity with redshift space distortions using the power spectrum multipoles. *Mon. Not. R. Astron. Soc.* , 443:1065–1089, Sept. 2014.

[23] F. Beutler, H.-J. Seo, A. J. Ross, P. McDonald, S. Saito, A. S. Bolton, J. R. Brownstein, C.-H. Chuang, A. J. Cuesta, D. J. Eisenstein, A. Font-Ribera, J. N. Grieb, N. Hand, F.-S. Kitaura, C. Modi, R. C. Nichol, W. J. Percival, F. Prada, S. Rodriguez-Torres, N. A. Roe, N. P. Ross, S. Salazar-Albornoz, A. G. Sánchez, D. P. Schneider, A. Slosar, J. Tinker, R. Tojeiro, M. Vargas-Magaña, and J. A. Vazquez. The clustering of galaxies in the completed SDSS-III Baryon Oscillation Spectroscopic Survey: baryon acoustic oscillations in the Fourier space. *Mon. Not. R. Astron. Soc.* , 464:3409–3430, Jan. 2017.

[24] F. Beutler, H.-J. Seo, S. Saito, C.-H. Chuang, A. J. Cuesta, D. J. Eisenstein, H. Gil-Marín, J. N. Grieb, N. Hand, F.-S. Kitaura, C. Modi, R. C. Nichol, M. D. Olmstead, W. J. Percival, F. Prada, A. G. Sánchez, S. Rodriguez-Torres, A. J. Ross, N. P. Ross, D. P. Schneider, J. Tinker, R. Tojeiro, and M. Vargas-Magaña. The clustering of galaxies in the completed SDSS-III Baryon Oscillation Spectroscopic Survey: anisotropic galaxy clustering in Fourier space. *Mon. Not. R. Astron. Soc.* , 466:2242–2260, Apr. 2017.

[25] M. Biagetti, L. Castiblanco, J. Noreña, and E. Sefusatti. The Covariance of Squeezed Bispectrum Configurations. *arXiv e-prints*, page arXiv:2111.05887, Nov. 2021.

[26] D. Bianchi, H. Gil-Marín, R. Ruggeri, and W. J. Percival. Measuring line-of-sight-dependent Fourier-space clustering using FFTs. *Mon. Not. R. Astron. Soc.* , 453:L11–L15, Oct. 2015.

[27] D. Blas, M. Garny, M. M. Ivanov, and S. Sibiryakov. Time-sliced perturbation theory for large scale structure I: general formalism. *Journal of Cosmology and Astro-Particle Physics*, 2016(7):052, Jul 2016.

[28] J. Byun and E. Krause. Modal compression of the redshift-space galaxy bispectrum, 2022.

[29] G. Cabass, M. Ivanov, O. Philcox, M. Simonović, and M. Zaldarriaga. Constraints on multi-field inflation from the boss galaxy survey, 04 2022.

[30] G. Cabass, M. M. Ivanov, O. H. E. Philcox, M. Simonović, and M. Zaldarriaga. Constraints on single-field inflation from the boss galaxy survey, 2022.

[31] J. J. M. Carrasco, M. P. Hertzberg, and L. Senatore. The effective field theory of cosmological large scale structures. *Journal of High Energy Physics*, 9:82, Sept. 2012.

[32] E. Castorina and M. White. Beyond the plane-parallel approximation for redshift surveys. *Mon. Not. R. Astron. Soc.* , 476:4403–4417, June 2018.

[33] K. C. Chan, R. Scoccimarro, and R. K. Sheth. Gravity and large-scale nonlocal bias. *Phys. Rev. D* , 85(8):083509, Apr. 2012.

[34] A. Chudaykin and M. M. Ivanov. Measuring neutrino masses with large-scale structure: Euclid forecast with controlled theoretical error. *Journal of Cosmology and Astro-Particle Physics*, 2019(11):034, Nov. 2019.

[35] M. Colavincenzo, E. Sefusatti, P. Monaco, L. Blot, M. Crocce, M. Lippich, A. G. Sánchez, M. A. Alvarez, A. Agrawal, S. Avila, A. Balaguera-Antolínez, R. Bond, S. Codis, C. Dalla Vecchia, A. Dorta, P. Fosalba, A. Izard, F.-S. Kitaura, M. Pellejero-Ibanez, G. Stein, M. Vakili, and G. Yepes. Comparing approximate methods for mock catalogues and covariance matrices - III: bispectrum. *Mon. Not. R. Astron. Soc.* , 482:4883–4905, Feb. 2019.

[36] S. Colombi, A. Jaffe, D. Novikov, and C. Pichon. Accurate estimators of power spectra in N-body simulations. *Mon. Not. R. Astron. Soc.* , 393:511–526, Feb. 2009.

[37] P. Creminelli, G. D'Amico, M. Musso, and J. Noreña. The (not so) squeezed limit of the primordial 3-point function. *Journal of Cosmology and Astro-Particle Physics*, 11:38, Nov. 2011.

[38] G. D'Amico, Y. Donath, M. Lewandowski, L. Senatore, and P. Zhang. The boss bispectrum analysis at one loop from the effective field theory of large-scale structure, 2022.

[39] G. d'Amico, J. Gleyzes, N. Kokron, K. Markovic, L. Senatore, P. Zhang, F. Beutler, and H. Gil-Marín. The cosmological analysis of the SDSS/BOSS data from the Effective Field Theory of Large-Scale Structure. *Journal of Cosmology and Astro-Particle Physics*, 2020(5):005, May 2020.

[40] G. D'Amico, M. Lewandowski, L. Senatore, and P. Zhang. Limits on primordial non-gaussianities from boss galaxy-clustering data, 2022.

[41] A. Dekel and O. Lahav. Stochastic Nonlinear Galaxy Biasing. *Astrophys. J.* , 520(1):24–34, Jul 1999.

[42] DES Collaboration, T. M. C. Abbott, F. B. Abdalla, S. Avila, M. Banerji, E. Baxter, K. Bechtol, M. R. Becker, E. Bertin, J. Blazek, S. L. Bridle, D. Brooks, D. Brout, D. L. Burke, A. Campos, A. Carnero Rosell, M. Carrasco Kind, J. Carretero, F. J. Castander, R. Cawthon, C. Chang, A. Chen, M. Crocce, C. E. Cunha, L. N. da Costa, C. Davis, J. De Vicente, J. DeRose, S. Desai, E. Di Valentino, H. T. Diehl, J. P. Dietrich, S. Dodelson, P. Doel, A. Drlica-Wagner, T. F. Eifler, J. Elvin-Poole, A. E. Evrard, E. Fernandez, A. Ferté, B. Flaugher, P. Fosalba, J. Frieman, J. García-Bellido, D. W. Gerdes, T. Giannantonio, D. Gruen, R. A. Gruendl, J. Gschwend, G. Gutierrez, W. G. Hartley, D. L. Hollowood, K. Honscheid, B. Hoyle, D. Huterer, B. Jain, T. Jeltema, M. W. G. Johnson, M. D. Johnson, A. G. Kim, E. Krause, K. Kuehn, N. Kuropatkin, O. Lahav, S. Lee, P. Lemos, C. D. Leonard, T. S. Li, M. Lima, H. Lin, M. A. G. Maia, J. L. Marshall, P. Martini, F. Menanteau, C. J. Miller, R. Miquel, V. Miranda, J. J. Mohr, J. Muir, R. C. Nichol, B. Nord, R. L. C. Ogando, A. A. Plazas, M. Raveri, R. P. Rollins, A. K. Romer, A. Roodman, R. Rosenfeld, S. Samuroff, E. Sanchez, V. Scarpine, R. Schindler, M. Schubnell, D. Scolnic, L. F. Secco, S. Serrano, I. Sevilla-Noarbe, M. Smith, M. Soares-Santos, F. Sobreira, E. Suchyta, M. E. C. Swanson, G. Tarle, D. Thomas, M. A. Troxel, V. Vikram, A. R. Walker, N. Weaverdyck, R. H. Wechsler, J. Weller, B. Yanny, Y. Zhang, and J. Zuntz. Dark Energy Survey Year 1 Results: Constraints on Extended Cosmological Models from Galaxy Clustering and Weak Lensing. *ArXiv e-prints*, Oct. 2018.

[43] DESI Collaboration, A. Aghamousa, J. Aguilar, S. Ahlen, S. Alam, L. E. Allen, C. Allende Prieto, J. Annis, S. Bailey, C. Balland, and et al. The DESI Experiment Part I: Science,Targeting, and Survey Design. *ArXiv e-prints*, Oct. 2016.

[44] V. Desjacques. Baryon acoustic signature in the clustering of density maxima. *Phys. Rev. D* , 78(10):103503–+, Nov. 2008.

[45] V. Desjacques, M. Crocce, R. Scoccimarro, and R. K. Sheth. Modeling scale-dependent bias on the baryonic acoustic scale with the statistics of peaks of Gaussian random fields. *Phys. Rev. D* , 82(10):103529, Nov. 2010.

[46] V. Desjacques, D. Jeong, and F. Schmidt. Large-scale galaxy bias. Phys. Rep., 733:1–193, Feb. 2018.

[47] V. Desjacques, D. Jeong, and F. Schmidt. The galaxy power spectrum and bispectrum in redshift space. *Journal of Cosmology and Astro-Particle Physics*, 2018(12):035, Dec. 2018.

[48] G. Dvali, A. Gruzinov, and M. Zaldarriaga. New mechanism for generating density perturbations from inflation. *Phys. Rev. D* , 69(2):023505–+, Jan. 2004.

[49] A. Eggemeier, R. Scoccimarro, M. Crocce, A. Pezzotta, and A. G. Sánchez. Testing one-loop galaxy bias: Power spectrum. *Phys. Rev. D* , 102(10):103530, Nov. 2020.

[50] A. Eggemeier, R. Scoccimarro, and R. E. Smith. Bias loop corrections to the galaxy bispectrum. *Phys. Rev. D* , 99(12):123514, June 2019.

[51] A. Eggemeier, R. Scoccimarro, R. E. Smith, M. Crocce, A. Pezzotta, and A. G. Sánchez. Testing one-loop galaxy bias: Joint analysis of power spectrum and bispectrum. *Phys. Rev. D* , 103(12):123550, June 2021.

[52] A. Einstein. Cosmological considerations on the general theory of relativity. In *The Principle of Relativity. Dover Books on Physics. June 1*, pages 175–188. 1952.

[53] D. J. Eisenstein, I. Zehavi, D. W. Hogg, R. Scoccimarro, M. R. Blanton, R. C. Nichol, R. Scranton, H.-J. Seo, M. Tegmark, Z. Zheng, S. F. Anderson, J. Annis, N. A. Bahcall, J. Brinkmann, S. Burles, F. J. Castander, A. Connolly, I. Csabai, M. Doi, M. Fukugita, J. A. Frieman, K. Glazebrook, J. E. Gunn, J. S. Hendry, G. Hennessy, Z. Ivezić, S. Kent, G. R. Knapp, H. Lin, Y.-S. Loh, R. H. Lupton, B. Margon, T. A. McKay, A. Meiksin, J. A. Munn, A. Pope, M. W. Richmond, D. Schlegel, D. P. Schneider, K. Shimasaku, C. Stoughton, M. A. Strauss, M. SubbaRao, A. S. Szalay, I. Szapudi, D. L. Tucker, B. Yanny, and D. G. York. Detection of the baryon acoustic peak in the large-scale correlation function of sdss luminous red galaxies. *Astrophys. J.* , 633:560–574, Nov. 2005.

[54] X. Fang, T. Eifler, and E. Krause. 2D-FFTLog: Efficient computation of real space covariance matrices for galaxy clustering and weak lensing. *arXiv e-prints*, page arXiv:2004.04833, Apr. 2020.

[55] H. A. Feldman, N. Kaiser, and J. A. Peacock. Power-spectrum analysis of three-dimensional redshift surveys. *Astrophys. J.* , 426:23–37, May 1994.

[56] P. G. Ferreira, J. Magueijo, and K. M. Gorski. Evidence for non-gaussianity in the cobe dmr 4 year sky maps. *Astrophys. J. Lett.* , 503:L1, Aug. 1998.

[57] D. Foreman-Mackey, D. W. Hogg, D. Lang, and J. Goodman. emcee: The MCMC Hammer. *Publications of the Astronomical Society of the Pacific*, 125(925):306, Mar 2013.

[58] M. Frigo and S. G. Johnson. FFTW: Fastest Fourier Transform in the West, Jan. 2012. Astrophysics Source Code Library.

[59] J. N. Fry and E. Gaztañaga. Biasing and hierarchical statistics in large-scale structure. *Astrophys. J.* , 413:447–452, Aug. 1993.

[60] T. Fujita, V. Mauerhofer, L. Senatore, Z. Vlah, and R. Angulo. Very massive tracers and higher derivative biases. *Journal of Cosmology and Astro-Particle Physics*, 2020(1):009, Jan. 2020.

[61] P. Gagrani and L. Samushia. Information Content of the Angular Multipoles of Redshift-Space Galaxy Bispectrum. *Mon. Not. R. Astron. Soc.* , 467:928–935, May 2017.

[62] A. Gelman, J. B. Carlin, H. S. Stern, and D. B. Rubin. *Bayesian Data Analysis*. Chapman and Hall/CRC, 2nd ed. edition, 2004.

[63] A. Gelman and D. B. Rubin. Inference from Iterative Simulation Using Multiple Sequences. *Statistical Science*, 7(4):457 – 472, 1992.

[64] H. Gil-Marín, J. Noreña, L. Verde, W. J. Percival, C. Wagner, M. Manera, and D. P. Schneider. The power spectrum and bispectrum of SDSS DR11 BOSS galaxies - I. Bias and gravity. *Mon. Not. R. Astron. Soc.* , 451:539–580, July 2015.

[65] H. Gil-Marín, W. J. Percival, J. R. Brownstein, C.-H. Chuang, J. N. Grieb, S. Ho, F.-S. Kitaura, C. Maraston, F. Prada, S. Rodríguez-Torres, A. J. Ross, L. Samushia, D. J. Schlegel, D. Thomas, J. L. Tinker, and G.-B. Zhao. The clustering of galaxies in the SDSS-III Baryon Oscillation Spectroscopic Survey: RSD measurement from the LOS-dependent power spectrum of DR12 BOSS galaxies. *Mon. Not. R. Astron. Soc.* , 460:4188–4209, Aug. 2016.

[66] H. Gil-Marín, W. J. Percival, A. J. Cuesta, J. R. Brownstein, C.-H. Chuang, S. Ho, F.-S. Kitaura, C. Maraston, F. Prada, S. Rodríguez-Torres, A. J. Ross, D. J. Schlegel, D. P. Schneider, D. Thomas, J. L. Tinker, R. Tojeiro, M. Vargas Magaña, and G.-B. Zhao. The clustering of galaxies in the SDSS-III Baryon Oscillation Spectroscopic Survey: BAO measurement from the LOS-dependent power spectrum of DR12 BOSS galaxies. *Mon. Not. R. Astron. Soc.* , 460:4210–4219, Aug. 2016.

[67] H. Gil-Marín, W. J. Percival, L. Verde, J. R. Brownstein, C.-H. Chuang, F.-S. Kitaura, S. A. Rodríguez-Torres, and M. D. Olmstead. The clustering of galaxies in the SDSS-III Baryon Oscillation Spectroscopic Survey: RSD measurement from the power spectrum and bispectrum of the DR12 BOSS galaxies. *Mon. Not. R. Astron. Soc.* , 465:1757–1788, Feb. 2017.

[68] H. Gil-Marín, L. Verde, J. Noreña, A. J. Cuesta, L. Samushia, W. J. Percival, C. Wagner, M. Manera, and D. P. Schneider. The power spectrum and bispectrum of SDSS DR11 BOSS galaxies - II. Cosmological interpretation. *Mon. Not. R. Astron. Soc.* , 452:1914–1921, Sept. 2015.

[69] H. Gil-Marín, C. Wagner, J. Noreña, L. Verde, and W. Percival. Dark matter and halo bispectrum in redshift space: theory and applications. *Journal of Cosmology and Astro-Particle Physics*, 12:029, Dec. 2014.

[70] D. Ginzburg, V. Desjacques, and K. C. Chan. Shot noise and biased tracers: A new look at the halo model. *Phys. Rev. D* , 96(8):083528, Oct. 2017.

[71] D. W. Gong-Bo Zhao, Y. Wang, W. J. Percival, R. Ruggeri, F. Zhu, R. Tojeiro, A. D. Myers, C.-H. Chuang, F. Baumgarten, C. Zhao, H. Gil-Marín, A. J. Ross, E. Burtin, P. Zarrouk, J. Bautista, J. Brinkmann, K. Dawson, J. R. Brownstein, A. de la Macorra, D. P. Schneider, and A. Shafieloo. The clustering of the SDSS-IV extended Baryon Oscillation Spectroscopic Survey DR14 quasar sample: Anisotropic Baryon Acoustic Oscillations measurements in Fourier-space with optimal redshift weights. *ArXiv e-prints*, Jan. 2018.

[72] J. Goodman and J. Weare. Ensemble samplers with affine invariance. *Communications in Applied Mathematics and Computational Science, Vol. 5, No. 1, p. 65-80, 2010*, 5:65–80, 2010.

[73] M. H. Goroff, B. Grinstein, S.-J. Rey, and M. B. Wise. Coupling of modes of cosmological mass density fluctuations. *Astrophys. J.* , 311:6–14, Dec. 1986.

[74] J. N. Grieb, A. G. Sánchez, S. Salazar-Albornoz, and C. Dalla Vecchia. Gaussian covariance matrices for anisotropic galaxy clustering measurements. *Mon. Not. R. Astron. Soc.* , 457:1577–1592, Apr. 2016.

[75] D. Gualdi, H. Gil-Marín, M. Manera, B. Joachimi, and O. Lahav. GEOMAX: beyond linear compression for three-point galaxy clustering statistics. *Mon. Not. R. Astron. Soc.* , 497(1):776–792, July 2020.

[76] D. Gualdi, H. Gil-Marín, and L. Verde. Joint analysis of anisotropic power spectrum, bispectrum and trispectrum: application to N-body simulations. *Journal of Cosmology and Astro-Particle Physics*, 2021(7):008, July 2021.

[77] D. Gualdi and L. Verde. Galaxy redshift-space bispectrum: the importance of being anisotropic. *Journal of Cosmology and Astro-Particle Physics*, 2020(6):041, June 2020.

[78] A. H. Guth. Inflationary universe: A possible solution to the horizon and flatness problems. *Phys. Rev. D*, 23:347–356, Jan 1981.

[79] A. H. Guth, D. I. Kaiser, and Y. Nomura. Inflationary paradigm after Planck 2013. *Physics Letters B*, 733:112–119, June 2014.

[80] C. Hahn and F. Villaescusa-Navarro. Constraining M_ν with the bispectrum. Part II. The information content of the galaxy bispectrum monopole. *Journal of Cosmology and Astro-Particle Physics*, 2021(4):029, Apr. 2021.

[81] C. Hahn, F. Villaescusa-Navarro, E. Castorina, and R. Scoccimarro. Constraining M_ν with the bispectrum. Part I. Breaking parameter degeneracies. *Journal of Cosmology and Astro-Particle Physics*, 2020(3):040, Mar. 2020.

[82] N. Hand, Y. Feng, F. Beutler, Y. Li, C. Modi, U. Seljak, and Z. Slepian. nbodykit: An Open-source, Massively Parallel Toolkit for Large-scale Structure. *Astron. J.* , 156(4):160, Oct. 2018.

[83] J. Hartlap, T. Schrabback, P. Simon, and P. Schneider. The non-Gaussianity of the cosmic shear likelihood or how odd is the Chandra Deep Field South? *Astron. Astrophys.* , 504:689–703, Sept. 2009.

[84] I. Hashimoto, Y. Rasera, and A. Taruya. Precision cosmology with redshift-space bispectrum: A perturbation theory based model at one-loop order. *Phys. Rev. D* , 96(4):043526, Aug. 2017.

[85] G. Hinshaw, D. Larson, E. Komatsu, D. N. Spergel, C. L. Bennett, J. Dunkley, M. R. Nolta, M. Halpern, R. S. Hill, N. Odegard, L. Page, K. M. Smith, J. L. Weiland, B. Gold, N. Jarosik, A. Kogut, M. Limon, S. S. Meyer, G. S. Tucker, E. Wollack, and E. L. Wright. Nine-Year Wilkinson Microwave Anisotropy Probe (WMAP) Observations: Cosmological Parameter Results. *ArXiv e-prints*, Dec. 2012.

[86] E. Hivon, F. R. Bouchet, S. Colombi, and R. Juszkiewicz. Redshift distortions of clustering: a Lagrangian approach. *Astron. Astrophys.* , 298:643, June 1995.

[87] E. Hubble. A relation between distance and radial velocity among extra-galactic nebulae. *Proceedings of the National Academy of Sciences of the United States of America*, 15(3):168–173, 1929.

[88] M. M. Ivanov, O. H. E. Philcox, T. Nishimichi, M. Simonović, M. Takada, and M. Zaldarriaga. Precision analysis of the redshift-space galaxy bispectrum. *arXiv e-prints*, page arXiv:2110.10161, Oct. 2021.

[89] M. M. Ivanov and S. Sibiryakov. Infrared resummation for biased tracers in redshift space. *Journal of Cosmology and Astro-Particle Physics*, 2018(7):053, Jul 2018.

[90] M. M. Ivanov, M. Simonović, and M. Zaldarriaga. Cosmological parameters from the BOSS galaxy power spectrum. *Journal of Cosmology and Astro-Particle Physics*, 2020(5):042, May 2020.

[91] Y. P. Jing. Correcting for the Alias Effect When Measuring the Power Spectrum Using a Fast Fourier Transform. *Astrophys. J.* , 620:559–563, Feb. 2005.

[92] A. Joyce, B. Jain, J. Khoury, and M. Trodden. Beyond the cosmological standard model. Phys. Rep., 568:1–98, Mar. 2015.

[93] R. Juszkiewicz, D. H. Weinberg, P. Amsterdamski, M. Chodorowski, and F. Bouchet. Weakly nonlinear Gaussian fluctuations and the edgeworth expansion. *Astrophys. J.* , 442:39–56, Mar. 1995.

[94] N. Kaiser. Clustering in real space and in redshift space. *Mon. Not. R. Astron. Soc.* , 227:1–21, July 1987.

[95] Y. Kobayashi, T. Nishimichi, M. Takada, and H. Miyatake. Full-shape cosmology

analysis of the sdss-iii boss galaxy power spectrum using an emulator-based halo model: A $5\sigma_8$. *Phys. Rev. D*, 105:083517, Apr 2022.

[96] R. Laureijs, J. Amiaux, S. Arduini, J. . Augueres, J. Brinchmann, R. Cole, M. Cropper, C. Dabin, L. Duvet, A. Ealet, and et al. Euclid Definition Study Report. *ArXiv: 1110.3193*, Oct. 2011.

[97] T. Lazeyras and F. Schmidt. Beyond LIMD bias: a measurement of the complete set of third-order halo bias parameters. *Journal of Cosmology and Astro-Particle Physics*, 9:008, Sept. 2018.

[98] T. Lazeyras, C. Wagner, T. Baldauf, and F. Schmidt. Precision measurement of the local bias of dark matter halos. *Journal of Cosmology and Astro-Particle Physics*, 2:018, Feb. 2016.

[99] J. Lesgourgues. The Cosmic Linear Anisotropy Solving System (CLASS) I: Overview. *ArXiv: 1104.2932*, Apr. 2011.

[100] M. Levi, C. Bebek, T. Beers, R. Blum, R. Cahn, D. Eisenstein, B. Flaugher, K. Honscheid, R. Kron, O. Lahav, P. McDonald, N. Roe, D. Schlegel, and representing the DESI collaboration. The DESI Experiment, a whitepaper for Snowmass 2013. *ArXiv: 1308.0847*, Aug. 2013.

[101] A. Lewis. GetDist: a Python package for analysing Monte Carlo samples. *arXiv e-prints*, page arXiv:1910.13970, Oct 2019.

[102] A. Lewis, A. Challinor, and A. Lasenby. Efficient computation of cosmic microwave background anisotropies in closed friedmann-robertson-walker models. *Astrophys. J.* , 538:473–476, Aug. 2000.

[103] M. Lippich, A. G. Sánchez, M. Colavincenzo, E. Sefusatti, P. Monaco, L. Blot, M. Crocce, M. A. Alvarez, A. Agrawal, S. Avila, A. Balaguera-Antolínez, R. Bond, S. Codis, C. Dalla Vecchia, A. Dorta, P. Fosalba, A. Izard, F.-S. Kitaura, M. Pellejero-Ibanez, G. Stein, M. Vakili, and G. Yepes. Comparing approximate methods for mock catalogues and covariance matrices - I. Correlation function. *Mon. Not. R. Astron. Soc.* , 482:1786–1806, Nov. 2019.

[104] L. Lombriser and N. A. Lima. Challenges to self-acceleration in modified gravity from gravitational waves and large-scale structure. *Physics Letters B*, 765:382–385, feb 2017.

[105] S. Matarrese, L. Verde, and A. F. Heavens. Large-scale bias in the universe: bispectrum method. *Mon. Not. R. Astron. Soc.* , 290:651–662, Oct. 1997.

[106] T. Matsubara. Stochasticity of Bias and Nonlocality of Galaxy Formation: Linear Scales. *Astrophys. J.* , 525(2):543–553, Nov. 1999.

[107] P. McDonald. Clustering of dark matter tracers: Renormalizing the bias parameters. *Phys. Rev. D* , 74(10):103512–+, Nov. 2006.

[108] P. McDonald and A. Roy. Clustering of dark matter tracers: generalizing bias for the coming era of precision LSS. *Journal of Cosmology and Astro-Particle Physics*, 8:020, Aug. 2009.

[109] J. E. McEwen, X. Fang, C. M. Hirata, and J. A. Blazek. FAST-PT: a novel algorithm to calculate convolution integrals in cosmological perturbation theory. *Journal of Cosmology and Astro-Particle Physics*, 9:015, Sept. 2016.

[110] A. L. Melott, T. Buchert, and A. G. Weiss. Testing higher-order Lagrangian perturbation theory against numerical simulations. II. Hierarchical models. *Astron. Astrophys.* , 294:345–365, Feb 1995.

[111] P. Monaco. Approximate Methods for the Generation of Dark Matter Halo Catalogs in the Age of Precision Cosmology. *Galaxies*, 4:53, Oct. 2016.

[112] P. Monaco, E. Sefusatti, S. Borgani, M. Crocce, P. Fosalba, R. K. Sheth, and T. Theuns. An accurate tool for the fast generation of dark matter halo catalogues. *Mon. Not. R. Astron. Soc.* , 433:2389–2402, Aug. 2013.

[113] P. Monaco, T. Theuns, and G. Taffoni. The pinocchio algorithm: pinpointing orbit-crossing collapsed hierarchical objects in a linear density field. *Mon. Not. R. Astron. Soc.* , 331:587–608, Apr. 2002.

[114] E. Munari, P. Monaco, E. Sefusatti, E. Castorina, F. G. Mohammad, S. Anselmi, and S. Borgani. Improving fast generation of halo catalogues with higher order Lagrangian perturbation theory. *Mon. Not. R. Astron. Soc.* , 465:4658–4677, Mar. 2017.

[115] E. O. Nadler, A. Perko, and L. Senatore. On the bispectra of very massive tracers in the Effective Field Theory of Large-Scale Structure. *Journal of Cosmology and Astro-Particle Physics*, 2:058, Feb. 2018.

[116] T. Nishimichi. Scale dependence of the halo bias in general local-type non-Gaussian models I: analytical predictions and consistency relations. *Journal of Cosmology and Astro-Particle Physics*, 2012(8):037, Aug. 2012.

[117] T. Nishimichi, G. D'Amico, M. M. Ivanov, L. Senatore, M. Simonović, M. Takada, M. Zaldarriaga, and P. Zhang. Blinded challenge for precision cosmology with large-scale structure: Results from effective field theory for the redshift-space galaxy power spectrum. *Phys. Rev. D* , 102(12):123541, Dec. 2020.

[118] A. Oddo, F. Rizzo, E. Sefusatti, C. Porciani, and P. Monaco. Cosmological parameters from the likelihood analysis of the galaxy power spectrum and bispectrum in real space. *Journal of Cosmology and Astro-Particle Physics*, 2021(11):038, Nov. 2021.

[119] A. Oddo, E. Sefusatti, C. Porciani, P. Monaco, and A. G. Sánchez. Toward a robust inference method for the galaxy bispectrum: likelihood function and model selection. *Journal of Cosmology and Astro-Particle Physics*, 2020(3):056, Mar. 2020.

[120] K. Pardede, F. Rizzo, M. Biagetti, E. Castorina, E. Sefusatti, and P. Monaco. Bispectrum-window convolution via hankel transform, 2022.

[121] D. W. Pearson and L. Samushia. A Detection of the Baryon Acoustic Oscillation features in the SDSS BOSS DR12 Galaxy Bispectrum. *Mon. Not. R. Astron. Soc.* , 478(4):4500–4512, Aug. 2018.

[122] P. J. E. Peebles. *The large-scale structure of the universe*. Princeton, N.J., Princeton University Press, 1980. 435 p., 1980.

[123] P. J. E. Peebles. Large-scale background temperature and mass fluctuations due to scale-invariant primeval perturbations. *Astrophys. J. Lett.* , 263:L1–L5, Dec. 1982.

[124] W. J. Percival, A. J. Ross, A. G. Sánchez, L. Samushia, A. Burden, R. Crittenden, A. J. Cuesta, M. V. Magana, M. Manera, F. Beutler, C.-H. Chuang, D. J. Eisenstein, S. Ho, C. K. McBride, F. Montesano, N. Padmanabhan, B. Reid, S. Saito, D. P. Schneider, H.-J. Seo, R. Tojeiro, and B. A. Weaver. The clustering of Galaxies in the SDSS-III Baryon Oscillation Spectroscopic Survey: including covariance matrix errors. *Mon. Not. R. Astron. Soc.* , 439:2531–2541, Apr. 2014.

[125] A. Perko, L. Senatore, E. Jennings, and R. H. Wechsler. Biased Tracers in Redshift Space in the EFT of Large-Scale Structure. *ArXiv e-prints*, Oct. 2016.

[126] O. H. E. Philcox. Cosmology Without Window Functions: Cubic Estimators for the Galaxy Bispectrum. *arXiv e-prints*, page arXiv:2107.06287, July 2021.

[127] O. H. E. Philcox and M. M. Ivanov. The BOSS DR12 Full-Shape Cosmology: ΛCDM Constraints from the Large-Scale Galaxy Power Spectrum and Bispectrum Monopole. *arXiv e-prints*, page arXiv:2112.04515, Dec. 2021.

[128] O. H. E. Philcox and Z. Slepian. Beyond Yamamoto: Anisotropic Power Spectra and Correlation Functions with Pairwise Lines-of-Sight. *arXiv e-prints*, page arXiv:2102.08384, Feb. 2021.

[129] Planck Collaboration, N. Aghanim, Y. Akrami, M. Ashdown, J. Aumont, C. Baccigalupi, M. Ballardini, A. J. Banday, R. B. Barreiro, N. Bartolo, S. Basak, R. Battye, K. Benabed, J. P. Bernard, M. Bersanelli, P. Bielewicz, J. J. Bock, J. R. Bond, J. Borrill, F. R. Bouchet, F. Boulanger, M. Bucher, C. Burigana, R. C. Butler, E. Calabrese, J. F. Cardoso, J. Carron, A. Challinor, H. C. Chiang, J. Chluba, L. P. L. Colombo, C. Combet, D. Contreras, B. P. Crill, F. Cuttaia, P. de Bernardis, G. de Zotti, J. Delabrouille, J. M. Delouis, E. Di Valentino, J. M. Diego, O. Doré, M. Douspis, A. Ducout, X. Dupac, S. Dusini, G. Efstathiou, F. Elsner, T. A. Enßlin, H. K. Eriksen,

Y. Fantaye, M. Farhang, J. Fergusson, R. Fernandez-Cobos, F. Finelli, F. Forastieri, M. Frailis, A. A. Fraisse, E. Franceschi, A. Frolov, S. Galeotta, S. Galli, K. Ganga, R. T. Génova-Santos, M. Gerbino, T. Ghosh, J. González-Nuevo, K. M. Górski, S. Gratton, A. Gruppuso, J. E. Gudmundsson, J. Hamann, W. Handley, F. K. Hansen, D. Herranz, S. R. Hildebrandt, E. Hivon, Z. Huang, A. H. Jaffe, W. C. Jones, A. Karakci, E. Keihänen, R. Keskitalo, K. Kiiveri, J. Kim, T. S. Kisner, L. Knox, N. Krachmalnicoff, M. Kunz, H. Kurki-Suonio, G. Lagache, J. M. Lamarre, A. Lasenby, M. Lattanzi, C. R. Lawrence, M. Le Jeune, P. Lemos, J. Lesgourgues, F. Levrier, A. Lewis, M. Liguori, P. B. Lilje, M. Lilley, V. Lindholm, M. López-Caniego, P. M. Lubin, Y. Z. Ma, J. F. Macías-Pérez, G. Maggio, D. Maino, N. Mandolesi, A. Mangilli, A. Marcos-Caballero, M. Maris, P. G. Martin, M. Martinelli, E. Martínez-González, S. Matarrese, N. Mauri, J. D. McEwen, P. R. Meinhold, A. Melchiorri, A. Mennella, M. Migliaccio, M. Millea, S. Mitra, M. A. Miville-Deschênes, D. Molinari, L. Montier, G. Morgante, A. Moss, P. Natoli, H. U. Nørgaard-Nielsen, L. Pagano, D. Paoletti, B. Partridge, G. Patanchon, H. V. Peiris, F. Perrotta, V. Pettorino, F. Piacentini, L. Polastri, G. Polenta, J. L. Puget, J. P. Rachen, M. Reinecke, M. Remazeilles, A. Renzi, G. Rocha, C. Rosset, G. Roudier, J. A. Rubiño-Martín, B. Ruiz-Granados, L. Salvati, M. Sandri, M. Savelainen, D. Scott, E. P. S. Shellard, C. Sirignano, G. Sirri, L. D. Spencer, R. Sunyaev, A. S. Suur-Uski, J. A. Tauber, D. Tavagnacco, M. Tenti, L. Toffolatti, M. Tomasi, T. Trombetti, L. Valenziano, J. Valiviita, B. Van Tent, L. Vibert, P. Vielva, F. Villa, N. Vittorio, B. D. Wandelt, I. K. Wehus, M. White, S. D. M. White, A. Zacchei, and A. Zonca. Planck 2018 results. VI. Cosmological parameters. *Astron. Astrophys.* , 641:A6, Sept. 2020.

[130] D. Potter, J. Stadel, and R. Teyssier. PKDGRAV3: beyond trillion particle cosmological simulations for the next era of galaxy surveys. *Computational Astrophysics and Cosmology*, 4(1):2, May 2017.

[131] L. Pozzetti, C. M. Hirata, J. E. Geach, A. Cimatti, C. Baugh, O. Cucciati, A. Merson, P. Norberg, and D. Shi. Modelling the number density of hi/iemitters for future spectroscopic near-IR space missions. *Astronomy &amp Astrophysics*, 590:A3, apr 2016.

[132] S. Pueblas and R. Scoccimarro. Generation of vorticity and velocity dispersion by orbit crossing. *Phys. Rev. D* , 80(4):043504, Aug. 2009.

[133] A. G. Riess, A. V. Filippenko, P. Challis, A. Clocchiatti, A. Diercks, P. M. Garnavich, R. L. Gilliland, C. J. Hogan, S. Jha, R. P. Kirshner, B. Leibundgut, M. M. Phillips, D. Reiss, B. P. Schmidt, R. A. Schommer, R. C. Smith, J. Spyromilio, C. Stubbs, N. B. Suntzeff, and J. Tonry. Observational Evidence from Supernovae for an Accelerating Universe and a Cosmological Constant. *Astron. J.* , 116:1009–1038, Sept. 1998.

[134] A. G. Riess, L. Macri, S. Casertano, H. Lampeitl, H. C. Ferguson, A. V. Filippenko,

S. W. Jha, W. Li, and R. Chornock. A 3% Solution: Determination of the Hubble Constant with the Hubble Space Telescope and Wide Field Camera 3. *Astrophys. J.* , 730:119, Apr. 2011.

[135] A. G. Riess, W. Yuan, L. M. Macri, D. Scolnic, D. Brout, S. Casertano, D. O. Jones, Y. Murakami, L. Breuval, T. G. Brink, A. V. Filippenko, S. Hoffmann, S. W. Jha, W. D. Kenworthy, J. Mackenty, B. E. Stahl, and W. Zheng. A comprehensive measurement of the local value of the hubble constant with 1 km/s/mpc uncertainty from the hubble space telescope and the sh0es team, 2021.

[136] F. Rizzo, C. Moretti, K. Pardede, A. Eggemeier, A. Oddo, E. Sefusatti, C. Porciani, and P. Monaco. The halo bispectrum multipoles in redshift space, 2022.

[137] H. P. Robertson. Kinematics and World-Structure. *Astrophys. J.* , 82:284, Nov. 1935.

[138] V. C. Rubin and J. F. W. Kent. Rotation of the andromeda nebula from a spectroscopic survey of emission regions. *The Astrophysical Journal*, 159:379, feb 1970.

[139] R. Ruggeri, W. J. Percival, H. Gil-Marín, F. Beutler, E.-M. Mueller, F. Zhu, N. Padmanabhan, G.-B. Zhao, P. Zarrouk, A. G. Sánchez, J. Bautista, J. Brinkmann, J. R. Brownstein, F. Baumgarten, C.-H. Chuang, K. Dawson, H.-J. Seo, R. Tojeiro, and C. Zhao. The clustering of the SDSS-IV extended Baryon Oscillation Spectroscopic Survey DR14 quasar sample: measuring the evolution of the growth rate using redshift-space distortions between redshift 0.8 and 2.2. *Mon. Not. R. Astron. Soc.* , 483:3878–3887, Mar. 2019.

[140] L. Samushia, E. Branchini, and W. Percival. Geometric Biases in Power-Spectrum Measurements. *ArXiv e-prints*, Apr. 2015.

[141] A. G. Sánchez, J. N. Grieb, S. Salazar-Albornoz, S. Alam, F. Beutler, A. J. Ross, J. R. Brownstein, C.-H. Chuang, A. J. Cuesta, D. J. Eisenstein, F.-S. Kitaura, W. J. Percival, F. Prada, S. Rodríguez-Torres, H.-J. Seo, J. Tinker, R. Tojeiro, M. Vargas-Magaña, J. A. Vazquez, and G.-B. Zhao. The clustering of galaxies in the completed SDSS-III Baryon Oscillation Spectroscopic Survey: combining correlated Gaussian posterior distributions. *Mon. Not. R. Astron. Soc.* , 464:1493–1501, Jan. 2017.

[142] A. G. Sánchez, R. Scoccimarro, M. Crocce, J. N. Grieb, S. Salazar-Albornoz, C. Dalla Vecchia, M. Lippich, F. Beutler, J. R. Brownstein, C.-H. Chuang, D. J. Eisenstein, F.-S. Kitaura, M. D. Olmstead, W. J. Percival, F. Prada, S. Rodríguez-Torres, A. J. Ross, L. Samushia, H.-J. Seo, J. Tinker, R. Tojeiro, M. Vargas-Magaña, Y. Wang, and G.-B. Zhao. The clustering of galaxies in the completed SDSS-III Baryon Oscillation Spectroscopic Survey: Cosmological implications of the configuration-space clustering wedges. *Mon. Not. R. Astron. Soc.* , 464:1640–1658, Jan. 2017.

[143] F. Schmidt. Towards a self-consistent halo model for the nonlinear large-scale structure. *Phys. Rev. D* , 93(6):063512, Mar. 2016.

[144] R. Scoccimarro. The bispectrum: From theory to observations. *Astrophys. J.* , 544:597–615, Dec. 2000.

[145] R. Scoccimarro. Gravitational clustering from χ^2 initial conditions. *Astrophys. J.* , 542:1–8, Oct. 2000.

[146] R. Scoccimarro. Redshift-space distortions, pairwise velocities, and nonlinearities. *Phys. Rev. D* , 70(8):083007–+, Oct. 2004.

[147] R. Scoccimarro. Fast estimators for redshift-space clustering. *Phys. Rev. D* , 92(8):083532, Oct. 2015.

[148] R. Scoccimarro, H. M. P. Couchman, and J. A. Frieman. The bispectrum as a signature of gravitational instability in redshift space. *Astrophys. J.* , 517:531–540, June 1999.

[149] E. Sefusatti, M. Crocce, and V. Desjacques. The halo bispectrum in N-body simulations with non-Gaussian initial conditions. *Mon. Not. R. Astron. Soc.* , 425:2903–2930, Oct. 2012.

[150] E. Sefusatti, M. Crocce, R. Scoccimarro, and H. M. P. Couchman. Accurate estimators of correlation functions in Fourier space. *Mon. Not. R. Astron. Soc.* , 460:3624–3636, Aug. 2016.

[151] E. Sellentin and A. F. Heavens. Parameter inference with estimated covariance matrices. *Mon. Not. R. Astron. Soc.* , 456:L132–L136, Feb. 2016.

[152] A. Semenaite, A. G. Sánchez, A. Pezzotta, J. Hou, R. Scoccimarro, A. Eggemeier, M. Crocce, C.-H. Chuang, A. Smith, C. Zhao, J. R. Brownstein, G. Rossi, and D. P. Schneider. Cosmological implications of the full shape of anisotropic clustering measurements in BOSS and eBOSS. *arXiv e-prints*, page arXiv:2111.03156, Nov. 2021.

[153] H.-J. Seo and D. J. Eisenstein. Probing Dark Energy with Baryonic Acoustic Oscillations from Future Large Galaxy Redshift Surveys. *Astrophys. J.* , 598:720–740, Dec. 2003.

[154] R. K. Sheth, K. C. Chan, and R. Scoccimarro. Nonlocal Lagrangian bias. *Phys. Rev. D* , 87(8):083002, Apr. 2013.

[155] Z. Slepian, D. J. Eisenstein, J. A. Blazek, J. R. Brownstein, C.-H. Chuang, H. Gil-Marín, S. Ho, F.-S. Kitaura, J. E. McEwen, W. J. Percival, A. J. Ross, G. Rossi, H.-J. Seo, A. Slosar, and M. Vargas-Magaña. Constraining the Baryon-Dark Matter Relative Velocity with the Large-Scale 3-Point Correlation Function of the SDSS BOSS DR12 CMASS Galaxies. *ArXiv e-prints*, July 2016.

[156] A. Slosar, V. Iršič, D. Kirkby, S. Bailey, N. G. Busca, T. Delubac, J. Rich, É. Aubourg, J. E. Bautista, V. Bhardwaj, M. Blomqvist, A. S. Bolton, J. Bovy, J. Brownstein,

B. Carithers, R. A. C. Croft, K. S. Dawson, A. Font-Ribera, J.-M. Le Goff, S. Ho, K. Honscheid, K.-G. Lee, D. Margala, P. McDonald, B. Medolin, J. Miralda-Escudé, A. D. Myers, R. C. Nichol, P. Noterdaeme, N. Palanque-Delabrouille, I. Pâris, P. Petitjean, M. M. Pieri, Y. Piškur, N. A. Roe, N. P. Ross, G. Rossi, D. J. Schlegel, D. P. Schneider, N. Suzuki, E. S. Sheldon, U. Seljak, M. Viel, D. H. Weinberg, and C. Yèche. Measurement of baryon acoustic oscillations in the Lyman-α forest fluctuations in BOSS data release 9. *Journal of Cosmology and Astro-Particle Physics*, 4:26, Apr. 2013.

[157] R. E. Smith, R. Scoccimarro, and R. K. Sheth. Scale dependence of halo and galaxy bias: Effects in real space. *Phys. Rev. D* , 75(6):063512–+, Mar. 2007.

[158] Y.-S. Song, A. Taruya, and A. Oka. Cosmology with anisotropic galaxy clustering from the combination of power spectrum and bispectrum. *Journal of Cosmology and Astro-Particle Physics*, 8:007, Aug. 2015.

[159] D. N. Spergel and P. J. Steinhardt. Observational evidence for self-interacting cold dark matter. *Physical Review Letters*, 84(17):3760–3763, apr 2000.

[160] V. Springel, N. Yoshida, and S. D. M. White. GADGET: a code for collisionless and gasdynamical cosmological simulations. *New Astronomy*, 6:79–117, Apr. 2001.

[161] N. S. Sugiyama, S. Saito, F. Beutler, and H.-J. Seo. A complete FFT-based decomposition formalism for the redshift-space bispectrum. *Mon. Not. R. Astron. Soc.* , 484:364–384, Mar. 2019.

[162] A. Taruya, T. Nishimichi, and S. Saito. Baryon acoustic oscillations in 2D: Modeling redshift-space power spectrum from perturbation theory. *Phys. Rev. D* , 82(6):063522, Sept. 2010.

[163] A. Taruya and J. Soda. Stochastic Biasing and the Galaxy-Mass Density Relation in the Weakly Nonlinear Regime. *Astrophys. J.* , 522(1):46–58, Sept. 1999.

[164] A. N. Taylor, B. Joachimi, and T. D. Kitching. Putting the precision in precision cosmology: How accurate should your data covariance matrix be? *Mon. Not. R. Astron. Soc.* , 432:1928–1946, July 2013.

[165] L. Verde, A. F. Heavens, S. Matarrese, and L. Moscardini. Large-scale bias in the universe - ii. redshift-space bispectrum. *Mon. Not. R. Astron. Soc.* , 300:747–756, Nov. 1998.

[166] Z. Vlah, U. Seljak, M. Yat Chu, and Y. Feng. Perturbation theory, effective field theory, and oscillations in the power spectrum. *Journal of Cosmology and Astro-Particle Physics*, 2016(3):057, Mar. 2016.

[167] A. G. Walker. On Milne's Theory of World-Structure*. *Proceedings of the London Mathematical Society*, s2-42(1):90–127, 01 1937.

[168] M. J. Wilson, J. A. Peacock, A. N. Taylor, and S. de la Torre. Rapid modelling of the redshift-space power spectrum multipoles for a masked density field. *Mon. Not. R. Astron. Soc.* , 464:3121–3130, Jan. 2017.

[169] K. Yamamoto, M. Nakamichi, A. Kamino, B. A. Bassett, and H. Nishioka. A Measurement of the Quadrupole Power Spectrum in the Clustering of the 2dF QSO Survey. *Publ. Astron. Soc. Japan* , 58:93–102, Feb. 2006.

[170] V. Yankelevich and C. Porciani. Cosmological information in the redshift-space bispectrum. *Mon. Not. R. Astron. Soc.* , Nov. 2018.

[171] Y. B. Zeldovich. Gravitational instability: An approximate theory for large density perturbations. *Astron. Astrophys.* , 5:84–89, Mar. 1970.

[172] M. Zennaro, R. E. Angulo, S. Contreras, M. Pellejero-Ibáñez, and F. Maion. Priors on lagrangian bias parameters from galaxy formation modelling. *arXiv e-prints*, page arXiv:2110.05408, Oct 2021.

[173] I. Zlatev, L. Wang, and P. J. Steinhardt. Quintessence, cosmic coincidence, and the cosmological constant. *Physical Review Letters*, 82:896–899, Feb. 1999.

[174] F. Zwicky. Die Rotverschiebung von extragalaktischen Nebeln. *Helvetica Physica Acta*, 6:110–127, Jan. 1933.